

UNIVERSITY OF OKLAHOMA  
GRADUATE COLLEGE

THE IMPACT OF PRECIPITATION PHYSICAL PROCESSES ON THE  
POLARIMETRIC RADAR VARIABLES

A DISSERTATION  
SUBMITTED TO THE GRADUATE FACULTY  
in partial fulfillment of the requirements for the  
Degree of  
DOCTOR OF PHILOSOPHY

By  
MATTHEW ROBERT KUMJIAN  
Norman, Oklahoma  
2012

THE IMPACT OF PRECIPITATION PHYSICAL PROCESSES ON THE  
POLARIMETRIC RADAR VARIABLES

A DISSERTATION APPROVED FOR THE  
SCHOOL OF METEOROLOGY

BY

---

Dr. Alexander V. Ryzhkov, Co-Chair

---

Dr. Howard B. Bluestein, Co-Chair

---

Dr. Dušan S. Zrnić

---

Dr. Alan Shapiro

---

Dr. Guifu Zhang

---

Dr. Eric R.I. Abraham

© Copyright by MATTHEW ROBERT KUMJIAN 2012  
All Rights Reserved.

## Acknowledgements

I want to express my gratitude to the members of my doctoral committee, who have dealt with numerous meetings, endless paperwork, and a number of inconveniences without complaints: Alexander Ryzhkov, Eric Abraham, Howie Bluestein, Alan Shapiro, Guifu Zhang, and Dušan Zrníc.

I thank Prof. Guifu Zhang for all the help and encouragement he's given me over the past 6 years. He has always been supportive (and always thought I should have finished within a year or two of starting...). In addition, he provided me the valuable opportunity to teach in his courses, the fun experience of collecting hail, and, of course, several outstanding home-cooked Chinese meals.

Professor Alan Shapiro is a true mentor whose advice has been unwaveringly objective and honest, and whose infectious cynicism is a great source of wisdom and entertainment. I will never forget the camping trips and their valuable life lessons ("There is no such thing as too much garlic"), which I hope to remain a part of! The infamous Grill Fests were the highlights of the semesters. Prof. Shapiro is also one of the few who will show up at a dive bar on a Wednesday night ("F-5 IPA, yeaaa gotta have it!") to hang out with the students, which leaves indelible impressions on all of us.

I thank Professor Eric Abraham for the encouragement and advice given over the years, dating back to our undergraduate physics late-night "help sessions." He has provided some of the best school and career advice I've received, and I highly value his service as outside member on my committee. I hope to make a positive impression on my students as he did for me.

For his willingness to serve as the SoM chair of my committee, I express my

gratitude to Prof. Howie Bluestein. I appreciate his advice and encouragement over the years. When I was a youngster, his appearance in popular books on weather and storms served as an inspiration for me and got me thinking about the University of Oklahoma. I look forward to seeing him in Boulder next year for an excursion “through the melting layer”.

There is much that can be said about the legend himself, Dr. Dušan Zrnić. I am grateful and honored to have been a part of his research group, and for continually making his presence known. I will miss our philosophical talks about all topics, ranging from the meaning of the universe to *Gilgamesh*, and from the absurdities of some religious beliefs to the meaning of being a Professor. He made life in the cubicle enjoyable and entertaining, and his encouragement and helpful suggestions over the years are very much appreciated.

It is impossible to fully express my gratitude to Alexander Ryzhkov, whose guidance, understanding, and mentorship have profoundly influenced my life for the better. Working with him was the best thing that happened for my graduate studies. The number of opportunities he’s given me is incredible, and for this I am thankful. I have learned so much from his leadership and teaching, both in the realms of science (e.g., his profound influence on my academic career) and in life (e.g., the Три Заповеди Российского Ээка; see Appendix B). I strive to be able to one day achieve his level of scientific expertise, and I hope to pass on to future generations of scientists the positive influence he’s had on me. I look forward to our future collaboration and conversations!

Aside from my committee, there are numerous friends and colleagues that have been helpful in innumerable ways. I am thankful for the useful discussions and support

from David Parsons, Evgeni Fedorovich, Kelvin Droegemeier, and Yoshi Sasaki at SoM. I thank the rest of the RRDD group at NSSL (past and present): Valery Melnikov, Terry Schuur, Sebastián Torres, Dick Doviak, Pam Heinselman, Joey Picca, Jelena Andrić, Doug Forsyth, and Tonia Rollins. Great thanks to the “tool maker,” John Krause, whose code was used to produce many of the images presented in this dissertation. At ARRC, I’ve enjoyed my discussions and time with David Bodine, Bob Palmer, Tian Yu, Phil Stepanian, JoAnn Mehl, Krysta Bruehl, Phil Chilson, Jim Kurdzo, Boon Leng Cheong, and Qing Cao. I’d also like to express my thanks to Dan Dawson, Mike French, Jeff Snyder, Mike Buban, Kiel Ortega, Chris Schwarz, Dan Betten, Jana Houser, and the many others with whom I’ve spent fun times and had useful discussions. Thanks to the SoM “moms”, without whom I would still be lost: Celia Jones, Marcia Pallutto, Nancy Campbell, and Becky Steely. I am deeply grateful to Alex Schenkman, Charlotte Wainwright, and Scott and Michelle Ganson for their support and friendship, and for the many (*many*) hours we’ve spent together; I’ve enjoyed every moment of it.

Funding for this work comes from NSF Grant ATM-0532107; NOAA/OAR under NOAA/OU Cooperative Agreements #NA17RJ1227 and #NA11OAR4320072, U.S. Dept. of Commerce; Agreement 7000132024 with the MIT Lincoln Laboratory; and my doctoral fellowship from the University of Bonn, funded by the Deutsche Forschungsgemeinschaft (DFG) as part of the Transregional Research Center on “Patterns in Landsurface-Vegetation-Atmosphere Interactions” (TR32). Data from BOXPOL are courtesy of Meteorologisches Institut der Universität Bonn, with thanks to Clemens Simmer, Silke Trömel, and Malte Diederich. OU-PRIME is owned and

operated by the Atmospheric Radar Research Center at the University of Oklahoma. Research-grade polarimetric radar data from KOUN are possible because of the tireless efforts of CIMMS/NSSL engineers and scientists who maintained and operated the radar. I'd also like to thank Pengfei Zhang and Dan Suppes, for their help in teaching me how to obtain, convert, and display polarimetric radar data from upgraded WSR-88Ds.

Finally, it is with the unwavering love, support, and encouragement from my family that I was able to achieve my doctorate. They have always been my greatest supporters and have never questioned my crazy idea to move to Oklahoma for nearly a decade to pursue study of my childhood fascination with the sky. Thank you so very much for everything that you have done for me.

# Table of Contents

Acknowledgements .....	iv
Table of Contents .....	viii
List of Tables .....	xii
List of Figures.....	xiii
Abstract.....	xxvii
Chapter 0: Introduction.....	1
Chapter 1: Polarimetric Radar Variables: Theoretical Formulation.....	5
1. Electromagnetic Scattering Basics .....	5
2. Calculating the Complex Scattering Functions .....	9
3. The Covariance Matrix.....	12
4. Polarimetric Radar Variables from the Covariance Matrix.....	14
5. Forward-scattering variables .....	19
6. Special cases for angular moments.....	28
Chapter 2: Polarimetric Radar Variables: Physical Description .....	32
1. Radar reflectivity factor.....	32
2. Differential reflectivity factor.....	41
3. Differential propagation phase shift .....	51
4. Co-polar cross-correlation coefficient .....	58
5. Backscatter differential phase shift .....	67
6. Linear depolarization ratio .....	74
7. Co-cross-polar correlation coefficients .....	80
8. Specific attenuation .....	82



9. Specific differential attenuation .....	87
Chapter 3: Artifacts in Dual-Polarization Radar Data.....	94
1. Attenuation / Differential Attenuation.....	94
2. Nonuniform Beam Filling .....	96
3. Depolarization streaks .....	98
4. Polarimetric Three-Body Scattering Signature (PTBSS).....	102
Chapter 4: The Impact of Raindrop Conduction and Temperature on the Polarimetric Radar Variables. ....	108
1. Introduction .....	108
2. Model description.....	108
3. Model Results.....	111
4. Impact of Temperature on Scattering.....	115
Chapter 5: The Impact of Size Sorting on the Polarimetric Radar Variables .....	117
1. Introduction .....	117
2. Size Sorting in Bulk and Bin Model Configurations.....	121
3. Size sorting models.....	124
4. Polarimetric Radar Observations.....	148
5. Discussion.....	154
6. Summary.....	162
Chapter 6: The Impact of Raindrop Evaporation on the Polarimetric Radar Variables. .....	165
1. Introduction. ....	165
2. Physics of Evaporation.....	168

3. Model Description .....	173
4. Model Results .....	180
5. Rainfall Rate Estimation.....	196
6. Comparison with Observations .....	202
7. Summary of Conclusions .....	203
Chapter 7: The Impact of Coalescence on the Polarimetric Radar Variables. ....	207
1. Introduction. ....	207
2. Physics of Coalescence: a <i>Gedankenexperiment</i> .....	209
3. Observed Data. ....	211
4. Microphysical Retrievals: Methods.....	214
5. Microphysical Retrievals: Results.....	217
6. Discussion and Conclusions. ....	222
Chapter 8: The Impact of Freezing on the Polarimetric Radar Variables. ....	224
1. Introduction .....	224
2. Overview of the Physics of Freezing Drops.....	228
3. The Model .....	232
4. Model Results.....	241
5. Discussion and Summary .....	253
Chapter 9: Summary, Conclusions, and Future Work.....	259
Appendix A: Computing the Complex Dielectric Factor.....	263
1. Complex Dielectric Factors for Pure Water and Ice .....	263
2. Complex Dielectric Factors for Mixtures.....	266
3. Impact of the distribution of liquid water on the polarimetric radar variables...	269

Appendix B.....	279
References .....	280

## List of Tables

Table 5.1: Fall speed relations used in Fig. 5.1. In each equation, $D$ is in mm and the fall speed is in $\text{m s}^{-1}$ .	122
Table 6.1: Results of simulated evaporative changes in the polarimetric variables at S and C bands from the three soundings in Fig. 6.9. Simulations used the MP distribution with a rainfall rate aloft of $5 \text{ mm hr}^{-1}$ .	195
Table 6.2: As in Table 1, but the $\Gamma, \mu = -1$ and $\Gamma, \mu = 5$ distributions are used, respectively, the values resulting from each DSD model separated by a comma in the table. Magnitudes of $\Delta\rho_{\text{hv}}$ less than $10^{-4}$ are indicated as $\approx 0$ .	196
Table 6.3: Evaporative change in rainfall rate for each of the three soundings for the three rainfall algorithms $R(Z_H)$ , $R(Z_H, Z_{DR})$ , and $R(K_{DP})$ (eqns. 6.34 – 6.36, respectively) based on the MP DSD along with the “true” rainfall rate calculated from the actual DSD.	198
Table 8.1: Explanation of symbols used throughout the equations and the text.	258

## List of Figures

Fig. 1.1: Geometry of scattering.....	6
Fig. 1.2: View of the polarization plane (blue circle) illuminating a raindrop canted within the plane of polarization at angle $\alpha$ . The direction of wave propagation $\mathbf{k}$ is into the page. The raindrop's major and minor axes (yellow arrows) are in the $\mathbf{e}_b$ and $\mathbf{e}_a$ directions, respectively.....	8
Fig. 1.3: Shape factors $L_a$ and $L_b$ for oblate (top panel) and prolate (bottom panel) spheroids.....	12
Fig. 1.4: Geometry of the two-layer spheroid, with an inner spheroid of dielectric constant $\epsilon_1$ and outer dielectric $\epsilon_2$ . The silhouette of the inner spheroid is shown by the gray dashed curve. ....	12
Fig. 1.5: Schematic illustrating propagation effects of differential propagation phase shift and attenuation. Each panel shows successive times; the vertically-polarized signal is represented by the orange arrow, and the horizontally-polarized signal by the blue arrow, and propagation direction is given by the black vector, $\mathbf{k}$ . The gradual separation of the H and V signals as they propagate through the rain represents the differential propagation phase shift. Signal amplitude is portrayed by the color shading of the arrows: the fading of the arrows represents attenuation.....	21
Fig. 1.6: Schematic illustrating the depolarization of the incident electromagnetic wave as a result of hydrometeor canting. (a) The canted raindrop, characterized by major axis $b$ and minor axis $a$ (depicted by the yellow arrows) is illuminated by an incident horizontally-polarized wave depicted by the glowing green arrow. Because there is a component of the incident wave that is aligned with both axes of the drop (black dashed line), (b) both dipoles of the drop are excited, as depicted by the orange glowing arrows. (c) These excited dipoles emit secondary radiation that can be decomposed into horizontal and vertical components (the green dashed lines indicate the decomposition of the radiation emitted by the major axis $b$ , and the cyan lines represent the decomposition of the radiation emitted by the minor axis $a$ ). (d) The scattered radiation in the forward and backward directions now has a cross-polar (vertically-polarized) component. ....	22
Fig. 1.7: Special cases where analytical formulas exist for the angular moments: (a) Completely random particle orientation, (b) random orientation in the horizontal plane, (c) two-dimensional axisymmetric Gaussian distribution of canting angles. In each case, the gray shaded regions represent the space of possible particle orientations.....	31
Fig. 2.1a. Normalized radar reflectivity factors at orthogonal polarizations (H in blue, V in black) for (a) S ( $\lambda = 10.97$ cm), (b) C ( $\lambda = 5.40$ cm), and (c) X ( $\lambda = 3.2$ cm) bands. Solid curves represent drop temperatures of 0 °C; dashed curves represent drop temperatures of 20 °C.....	35

Fig. 2.1b: Normalized radar reflectivity factor at horizontal polarization ( $Z_H$ ) for raindrops, shown for S band (black), C band (blue), and X band (red) at two temperatures: 0 °C (solid curves) and 20 °C (dashed curves).....	36
Fig 2.2: Normalized reflectivity factor at horizontal polarization ( $Z_H$ ) for raindrops (dotted lines) and ice pellets (solid lines), shown for S, C, and X bands (black, blue, and red curves). Ice pellets are considered the same size and shape as raindrops, but have a distribution of canting angles $\sigma = 40^\circ$ . .....	37
Fig. 2.3: Normalized reflectivity factor at horizontal polarization ( $Z_H$ ) for dry, oblate (axis ratio = 0.8, $\sigma = 40^\circ$ ) hailstones, at S, C, and X bands (black, blue, and red curves). .....	38
Fig. 2.4: Normalized reflectivity factor at horizontal polarization ( $Z_H$ ) for dry snow (thick curves), ice pellets (thin curves), and raindrops (dotted curves), at S, C, and X bands (black, blue, and red curves). Dry snowflakes are assumed to be oblate spheroids with axis ratio of 0.6, with density given by the empirical formula of Brandes et al. (2007). .....	39
Fig. 2.5: Normalized reflectivity factor at horizontal polarization ( $Z_H$ ) for melting snowflakes, shown for S, C, and X bands (black, blue, and red curves). Melting snowflakes treated using the model of Ryzhkov et al. (2008) and Giangrande (2007), at the level of the $Z_{DR}$ maximum in the brightband.....	40
Fig. 2.6: Normalized reflectivity factor at horizontal polarization ( $Z_H$ ) for wet hailstones, shown for S, C, and X bands (black, blue, and red curves). Melting hailstones are treated using the model of Ryzhkov et al. (2009), at the ground level....	41
Fig. 2.7: Comparison of the oblate spheroidal shapes of a French-style dinner roll (left panel) to a 6-mm raindrop (right panel). Raindrop photograph adapted from Thurai et al. (2009).....	44
Fig. 2.8: Differential reflectivity ( $Z_{DR}$ ) for raindrops at S, C, and X bands (black, blue, and red curves). Shown for two temperatures: 0 °C (top) and 20 °C (bottom).....	44
Fig. 2.9: Differential reflectivity ( $Z_{DR}$ ) for frozen raindrops (ice pellets), shown for S, C, and X bands (black, blue, and red curves, respectively). Particle axis ratios are identical to those of raindrops; the width of canting angle distribution $\sigma = 40^\circ$ .....	45
Fig. 2.10: Differential reflectivity ( $Z_{DR}$ ) for dry hailstones, at S, C, and X bands (black, blue, and red curves). The aspect ratio of hailstones > 1 cm in diameter is fixed at 0.8. ....	46
Fig. 2.12: Differential reflectivity ( $Z_{DR}$ ) for melting snowflakes, at S, C, and X bands (black, blue, and red curves).....	49

Fig. 2.13: Observed vertical cross section (RHI) of  $Z_H$  (left) and  $Z_{DR}$  (right) showing a melting layer bright band between about 2.5 and 3.0 km in height. The data are from the Bonn X-band Polarimetric (BOXPOL) radar, collected on 22 June 2011 at 1144 UTC. Courtesy of the Meteorologisches Institut at the Universität Bonn. .... 50

Fig. 2.14: Differential reflectivity ( $Z_{DR}$ ) for wet hailstones, for S, C, and X bands (black, blue, and red curves)..... 51

Fig. 2.15: Normalized specific differential phase shift ( $K_{DP}$ ) for raindrops, at S, C, and X bands (black, blue, and red curves). Shown for two temperatures: 0 °C (top) and 20 °C. .... 53

Fig. 2.16: Normalized specific differential phase shift ( $K_{DP}$ ) for ice pellets, at S, C, and X bands (black, blue, and red curves). .... 55

Fig. 2.17: Normalized specific differential phase shift ( $K_{DP}$ ) for dry hailstones, at S, C, and X bands (black, blue, and red curves)..... 55

Fig. 2.18: Normalized specific differential phase shift ( $K_{DP}$ ) for melting snowflakes, at S, C, and X bands (black, blue, and red curves)..... 57

Fig. 2.19: Normalized specific differential phase shift ( $K_{DP}$ ) for wet hailstones, at S, C, and X bands (black, blue, and red curves)..... 58

Fig. 2.20: Display of (top)  $Z_H$  and (bottom)  $\rho_{hv}$  from the polarimetric WSR-88D radar in Key West, Florida (KBYX) on 7 February 2012, at 2128 UTC. Data show chaff mixed with precipitation. The chaff is clearly identified by  $\rho_{hv}$  as bands of extremely low  $\rho_{hv}$  values ( $< 0.70$ ), whereas the precipitation has  $\rho_{hv}$  near unity..... 62

Fig. 2.21: Display of (top)  $Z_H$  and (bottom)  $\rho_{hv}$  from the polarimetric WSR-88D radar in Melbourne, Florida (KMLB) on 31 January 2012, at 2114 UTC. Data show a large grassfire north of the radar. The smoke and ash from the fire is clearly identified by  $\rho_{hv}$  values ( $< 0.50$ ), whereas the clouds have  $\rho_{hv}$  near unity. .... 63

Fig. 2.22: Display of (top)  $Z_H$  and (bottom)  $\rho_{hv}$  from the polarimetric WSR-88D radar in Huntsville, AL (KHYX) on 3 March 2012, at 0545 UTC. Data show a widespread region of biological scatterers, including insects and birds as very low  $\rho_{hv}$ , as well as a few precipitation cells evident by  $\rho_{hv}$  near unity. .... 64

Fig. 2.23: Display of (top)  $Z_H$  and (bottom)  $\rho_{hv}$  from the polarimetric WSR-88D radar in Langley Hill, Washington (KLGX) on 7 February 2012, at 2242 UTC. Data show sea clutter mixed with precipitation. The sea clutter is clearly identified by  $\rho_{hv}$  values ( $< 0.70$ ), whereas the precipitation has much higher  $\rho_{hv}$  ( $> 0.90$ )..... 65

Fig. 2.24: Display of (top left)  $Z_H$ , (top right) Doppler velocity, (bottom left)  $\rho_{hv}$ , and (bottom right)  $Z_{DR}$  from the polarimetric WSR-88D radar in Springfield, Missouri

(KSGF) on 29 February 2012, at 0605 UTC. Data show a tornadic debris signature, marked by high  $Z_H$ , low  $Z_{DR}$ , very low  $\rho_{hv}$  collocated with a vortex signature in the Doppler velocities, located at approximately  $x = 22$  km,  $y = 39$  km. .... 66

Fig. 2.25: Display of  $\rho_{hv}$  from the BOXPOL radar. Data are from the same scan as Figure 2.13. A dramatic decrease in  $\rho_{hv}$  is evident in the melting layer. The decrease in  $\rho_{hv}$  with range is a result of decreased signal-to-noise ratio, and possibly of nonuniform beam filling..... 67

Fig. 2.26: Backscatter differential phase shift ( $\delta$ ) for raindrops, at S, C, and X bands (black, blue, and red curves). Shown for two temperatures: 0 °C (top) and 20 °C (bottom). .... 69

Fig. 2.27: Backscatter differential phase shift ( $\delta$ ) for ice pellets, at S, C, and X bands (black, blue, and red curves)..... 70

Fig. 2.28: Backscatter differential phase shift ( $\delta$ ) for dry hailstones, at S, C, and X bands (black, blue, and red curves). .... 70

Fig. 2.29: Backscatter differential phase  $\delta$  for melting snowflakes at S, C, and X bands (black, blue, and red curves)..... 72

Fig. 2.30: As in Figure 2.13, but  $\Phi_{DP}$  is shown. Note the “bump” in  $\Phi_{DP}$  through the melting layer, caused by backscatter differential phase off large, wet snow aggregates. .... 73

Fig. 2.31: Schematic illustrating the difficulty estimating  $K_{DP}$  (the slope of the dashed straight lines) in the presence of a  $\delta$  bump on the radial profile of the measured  $\Phi_{DP}$  (blue curve). Erroneously large positive and negative errors in the  $K_{DP}$  estimates are depicted in red, whereas the true  $K_{DP}$  is shown in green..... 73

Fig. 2.32: Backscatter differential phase shift ( $\delta$ ) for melting hailstones, at S, C, and X bands (black, blue, and red curves). .... 74

Fig. 2.33: Linear depolarization ratio ( $L_{DR}$ ) for raindrops, at S, C, and X bands (black, blue, and red curves). Shown for two temperatures: 0 °C (top), and 20 °C (bottom). ... 76

Fig. 2.34: Linear depolarization ratio ( $L_{DR}$ ) for ice pellets, at S, C, and X bands (black, blue, and red curves)..... 77

Fig. 2.35: Linear depolarization ratio ( $L_{DR}$ ) for dry hailstones, at S, C, and X bands (black, blue, and red curves)..... 77

Fig. 2.36: Linear depolarization ratio ( $L_{DR}$ ) for dry snowflakes, at S, C, and X bands (black, blue, and red curves). Snowflakes considered as oblate spheroids (aspect ratio 0.7), with density decreasing as a function of size following Brandes et al. (2007).



Complex scattering amplitudes were computed using the Rayleigh approximation. The canting angle distribution width $\sigma = 40^\circ$ . .....	78
Fig. 2.37: Linear depolarization ratio ( $L_{DR}$ ) for melting snowflakes, at S, C, and X bands (black, blue, and red curves).....	79
Fig. 2.38: Linear depolarization ratio ( $L_{DR}$ ) for wet hailstones, at S, C, and X bands (black, blue, and red curves).....	80
Fig. 2.39: Normalized specific attenuation ( $A_H$ ) for raindrops at S, C, and X bands (black, blue, and red curves). Shown for two temperatures: 0 °C (top), and 20 °C (bottom). .....	83
Fig. 2.40: Normalized specific attenuation ( $A_H$ ) for ice pellets, at S, C, and X bands (black, blue, and red curves).....	84
Fig. 2.41: Normalized specific attenuation ( $A_H$ ) for dry hailstones, at S, C, and X bands (black, blue, and red curves).....	85
Fig. 2.42: Normalized specific attenuation ( $A_H$ ) for melting snow, at S, C, and X bands (black, blue, and red curves).....	86
Fig. 2.43: Normalized specific attenuation ( $A_H$ ) for wet hail, at S, C, and X bands (black, blue, and red curves). Note that it is the same scale as for dry hailstones. ....	86
Fig. 2.44: Specific differential attenuation ( $A_{DP}$ ) for raindrops, at S, C, and X bands (black, blue, and red curves). Shown for two temperatures: 0 °C (top), and 20 °C (bottom). .....	88
Fig. 2.45: Specific differential attenuation ( $A_{DP}$ ) for ice pellets, at S, C, and X bands (black, blue, and red curves).....	89
Fig. 2.46: Specific differential attenuation ( $A_{DP}$ ) for dry hailstones, at S, C, and X bands (black, blue, and red curves).....	89
Fig. 2.47: Specific differential attenuation ( $A_{DP}$ ) in melting snowflakes at S, C, and X bands (black, blue, and red curves). .....	91
Fig. 2.48: Data from a vertical cross section through a winter stratiform precipitation event on 27 January 2009 at 2317 UTC, taken with the S-band KOUN along the 181° azimuth. The radial streak of negative $Z_{DR}$ emanating from about 50 km range is caused by differential attenuation.....	91
Fig. 2.49: Specific differential attenuation ( $A_{DP}$ ) in wet hailstones at S, C, and X bands (black, blue, and red curves).....	92

Fig. 2.50: Observations of (a)  $Z_H$ , and (b)  $Z_{DR}$  with the S-band polarimetric WSR-88D near Vance Air Force Base in Oklahoma (KVNK). Data are from  $0.5^\circ$  in elevation, on 3 February 2012, at 0335 UTC. The radial streaks of negative  $Z_{DR}$  are indications of differential attenuation..... 93

Fig. 3.1: Two-panel plot of  $Z_H$  (top) and  $Z_{DR}$  (bottom) from the polarimetric WSR-88D radar near Huntsville, AL (KHTX) collected on 2 March 2012, at 2254 UTC. Data were sampled at the  $0.5^\circ$  elevation angle. The example shows differential attenuation, evident as the swath of negative  $Z_{DR}$  values downrange of the supercell storm. .... 96

Fig. 3.2: Four-panel display of  $Z_H$  (top left),  $Z_{DR}$  (top right),  $\rho_{hv}$  (bottom left), and  $\Phi_{DP}$  (bottom right), collected with the polarimetric WSR-88D radar near Memphis, TN (KNQA) on 1 February 2012, at 2215 UTC. Data show the effects of nonuniform beam filling, especially in the radial streaks of reduced  $\rho_{hv}$ , as well as differential attenuation in  $Z_{DR}$ ..... 97

Fig. 3.3: Schematic illustrating nonuniform beamfilling (NBF). In this example, the bottom portion of the beam intercepts heavy rain characterized by large  $\Phi_{DP}$  values while the top of the beam intercepts ice-phase particles (with low  $\Phi_{DP}$ ) above the freezing level. This large spread of  $\Phi_{DP}$  results in a reduction of  $\rho_{hv}$ ..... 98

Fig. 3.4: Four-panel display of  $Z_H$  (top left),  $Z_{DR}$  (top right),  $\Phi_{DP}$  (bottom left), and  $\rho_{hv}$  (bottom right). Shown is an example of depolarization streaks, from Tropical Storm Erin (19 August 2007, 0856 UTC). Data were collected with the research WSR-88D radar (KOUN) in Norman, OK at  $8.0^\circ$  elevation..... 101

Fig. 3.5: Cartoon illustrating the depolarization of the signal by crystals oriented in an electric field ( $\mathbf{E}$ ). The original polarization of the transmitted wave (blue, only H-polarization is shown) is depolarized by the canted ice crystals, changing the polarization state of the propagating wave (red vector). From the moment of depolarization in the canted medium (green circle), the rest of the signal further along the radial is compromised, evident as a radial streak of positive or negative  $Z_{DR}$ . The sign of  $Z_{DR}$  depends on the accumulated  $\Phi_{DP}$  along the propagation path leading up to the canted crystals, the system differential phase upon transmission, and the orientation angle of the crystals (Ryzhkov and Zrnić 2007). .... 102

Fig. 3.6: Three-panel display of  $Z_H$  (top),  $Z_{DR}$  (middle), and  $\rho_{hv}$  (bottom) from the polarimetric WSR-88D radar near Knoxville, TN (KMRX). Shown is an example of a polarimetric three-body scattering signature (PTBSS), observed on 2 March 2012 at 2318 UTC, at elevation  $2.4^\circ$ . The PTBSS extends nearly 50 km behind the hail core. Note the large positive  $Z_{DR}$  ( $> 4$  dB) just beyond the hail core, followed by predominantly negative values downrange. Values of  $\rho_{hv}$  are extremely low ( $< 0.6$ ) throughout..... 103

Fig. 3.7: Schematic illustrating the polarimetric TBSS. In the top panel, selected paths of electromagnetic radiation are shown. Radiation scatters off the hailstones and

towards the ground at two off-nadir angles ( $\theta_a$  and  $\theta_b$ ). The measured  $Z_{DR}$  in the PTBSS is the product of three ratios: I. The “bistatic  $Z_{DR}$ ” (Aydin et al. 1998), which is the ratio of the powers of the radiation scattered downward by the hailstones ( $P_H/P_V$ ); II. The ratio of the ground backscattering cross section at H and V polarizations ( $\sigma_H / \sigma_V$ ); and a factor representing the differential attenuation suffered by the signal as it propagates through the hailstones and off the ground ( $L_H / L_V$ ). The left column schematically shows these three factors for  $\theta_a$ , close to nadir, whereas the right column shows the three factors for  $\theta_b > \theta_a$ . Adapted from Picca and Ryzhkov (2012), with changes. .... 106

Fig. 3.8: Bistatic  $Z_{DR}$  produced by dry, oblate hailstones (axis ratio 0.8) for S and C bands (black solid and gray dashed lines, respectively). From Kumjian et al. (2010b). ..... 107

Fig. 4.1: Temperature of raindrops ( $^{\circ}\text{C}$ , color shading) as a function of drop size (mm) and height (m AGL). Drops were initialized at the top of the domain with temperature  $0^{\circ}\text{C}$ . The lapse rate ( $\Gamma$ ) is  $6.5^{\circ}\text{C km}^{-1}$ , with initial temperature  $3^{\circ}\text{C}$  at the top of the domain. .... 112

Fig. 4.2: As in Fig. 4.1, but the difference between the drop temperature and air temperature ( $\Delta T$ ) is shown. A negative difference indicates that the drops are colder than the ambient air at that level. .... 113

Fig. 4.3: Equilibrium temperature difference ( $\Delta T$  in  $^{\circ}\text{C}$ ) as a function of drop size (in mm) for lapse rates ( $\Gamma$  in  $^{\circ}\text{C km}^{-1}$ ) between 1 and  $10^{\circ}\text{C km}^{-1}$ . All drop sizes attain their equilibrium temperature difference after free fall of about 2 km. .... 114

Fig. 4.4: Complex dielectric of liquid water drops as a function of temperature for three radar wavelengths: S, (black curves), C, (dark gray curves) and X (light gray curves). (left) Real part, in solid lines, and (right) imaginary part, in dashed lines. .... 116

Fig. 4.5:  $Z_{DR}$  (left) and  $\delta$  (right) as a function of raindrop temperature, computed for a resonance-sized raindrop 5.9 mm in diameter at C band. .... 116

Fig. 5.1: Raindrop terminal fall speed as a function of diameter. Observations of Gunn and Kinzer (1949) are shown as open circle markers. The Atlas et al. (1973) exponential relation (gray solid curve), Atlas and Ulbrich (1977) power law relation (gray dotted line), Brandes et al. (2002) polynomial relation (eqn. 5.1; thick black line), and the functional relation used in bulk microphysics parameterization schemes (“Bulk MPS,” thick gray dashed line, from Umlinger 1981) are overlaid. .... 122

Fig. 5.2: DSDs from the sedimentation model. The initial DSD aloft is shown by the thin dotted line in both panels. (a) At  $t = 333$  s, at height level  $z = 1000$  m AGL, the one-moment bulk microphysics scheme (“1M bulk”) solution is given by the solid black line, the two-moment solution (“2M bulk”) is given by the dashed black line, and the three-moment (“3M bulk”) scheme solution is shown in the solid line with asterisk markers. The reference bin solutions are shown in solid red and blue lines, the

difference being the assumed fall speed relation. (b) As in (a), but surface ( $z = 0$  m) DSDs at  $t = 333$  s from the reference bin solutions. Note that in (a), the bin solutions overlap. .... 129

Fig. 5.3: Vertical profiles of the S-band polarimetric radar variables predicted by the sedimentation model at  $t = 333$  seconds. The solutions for the one-moment (solid black line), two-moment (dashed black line), and three-moment (dotted black line) bulk schemes are compared to the reference solutions (red and blue solid curves). Variables shown are calculated for S band: (a)  $Z_H$ , (b)  $Z_{DR}$ , (c)  $K_{DP}$ , and (d)  $\rho_{hv}$ . For the bulk schemes, all variables are censored where  $Z_H \leq 0$  dBZ. .... 132

Fig. 5.4: Relative errors in the polarimetric variables computed from the three-moment scheme with different values of maximum shape parameter  $\alpha$ : 10 (black solid line), 20 (dashed black line), 30 (solid gray line), and 40 (dash-dot gray line). Variables shown are (a)  $Z_H$ , (b)  $Z_{DR}$ , and (c)  $K_{DP}$ . The Brandes et al. bin solution is considered “truth” for these error calculations. Positive errors correspond to overestimations by the 3M scheme, negative errors to underestimations. .... 134

Fig. 5.5: Results from the 1D updraft model, showing the ground-level (a)  $Z_H$  and (b)  $Z_{DR}$  as a function of the updraft speed at the top of the domain  $w(h = 3$  km). .... 137

Fig. 5.6: Schematic of the two-dimensional wind shear model configuration. Storm-relative wind ( $u - u_{storm}$ ) profile is shown to the left. The domain and example resulting  $Z_H$  distribution (shaded in dBZ) is shown to the right. The “cloud” rainwater mixing ratio ( $q$ ) profile is shown above the domain ( $g\ kg^{-1}$ ). .... 139

Fig. 5.7: Results from the two-dimensional wind shear model using the bin formulation. Panels show the two-dimensional fields of (a)  $Z_H$ , (b)  $Z_{DR}$ , (c)  $K_{DP}$ , and (d)  $\rho_{hv}$ . Overlaid on panel (a) is the  $Z_{DR}$  contours (0.5 – 2.5 dB in 0.5 dB increments), whereas panels (b)-(d) have  $Z_H$  contours 10 – 40 dBZ (in 10-dBZ increments) overlaid. For  $Z_H < 0$  dBZ, all fields are set to zero. .... 140

Fig. 5.8: As in Fig. 5.7, except the results are from the single-moment bulk scheme configuration. .... 141

Fig. 5.9: As in Figs. 5.7 and 5.8, except the results from the two-moment bulk scheme configuration are shown. Note the changes in the color scales of  $Z_H$ ,  $Z_{DR}$  and  $K_{DP}$ . .. 143

Fig. 5.10: Fields of rainwater mixing ratio ( $q$ , in  $g\ kg^{-1}$  and contoured in black) and total number concentration ( $N_{TOT}$ , in  $m^{-3}$  and contoured in gray) from the two-dimensional wind shear model run using the two-moment scheme shown in Fig. 5.9. .... 144

Fig. 5.11: As in Figs. 5.7 – 5.9, except results from the three-moment bulk scheme configuration are shown. .... 145

- Fig. 5.12:  $Z_{DR}$  difference fields between (a) the bin model and the 1M bulk scheme, (b) the bin model and the 2M bulk scheme, and (c) the bin model and the 3M bulk scheme. Contours in 0.5-dB intervals are overlaid (solid lines for positive differences, dashed lines for negative). ..... 147
- Fig. 5.13: Observations from 17 June 2005, at 0544 UTC, along the azimuth  $191^\circ$ .  $Z_{DR}$  (in dB) is shaded, with  $Z_H$  contours of 30, 40, and 50 dBZ overlaid. The abscissa is range (distance) from the KOUN radar. The high  $Z_{DR}$  region near the ground at a range of about 85 km is from biological scatterers (i.e., insects and/or birds). ..... 149
- Fig. 5.14: Example PPI from 30 May 2004 at  $0.5^\circ$  elevation, at 0044 UTC. The color shading is  $Z_{DR}$  (dB), with the 30-, 40-, 50-, and 55-dBZ contours of  $Z_H$  overlaid. Distances are relative to the location of the KOUN radar. .... 150
- Fig. 5.15: RHI scans of  $Z_H$  (left) and  $Z_{DR}$  (right), taken at 0404 UTC 22 June 2011 from the Bonn X-band Polarimetric radar (BOXPOL) operated by the Meteorological Institute at the Universität Bonn (Germany). Data are from the  $309.5^\circ$  azimuth. .... 151
- Fig. 5.16: Vertical profile of Doppler velocity extracted from the RHI shown in Figure 5.15, at a range of 29 km. .... 152
- Fig. 5.17: As in Fig. 5.15, but from 0944 UTC (top panels) and 0949 UTC (bottom panels) on 22 June 2011. Data from BOXPOL, operated by the Meteorological Institute at the Universität Bonn (Germany). .... 153
- Fig. 5.18: As in Figs. 5.15 and 5.17, but from 1454 UTC on 22 June 2011. Data from BOXPOL, operated by the Meteorological Institute at the Universität Bonn (Germany). ..... 154
- Fig. 5.19: Comparison of relations between DSD parameters by Cao et al. (2008), indicated by the solid black line, and Milbrandt and McTaggart-Cowan (2010; MM 2010), indicated by the dashed gray line. (a) The relation between DSD slope parameter  $\Lambda$  and shape parameter  $\alpha$  is shown. (b) The relation between mean-mass diameter  $D_m$  and shape parameter  $\alpha$  is shown. Relations were determined by Eqns. (5.16-5.17). ..... 158
- Figure 5.20: Number of drops sampled by the 2D video disdrometer. The vertical axis indicates height AGL of the DSD at the time shown in Figure 5.2 (this can be thought of as roughly corresponding to time). The vertical bar at 50 drops indicates the minimum sampling ability of the disdrometer. Calculations performed on the DSDs simulated by the bin solution of the 1D fallout model (Fig. 5.2). ..... 159
- Fig. 6.1: Cartoon illustrating net vapor diffusion (a) onto a drop from the ambient environment (condensation), and (b) away from a drop into the ambient environment (evaporation). The dashed gray line represents a volume around the drop demarcating the near-drop environment and the ambient environment. .... 169

Fig. 6.2: Cartoon illustrating how evaporation can cause an increase in the median drop size  $D_m$  of a distribution. The solid blue line indicates the drop size distribution (DSD) before evaporation occurs; the dashed orange line represents the modified DSD owing to evaporation. .... 172

Fig. 6.3: DSD models used for the simulations. The Marshall-Palmer exponential distribution (solid black line); the  $\mu = -1$  gamma model (solid dark gray line); the  $\mu = 1$  gamma model (solid light gray line); the gamma model with  $\mu = 3$  (dashed black line); and the model with  $\mu = 5$  (dashed dark gray line). All models are for rainfall rates of  $5 \text{ mm hr}^{-1}$ . .... 182

Fig. 6.5: Sensitivity of the evaporative change in the S-band dual-polarization variables to various constant relative humidity profiles for the 5 DSD models. The domain depth is 2 km and isothermal at  $20^\circ\text{C}$ . The plotting convention for the DSD models is the same as in Fig. 6.2. The panels display evaporative changes in (a)  $Z_H$ , (b)  $Z_{DR}$ , (c)  $K_{DP}$ , and (d)  $\rho_{hv}$ . .... 187

Fig. 6.6: As in Fig. 6.5, but for C band..... 188

Fig. 6.7: Calculations of the evaporative changes in each of the polarimetric variables (each row is a variable) based on a 3-km deep idealized well-mixed layer, with a surface temperature of  $30^\circ\text{C}$ . The surface relative humidity (RH) values are shown along the abscissa. Each column represents a DSD model, as indicated. The solid lines represent S-band values and the dashed lines represent C-band values..... 189

Fig. 6.8: Sensitivity of the evaporative change in the polarimetric variables to rainfall rate for the exponential DSD. The 3-km deep domain has a dry adiabatic temperature (surface temperature of  $30^\circ\text{C}$ ) with a surface relative humidity of 75%. S-band values are shown in solid lines and C-band values are in dashed lines. In the left panel,  $\Delta Z_H$  (black) and  $\Delta K_{DP}$  (gray) are shown, both in dB. In the right panel, black represents  $\Delta Z_{DR}$  and gray represents  $\Delta \rho_{hv}$ . .... 190

Fig. 6.9: Observed low-level (surface to approximately 3 km AGL) soundings used for the evaporation model simulations, representing three different evaporation scenarios: (a) Albuquerque, New Mexico on 16 August 2007 at 0000 UTC; (b) Norman, Oklahoma on 24 May 2008 at 1800 UTC, and (c) Wallops Island, Virginia on 7 October 2009 at 0000 UTC. Thick black solid (dashed) line indicates the temperature (dewpoint temperature) profile. The horizontal line with asterisk markers at the top of each sounding indicates the 3-km AGL height..... 192

Fig. 6.10: Simulated vertical profiles of polarimetric variables for the Albuquerque sounding (Fig. 6.9a). The solid line indicates S band and the dashed line indicates C band. Variables shown are (a)  $Z_H$ , (b)  $Z_{DR}$ , (c)  $K_{DP}$ , and (d)  $\rho_{hv}$ . The MP DSD model is used at the cloud base, with a rainfall rate of  $5 \text{ mm hr}^{-1}$  aloft. .... 194

Fig. 6.11: Vertical profiles of rainfall rates for the three soundings. The thick solid line is the actual  $R$  determined from the DSD at each level. The dash-dot line is  $R(Z_H)$  (eqn. 6.34), the dashed line is  $R(K_{DP})$  (eqn. 6.35), and the dotted line is  $R(Z_H, Z_{DR})$  (eqn. 6.36). At cloud base, the MP model is used for these simulations, with a rainfall rate of  $5 \text{ mm hr}^{-1}$  aloft. .... 198

Fig. 6.12: The dependence of relative change in rainfall rate  $\Delta R/R$  on S-band  $Z_{DR}$  aloft and surface relative humidity. Results are of calculations using a 3-km deep idealized well-mixed layer with surface temperature of  $30 \text{ }^\circ\text{C}$ . Each curve corresponds to a different value of surface relative humidity (solid black line for 55%, solid gray line for 75%, and dashed gray line for 95%). Only constrained gamma models (with  $5 \text{ mm hr}^{-1}$  rainfall rate) are used in the calculations, where  $\Delta R/R$  is independent of  $Z_H$  aloft. The gray numbers along the abscissa correspond to the shape parameter ( $\mu$ ) values associated with the given  $Z_{DR}$ . .... 201

Fig. 6.13: As in Figure 6.12, except here C-band values are shown. .... 202

Fig. 7.1: Genuine RHI scan collected with BOXPOL on 22 June 2011 at 1454 UTC, along the  $309.5^\circ$  azimuth. Polarimetric radar variables shown are (top)  $Z_H$ , and (bottom)  $Z_{DR}$ . The cell of interest is located between 13 and 14 km range. .... 212

Fig. 7.2: Median vertical profile of  $Z_H$  through the storm in Figure 7.1, constructed from 10 extracted vertical profiles at ranges 13 – 14 km. .... 213

Fig. 7.3: Median vertical profile of  $Z_{DR}$  through the storm in Figure 7.1, constructed from 10 extracted vertical profiles at ranges 13 – 14 km. .... 213

Fig. 7.4: Scatter of the range of  $\Lambda$ - $Z_{DR}$  points observed in nature (black points), overlaid with the  $Z_{DR}$  from the Cao et al. (2008) relation (green). Calculations made at X band, for raindrops with temperature =  $15 \text{ }^\circ\text{C}$ . .... 215

Fig. 7.5: Vertical profiles of slope parameter  $\Lambda$  (left) and shape parameter  $\mu$  (right) retrieved from polarimetric radar measurements. .... 216

Fig. 7.6: Observed sounding from Essen, Germany, on 22 June 2011 at 12 UTC. .... 217

Fig. 7.7: Retrieved  $Z_{DR}$  (blue curve) and the observed  $Z_{DR}$  (green curve) profiles as a function of height. .... 219

Fig. 7.8: As in Figure 7.7, but the retrieved (blue) and observed (green)  $Z_H$  profiles are shown. .... 219

Fig. 7.9: Relative error (%) of the retrieved  $Z_H$  profile for 1454 UTC on 22 June 2011. .... 220

Figure 7.10: Retrieved DSD at each height level, with each color indicating a certain depth. As expected with coalescence growth, the initially narrow DSD broadens and acquires a shallower slope, indicative of an increase in concentration of large drops and a decrease in concentration of small drops (sizes < 2 mm)..... 221

Fig. 7.11: Retrieved profiles of  $K_{DP}$  (left panel) and  $\rho_{hv}$  (right panel) from 22 June 2011, 1454 UTC..... 222

Fig. 8.1: Example of polarimetric data presented as a vertical cross-section through a supercell storm on 10 May 2003, at 0346 UTC, observed with the S-band polarimetric WSR-88D in Norman, Oklahoma. From left-to-right, panels show  $Z_H$ ,  $Z_{DR}$ , and  $\rho_{hv}$ . A  $Z_{DR}$  column is evident at about 44 km range. Note that the environmental melting level is at 4.2 km above the ground, and the updraft-perturbed melting level is near 5.2 km, assuming a surface-based parcel. .... 226

Fig. 8.2: Photograph of a 1-mm drop, from Johnson and Hallett (1968). The outer ice shell has just begun to form, and dendritic growth is evident in the drop core. The photograph was taken 10 seconds after nucleation, and complete freezing took another 40 seconds. .... 230

Fig. 8.3: Time for raindrops to freeze (color shading in seconds), following the assumptions and calculations of PK97. The drops are assumed to be nucleated and remain at a given ambient temperature. Calculations are based on PK97's eqn. (16-36). White shading indicates times over 300 seconds. .... 231

Fig. 8.4: Schematic illustrating the fraction of drops nucleated as a function of supercooled temperature  $T_s$ . The median supercooled temperature  $T_{sm}$  indicates the temperature at which 50% of the drops of a given size are nucleated. Note that  $T_s$  and  $T_{sm}$  are positive; also labeled on the abscissa is  $T_0$  ( $= 0$  °C)..... 237

Fig. 8.5: Vertical profiles of (a)  $Z_H$ , (b)  $Z_{DR}$ , (c)  $\rho_{hv}$ , and (d)  $L_{DR}$  computed from output of the freezing model, shown in meters above the melting level (AML). The model parameters used for the calculations include the default DSD with varying updraft maximum intensity: 19 m s<sup>-1</sup> (solid curves), 25 m s<sup>-1</sup> (dashed curves), and 30 m s<sup>-1</sup> (dotted curves). These calculations are for S band, employing the Rayleigh approximation. In each case,  $w_0 = 15$  m s<sup>-1</sup>, and  $h_{max} = 5$  km..... 243

Fig. 8.6: Vertical profiles of the number concentration (in m<sup>-3</sup>) of the 61<sup>st</sup> size bin corresponding to a liquid drop of size 6.05 mm. The concentration of raindrops is shown in the black solid line, partially-frozen drops (or “slush”) in the dashed dark gray line, and completely frozen ice pellets in the dotted gray line. The default DSD and updraft with  $w_{max} = 25$  m s<sup>-1</sup> are used, with  $w_0 = 15$  m s<sup>-1</sup> and  $h_{max} = 5$  km..... 244

Fig. 8.7: Height of the freezing zone above the melting level as a function of the updraft speed. The default DSD is assumed. For these idealized calculations, the updraft profile is constant throughout the domain, varying from 11 m s<sup>-1</sup> to 50 m s<sup>-1</sup>. .... 245



Fig. 8.8: Vertical profiles of  $Z_{DR}$  resulting from model runs with different nucleation schemes. The default scheme described in the text is shown with the black curve and includes the size-dependent mean nucleating temperature and stochastic nucleation process. The dashed dark gray curve represents the runs when all drops are assigned a mean nucleating temperature of  $T_m = -9.6$  °C (the  $T_m$  of the largest drop size in the default run). The gray dotted curve represents a simulation when all drops are assigned a  $T_m = -9.6$  °C and no probability distribution function (PDF); in other words, the stochastic component of nucleation has been removed, and all drops in each size bin simply nucleate at  $T_m$ . ..... 247

Fig. 8.9: Observations from the C-band OU-PRIME on 24 April 2011, at 1909 UTC, along the azimuth 233.3°. Panels shown are (a)  $Z_H$ , and (b)  $Z_{DR}$ . Range rings are shown every 5 km. The  $Z_{DR}$  column of interest is centered at a range of about 29 km. .... 250

Fig. 8.10: (a) Fifteen observed vertical profiles of  $Z_{DR}$  extracted from the RHI in Figure 8.9, from the  $Z_{DR}$  column centered at a range of about 29 km (gray lines), compared to the model  $Z_{DR}$  profile (thick black curve). (b) As in (a), but  $Z_H$  profiles are shown... 251

Fig. 8.11: Vertical cross-sections of  $Z_H$  (left) and  $Z_{DR}$  (right) taken along the 309.5° azimuth on 24 June 2011, at 1034 UTC by the X-band BOXPOL radar. Data are courtesy of the Meteorological Institute of the University of Bonn. The  $Z_{DR}$  column of interest is centered at about 23 km range. .... 252

Fig. 8.12: As in Figure 8.10, but for 11 vertical profiles extracted from the RHI in Figure 8.11..... 252

Fig. 9.1: Pictorial catalog of the qualitative polarimetric fingerprints of different microphysical processes. The direction of the arrows indicates the direction of the change in the radar variable owing to the given process. Sideways arrows indicate changes can be in either direction. For a given process, the size of the arrow indicates the magnitude of the change relative to the other variables in a qualitative sense..... 262

Fig. A1: Values of the (a) real part, and (b) imaginary part of the complex dielectric for water, computed based on the expressions of Ray (1972) for three radar wavelengths: S band (black curves), C band (blue curves), and X band (red curves). .... 265

Fig. A2: As in Figure A1, except for ice. .... 265

Fig. A3: Schematic cartoon illustrating several different models for treating mixed-phase hydrometeors. (a) Ice matrix with water inclusions; (b) water matrix with ice inclusions; (c) water-coated with an ice core; (d) ice-coated with a water core. .... 269

Fig. A4: Normalized values of the radar reflectivity factor at horizontal polarization ( $Z_H$ ) as a function of liquid water volume fraction computed for a 6-mm particle, using four models of water distribution: ice coat with water core (black solid curves), spongy with an ice matrix and water inclusions (black dashed curves), water coat with an ice

core (gray solid curves), and spongy with a water matrix and ice inclusions (gray dashed curves). Calculations performed using a T-Matrix code, for three radar wavelengths: (a) S band (10.97 cm), (b) C band (5.4 cm), and (c) X band (3.2 cm). Particle axis ratio is that of an equivalent-sized raindrop..... 272

Fig. A5: As in Fig. A4, but differential reflectivity factor ( $Z_{DR}$ ) is shown. .... 273

Fig. A6: As in Figs. A4-A5, but normalized values of specific differential phase shift ( $K_{DP}$ ) are shown..... 274

Fig. A7: As in Figs. A4-A6, but the backscatter differential phase shift ( $\delta$ ) is shown. 275

Fig. A8: As in Figs. A4-A7, but the linear depolarization ratio ( $L_{DR}$ ) is shown. .... 276

Fig. A9: As in Figs. A4-A8, but normalized values of the specific attenuation at horizontal polarization ( $A_H$ ) are shown. .... 277

Fig. A10: As in Figs. A4-A9, but specific differential attenuation ( $A_{DP}$ ) is shown. .... 278

Fig. B1: Три Заповеди российского Зэка (Three Commandments of the Russian Convict). .... 279

## **Abstract**

The ongoing upgrade of the National Weather Service WSR-88D radar network to polarimetric capabilities, as well as similar upgrades worldwide, will soon provide a wealth of data and information regarding storm precipitation physics. Fully understanding how a variety of microphysical processes are revealed in polarimetric data is necessary for the best use of these new data by operational and research meteorologists. The focus of this study is to quantify a number of these precipitation physics “fingerprints” in the polarimetric radar variables by using a synthesis of explicit microphysical modeling, electromagnetic scattering calculations, thought experiments, and polarimetric radar observations.

The complete set of polarimetric variables available from linearly-orthogonal dual-polarization radars are derived from basic electromagnetic scattering principles. A detailed physical description of these variables is then provided for applications in precipitation and other atmospheric scatterers, as is a summary of common data artifacts. The impact of various precipitation physical processes on these radar variables is then quantified. Using explicit microphysical models, scattering calculations, observations, and thought experiments, the microphysical fingerprints are determined and quantified for raindrop thermal conduction, raindrop size sorting by sedimentation, updrafts, and vertical wind shear, evaporation of raindrops, coalescence of raindrops, and freezing of raindrops in deep convective storm updrafts. A catalogue of the qualitative fingerprints of a number of precipitation processes is summarized.

## Chapter 0: Introduction

The dual-polarization upgrade of the United States National Weather Service (NWS) Weather Surveillance Radar 1988 Doppler (WSR-88D) network is underway. By the middle of 2013, all 159 WSR-88D radars will be equipped with polarimetric capabilities, ushering in a new era for operational and research meteorology. Soon, all NWS meteorologists will have at their disposal a wealth of new information gained from these new polarimetric radar measurements. Similar polarimetric upgrades to radars are occurring worldwide. Thus, radar polarimetry is an emerging tool that can be applied to numerous operational situations and used to improve warnings, short-term forecasts, and quantitative precipitation estimation. In addition to the numerous operational benefits, the polarimetric upgrade offers a new realm of research opportunities, especially in the realm of precipitation microphysics. No longer will the experimental domain of precipitation physics be limited to the cloud chamber or the wind tunnel; the laboratory will soon be the entire continental United States.

These new opportunities will build on several decades of work in the field of radar polarimetry. Such research efforts date back to the 1950s, with work by A. Shupyatsky (A. Шупяцкий) and collaborators at the Central Aerological Observatory, in the Soviet Union (e.g., Shupyatsky 1959; Gerzeshon and Shupyatsky 1961; Shupyatsky and Morgunov 1963; Minervin and Shupyatsky 1963; Morgunov and Shupyatsky 1964). Beginning with this pioneering work from the Golden Age of science in the USSR, the history of developments in the field is described in Seliga et al. (1990), including the considerable work by Canadian scientists with circular polarization radar (e.g., McCormick and Hendry 1970, 1975; Hendry and McCormick

1974). The “modern era” of research with orthogonal linear polarization radar began in the United States with the papers by Seliga and Bringi (1976, 1978). Significant contributions by Jameson (1983a,b, 1985a,b), Sachidananda and Zrnić (1985, 1986, 1987), Jameson and Mueller (1985), and Balakrishnan and Zrnić (1990a,b) improved the understanding and interpretation of the variables available with linearly orthogonal polarimetric radars.

Much of the ensuing work focused primarily on operational applications of polarimetric radar data, including quantitative precipitation estimation and hydrometeor classification. In contrast, polarimetric radar observations have been underutilized for research into precipitation physics. This dissertation contributes to this endeavor. The purpose of this study is to quantify the polarimetric “fingerprints” of different microphysical processes through a synthesis of observational data analysis, theory, and explicit microphysical modeling.

One approach to modeling precipitation physics is to isolate processes in simplified, one-dimensional models that treat the physics explicitly. (The alternative, used in most storm-scale numerical weather prediction models, is to treat all physical processes through the use of microphysics parameterization schemes.) The benefit of the simplified modeling approach is that a single process is isolated and can be explored in a variety of conditions, with the experimenter maintaining full control and understanding of the model. Additionally, because of the drastically-reduced computational expense, the physical process may be treated explicitly in a spectral model framework, thereby more closely approximating the process in nature. The drawbacks of such an approach are that the models are idealistic, typically do not

account for the parent storm or its circulations, and may neglect other processes that are important in nature. Whereas the parameterization scheme approach is more general and is coupled to a full dynamical model, the important physics at work in a given situation can be ambiguous, obfuscated by interactions with all other processes in the model. Additionally, microphysics parameterizations assume *a priori* a particle size distribution governed by only one to three moments of the distribution; this severely limits the ability of such schemes to accurately reproduce a variety of physical processes that preferentially affect certain portions of the particle size distribution.

Taking these factors into consideration, this study has adopted the philosophy of the simplistic model approach. Notwithstanding the aforementioned caveats of this approach, it allows one to fully explore the impact of certain physical processes on the polarimetric variables. In a more general model, the elucidation of the underlying physics is extremely difficult, if not impossible. By beginning with a simple modeling approach, the polarimetric radar fingerprint of each microphysical process can be unambiguously described. In this way, the dominant processes can be identified in observational data, facilitating a physical interpretation of the observations and providing a benchmark for comparisons with numerical simulations. Such comparisons can be used to identify and quantify sources of error in microphysics parameterization schemes used in convection-permitting numerical models, ultimately paving a path to refinement and validation of such schemes.

The remainder of the dissertation will be formatted as follows. The next chapter provides a theoretical basis for and formulation of all polarimetric radar variables. Chapter 2 is a discussion of the physical interpretation of the polarimetric radar

variables in different types of atmospheric scatterers. Chapter 3 provides a summary and description of common artifacts in dual-polarization radar data. Each proceeding chapter will explore a different precipitation physical process, including the development of the microphysics model, electromagnetic scattering model, and model results. These processes include thermal conduction for raindrops (Chapter 4), size sorting of raindrops (Chapter 5; with material from Kumjian and Ryzhkov 2012), evaporation of raindrops (Chapter 6; with material from Kumjian and Ryzhkov 2010), a preliminary investigation into the collisional processes of coalescence and breakup (Chapter 7, with material from Kumjian et al. 2012b), and freezing of raindrops within convective updrafts (Chapter 8; with material from Kumjian et al. 2012a). A catalog of the impact of precipitation physical processes is summarized in Chapter 9. Appendix A includes formulae for computing the complex dielectric of particles, as well as demonstrates the impact of the choice of model for distributing liquid water on or in a particle on the polarimetric radar variables. Because several of the chapters are derived from published papers, they are formatted as to be self-contained, including their own introductory and background material, as well as their own summary and conclusions.

## Chapter 1: Polarimetric Radar Variables: Theoretical Formulation

This chapter presents a theoretical formulation of all dual-polarization radar variables, derived from first principles of basic electromagnetic scattering theory.

### 1. Electromagnetic Scattering Basics

Consider an individual hydrometeor illuminated by electromagnetic radiation. The incident electric field can be expressed as a complex vector  $\vec{E}_i$ , which describes the amplitude and phase of the radiation and can be decomposed into its components in one or more polarizations. The scattered electric field vector  $\vec{E}_s$  is related to  $\vec{E}_i$  by the scattering matrix  $\mathbf{S}$ ,

$$\vec{E}_s = \frac{e^{-jkR}}{R} \mathbf{S} \vec{E}_i \quad (1.1)$$

where the wavenumber  $k = 2\pi/\lambda$  and  $R$  is the range (typically, with respect to the radar). In the orthogonal linear polarization basis,  $\mathbf{S}$  for the hydrometeor is expressed as

$$\mathbf{S} = \begin{bmatrix} S_{hh} & S_{hv} \\ S_{vh} & S_{vv} \end{bmatrix} \quad (1.2)$$

The elements of the scattering matrix are the complex scattering functions<sup>1</sup>  $s_{xy}$ . The subscripts  $x$  and  $y$  represent the scattered and incident wave polarizations, respectively.

For linearly-orthogonal dual-polarization radar applications, we can expand (1.1):

$$\begin{bmatrix} E_{hs} \\ E_{vs} \end{bmatrix} = \frac{e^{-jkR}}{R} \begin{bmatrix} s_{hh}(\hat{e}_i, \hat{e}_s) & s_{hv}(\hat{e}_i, \hat{e}_s) \\ s_{vh}(\hat{e}_i, \hat{e}_s) & s_{vv}(\hat{e}_i, \hat{e}_s) \end{bmatrix} \begin{bmatrix} E_{hi} \\ E_{vi} \end{bmatrix}, \quad (1.3)$$

where  $\hat{e}_s$  and  $\hat{e}_i$  are the unit directional vectors of the scattered and incident waves.

Because weather radars tend to be monostatic systems, we are interested in the

---

<sup>1</sup> Note that these are conventionally called scattering “amplitudes,” which is a bit of a misnomer because the elements of the scattering matrix are in fact complex numbers. Here, we adopt the term “function”



backscattered signal. If we define  $\mathbf{k} = \hat{e}_i$  as the direction of the incident wave propagation, then the backscattered signal direction is  $\hat{e}_s = -\mathbf{k}$ . In general, hydrometeors can be canted with respect to the plane of polarization. The geometry of such scattering is shown in Figure 1.1. The hydrometeor canting can be described by two angles: (1) canting of the particle within the plane of polarization,  $\alpha$ , and (2) the canting of the particle out of the plane of polarization,  $\psi$ . The angle  $\alpha$  is taken between the projections of the true vertical and the axis of symmetry of the hydrometeor  $\mathbf{N}$  onto the plane of polarization. The angle  $\psi$  is simply  $90^\circ - \beta$ , where  $\beta$  is the radar antenna elevation angle.

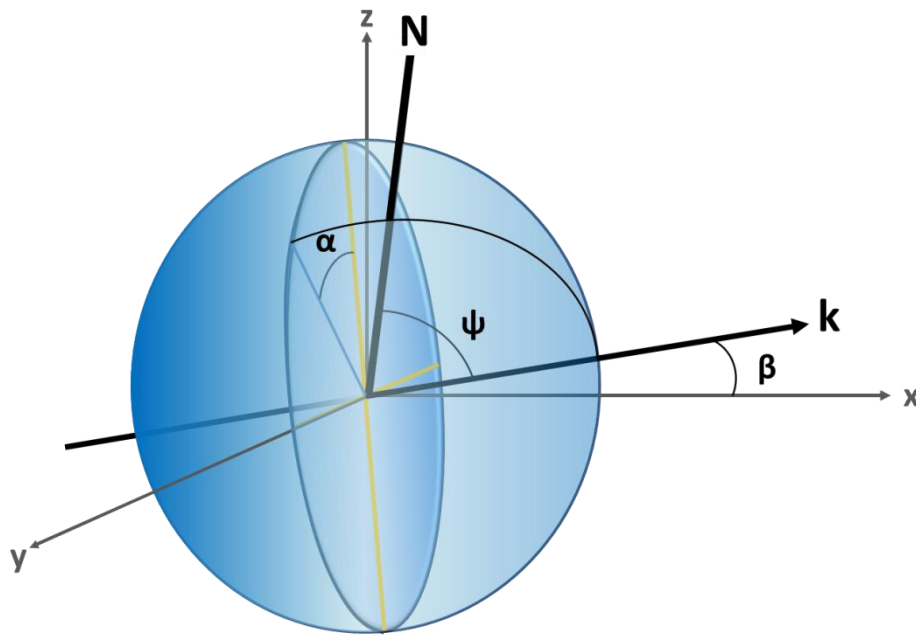


Fig. 1.1: Geometry of scattering. The Cartesian axes  $x$ ,  $y$ , and  $z$  are shown in gray ( $z$  represents the true vertical). The plane with orthogonal yellow lines represents the plane of polarization, which is embedded within a spheroidal hydrometeor with symmetry axis  $\mathbf{N}$ . The direction of wave propagation is  $\mathbf{k}$ , which is at elevation angle  $\beta$ . The particle orientation is given by two angles:  $\alpha$ , which is its canting angle within the plane of polarization (with respect to vertical polarization), and  $\psi$ , which is the angle between the propagation direction and symmetry axis of the particle (in other words,  $90^\circ - \psi$  represents the canting angle out of the plane of polarization).

Simple geometric considerations (Fig. 1.2) allow us to account for canting within the plane of polarization (i.e.,  $\alpha \neq 0^\circ$ ). The incident radiation at both polarizations will each have components along (and thus excite) the dipoles aligned with the particle's major and minor axes ( $b$  and  $a$ ). Thus, the incident radiation at H and V polarizations can be expressed as

$$E_{hi}\widehat{e}_h = (E_{bi})_h\widehat{e}_b + (E_{ai})_h\widehat{e}_a = E_{hi}\cos\alpha\widehat{e}_b + E_{hi}\sin\alpha\widehat{e}_a \quad (1.4a)$$

$$E_{vi}\widehat{e}_v = (E_{bi})_v\widehat{e}_b + (E_{ai})_v\widehat{e}_a = -E_{vi}\sin\alpha\widehat{e}_b + E_{vi}\cos\alpha\widehat{e}_a \quad (1.4b)$$

where we have defined the unit directional vectors  $\widehat{e}_h$  and  $\widehat{e}_v$  as the direction of H and V polarizations, and  $\widehat{e}_b$  and  $\widehat{e}_a$  as along the particle's major and minor axes (see Fig. 1.2). Note that the relation between the principal polarization axes and the particle's major and minor axes is given by a simple rotation matrix,  $\mathbb{R}(\alpha)$ :

$$\begin{bmatrix} \widehat{e}_b \\ \widehat{e}_a \end{bmatrix} = \begin{bmatrix} \cos\alpha & -\sin\alpha \\ \sin\alpha & \cos\alpha \end{bmatrix} \begin{bmatrix} \widehat{e}_h \\ \widehat{e}_v \end{bmatrix} \equiv \mathbb{R}(\alpha) \begin{bmatrix} \widehat{e}_h \\ \widehat{e}_v \end{bmatrix}. \quad (1.5)$$

The scattered radiation is proportional to the component of incident radiation that illuminates each dipole, as well as the complex scattering function<sup>2</sup> of each dipole:

$$\begin{bmatrix} E_{bs} \\ E_{as} \end{bmatrix} = \frac{e^{-jkR}}{R} \begin{bmatrix} s_{bb} & 0 \\ 0 & s_{aa} \end{bmatrix} \mathbb{R}(\alpha) \begin{bmatrix} E_{hi} \\ E_{vi} \end{bmatrix}. \quad (1.6)$$

However, because the radar receives signals at H and V polarization, we must rotate the reference frame back to (H,V) using the inverse of the rotation matrix,  $\mathbb{R}^{-1}(\alpha)$ :

$$\begin{bmatrix} E_{hs} \\ E_{vs} \end{bmatrix} = \frac{e^{-jkR}}{R} \mathbb{R}^{-1}(\alpha) \begin{bmatrix} s_{bb} & 0 \\ 0 & s_{aa} \end{bmatrix} \mathbb{R}(\alpha) \begin{bmatrix} E_{hi} \\ E_{vi} \end{bmatrix}. \quad (1.7)$$

It is clear from inspection of eqns. (1.3) and (1.7) that the scattering matrix  $\mathbf{S}$  can be written as

---

<sup>2</sup> Now that the geometry is such that the axes are the principal axes of the canted drop, there is no depolarization (i.e., the scattering matrix in the rotated reference frame is diagonal).

$$\mathbf{S} = \mathbb{R}^{-1}(\alpha) \begin{bmatrix} s_{bb} & 0 \\ 0 & s_{aa} \end{bmatrix} \mathbb{R}(\alpha)$$

$$= \begin{bmatrix} s_{bb} \cos^2 \alpha + s_{aa} \sin^2 \alpha & (s_{aa} - s_{bb}) \sin \alpha \cos \alpha \\ (s_{aa} - s_{bb}) \sin \alpha \cos \alpha & s_{aa} \cos^2 \alpha + s_{bb} \sin^2 \alpha \end{bmatrix}, \quad (1.8)$$

following Holt (1984) and Ryzhkov (2001).

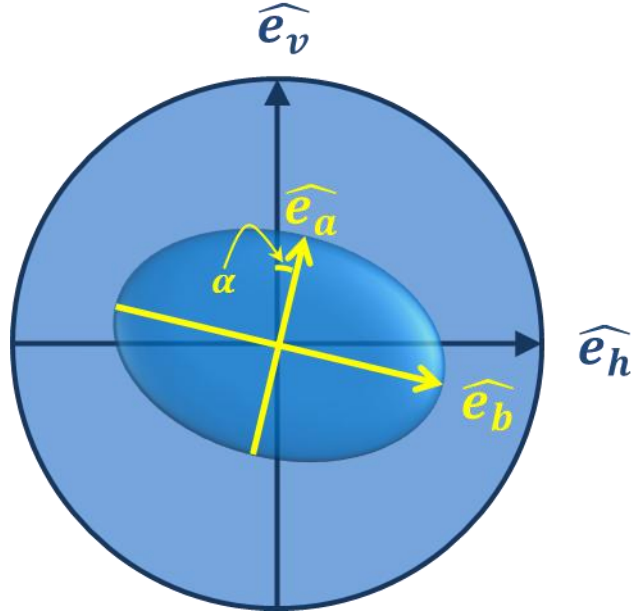


Figure 1.2: View of the polarization plane (blue circle) illuminating a raindrop canted within the plane of polarization at angle  $\alpha$ . The direction of wave propagation  $\mathbf{k}$  is into the page. The raindrop's major and minor axes (yellow arrows) are in the  $\hat{e}_b$  and  $\hat{e}_a$  directions, respectively.

Equation 1.8 is a special case of when the particle's symmetry axis  $\mathbf{N}$  is aligned within the plane of polarization (i.e.,  $\psi = 0^\circ$ ). In general, however,  $\psi \neq 0^\circ$ , in which case the complex scattering functions  $s_{bb}$  and  $s_{aa}$  are functions of  $\psi$ . Holt and Shepherd (1979) derive these functions in the Rayleigh approximation in what is known as the “backscatter rule”:

$$s_{bb} = f_b, \quad s_{aa} = f_a \sin^2 \psi + f_b \cos^2 \psi, \quad (1.9)$$

where  $f_a$  ( $f_b$ ) is the complex scattering function of the particle if the electric field vector is parallel (perpendicular) to the its symmetry axis. Holt (1984) demonstrates that this

approximation is valid in raindrops for radar wavelengths  $\lambda > 0.9$  cm and for elevation angles  $\beta < 10^\circ$ . At S band, this “backscatter rule” is valid for most hydrometeors except large hail. Thus, substituting eqn. (1.9) into eqn. (1.8), we obtain

$$\mathbf{S} = \begin{bmatrix} f_a \sin^2 \alpha \sin^2 \psi + f_b (\sin^2 \alpha \cos^2 \psi + \cos^2 \alpha) & \dots \\ f_a \sin^2 \psi \sin \alpha \cos \alpha + f_b (\cos^2 \psi \sin \alpha \cos \alpha - \sin \alpha \cos \alpha) & \dots \\ f_a \sin^2 \psi \sin \alpha \cos \alpha + f_b (\cos^2 \psi \sin \alpha \cos \alpha - \sin \alpha \cos \alpha) & \dots \\ f_b (\sin^2 \alpha + \cos^2 \alpha \cos^2 \psi) + f_a \cos^2 \alpha \sin^2 \psi & \dots \end{bmatrix} \quad (1.10)$$

After using several trig identities, the expression simplifies to

$$\mathbf{S} = \begin{bmatrix} (f_a - f_b) \sin^2 \psi \sin^2 \alpha + f_b & (f_a - f_b) \sin^2 \psi \sin \alpha \cos \alpha \\ (f_a - f_b) \sin^2 \psi \sin \alpha \cos \alpha & (f_a - f_b) \sin^2 \psi \cos^2 \alpha + f_b \end{bmatrix} \quad (1.11)$$

## 2. Calculating the Complex Scattering Functions

The complex scattering functions  $f_{a,b}$  in eqn. (1.11) characterize the electromagnetic response of particles illuminated by incident radiation. In general,  $f_{a,b}$  are functions of the wavelength of the incident radiation, and the irradiated particle’s properties, including size, shape, temperature, and composition. The particle’s composition affects its complex dielectric factor  $\varepsilon = \varepsilon' - j \varepsilon''$ , which is a measure of a material’s electromagnetic response when irradiated. The complex scattering functions can be calculated using approximate analytical formulas (e.g., Rayleigh 1871; see also Doviak and Zrnić 1993), or more rigorous numerical techniques such as the T-Matrix method (e.g., Waterman 1969; Vivekanandan et al. 1991; Mishchenko 2000) or the discrete dipole approximation (see reviews by Draine 1988; Draine and Flatau 1994). The range of validity for these methods depends on the wavelength of the incident radiation  $\lambda$ , as well as the characteristic size and composition of the particle being

radiated. For hydrometeors treated as spheroids, it is convenient to use the resonance parameter

$$\mathfrak{R} = \frac{D\sqrt{|\varepsilon|}}{\lambda} \quad , \quad (1.12)$$

where  $D$  is the equivalent spherical diameter of the spheroid, and  $\varepsilon$  is the complex dielectric factor. The resonance parameter is unity at the peak of the first resonance; depending on the application and desired accuracy, thresholds of 0.6 – 0.8 are used to determine the limits of the Rayleigh approximation (e.g., Ryzhkov et al. 2011).

*a. Rayleigh Approximation*

Under the Rayleigh approximation to the Mie (1908) solution of scattering by a sphere, the complex scattering functions are given by

$$f_{a,b}^{(0)} = f_{a,b}^{(\pi)} = \frac{\pi^2 D^3}{6\lambda^2} \xi_{a,b} \quad , \quad (1.13)$$

where the polarizability factors of the particle along its minor and major axes are

$$\xi_{a,b} = \frac{1}{L_{a,b} + \frac{1}{\varepsilon - 1}} \quad . \quad (1.14)$$

Note in eqn. (1.13) that the forward and backward scattering functions (superscript 0 and  $\pi$ , respectively) are identical in the Rayleigh approximation. In eqn. (1.14), we have defined the shape parameters  $L_{a,b}$ , which are functions only of the particle axis ratio,  $\gamma = b/a$ . For spherical particles,  $\gamma = 1$ , and the shape parameters  $L_a = L_b = 1/3$ . For oblate particles,  $b > a$ , and

$$L_a = \frac{\gamma^2}{\gamma^2 - 1} \left[ 1 - \frac{\arctan(\sqrt{\gamma^2 - 1})}{\sqrt{\gamma^2 - 1}} \right]; \quad L_b = \frac{1}{2}(1 - L_a) \quad . \quad (1.15)$$

For the case of prolate spheroids,  $b < a$ , and the shape parameters are given by

$$L_a = \frac{\gamma^2}{1 - \gamma^2} \left[ \frac{1}{2\sqrt{1 - \gamma^2}} \ln \left( \frac{1 + \sqrt{1 - \gamma^2}}{1 - \sqrt{1 - \gamma^2}} \right) - 1 \right]; \quad L_b = \frac{1}{2}(1 - L_a) \quad . \quad (1.16)$$

The shape factors are shown in Figure 1.3. If we assume the particle is spherical with the same volume as the oblate or prolate spheroid, eqn. (1.13) can be simplified to

$$f_{a,b}^{(0)} = f_{a,b}^{(\pi)} = \frac{\pi^2 D^3}{2\lambda^2} \frac{\varepsilon - 1}{\varepsilon + 2} \quad . \quad (1.17)$$

In the case of mixed-phase particles (e.g., melting hail, freezing raindrops), it is convenient to use the two-layer spheroid model (e.g., Bohren and Huffman 1983). If the volume fraction of the inner spheroid is  $\zeta_1$ , the complex scattering functions of the two-layer particle are given by

$$f_{a,b} = \frac{\pi^2 D^3}{6\lambda^2} \frac{(\varepsilon_2 - 1)[\varepsilon_2 + L_{a,b}(1 - \zeta_1)(\varepsilon_1 - \varepsilon_2)] + \zeta_1 \varepsilon_2 (\varepsilon_1 - \varepsilon_2)}{[\varepsilon_2 + L_{a,b}(1 - \zeta_1)(\varepsilon_1 - \varepsilon_2)][1 + L_{a,b}(\varepsilon_2 - 1)] + \zeta_1 L_{a,b} \varepsilon_2 (\varepsilon_1 - \varepsilon_2)} \quad . \quad (1.18)$$

In eqn. (1.18), the complex dielectric factors  $\varepsilon_1$  and  $\varepsilon_2$  correspond to the inner and outer spheroid, respectively (Fig. 1.4).

The Rayleigh formulas work well for computing radar variables based on the “real” parts of the complex scattering functions, for values of resonance parameter  $\Re \ll 1.0$ . However, they should not be used to calculate variables related to the “imaginary” parts of the scattering functions for any value of  $\Re$ , as the values provided are inaccurate.

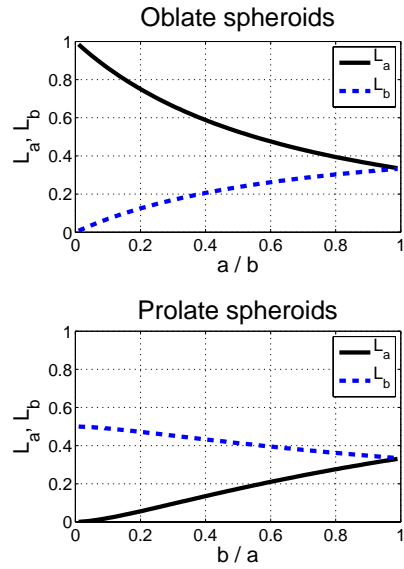


Fig. 1.3: Shape factors  $L_a$  and  $L_b$  for oblate (top panel) and prolate (bottom panel) spheroids.

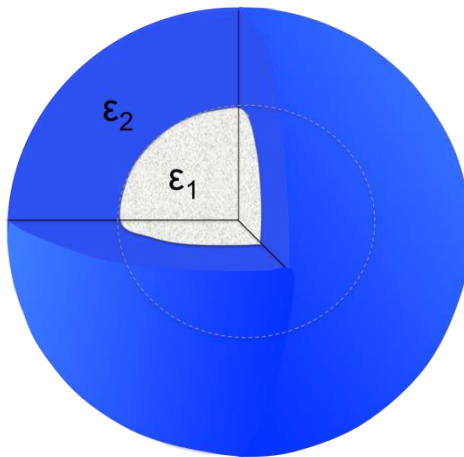


Fig. 1.4: Geometry of the two-layer spheroid, with an inner spheroid of dielectric constant  $\epsilon_1$  and outer dielectric  $\epsilon_2$ . The silhouette of the inner spheroid is shown by the gray dashed curve.

### 3. The Covariance Matrix

Radar meteorologists process the received raw complex voltages to obtain the second-order moments, because the expected value or mean (first order moment) composite voltage over an ensemble of hydrometeors sums to zero owing to the random

phase of the individual contributions (Zrnić 1991). A fully polarimetric radar can measure all quantities in the “covariance matrix”  $\mathbf{C}$ , defined in the linear (HV) basis as (Zrnić 1991)

$$\mathbf{C} = \begin{bmatrix} \langle s_{hh}s_{hh}^* \rangle & \langle s_{hv}s_{hh}^* \rangle & \langle s_{vv}s_{hh}^* \rangle \\ \langle s_{hh}s_{hv}^* \rangle & \langle s_{hh}s_{hv}^* \rangle & \langle s_{vv}s_{hv}^* \rangle \\ \langle s_{hh}s_{vv}^* \rangle & \langle s_{hv}s_{vv}^* \rangle & \langle s_{vv}s_{vv}^* \rangle \end{bmatrix} = \begin{bmatrix} \langle |s_{hh}|^2 \rangle & \langle s_{hv}s_{hh}^* \rangle & \langle s_{vv}s_{hh}^* \rangle \\ \langle s_{hh}s_{hv}^* \rangle & \langle |s_{hv}|^2 \rangle & \langle s_{vv}s_{hv}^* \rangle \\ \langle s_{hh}s_{vv}^* \rangle & \langle s_{hv}s_{vv}^* \rangle & \langle |s_{vv}|^2 \rangle \end{bmatrix}. \quad (1.19)$$

In eqn. (1.19), angle brackets denote ensemble averaging, and the asterisk represents the complex conjugate. Note that the covariance matrix in (1.19) has been reduced from its more general 4x4 form by assuming reciprocity ( $s_{hv} \approx s_{vh}$ ). The diagonal elements of (1.19) are magnitudes only and represent the received co-polar H, cross-polar, and co-polar V powers. These diagonal elements contain no phase information, whereas the off-diagonal elements are complex and thus contain both power and phase information. This is evident by examining one of these elements (e.g.,  $\mathbf{C}_{13}$ ) in expanded form:

$$\langle s_{vv}s_{hh}^* \rangle = \langle |s_{vv}s_{hh}^*| \exp[j(\delta_{vv} - \delta_{hh})] \rangle.$$

The phase angles  $\delta_{ij} = \varphi_i - \varphi_j$  represent the phase lag or lead between the backscattered radiation ( $i$  polarization) and the incident radiation ( $j$  polarization) at the location of the scatterer. In other words, in the absence of propagation effects, the co-polar phase angle  $\delta_{ii}$  represents the phase shift imparted on the  $i$ -polarization radiation upon backscatter. Thus, the argument of the element  $\mathbf{C}_{13}$  is the co-polar differential phase shift upon backscatter, herein denoted as

$$\delta \equiv \delta_{vv} - \delta_{hh}.$$

Because of the symmetry in (1.19), the element  $\mathbf{C}_{31}$  is simply  $-\delta$ ; thus, it is considered non-unique. The remaining off-diagonal elements that provide unique phase information are  $\mathbf{C}_{12}$  ( $\mathbf{C}_{21}$ ) and  $\mathbf{C}_{32}$  ( $\mathbf{C}_{23}$ ):



$$\mathbf{C}_{12} = \langle s_{hv} s_{hh}^* \rangle = \langle |s_{hv} s_{hh}^*| \exp[j(\delta_{hv} - \delta_{hh})] \rangle = \langle |s_{hv} s_{hh}^*| \exp(j\delta_{cr}^{(h)}) \rangle$$

$$\mathbf{C}_{32} = \langle s_{hv} s_{vv}^* \rangle = \langle |s_{hv} s_{vv}^*| \exp[j(\delta_{hv} - \delta_{vv})] \rangle = \langle |s_{hv} s_{vv}^*| \exp(j\delta_{cr}^{(v)}) \rangle.$$

Note that we have defined  $\delta_{cr}^{(h,v)}$  as the so-called *depolarization phase shifts* (Ryzhkov 2001). To summarize the phase information available in the covariance matrix, we define the ‘‘covariance phase matrix’’:

$$\mathbf{C}_\delta = \arg(\mathbf{C}) = \begin{bmatrix} 0 & \delta_{cr}^{(h)} & \delta \\ -\delta_{cr}^{(h)} & 0 & -\delta_{cr}^{(v)} \\ -\delta & \delta_{cr}^{(v)} & 0 \end{bmatrix}. \quad (1.20)$$

#### 4. Polarimetric Radar Variables from the Covariance Matrix

The elements of the covariance matrix are used to infer physical properties of the hydrometeors within the radar sampling volume. The co-polar power at H polarization ( $\mathbf{C}_{11}$  in eqn. 1.19) is related to the radar reflectivity factor at horizontal polarization:

$$Z_h = \frac{4\lambda^4}{\pi^4 |K_w|^2} \langle |s_{hh}|^2 \rangle. \quad (1.21)$$

In eqn. (1.21), the dielectric factor  $|(\epsilon - 1)/(\epsilon + 2)|^2$  is written as  $|K_w|^2$ . Note that the coefficient comes from a normalization such that for small scatterers,  $Z_h$  is identical to the Rayleigh reflectivity (based on eqn. 1.13). Similarly, the co-polar power at V polarization ( $\mathbf{C}_{33}$ ) is related to the radar reflectivity factor at vertical polarization:

$$Z_v = \frac{4\lambda^4}{\pi^4 |K_w|^2} \langle |s_{vv}|^2 \rangle. \quad (1.22)$$

The ratio of these co-polar powers is the differential reflectivity factor:

$$Z_{dr} = \langle |s_{hh}|^2 \rangle / \langle |s_{vv}|^2 \rangle. \quad (1.23)$$

The cross-polar power ( $C_{22}$ ) is compared to the co-polar powers in the linear depolarization ratio,

$$L_{dr}^{(h)} = \langle |s_{hv}|^2 \rangle / \langle |s_{hh}|^2 \rangle \quad , \quad (1.24)$$

and

$$L_{dr}^{(v)} = \langle |s_{hv}|^2 \rangle / \langle |s_{vv}|^2 \rangle \quad . \quad (1.25)$$

The off-diagonal elements of  $\mathbf{C}$  are used in correlation coefficients. The most common is the co-polar cross-correlation coefficient, taken at zero lag time,

$$\rho_{hv} = \langle s_{vv} s_{hh}^* \rangle / \sqrt{\langle |s_{hh}|^2 \rangle \langle |s_{vv}|^2 \rangle} \quad . \quad (1.26)$$

The remaining coefficients take the correlation between the co-polar and cross-polar signals, and are sometimes referred to as the co-cross-polar correlation coefficients (e.g., Ryzhkov 2001; Ryzhkov et al. 2002b):

$$\rho_{xh} = \langle s_{hv} s_{hh}^* \rangle / \sqrt{\langle |s_{hv}|^2 \rangle \langle |s_{hh}|^2 \rangle} \quad (1.27)$$

$$\rho_{xv} = \langle s_{hv} s_{vv}^* \rangle / \sqrt{\langle |s_{hv}|^2 \rangle \langle |s_{vv}|^2 \rangle} \quad . \quad (1.28)$$

The angled brackets denote averaging over the ensemble of hydrometeors within the radar sampling volume. Thus, these expected values can be written in terms of the distribution of the hydrometeor's physical properties, such as size, shape, and canting angle. In the most general form,

$$\langle s_{ij} s_{kl}^* \rangle = \int_0^\infty N(\vec{\mathbf{X}}) s_{ij} s_{kl}^* d\vec{\mathbf{X}} \quad , \quad (1.29)$$

where  $N(\vec{\mathbf{X}})$  is the probability density of hydrometeor properties, which are defined by the vector  $\vec{\mathbf{X}}$ . Using  $\mathbf{S}_{11}$  from eqn. (1.11) in eqn. (1.29), substituting the result into (1.21), and assuming that the particle size and shape distributions are independent from

the distribution of orientation angles, we obtain a revised expression for radar reflectivity factor at horizontal polarization (Ryzhkov 1991)

$$Z_h = \frac{4\lambda^4}{\pi^4 |K_w|^2} \int_0^\infty \{ |f_b|^2 - 2(|f_b|^2 - f_a f_b^* - f_a^* f_b) \sin^2 \psi \sin^2 \alpha + |f_b - f_a|^2 \sin^4 \psi \sin^4 \alpha \} N(D) dD. \quad (1.30)$$

The second term in the integrand of eqn. (1.30) can be simplified by noting that  $|f_b|^2 - f_a f_b^* - f_a^* f_b = \text{Re}\{f_b^*(f_b - f_a)\}$ . Similarly, using  $\mathbf{S}_{22}$  in eqn. (1.29) and substituting into (1.22), the radar reflectivity factor at vertical polarization becomes

$$Z_v = \frac{4\lambda^4}{\pi^4 |K_w|^2} \int_0^\infty \{ |f_b|^2 - 2 \text{Re}\{f_b^*(f_b - f_a)\} \sin^2 \psi \cos^2 \alpha + |f_b - f_a|^2 \sin^4 \psi \cos^4 \alpha \} N(D) dD, \quad (1.31)$$

and using  $\mathbf{S}_{21} = \mathbf{S}_{12}$  and equation (1.29) in equations (1.24) – (1.25), the linear depolarization ratios become

$$L_{dr}^{(h,v)} = \frac{4\lambda^4}{\pi^4 |K_w|^2} \frac{1}{Z_{h,v}} \int_0^\infty \{ |f_b - f_a|^2 \sin^4 \psi \sin^2 \alpha \cos^2 \alpha \} N(D) dD. \quad (1.32)$$

For meteorological applications, the magnitude of the cross-correlation coefficients is taken. This is because particles with large “imaginary” parts of the refractive index (and/or non-Rayleigh scatterers) produce nonzero phase shifts upon backscatter, which cause the correlation coefficients to become complex. Following the same analysis as above, the magnitude of the co-polar cross-correlation coefficient becomes

$$\begin{aligned}
|\rho_{hv}| = \frac{4\lambda^4}{\pi^4 |K_w|^2} \frac{1}{\sqrt{Z_h Z_v}} \left| \int_0^\infty \{ |f_b|^2 + |f_b - f_a|^2 \sin^4 \psi \sin^2 \alpha \cos^2 \alpha \right. \\
- f_b (f_b^* - f_a^*) \sin^2 \psi \sin^2 \alpha f_b^* (f_b \\
- f_a) \sin^2 \psi \cos^2 \alpha \} N(D) dD \Big| . \quad (1.33)
\end{aligned}$$

Similarly, the magnitudes of the co-cross-polar correlation coefficients may be written as

$$\begin{aligned}
|\rho_{xh}| = \left( \frac{4\lambda^4}{\pi^4 |K_w|^2} \right)^{\frac{3}{2}} \frac{1}{2 Z_h \sqrt{L_{dr}^{(h)}}} \left| \int_0^\infty \{ |f_b - f_a|^2 \sin^4 \psi \sin^2 \alpha \sin 2\alpha \right. \\
- f_b^* (f_b - f_a) \sin^2 \psi \sin 2\alpha \} N(D) dD \Big| \quad (1.34)
\end{aligned}$$

and

$$\begin{aligned}
|\rho_{xv}| = \left( \frac{4\lambda^4}{\pi^4 |K_w|^2} \right)^{\frac{3}{2}} \frac{1}{2 Z_v \sqrt{L_{dr}^{(v)}}} \left| \int_0^\infty \{ |f_b - f_a|^2 \sin^4 \psi \cos^2 \alpha \sin 2\alpha \right. \\
- f_b^* (f_b - f_a) \sin^2 \psi \sin 2\alpha \} N(D) dD \Big| . \quad (1.35)
\end{aligned}$$

The trigonometric terms in eqns. (1.30) – (1.35) are defined by Ryzhkov (1991, 2001) and Ryzhkov et al. (2011) as angular moments:

$$\begin{aligned}
A_1 &= \langle \sin^2 \psi \cos^2 \alpha \rangle, & A_2 &= \langle \sin^2 \psi \sin^2 \alpha \rangle, & A_3 &= \langle \sin^4 \psi \cos^4 \alpha \rangle, \\
A_4 &= \langle \sin^4 \psi \sin^4 \alpha \rangle, & A_5 &= \langle \sin^4 \psi \cos^2 \alpha \sin^2 \alpha \rangle, & A_6 &= \langle \sin^2 \psi \sin 2\alpha \rangle, \\
A_7 &= \langle \sin^4 \psi \cos^2 \alpha \sin 2\alpha \rangle, & A_8 &= \langle \sin^4 \psi \sin^2 \alpha \sin 2\alpha \rangle, \\
A_9 &= A_1 - A_2 = \langle \sin^2 \psi \cos 2\alpha \rangle. \quad (1.36)
\end{aligned}$$

Convenient analytical formulas for the angular moments in eqn. (1.36) exist for three special cases that are described in section 6. Substituting the definitions of the angular moments (1.36) into the expressions for the polarimetric radar variables derived above, and defining the coefficient as  $\mathcal{C} \equiv 4\lambda^4/\pi^4|K_w|^2$ , we arrive at expressions for all backscattering polarimetric radar variables in simplified notation:

$$Z_h = \mathcal{C} \int_0^{\infty} \{|f_b|^2 - 2\text{Re}[f_b^*(f_b - f_a)]A_2 + |f_b - f_a|^2A_4\}N(D)dD \quad (1.37)$$

$$Z_v = \mathcal{C} \int_0^{\infty} \{|f_b|^2 - 2\text{Re}[f_b^*(f_b - f_a)]A_1 + |f_b - f_a|^2A_3\}N(D)dD \quad (1.38)$$

$$Z_{dr} = \frac{Z_h}{Z_v} \quad (1.39)$$

$$L_{dr}^{(h,v)} = \frac{\mathcal{C}}{Z_{h,v}} \int_0^{\infty} \{|f_b - f_a|^2A_5\}N(D)dD \quad (1.40)$$

$$|\rho_{hv}| = \frac{\mathcal{C}}{\sqrt{Z_h Z_v}} \left| \int_0^{\infty} \{|f_b|^2 + |f_b - f_a|^2A_5 - f_b(f_b^* - f_a^*)A_2 - f_b^*(f_b - f_a)A_1\}N(D)dD \right| \quad (1.41)$$

$$|\rho_{xh}| = \frac{\mathcal{C}^{\frac{3}{2}}}{2 Z_h \sqrt{L_{dr}^{(h)}}} \left| \int_0^{\infty} \{|f_b - f_a|^2A_8 - f_b^*(f_b - f_a)A_6\}N(D)dD \right| \quad (1.42)$$

$$|\rho_{xv}| = \frac{\mathcal{C}^{\frac{3}{2}}}{2 Z_v \sqrt{L_{dr}^{(v)}}} \left| \int_0^{\infty} \{|f_b - f_a|^2A_7 - f_b^*(f_b - f_a)A_6\}N(D)dD \right| \quad (1.43)$$

Note that the lowercase subscripts denote linear units. In practice, owing to the huge dynamic range of the power-related variables, these variables are presented in logarithmic units, denoted by uppercase subscripts:

$$Z_H = 10 \log_{10}(Z_h), \quad Z_V = 10 \log_{10}(Z_v), \quad L_{DR} = 10 \log_{10}(L_{dr})$$

$$Z_{DR} = 10 \log_{10}(Z_{dr}) = Z_H - Z_V$$

## 5. Forward-scattering variables

Electromagnetic waves propagating in an atmosphere filled with gases and hydrometeors will undergo what are collectively known as propagation effects, which include the acquisition of an additional propagation phase shift, loss of amplitude owing to absorption and scattering in the medium (known as attenuation), and depolarization in the presence of canted hydrometeors. Figure 1.5 is a cartoon illustrating the effects of propagation phase shift and attenuation, and Figure 1.6 describes depolarization by a canted hydrometeor. These effects are described by imparting an additional complex phase shift on the propagating electromagnetic wave compared to what it would have after propagating the same distance in a vacuum. This can be thought of as the wave *slowing* as it propagates through a medium, characterized by an effective complex index of refraction

$$n_{h,v} = 1 + n^{(air)} + n_{h,v}^{(scat)} \quad , \quad (1.44)$$

that comprises contributions from the air  $n^{(air)}$  and the scatterers along the propagation path  $n^{(scat)}$ . The propagation phase shift is governed by the real parts of  $n_{h,v}$ , and the loss of amplitude or attenuation is governed by the imaginary parts of  $n_{h,v}$ . For weather radar frequencies, the real part of  $n^{(air)}$  is given by

$$Re[n^{(air)}] = \frac{77.6}{T(K)} \left( P(\text{hPa}) + \frac{4810 e(\text{hPa})}{T(K)} \right) 10^{-6} \quad , \quad (1.45)$$

where  $T$  is the temperature in degrees Kelvin,  $P$  is the pressure in hPa, and  $e$  is the vapor pressure (also given in hPa). The contribution to the effective refractive index from scatterers along the propagation path depends on their total number concentration, radar wavelength, and the forward scattering amplitude of hydrometeors, indicated by the superscript (0):

$$n_{h,v}^{(scat)} = \frac{\lambda^2}{2\pi} \langle s_{hh,vv}^{(0)} \rangle. \quad (1.46)$$

Because atmospheric scatterers tend to be anisotropic,  $\langle s_{hh}^{(0)} \rangle \neq \langle s_{vv}^{(0)} \rangle$ . Thus,  $n_h \neq n_v$ , which produces for differential propagation effects between horizontal and vertical polarizations (i.e., differential propagation phase shift and differential attenuation).

Recall the expression for an electromagnetic plane wave traveling a distance  $r$ :

$$\vec{E}(r) = E_h(r) \hat{e}_h + E_v(r) \hat{e}_v, \quad (1.47)$$

which can be separated into its amplitude and phase components

$$\vec{E}(r) = E_h(0) \exp[j(2\pi ft - kr - \varphi_h)] \hat{e}_h + E_v(0) \exp[j(2\pi ft - kr - \varphi_v)] \hat{e}_v. \quad (1.48)$$

It is common practice to separate the time-varying part:

$$\vec{E}(r) = E'_h \exp(j2\pi ft) \hat{e}_h + E'_v \exp(j2\pi ft) \hat{e}_v, \quad (1.49)$$

where

$$\begin{bmatrix} E'_h \\ E'_v \end{bmatrix} = \begin{bmatrix} E_h(0) \exp(-jkr - j\varphi_h) \\ E_v(0) \exp(-jkr - j\varphi_v) \end{bmatrix}. \quad (1.50)$$

The complex effective refractive index defined in eqn. (1.44) is combined with the wavenumber  $k$  to obtain the effective wavenumber

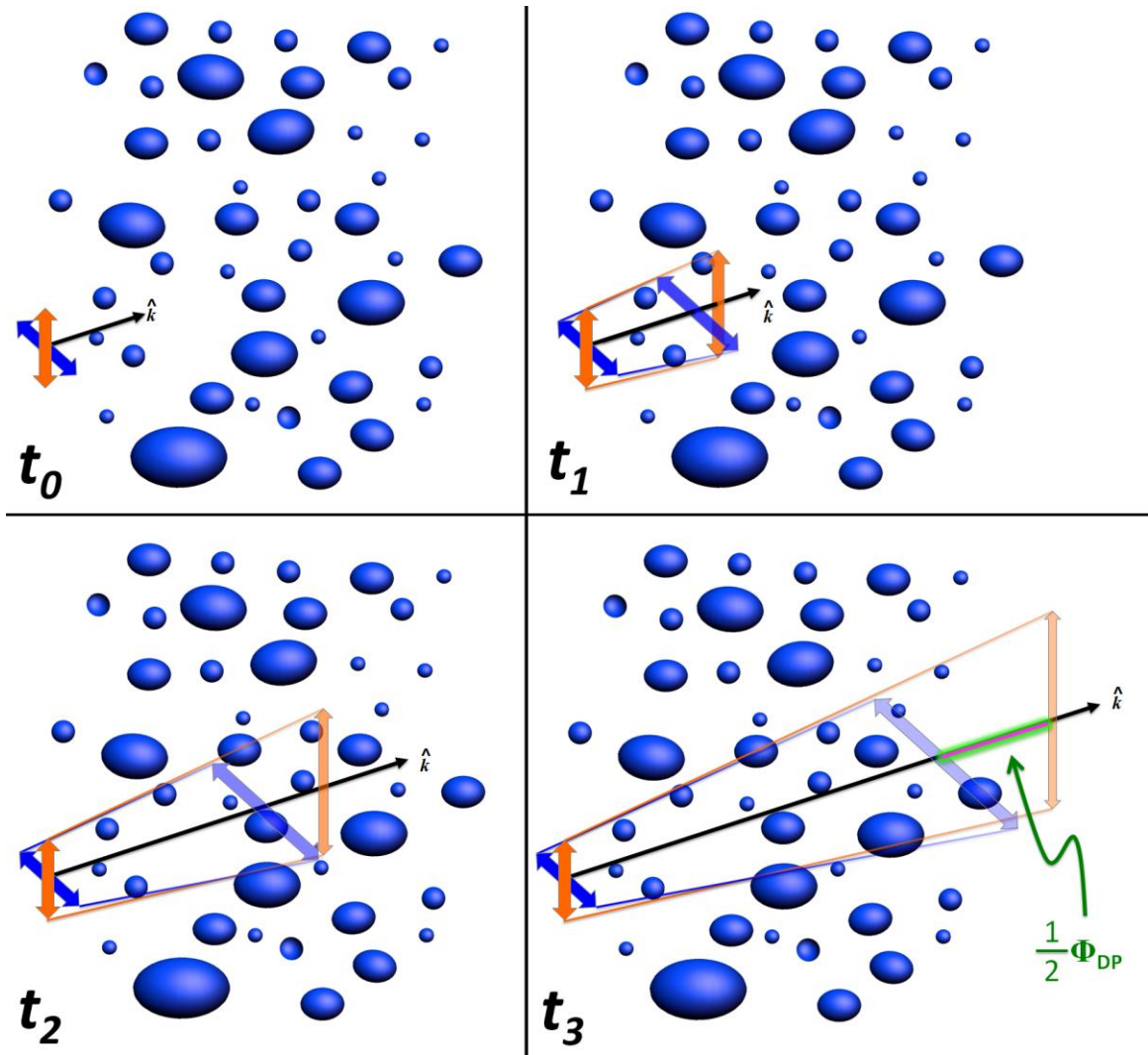


Fig. 1.5: Schematic illustrating propagation effects of differential propagation phase shift and attenuation. Each panel shows successive times; the vertically-polarized signal is represented by the orange arrow, and the horizontally-polarized signal by the blue arrow, and propagation direction is given by the black vector,  $\hat{\mathbf{k}}$ . The gradual separation of the H and V signals as they propagate through the rain represents the differential propagation phase shift. Signal amplitude is portrayed by the color shading of the arrows: the fading of the arrows represents attenuation.



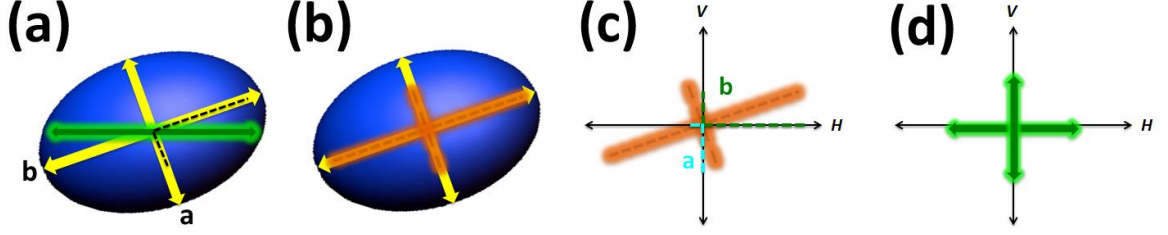


Fig. 1.6: Schematic illustrating the depolarization of the incident electromagnetic wave as a result of hydrometeor canting. (a) The canted raindrop, characterized by major axis  $b$  and minor axis  $a$  (depicted by the yellow arrows) is illuminated by an incident horizontally-polarized wave depicted by the glowing green arrow. Because there is a component of the incident wave that is aligned with both axes of the drop (black dashed line), (b) both dipoles of the drop are excited, as depicted by the orange glowing arrows. (c) These excited dipoles emit secondary radiation that can be decomposed into horizontal and vertical components (the green dashed lines indicate the decomposition of the radiation emitted by the major axis  $b$ , and the cyan lines represent the decomposition of the radiation emitted by the minor axis  $a$ ). (d) The scattered radiation in the forward and backward directions now has a cross-polar (vertically-polarized) component.

$$\tilde{k}_{h,v} = kn_{h,v} = k' + k_{h,v} \quad (1.51)$$

which is also complex. Note that we have separated contributions from propagation through air  $k' = k(1 + n^{(air)})$  and from propagation through hydrometeors  $k_{h,v} = kn_{h,v}^{(scat)}$ . From eqn. (1.46), we can see that

$$k_{h,v} = \lambda \langle s_{hh,vv}^{(0)} \rangle. \quad (1.52)$$

The contribution from hydrometeors to the effective wavenumber can be summarized in the matrix

$$\mathbb{P} = -j \begin{bmatrix} k_h & k_{hv} \\ k_{vh} & k_v \end{bmatrix} = -j\lambda \begin{bmatrix} \langle s_{hh}^{(0)} \rangle & \langle s_{hv}^{(0)} \rangle \\ \langle s_{vh}^{(0)} \rangle & \langle s_{vv}^{(0)} \rangle \end{bmatrix} = \begin{bmatrix} p_{hh} & p_{hv} \\ p_{vh} & p_{vv} \end{bmatrix}. \quad (1.53)$$

Note that the cross-polar components of eqn. (1.53) exist only if depolarization on propagation occurs (i.e., if the propagating wave acquires a cross-polarization component upon forwardscatter).

To account for propagation effects, the effective wavenumber in eqn. (1.51) replaces  $k$  in eqn. (1.50), resulting in

$$E_{h,v}'(r) = E_{h,v}(0) \exp(-j\tilde{k}_{h,v}r - j\varphi_{h,v}). \quad (1.54)$$

The phasors in eqn. (1.54) are solutions to the set of differential equations

$$\frac{d}{dr} \begin{bmatrix} E_h' \\ E_v' \end{bmatrix} = \mathbb{B} \begin{bmatrix} E_h' \\ E_v' \end{bmatrix} = \begin{bmatrix} B_{hh} & B_{hv} \\ B_{vh} & B_{vv} \end{bmatrix} \begin{bmatrix} E_h' \\ E_v' \end{bmatrix}. \quad (1.55)$$

If the mean canting angle of hydrometeors along the propagation path is equal to  $0^\circ$  or  $90^\circ$  (i.e., on average the particles' symmetry axes are aligned with the vertical or horizontal), then there is no depolarization on propagation. In this case, the matrix  $\mathbb{B}$  is diagonal, with its elements given by

$$\mathbb{B} = \begin{bmatrix} -j\tilde{k}_h & 0 \\ 0 & -j\tilde{k}_v \end{bmatrix} = \begin{bmatrix} -j(k' + k_h) & 0 \\ 0 & -j(k' + k_v) \end{bmatrix}. \quad (1.56)$$

Thus, the H- and V-polarization waves propagate independently. On the other hand, if the mean hydrometeor canting angle along the propagation path is not equal to  $0^\circ$  or  $90^\circ$ , then depolarization of the signal upon propagation occurs. This means that the wave's initial polarization state changes during propagation through a hydrometeor medium as it acquires a cross-polarized component of radiation. In this case, the matrix  $\mathbb{B}$  can be written as

$$\begin{aligned} \mathbb{B} &= \begin{bmatrix} -j(k' + k_h) & -jk_{hv} \\ -jk_{vh} & -j(k' + k_v) \end{bmatrix} = \begin{bmatrix} -j(k' + k_h) & -j\lambda \langle s_{hv}^{(0)} \rangle \\ -j\lambda \langle s_{vh}^{(0)} \rangle & -j(k' + k_v) \end{bmatrix} \\ &= \begin{bmatrix} -jk' + p_{hh} & p_{hv} \\ p_{vh} & -jk' + p_{vv} \end{bmatrix}. \end{aligned} \quad (1.57)$$

For the most general case, with  $\mathbb{B}$  given by (1.57), the solution to (1.55) is given by

$$\begin{bmatrix} E_h(r)' \\ E_v(r)' \end{bmatrix} = \mathbb{R}^{-1}(\alpha) \begin{bmatrix} \exp(-j\lambda_1 r) & 0 \\ 0 & \exp(-j\lambda_2 r) \end{bmatrix} \mathbb{R}(\alpha) \begin{bmatrix} E_h(0) \\ E_v(0) \end{bmatrix}, \quad (1.58)$$

where  $\lambda_1$  and  $\lambda_2$  are the eigenvalues,

$$\begin{aligned}\lambda_1 &= k' + \frac{j}{2}(p_{hh} + p_{vv} + \omega) \\ \lambda_2 &= k' + \frac{j}{2}(p_{hh} + p_{vv} - \omega)\end{aligned}, \quad (1.59)$$

with

$$\omega = \sqrt{(p_{hh} - p_{vv})^2 + 4p_{hv}p_{vh}}. \quad (1.60)$$

After substituting the rotation matrix from eqn. (1.5), the solution (1.58) becomes

$$\begin{bmatrix} E_h(r)' \\ E_v(r)' \end{bmatrix} = \mathbb{T} \begin{bmatrix} E_h(0) \\ E_v(0) \end{bmatrix} = \begin{bmatrix} T_{hh} & T_{hv} \\ T_{vh} & T_{vv} \end{bmatrix} \begin{bmatrix} E_h(0) \\ E_v(0) \end{bmatrix}, \quad (1.61)$$

where the transmission matrix  $\mathbb{T}$  is defined as

$$\mathbb{T} = \begin{bmatrix} e^{-j\lambda_1 r} \cos^2 \alpha + e^{-j\lambda_2 r} \sin^2 \alpha & (e^{-j\lambda_2 r} - e^{-j\lambda_1 r}) \sin \alpha \cos \alpha \\ (e^{-j\lambda_2 r} - e^{-j\lambda_1 r}) \sin \alpha \cos \alpha & e^{-j\lambda_1 r} \sin^2 \alpha + e^{-j\lambda_2 r} \cos^2 \alpha \end{bmatrix}. \quad (1.62)$$

The magnitudes of the elements in the transmission matrix correspond to losses by attenuation on propagation through a medium. As such, it is convenient to write the losses matrix

$$\mathbb{L} = \begin{bmatrix} l_{hh} & l_{hv} \\ l_{vh} & l_{vv} \end{bmatrix} = \begin{bmatrix} |T_{hh}|^2 & |T_{hv}|^2 \\ |T_{vh}|^2 & |T_{vv}|^2 \end{bmatrix}. \quad (1.63)$$

In the absence of depolarization on propagation, the cross-polar components of eqn. (1.53) vanish ( $p_{hv} = p_{vh} = 0$ ;  $\langle \alpha \rangle = 0$ ), and the eigenvalues (eqn. 1.59) become

$$\begin{aligned}\lambda_1 &= k' + jp_{hh} = k' + k_h = \tilde{k}_h \\ \lambda_2 &= k' + jp_{vv} = k' + k_v = \tilde{k}_v\end{aligned}, \quad (1.64)$$

and thus the phasor expression for  $E_{h,v}'$  can be written as in eqn. (1.54). Because the effective wavenumbers  $\tilde{k}_{h,v}$  are complex, it is convenient to separate contributions from the real and imaginary parts (i.e., the parts characterizing the propagation phase shift and attenuation losses). Using the definition in eqn. (1.52), this yields

$$E_h(r)' = E_h(0) \exp \left[ -j \left( \text{Re}\{k'\} + j\text{Im}\{k'\} + \lambda \text{Re}\{s_{hh}^{(0)}\} + j\lambda \text{Im}\{s_{hh}^{(0)}\} \right) r \right]$$

$$= E_h(0) \exp \left[ -j \left( \text{Re}\{k'\} + \lambda \text{Re}\{s_{hh}^{(0)}\} \right) r \right] \exp \left[ \text{Im}\{k'\} + \lambda \text{Im}\{s_{hh}^{(0)}\} \right] , \quad (1.65)$$

for the horizontally-polarized wave, and a similar expression

$$E_v(r)' = E_v(0) \exp \left[ -j \left( \text{Re}\{k'\} + \lambda \text{Re}\{s_{vv}^{(0)}\} \right) r \right] \exp \left[ \text{Im}\{k'\} + \lambda \text{Im}\{s_{vv}^{(0)}\} \right] \quad (1.66)$$

for the vertically-polarized wave. It is clear from eqns. (1.65) – (1.66) that the real part of the complex effective wavenumber  $\tilde{k}_{h,v}$  characterizes a phase shift, which we can define as

$$\Phi_{h,v} = \left( \text{Re}\{k'\} + \lambda \text{Re}\{s_{hh,vv}^{(0)}\} \right) r = \left[ 1 + \text{Re}\{n^{(air)}\} + \frac{\lambda^2}{2\pi} \text{Re}\{s_{hh,vv}^{(0)}\} \right] kr. \quad (1.67)$$

Similarly, we can relate the imaginary part of the effective wavenumber to elements of the losses matrix, or attenuation factors, using eqn. (1.63)

$$\begin{aligned} l_{hh,vv}(r) &= \exp \left[ \left( 2\text{Im}\{k'\} + 2\lambda \text{Im}\{s_{hh,vv}^{(0)}\} \right) r \right] \\ &= \exp \left[ \left( 2\text{Im}\{n^{(air)}\} + \frac{\lambda^2}{\pi} \text{Im}\{s_{hh,vv}^{(0)}\} \right) kr \right] . \end{aligned} \quad (1.68)$$

Thus, phasors (1.65) – (1.66) are written as

$$\begin{aligned} E_h(r)' &= E_h(0) \sqrt{l_{hh}(r)} \exp[-j\Phi_h(r)] \\ E_v(r)' &= E_v(0) \sqrt{l_{vv}(r)} \exp[-j\Phi_v(r)] \end{aligned} \quad (1.69)$$

The attenuation factors are usually expressed in logarithmic scale and can be written as the product of propagation distance  $r$  and the specific attenuation at horizontal and vertical polarizations  $A_{H,V}$ , as

$$10 \log(l_{hh,vv}) = A_{H,V} r, \quad (1.70)$$

where the specific attenuation is defined as

$$A_{H,V} = -8.686 \left[ k \text{Im}\{n^{(air)}\} + \lambda \text{Im}\{s_{hh,vv}^{(0)}\} \right] . \quad (1.71)$$

Note that the negative sign is a result of choosing the  $\exp(+j2\pi ft)$  convention for the time-varying part of the propagating electromagnetic wave. If, instead, the negative convention is used, the specific attenuation would be positive. The factor of 8.686 comes from twice (for two-way attenuation) the result of  $10 \log_{10}(e)$ .

For most weather radar frequencies, attenuation by atmospheric gases is very small compared to attenuation in hydrometeors; thus, the second term in eqn. (1.71) is dominant. For anisotropic particles,  $A_H \neq A_V$ , and so it is informative to take their difference, known as specific differential attenuation

$$A_{DP} = A_H - A_V = -8.686\lambda \operatorname{Im}\left\{\langle s_{hh}^{(0)} \rangle - \langle s_{vv}^{(0)} \rangle\right\}. \quad (1.72)$$

Though the contribution of atmospheric gases to the phase shifts  $\Phi_{h,v}$  is much larger than that of hydrometeors, it is anisotropic hydrometeors alone that can change the *difference* between these phase shifts at horizontal and vertical polarizations, known as the differential phase shift upon propagation

$$\Phi_{DP} = 2(\Phi_h - \Phi_v) = 2 \int_0^r K_{DP}(r') dr'. \quad (1.73)$$

In eqn. (1.73), the factor of 2 is because the measured propagation differential phase shift is two-way. Also in eqn. (1.73) we have introduced the specific differential phase shift, which is defined using eqns. (1.67) and (1.73) as

$$K_{DP} = \frac{\lambda^2}{2\pi} \operatorname{Re}\left\{\langle s_{hh}^{(0)} \rangle - \langle s_{vv}^{(0)} \rangle\right\} k = \lambda \operatorname{Re}\left\{\langle s_{hh}^{(0)} \rangle - \langle s_{vv}^{(0)} \rangle\right\}. \quad (1.74)$$

In the definitions (1.72) – (1.74), the angular brackets denote ensemble averaging, as before. Recall from eqn. (1.29) that this can be related to integration over the particle size distribution. Using this relation, and employing the approximation that  $f_{b,a} \approx f_{b,a}^{(0)}$ ,

which is valid for Rayleigh scatterers, we can express the specific attenuations and specific differential phase for the general case for hydrometeors canted within and out of the plane of polarization:

$$A_H = -8.686\lambda \int_0^{\infty} \left[ \text{Im}\{f_b^{(0)}\} - \text{Im}\{f_b^{(0)} - f_a^{(0)}\} \sin^2 \psi \sin^2 \alpha \right] N(D) dD , \quad (1.75)$$

$$A_V = -8.686\lambda \int_0^{\infty} \left[ \text{Im}\{f_b^{(0)}\} - \text{Im}\{f_b^{(0)} - f_a^{(0)}\} \sin^2 \psi \cos^2 \alpha \right] N(D) dD , \quad (1.76)$$

$$A_{DP} = -8.686\lambda \int_0^{\infty} \text{Im}\{f_b^{(0)} - f_a^{(0)}\} \sin^2 \psi \cos 2\alpha N(D) dD , \quad (1.77)$$

$$K_{DP} = \frac{180\lambda}{\pi} \int_0^{\infty} \text{Re}\{f_b^{(0)} - f_a^{(0)}\} \sin^2 \psi \cos 2\alpha N(D) dD , \quad (1.78)$$

where the factor of  $180/\pi$  in eqn. (1.78) converts from radians to degrees. Using the formulas for the angular moments presented in the previous section, we can write the variables as

$$A_H = -8.686 \cdot 10^{-3} \lambda \int_0^{\infty} \left[ \text{Im}\{f_b^{(0)}\} - \text{Im}\{f_b^{(0)} - f_a^{(0)}\} A_2 \right] N(D) dD , \quad (1.79)$$

$$A_V = -8.686 \cdot 10^{-3} \lambda \int_0^{\infty} \left[ \text{Im}\{f_b^{(0)}\} - \text{Im}\{f_b^{(0)} - f_a^{(0)}\} A_1 \right] N(D) dD , \quad (1.80)$$

$$A_{DP} = -8.686 \cdot 10^{-3} \lambda \int_0^{\infty} \text{Im}\{f_b^{(0)} - f_a^{(0)}\} A_9 N(D) dD , \quad (1.81)$$

and

$$K_{DP} = \frac{0.18\lambda}{\pi} \int_0^{\infty} \text{Re}\{f_b^{(0)} - f_a^{(0)}\} A_9(D) dD . \quad (1.82)$$

Note that the coefficients to eqns. (1.79) – (1.82) are modified such that the units of  $A_H$ ,  $A_V$ , and  $A_{DP}$  are in  $\text{dB km}^{-1}$ , and  $K_{DP}$  is in  $\text{deg km}^{-1}$ , given that scattering amplitudes  $f_{b,a}^{(0)}$  and radar wavelength  $\lambda$  are in mm, and the particle size distribution  $N(D)dD$  is in  $\text{m}^{-3}$ .

## 6. Special cases for angular moments

There exist at least three special cases for which there are simple analytical formulas for the angular moments (e.g., Ryzhkov 2001, Ryzhkov et al. 2011). These are: (a) completely random orientation of the hydrometeors, (b) random orientation of hydrometeors in the horizontal plane, and (c) a two-dimensional axisymmetric Gaussian distribution of canting angles (Fig. 1.7).

### *a. Completely random orientation*

For totally chaotic orientation of hydrometeors, the angular moments reduce to

$$A_1 = A_2 = \frac{1}{3}, \quad A_3 = A_4 = \frac{1}{5}, \quad A_5 = \frac{1}{15}, \quad A_6 = A_7 = A_8 = A_9 = 0. \quad (1.83)$$

This case can be applied to particles that are chaotically tumbling within the radar sampling volume, including (perhaps) tornadic debris.

### *b. Random orientation in the horizontal plane*

Owing to viscous drag, various types of small (low-Reynolds number) hydrometeors orient themselves such that their major axis is aligned in the horizontal. However, in the absence of any external forcing (e.g., a strong electric field), there is no preferential orientation in the horizontal plane. Such orientation is typical for columnar

ice crystals or needles. In this case, the angular moments are functions of only radar antenna elevation angle ( $\beta$ ; cf. Figure 1.1):

$$\begin{aligned} A_1 &= \frac{1}{2} \sin^2 \beta, & A_2 &= \frac{1}{2}, & A_3 &= \frac{3}{8} \sin^4 \beta, & A_4 &= \frac{3}{8}, & A_5 &= \frac{1}{8} \sin^2 \beta, \\ A_6 &= A_7 = A_8 = 0, & A_9 &= -\frac{1}{2} \cos^2 \beta. \end{aligned} \quad (1.84)$$

*c. Two-dimensional axisymmetric Gaussian distribution of orientations.*

For low radar antenna elevation angles  $\beta$ , and for angular distribution widths that are not very large, we can approximate an axisymmetric Gaussian distribution as

$$p(\psi, \alpha) = \frac{1}{2\pi\sigma_\psi\sigma_\alpha} \exp \left[ -\frac{(\psi - \langle\psi\rangle)^2}{2\sigma_\psi^2} - \frac{(\alpha - \langle\alpha\rangle)^2}{2\sigma_\alpha^2} \right], \quad (1.85)$$

where  $\langle\psi\rangle$  and  $\langle\alpha\rangle$  are the mean canting angles of the particles out of and within the plane of polarization, respectively (cf. Figure 1.1). The angular distribution widths along the  $\psi$  and  $\alpha$  directions are given by  $\sigma_\psi$  and  $\sigma_\alpha = \sigma_\psi / \sin\langle\psi\rangle$ . Note that the approximation (1.85) allows for averaging over the angles  $\psi$  and  $\alpha$  independently. This type of orientation angle dispersion represents a large array of hydrometeor types that are modeled as oblate spheroids, including raindrops, snowflakes, ice pellets, graupel particles, and hailstones. In this case, the angular moments may be expressed as

$$\begin{aligned} A_1 &= \frac{1}{4} (1 - r_\psi \cos 2\langle\psi\rangle)(1 + r_\alpha \cos 2\langle\alpha\rangle), \\ A_2 &= \frac{1}{4} (1 - r_\psi \cos 2\langle\psi\rangle)(1 - r_\alpha \cos 2\langle\alpha\rangle), \\ A_3 &= \left( \frac{3}{8} - \frac{1}{2} r_\psi \cos 2\langle\psi\rangle + \frac{1}{8} r_\psi^4 \cos 4\langle\psi\rangle \right) \left( \frac{3}{8} + \frac{1}{2} r_\alpha \cos 2\langle\alpha\rangle + \frac{1}{8} r_\alpha^4 \cos 4\langle\alpha\rangle \right), \end{aligned}$$



$$\begin{aligned}
A_4 &= \left( \frac{3}{8} - \frac{1}{2} r_\psi \cos 2\langle\psi\rangle + \frac{1}{8} r_\psi^4 \cos 4\langle\psi\rangle \right) \left( \frac{3}{8} - \frac{1}{2} r_\alpha \cos 2\langle\alpha\rangle + \frac{1}{8} r_\alpha^4 \cos 4\langle\alpha\rangle \right), \\
A_5 &= \left( \frac{3}{8} - \frac{1}{2} r_\psi \cos 2\langle\psi\rangle + \frac{1}{8} r_\psi^4 \cos 4\langle\psi\rangle \right) \frac{1}{8} (1 - r_\alpha^4 \cos 4\langle\alpha\rangle), \\
A_6 &= \frac{1}{2} (1 - r_\psi \cos 2\langle\psi\rangle) r_\alpha \sin 2\langle\alpha\rangle, \\
A_7 &= \left( \frac{3}{8} - \frac{1}{2} r_\psi \cos 2\langle\psi\rangle + \frac{1}{8} r_\psi^4 \cos 4\langle\psi\rangle \right) \left( \frac{1}{2} r_\alpha \sin 2\langle\alpha\rangle + \frac{1}{4} r_\alpha^4 \sin 4\langle\alpha\rangle \right), \\
A_8 &= \left( \frac{3}{8} - \frac{1}{2} r_\psi \cos 2\langle\psi\rangle + \frac{1}{8} r_\psi^4 \cos 4\langle\psi\rangle \right) \left( \frac{1}{2} r_\alpha \sin 2\langle\alpha\rangle - \frac{1}{4} r_\alpha^4 \sin 4\langle\alpha\rangle \right), \\
A_9 &= \frac{1}{2} (r_\alpha \cos 2\langle\alpha\rangle - r_\psi r_\alpha \cos 2\langle\psi\rangle \cos 2\langle\alpha\rangle). \tag{1.86}
\end{aligned}$$

In eqn. (1.86),  $r_\psi = \exp(-2\sigma_\psi)$  and  $r_\alpha = \exp(-2\sigma_\alpha)$ , with the angular distribution widths given in radians. The expressions in (1.86) can be simplified further if we assume that  $\langle\alpha\rangle = 0$ , and that the radar antenna elevation angles are low (such that  $\langle\psi\rangle$  is near  $\pi/2$ ). In this case,  $\sigma_\alpha = \sigma_\psi / \sin\langle\psi\rangle \approx \sigma_\psi \equiv \sigma$ , and thus  $r_\psi \approx r_\alpha \equiv r$ . Under these simplifications, the angular moments (1.86) can be expressed as

$$\begin{aligned}
A_1 &= \frac{1}{4} (1 + r)^2, & A_2 &= \frac{1}{4} (1 - r^2), & A_3 &= \left( \frac{3}{8} + \frac{1}{2} r + \frac{1}{8} r^4 \right)^2, \\
A_4 &= \left( \frac{3}{8} + \frac{1}{2} r + \frac{1}{8} r^4 \right) \left( \frac{3}{8} - \frac{1}{2} r + \frac{1}{8} r^4 \right), & A_5 &= \left( \frac{3}{8} + \frac{1}{2} r + \frac{1}{8} r^4 \right) \frac{1}{8} (1 - r^4), \\
A_6 &= A_7 = A_8 = 0, & A_9 &= \frac{1}{2} r (1 + r). \tag{1.87}
\end{aligned}$$

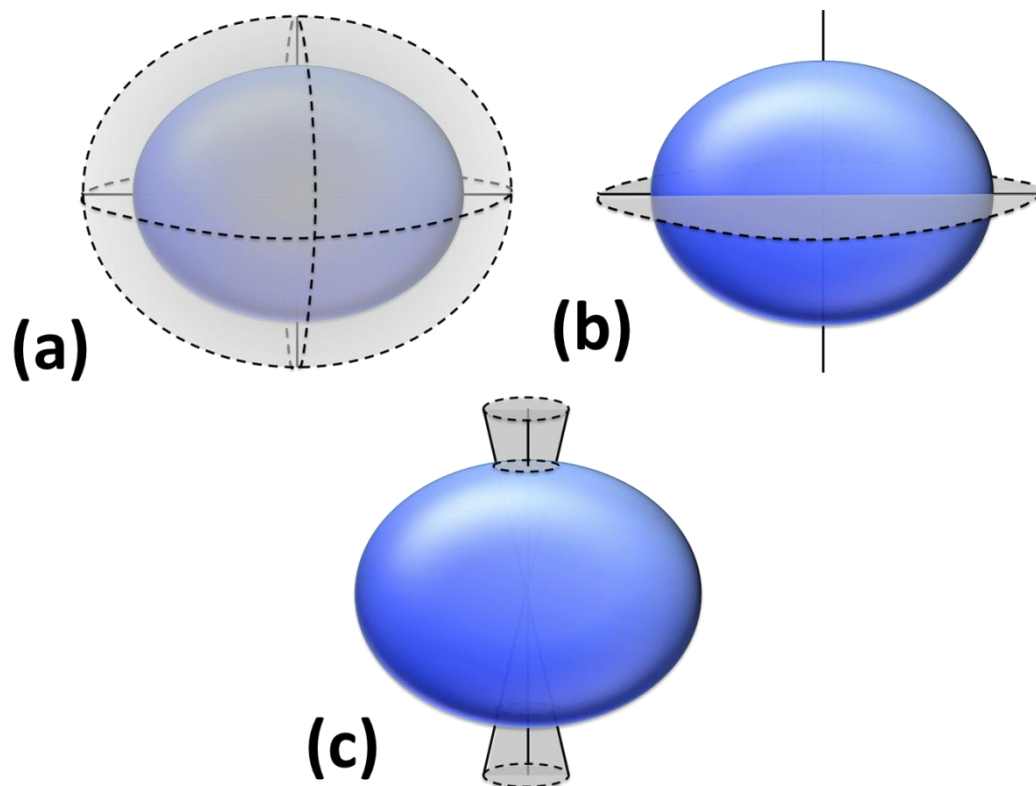


Fig. 1.7: Special cases where analytical formulas exist for the angular moments: (a) Completely random particle orientation, (b) random orientation in the horizontal plane, (c) two-dimensional axisymmetric Gaussian distribution of canting angles. In each case, the gray shaded regions represent the space of possible particle orientations.

## Chapter 2: Polarimetric Radar Variables: Physical Description

Theoretical formulations for the complete set of backscattering and forward scattering polarimetric radar variables available for radars transmitting signals at linearly-orthogonal polarizations (H and V) were presented in the previous chapter. Here, we present physical descriptions of these variables for weather radar applications. Sources in the literature include reviews by Herzegh and Jameson (1992), Doviak and Zrnić (1993), Zrnić and Ryzhkov (1999), Straka et al. (2000), Bringi and Chandrasekar (2001), and Ryzhkov et al. (2005a).

### 1. Radar reflectivity factor

The most basic radar measurand is related to the amplitude of the returned signal, called the radar reflectivity factor. Dual-polarization radars measure the radar reflectivity factor at both horizontal polarization (denoted as  $Z_H$ ) and vertical polarization ( $Z_V$ ). The amplitudes of the returned signals, and thus the radar reflectivity factors, are directly proportional to the backscattering cross sections of the target  $\sigma_{hh,vv}$ , which are related to the complex scattering functions as

$$\sigma_{hh,vv} = 4\pi |S_{hh,vv}|^2. \quad (2.1)$$

Note that the backscattering cross section (also called the “radar cross section”) has units of area. It can be thought of as the cross-sectional area of a sphere that, if scattering the transmitted radar signal isotropically, would produce the same amplitude as the received signal (e.g., Skolnick 1980; Doviak and Zrnić 1993). For small hydrometeors for which the Rayleigh approximation is valid,  $\sigma_{hh,vv}$  is proportional to the sixth power of the equivalent spherical diameter of the particle  $D^6$ . Thus, in the

Rayleigh approximation, the intrinsic  $Z_H$  and  $Z_V$  of hydrometeors are larger for larger particles. However, for larger hydrometeors that fall in the Mie (or “resonance”) scattering regime, this monotonic relation between hydrometeor size and  $Z_{H,V}$  no longer holds.

In addition to particle size,  $Z_{H,V}$  depend on the particle’s composition. The particle property important for electromagnetic applications is the effective complex dielectric factor (or relative permittivity)  $\epsilon$ , which depends on the particle’s physical composition, temperature, and the frequency of the incident radiation (see Appendix A). The relative permittivity of a hydrometeor can be thought of as a measure of how much energy is taken in from an incident electromagnetic field; this energy is then available to be radiated by the particle (i.e., scattered) or absorbed and dissipated to thermal energy (i.e., attenuation). The real part of the complex dielectric factor is related to scattering, whereas the imaginary part is related to attenuation. Thus, hydrometeors characterized by a large relative permittivity produce larger backscatter for a given size and shape. Because  $\epsilon_{water} \gg \epsilon_{ice}$ , wetter hydrometeors of a given size and shape generally produce larger backscatter and attenuation.

The quality of radar reflectivity factor measurements can be deteriorated by radar miscalibration, partial beam blockage, attenuation, and noise bias. The desired measurement accuracy for operational radars is about 1 – 2 dBZ (e.g., NEXRAD Joint System Program Office 1984; Ryzhkov et al. 2005b).

*a. Radar reflectivity factor in rain*

At all common weather radar wavelengths (S, C, and X bands), the intrinsic  $Z_H$  and  $Z_V$  of raindrops increase monotonically with increasing size (Fig. 2.1a,b), except for supergiant raindrops in excess of 8 mm. Recall that  $Z_{H,V}$  are also dependent on the concentration of hydrometeors within the radar sampling volume; thus, increased concentration of raindrops leads to larger  $Z_{H,V}$ . Therefore, heavier rain tends to be associated with larger  $Z_H$  and  $Z_V$ . The inherent ambiguity associated with its dependence on concentration *and* size means that  $Z_{H,V}$  alone cannot provide any information about the raindrop size distribution (DSD). As such, observations of heavy tropical rain characterized by very large concentrations of small raindrops may reveal the same  $Z_H$  or  $Z_V$  as the leading edge of a continental convective storm characterized by a sparse population of large drops. As we will see, the difference between  $Z_H$  and  $Z_V$  proves to be extremely useful in mitigating such ambiguities.

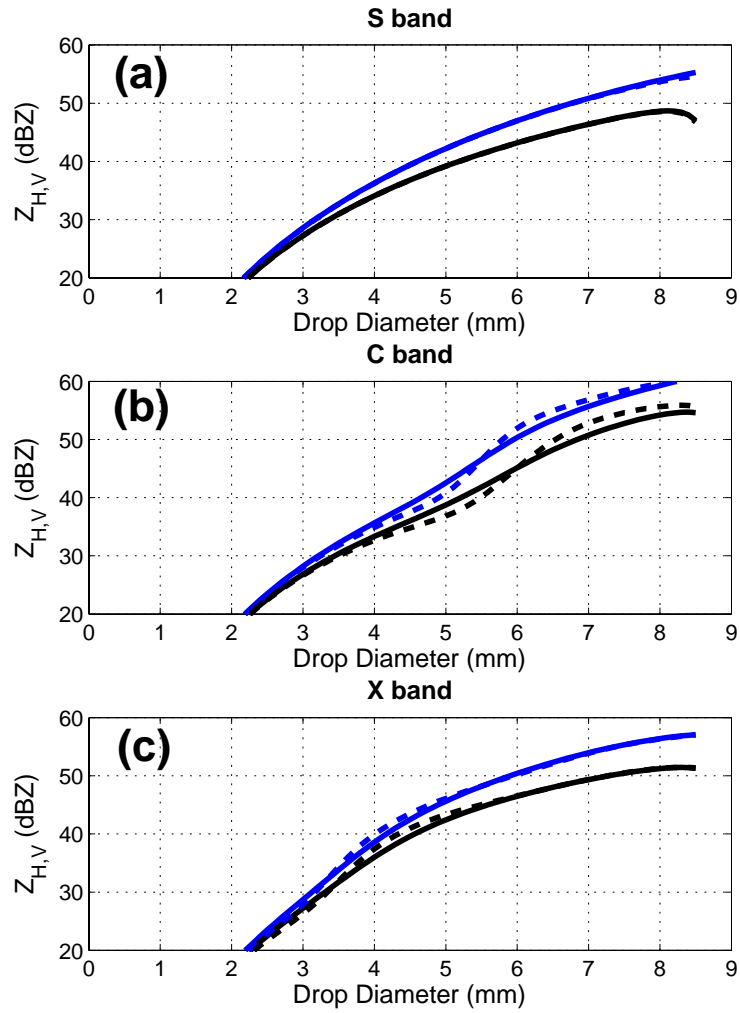


Fig. 2.1a. Normalized radar reflectivity factors at orthogonal polarizations (H in blue, V in black) for (a) S ( $\lambda = 10.97$  cm), (b) C ( $\lambda = 5.40$  cm), and (c) X ( $\lambda = 3.2$  cm) bands. Solid curves represent drop temperatures of 0 °C; dashed curves represent drop temperatures of 20 °C.

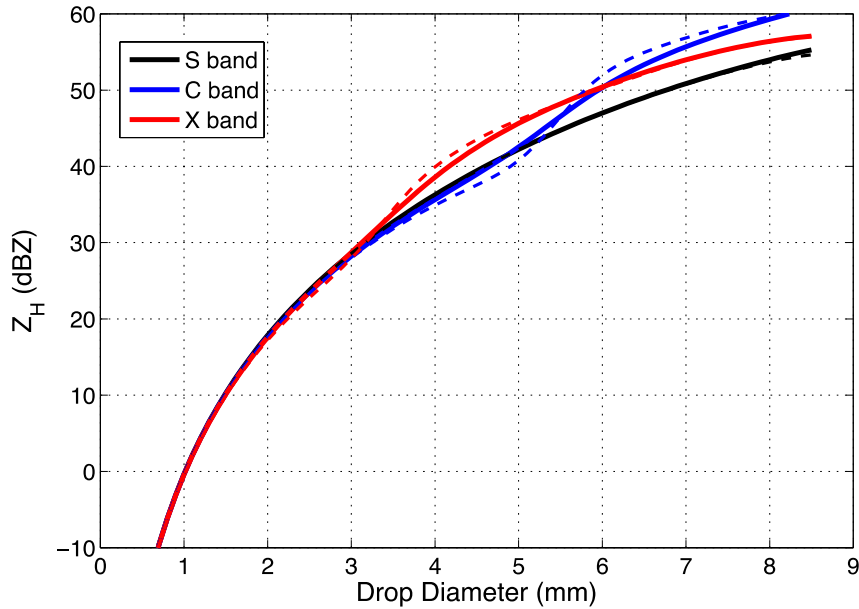


Fig. 2.1b: Normalized radar reflectivity factor at horizontal polarization ( $Z_H$ ) for raindrops, shown for S band (black), C band (blue), and X band (red) at two temperatures: 0 °C (solid curves) and 20 °C (dashed curves).

### *b. Radar reflectivity factor in solid ice particles*

The complex dielectric factor of ice is much smaller than that of water. As a result, the  $Z_{H,V}$  of solid ice particles (e.g., ice pellets, high-density hailstones) are smaller than the corresponding values for liquid particles of the same size and shape. This difference can be quantified by taking the ratio of the terms  $|K_i|^2/|K_w|^2$  (cf. eqn. 2.3), which results in a difference of about 6 – 7.2 dBZ between the logarithmic radar reflectivity factors of liquid particles and ice particles (for a review, see Smith 1984). Aside from this difference, the general trend is the same for small ice pellets as it is for raindrops (Fig. 2.2).

For larger ice particles such as hailstones, the relation between  $Z_{H,V}$  and particle size becomes very complex (Fig. 2.3), especially for particles of sufficient size to produce resonance scattering. Indeed, the oscillations evident in Fig. 2.3 reveal that for certain

size bands, larger hailstones have intrinsically *lower*  $Z_{H,V}$  than slightly smaller stones. This uncertainty is compounded by the aforementioned inherent ambiguity with concentration, which underscores the importance of not relying solely on  $Z_H$  or  $Z_V$  for information regarding hail size: larger  $Z_H$  does not necessarily imply larger hailstones (e.g., Kumjian et al. 2010a; Blair et al. 2011).

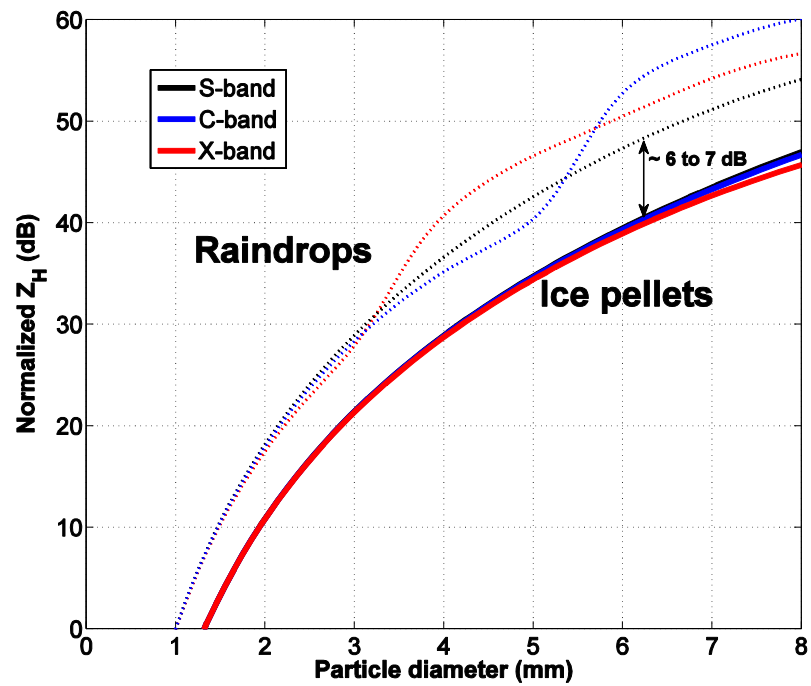


Fig 2.2: Normalized reflectivity factor at horizontal polarization ( $Z_H$ ) for raindrops (dotted lines) and ice pellets (solid lines), shown for S, C, and X bands (black, blue, and red curves). Ice pellets are considered the same size and shape as raindrops, but have a distribution of canting angles  $\sigma = 40^\circ$ .



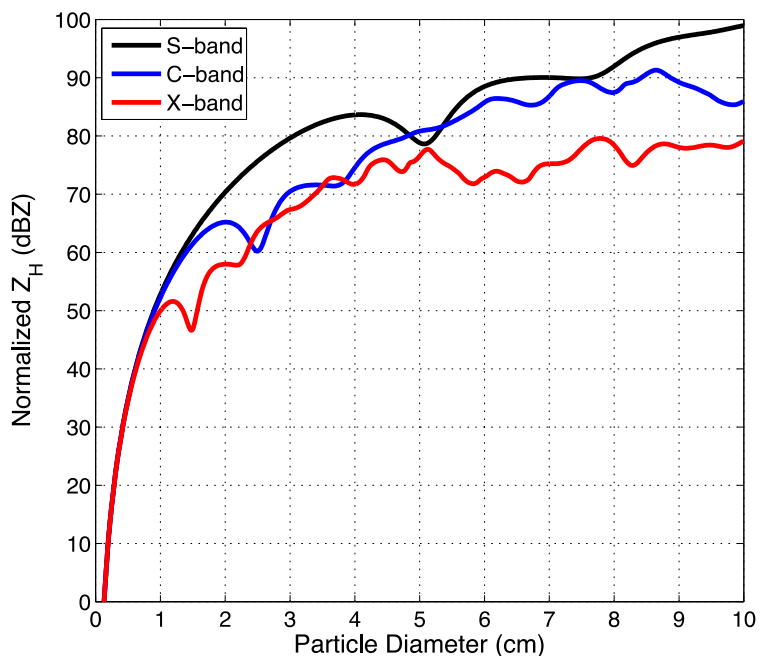


Fig. 2.3: Normalized reflectivity factor at horizontal polarization ( $Z_H$ ) for dry, oblate (axis ratio = 0.8,  $\sigma = 40^\circ$ ) hailstones, at S, C, and X bands (black, blue, and red curves).

*c. Reflectivity factor in dry snow*

Dry snowflakes comprise a mixture of ice and air with density less than that of solid ice. Aside from that, natural snowflakes are incredibly diverse, appearing with a wide range of densities, sizes, and shapes. For example, hexagonal plates up to a few millimeters in diameter have comparatively high density, close to that of solid ice, whereas snow aggregates can grow quite large ( $> 1$  cm) with very low density ( $< 100$  kg  $m^{-3}$ ). The larger sizes of aggregates tend to compensate for their low density, producing some of the largest  $Z_H$  values observed in dry snow.

Because dry snowflakes are sufficiently modeled using the Rayleigh approximation for oblate spheroids, we can make use of the Debye formula (eqn. A7)

$$\frac{\epsilon_{snow} - 1}{\epsilon_{snow} + 2} = \frac{\rho_{snow}}{\rho_{ice}} \frac{\epsilon_{ice} - 1}{\epsilon_{ice} + 2} \quad (2.2)$$

as well as the definition of the Rayleigh reflectivity factor to show that

$$Z = \frac{|K_i|^2}{|K_w|^2} \frac{1}{\rho_{ice}^2} \int_0^\infty \rho_{snow}^2(D) D^6 N(D) dD, \quad (2.3)$$

where the dielectric factor  $|K_{snow}|^2$  is written in terms of the dielectric factor for ice as  $|K_i|^2 \rho_{snow}^2(D) / \rho_{ice}^2$ . Numerous observational studies have found that the density of snow tends to be approximately inversely proportional to the diameter of the snowflake (e.g., Holroyd 1971; Fabry and Szyrmer 1999; Brandes et al. 2007). Thus, substituting  $\rho_{snow}(D) \propto D^{-1}$  into (2.3) demonstrates the fact that the reflectivity factors  $Z_{H,V}$  in snow are proportional  $D^4$ , rather than  $D^6$  (as for raindrops and ice pellets). This results in substantially smaller values of  $Z_{H,V}$  for dry snow aggregates than for raindrops or ice pellets of the same size (Fig. 2.4).

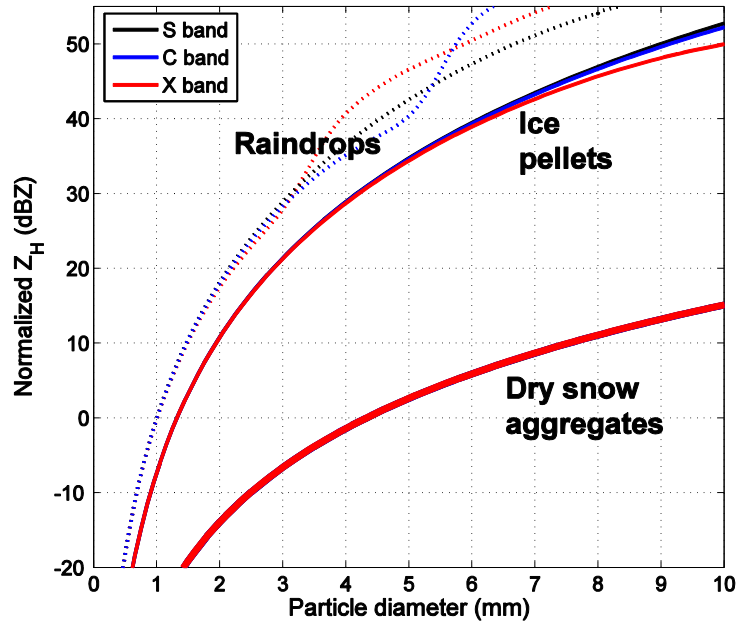


Fig. 2.4: Normalized reflectivity factor at horizontal polarization ( $Z_H$ ) for dry snow (thick curves), ice pellets (thin curves), and raindrops (dotted curves), at S, C, and X bands (black, blue, and red curves). Dry snowflakes are assumed to be oblate spheroids with axis ratio of 0.6,  $\sigma = 40^\circ$ , with density given by the empirical formula of Brandes et al. (2007).

*d. Reflectivity factor in mixed-phase particles*

The rapid increase in complex refractive index of an ice particle that acquires liquid water leads to an increase in  $Z_H$ . Thus, in general, the  $Z_H$  of a mixed-phase particle is correlated with its mass (or volume) fraction of liquid water. For example, the well-known melting layer “bright band” largely is a result of the increase in refractive index as dry snowflakes acquire liquid water during melting (Fig. 2.5). The peak  $Z_H$  in the melting layer is thought to arise from large, wet snow aggregates before they melt completely and collapse into smaller-sized raindrops (e.g., Doviak and Zrnić 1993). Similarly, melting hailstones produce a maximum in  $Z_H$  above the ground, at the location of the onset of shedding (e.g., Ryzhkov et al. 2009). Hailstones undergoing wet growth in convective updrafts are also characterized by very large  $Z_H$  (Fig. 2.6).

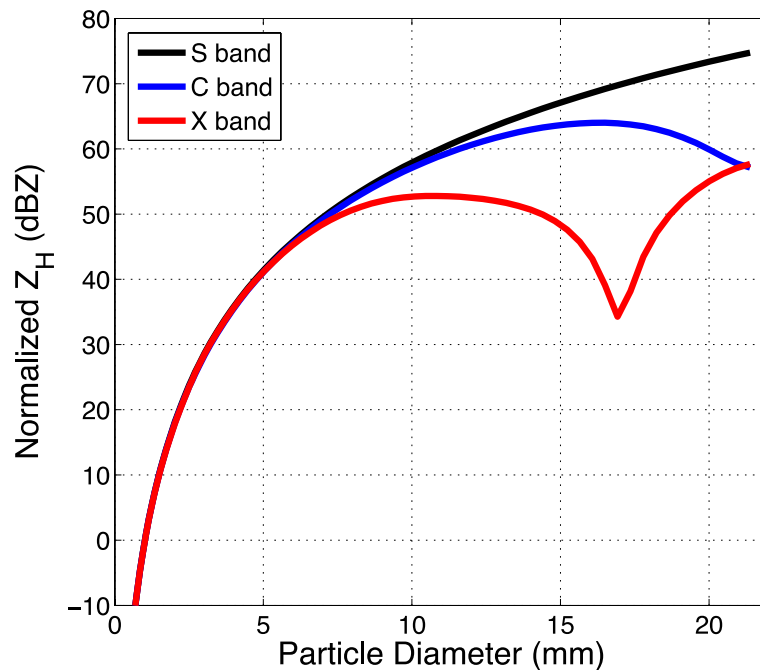


Fig. 2.5: Normalized reflectivity factor at horizontal polarization ( $Z_H$ ) for melting snowflakes, shown for S, C, and X bands (black, blue, and red curves). Melting snowflakes treated using the model of Ryzhkov et al. (2008) and Giangrande (2007), at the level of the  $Z_{DR}$  maximum in the brightband.

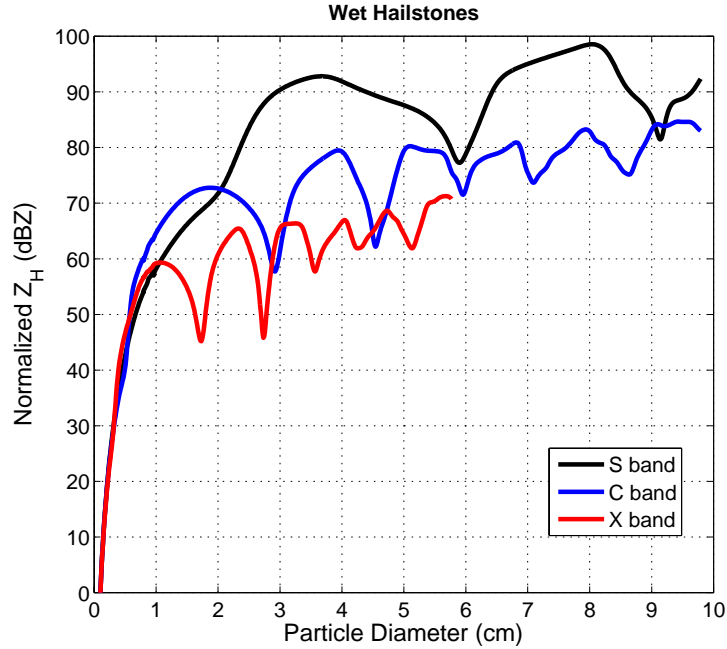


Fig. 2.6: Normalized reflectivity factor at horizontal polarization ( $Z_H$ ) for wet hailstones, shown for S, C, and X bands (black, blue, and red curves). Melting hailstones are treated using the model of Ryzhkov et al. (2009), at the ground level.

## 2. Differential reflectivity factor

As alluded to above, the added value of polarimetry comes when one compares the returned signals at orthogonal polarizations. The difference between the logarithmic  $Z_H$  and  $Z_V$  (or, ten times the logarithm of the ratio of the two) is called the differential reflectivity factor  $Z_{DR}$ . Because the dependence on concentration cancels out by taking the ratio of  $Z_h$  and  $Z_v$ ,  $Z_{DR}$  is independent of the total number concentration of particles within the resolution volume. It also means that  $Z_{DR}$  is independent of the absolute receiver and transmitter calibration.

For Rayleigh scatterers, the backscattering cross section is larger for larger particles. So, if a particle's horizontal axis is larger than its vertical axis (i.e., the particle is oblate), the backscattering cross section at horizontal polarization is larger than that at vertical polarization. Therefore,  $Z_{DR}$  is positive for oblate particles

(similarly,  $Z_{DR}$  is negative for prolate particles). Spherical particles (or those that tumble randomly) produce  $Z_{DR}$  of 0 dB. The behavior of  $Z_{DR}$  for resonance scatterers is more complex and is described below.

Differential reflectivity is immune to radar miscalibration, and is independent of particle concentration. However, signal quality is deteriorated in the presence of anisotropic beam blockage, noise bias, radome effects, and nonuniform beam filling (Ryzhkov 2007).  $Z_{DR}$  is affected by propagation effects, including differential attenuation. If the radar operates in the simultaneous transmission and reception mode (SHV; Doviak et al. 2000), signal depolarization upon propagation through hydrometeors with nonzero mean canting angle can cause cross-coupling of the H- and V-polarized waves, leading to noticeable biases in the measured  $Z_{DR}$  downrange of the depolarizing media (e.g., Ryzhkov and Zrnić 2007; Hubbert et al. 2010a,b). This latter point is described further in Chapter 3.

#### *a. Differential reflectivity in rain*

The use of  $Z_{DR}$  for rainfall measurements was suggested by Seliga and Bringi (1976). The shape of the larger, faster-falling raindrops is distorted owing to aerodynamic drag, causing the drops to become shaped rather like a French dinner roll (Fig. 2.7). Such raindrop oblateness increases with increasing raindrop size (e.g., Pruppacher and Beard 1970; Beard and Chuang 1987; Brandes et al. 2002; Thurai et al. 2009; and many others). So, the intrinsic  $Z_{DR}$  of a raindrop increases with its size (Fig. 2.8). In precipitation,  $Z_{DR}$  is a measure of the reflectivity-weighted mean drop size within the sampling volume.  $Z_{DR}$  is positive in rain, increasing from near 0 dB in

drizzle to  $> 4$  dB in heavy continental rain (e.g., Doviak and Zrnić 1993). Exceptions to this trend include heavy tropical rain, characterized by small drops (and thus lower overall  $Z_{DR}$ ), and situations of size sorting, in which large observed  $Z_{DR}$  values (collocated with low or moderate  $Z_H$ ) indicate a sparse population of large drops with very low rain rates (see Chapter 5; also Kumjian and Ryzhkov 2012).

Note that the C- and X-band curves in Fig. 2.8 display deviations from the monotonic increase in  $Z_{DR}$  with drop size. These “bumps” are a result of resonance scattering at the shorter wavelengths, and are a function of temperature. Resonance scattering produces an enhancement of the amplitude of the backscattered signal owing to constructive interference of the wave reflected off the front surface of the drop and that off the back surface. The most remarkable resonance occurs for 5 – 6 mm drops at C band; a lesser bump appears in 3 – 4 mm drops at X band. The difference in the amplitude of these resonance bumps is because of the difference in relative permittivity: resonance effects are stronger for smaller values of the imaginary part of the complex dielectric function, which is related to attenuation losses within the particle. Because the magnitude of the imaginary part of the complex dielectric function for water is smaller at C band than at X band, the resonance at C band is stronger (owing to larger attenuation with the particle at X band). If natural raindrops could reach the resonance size at S band (about 1.1 cm in diameter), the resonance effect would be strongest at S band. Increased temperature leads to smaller imaginary parts of the complex dielectric of water (see Appendix A); therefore, warmer raindrops produce stronger resonance effects. Chapter 4 discusses the determination of raindrop temperature.

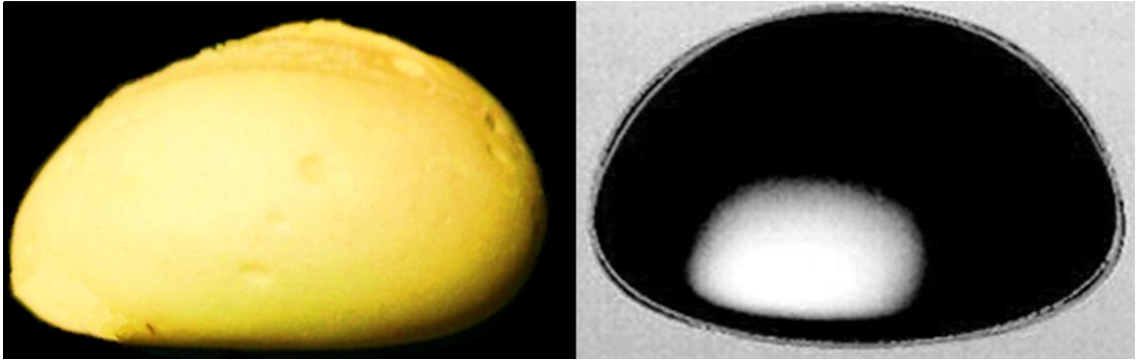


Fig. 2.7: Comparison of the oblate spheroidal shapes of a French-style dinner roll (left panel) to a 6-mm raindrop (right panel). Raindrop photograph adapted from Thurai et al. (2009).

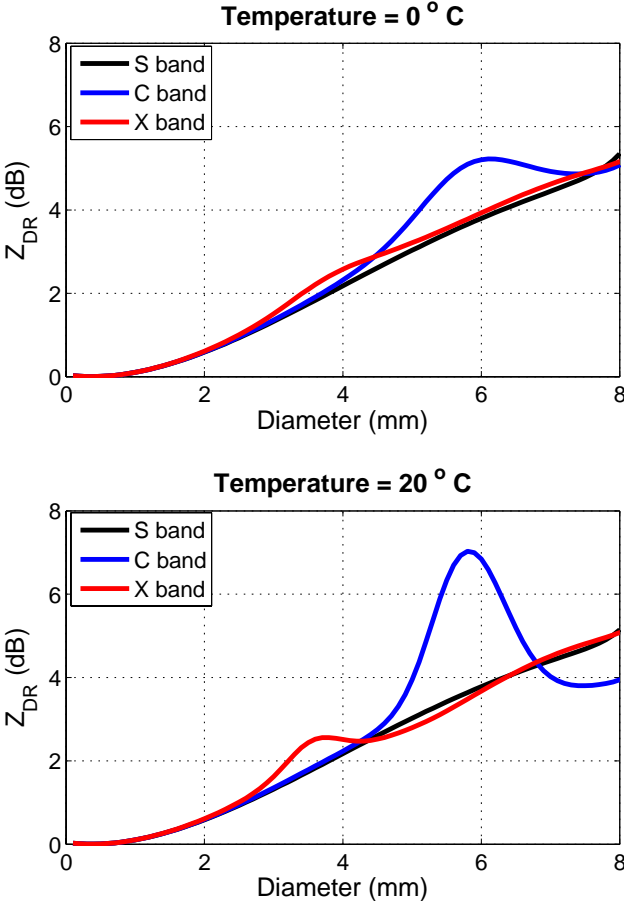


Fig. 2.8: Differential reflectivity ( $Z_{DR}$ ) for raindrops at S, C, and X bands (black, blue, and red curves). Shown for two temperatures: 0 °C (top) and 20 °C (bottom).

*b. Differential reflectivity in solid ice particles*

Because of the difference in complex dielectric between liquid water and ice, the  $Z_{DR}$  of a given particle size and shape is smaller for solid ice particles than liquid water particles. In addition, ice particles have increased widths of their canting angle distributions, which decreases the observed  $Z_{DR}$ . For small ice pellets (i.e., frozen raindrops), the  $Z_{DR}$  does not exceed about 0.3 dB at all weather radar wavelengths (Fig. 2.9).

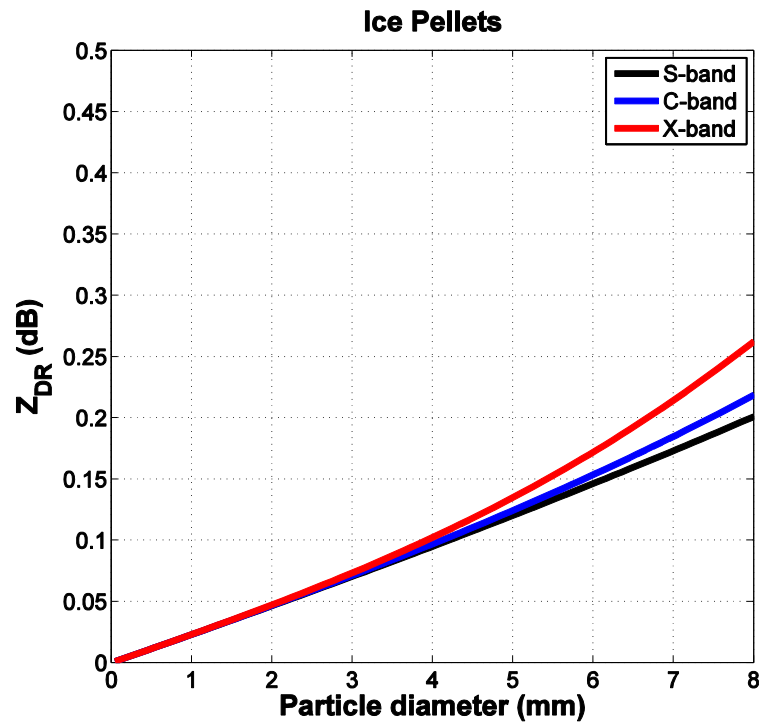


Fig. 2.9: Differential reflectivity ( $Z_{DR}$ ) for frozen raindrops (ice pellets), shown for S, C, and X bands (black, blue, and red curves, respectively). Particle axis ratios are identical to those of raindrops; the width of canting angle distribution  $\sigma = 40^\circ$ .

For larger solid ice particles such as hailstones, the functional dependence of  $Z_{DR}$  on size becomes rather complicated (Figure 2.10). Once resonance size is reached, the intrinsic  $Z_{DR}$  of *oblate* hailstones can drop to negative values. Negative values



occur in resonance scattering when the reflectivity factor at vertical polarization  $Z_V$  peaks above the reflectivity factor at horizontal polarization  $Z_H$ . For an oblate hailstone, the horizontal dimension of the stone is larger than the vertical dimension for given equivalent spherical diameter; thus, the electromagnetic resonance occurs first for the horizontal polarization radiation (this corresponds to the peak in  $Z_{DR}$  in Fig. 2.10). Resonance effects then lead to a decrease in  $Z_H$  for increasing size. However, once a hailstone is sufficiently large, the vertical polarization radiation reaches its first resonance peak. Because the hailstone is larger overall for the vertical polarization resonance size than the horizontal polarization resonance size, the peak in  $Z_V$  is larger than the peak in  $Z_H$ , which explains the larger magnitude of the negative  $Z_{DR}$  oscillations.

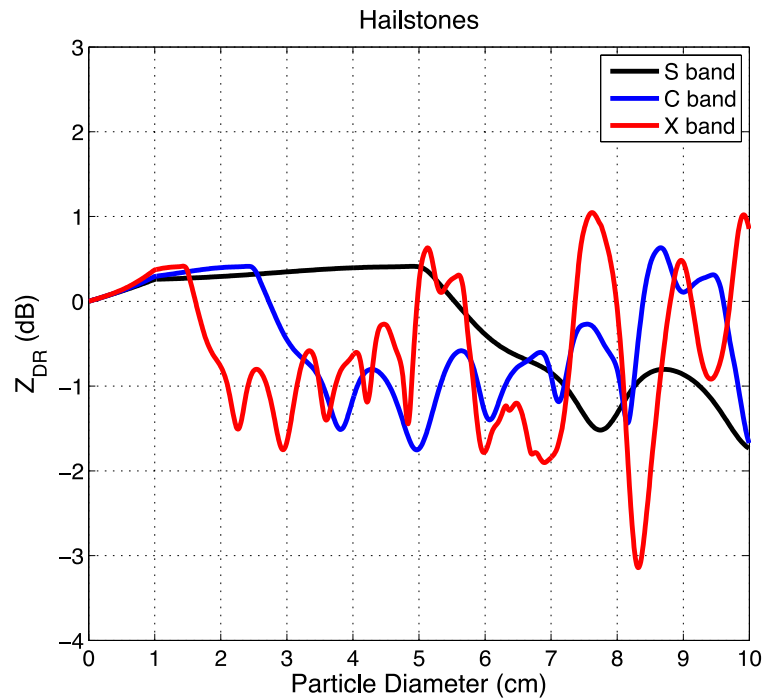


Fig. 2.10: Differential reflectivity ( $Z_{DR}$ ) for dry hailstones, at S, C, and X bands (black, blue, and red curves). The aspect ratio of hailstones  $> 1$  cm in diameter is fixed at 0.8.

Note that the amplitude of these negative  $Z_{DR}$  oscillations is damped by increased widths of the canting angle distribution; perfectly random orientation of hailstones would result in  $Z_{DR}$  of 0 dB, regardless of hailstone size or shape. However, observations of pronounced negative  $Z_{DR}$  values in severe convective storms that produced giant hail (e.g., Kumjian et al. 2010a,c; Picca and Ryzhkov 2012) indicate that some degree of alignment exists. Kumjian et al. (2010a) suggest the possibility of using such negative  $Z_{DR}$  values aloft as an indication of giant hail; however, it is unclear how reliable an indicator negative  $Z_{DR}$  values are. Further, other signatures such as dramatically reduced  $\rho_{hv}$  (Picca and Ryzhkov 2012) in the hail growth region of storms may be more reliable.

*c. Differential reflectivity in dry snow*

The  $Z_{DR}$  in dry snow varies substantially, depending on the habit of the ice crystals. Pristine oblate ice crystals such as hexagonal plates theoretically can produce  $Z_{DR}$  as high as 10 dB (e.g., Hogan et al 2002; Andrić et al. 2012). Pristine prolate crystals such as columns or needles can produce  $Z_{DR}$  values as large as 3 – 4 dB. On the other hand, snow aggregates tend to produce very low  $Z_{DR}$  values ( $< 0.5$  dB; Ryzhkov and Zrnić 1998a; Ryzhkov et al. 2005a), primarily owing to their very low density. Whereas  $Z_H$  or  $Z_V$  alone offer no indication of snow crystal type, fields of  $Z_{DR}$  in winter storms reveal striking structure (e.g., Fig. 2.11), indicative of various snow crystal habits. As observed in the figure, there tends to be an inverse correlation between  $Z_H$  and  $Z_{DR}$  in snow. For example, the lake-effect snow band in Figure 2.11 (located in southwestern

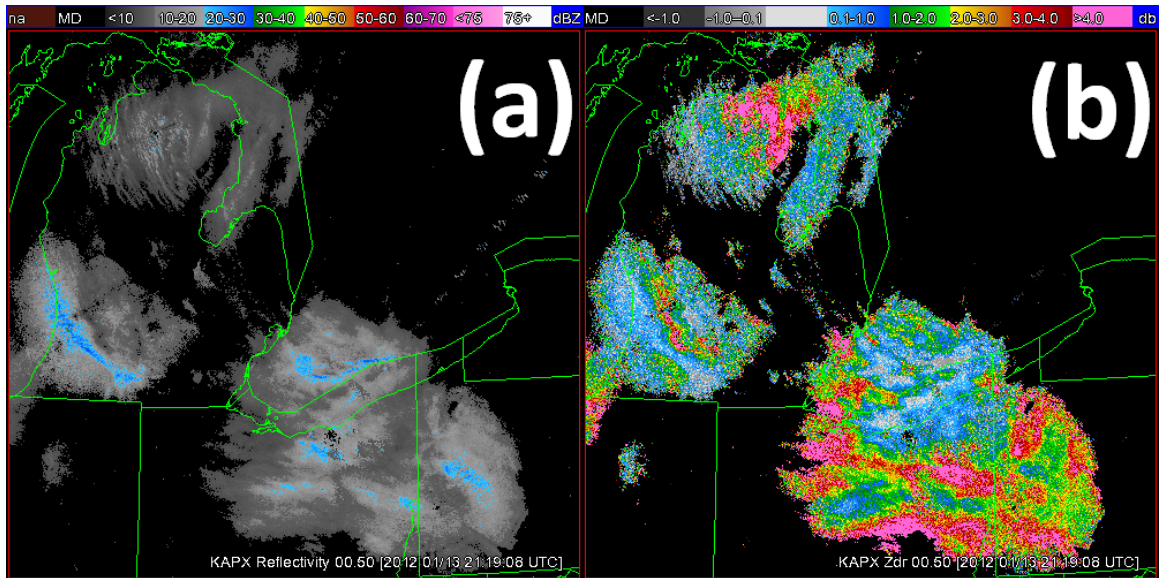


Fig. 2.11: Observations of a winter storm event on 13 January 2012, at 2119:08 UTC in the Great Lakes region of the United States. Observations from upgraded WSR-88D radars including KPBX (Pittsburgh), KCLE (Cleveland), KGRR (Grand Rapids), KLOT (Chicago), and KAPX (Gaylord). The 0.5° elevation scan is shown, with fields of (a)  $Z_H$ , and (b)  $Z_{DR}$ .

Michigan, coming off Lake Michigan) demonstrates the inverse correlation between  $Z_H$  and  $Z_{DR}$  in snow, as the heaviest snow is characterized by  $Z_H$  near 35 dBZ and  $Z_{DR}$  near 0 dB.  $Z_{DR}$  is considerably higher ( $> 3$  dB) on the periphery of this snow band. Aggregation of snowflakes destroys the polarimetric information necessary to determine crystal habit; the large size of the aggregates dominates the signal from smaller pristine crystals even if they are present (e.g., Bader et al. 1987). Thus, the periphery or edges of such high- $Z_H$  snow bands may be more useful in determining the dominant crystal habit.

#### *d. Differential reflectivity in mixed-phase particles*

Much like the impact of liquid water on  $Z_H$ ,  $Z_{DR}$  is strongly affected by the presence of liquid water on or in a particle. For particles of a given size and shape, increasing the liquid water fraction tends to increase in  $Z_{DR}$ . However, melting progresses at different

rates for different particle sizes. Additionally, for sufficiently large melting particles there is an upper limit to the amount of liquid water that is able to accumulate as a film on their surfaces before shedding commences (e.g., Rasmussen and Heymsfield 1987). Appropriate treatment of melting is necessary to accurately determine the electromagnetic scattering characteristics of such particles.

The intrinsic  $Z_{DR}$  of melting snowflakes is shown in Fig. 2.12. Note that the computed radar variables are sensitive to the treatment of the distribution of liquid water (e.g, see Fabry and Szyrmer 1999; also Appendix A). The large increase in  $Z_{DR}$  observed in the melting layer of stratiform precipitation (e.g., Fig. 2.13) is produced by melting snowflakes. However, preliminary efforts to model the melting of snowflakes *without* aggregation (e.g., Ryzhkov et al. 2008; Giangrande 2007) are incapable of reproducing the magnitude of the observed  $Z_{DR}$  increase routinely observed in the melting layer. This indicates that aggregation of melting snowflakes is a key process in producing large values of  $Z_{DR}$ .

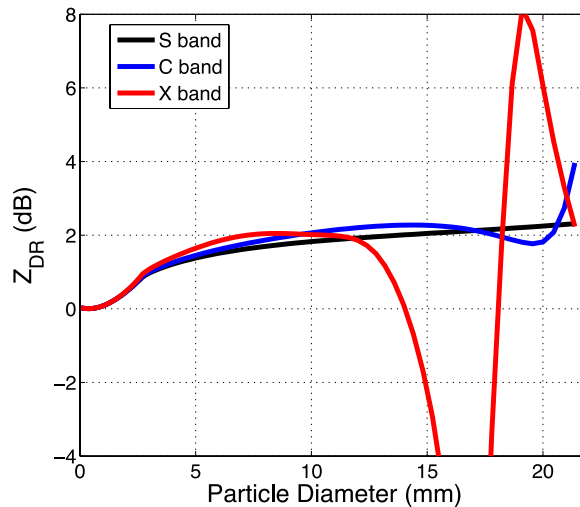


Fig. 2.12: Differential reflectivity ( $Z_{DR}$ ) for melting snowflakes, at S, C, and X bands (black, blue, and red curves).

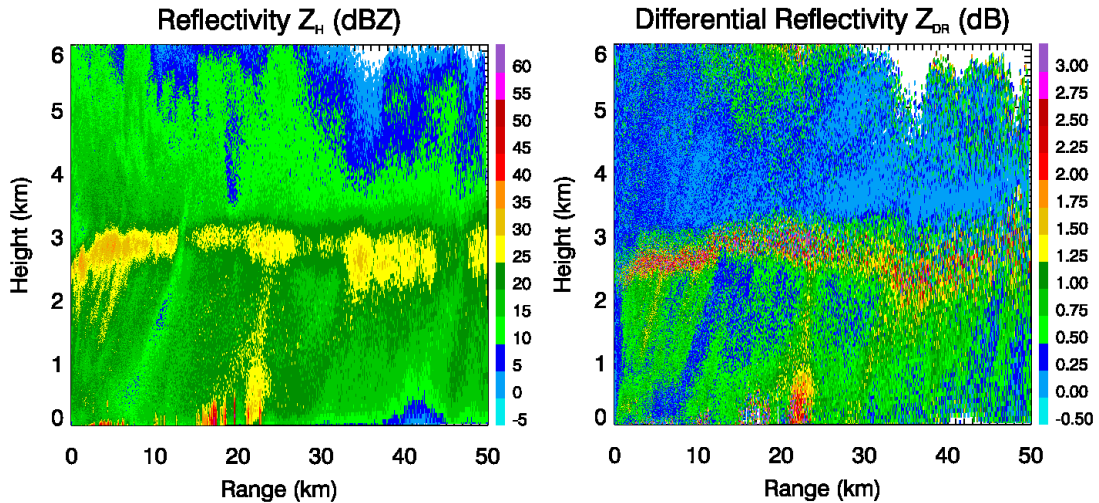


Fig. 2.13: Observed vertical cross section (RHI) of  $Z_H$  (left) and  $Z_{DR}$  (right) showing a melting layer bright band between about 2.5 and 3.0 km in height. The data are from the Bonn X-band Polarimetric (BOXPOL) radar, collected on 22 June 2011 at 1144 UTC. Courtesy of the Meteorologisches Institut at the Universität Bonn.

The intrinsic  $Z_{DR}$  in melting hailstones (Fig. 2.14) exhibits complicated behavior owing to resonance scattering effects at all radar wavelengths. For hailstones approximated by two-layer spheroids, as in Figure 2.14, the  $Z_{DR}$  tends to remain lower than the  $Z_{DR}$  for pure raindrops. Because large hailstones shed excess meltwater,  $Z_{DR}$  tends to remain comparatively small (positive or negative). Note that other choices for the modeled hailstone parameters may produce different results, and an appreciable amount of uncertainty exists in selecting some of these parameters (e.g., Ryzhkov et al. 2009; Kumjian et al. 2010a). Also, in storms the melting hail tends to be mixed with raindrops. The presence of large drops can increase the observed  $Z_{DR}$  (e.g., Ryzhkov et al. 2009). This effect is especially prevalent at C band, where observed  $Z_{DR}$  values in melting hail are consistently very large (Anderson et al. 2011).

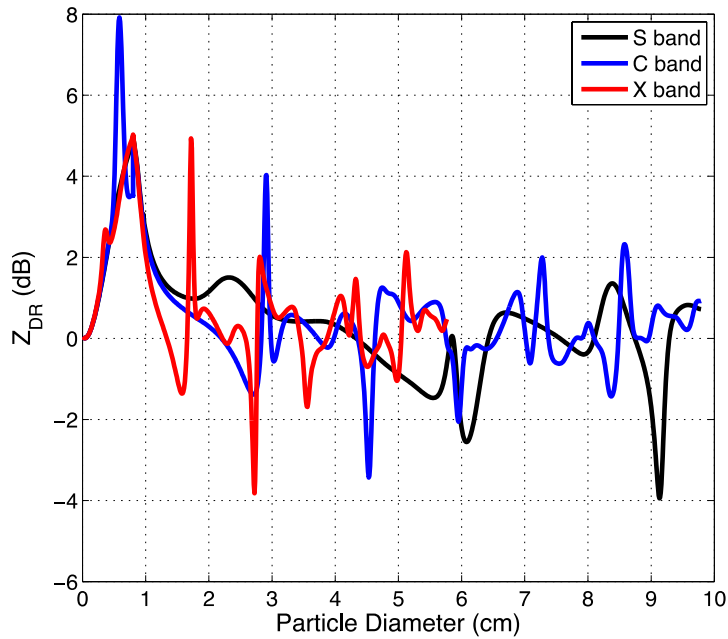


Fig. 2.14: Differential reflectivity ( $Z_{DR}$ ) for wet hailstones, for S, C, and X bands (black, blue, and red curves).

### 3. Differential propagation phase shift

The differential propagation phase shift  $\Phi_{DP}$  is the difference in phase between the H and V channels that accumulates upon (two-way) propagation of the radar signal through an anisotropic medium. Anisotropic scatterers along the propagation path are characterized by complex effective refractive indices (see Chapter 1), which are different at H and V polarizations. This can be thought of as the H- and V-polarization waves propagating at different speeds through the anisotropic medium. Because most hydrometeors are oblate, the accumulated phase shift is such that the H-polarization wave lags the V-polarization wave, defined as positive  $\Phi_{DP}$ .  $\Phi_{DP}$  increases as the oblateness and complex dielectric factor of hydrometeors increase; however, it is not affected by (i.e., is equal to zero in) spherical or randomly tumbling particles. Because  $\Phi_{DP}$  is a *phase* measurement (not power), it is immune to radar miscalibration, partial

beam blockage, attenuation, and is not biased by noise (e.g., Zrnić and Ryzhkov 1999). Thus, it is an attractive variable for use in quantitative precipitation estimation and attenuation correction.

By convention, properties of the media are designated as “specific” quantities (i.e., per unit distance). For example, losses in electromagnetic wave amplitude during propagation are described in terms of specific attenuation. Likewise, to conform to convention, we take one-half the range derivative of  $\Phi_{DP}$ , which is known as the specific differential phase  $K_{DP}$ .  $K_{DP}$  provides the accumulated differential phase shift per unit distance in the radial direction. Thus, it can be useful for identifying regions of heavy precipitation where a large differential phase shift has accumulated over a short distance. Because its calculation involves finite differencing,  $K_{DP}$  is difficult to estimate if  $\Phi_{DP}$  has large fluctuations, such as when the signal-to-noise ratio (and/or  $\rho_{hv}$ ) is low. Estimates of  $K_{DP}$  are prone to errors in the presence of nonuniform beam filling (e.g., Ryzhkov and Zrnić 1998b; Gosset 2004; Ryzhkov 2007; see also Chapter 3), and in the presence of backscatter differential phase  $\delta$ .

#### *a. Differential propagation phase shift in rain*

Use of  $K_{DP}$  for measurements of rain was introduced by Seliga and Bringi (1978), Jameson (1985a), and Sachidananda and Zrnić (1986, 1987). Owing to drop oblateness,  $\Phi_{DP}$  and  $K_{DP}$  are positive in pure rain. Because of the aforementioned qualities of  $K_{DP}$ , it is an attractive variable for use in rainfall estimation (e.g., Zrnić and Ryzhkov 1996; Ryzhkov and Zrnić 1996; Brandes et al. 2001; Ryzhkov et al. 2005a,d), particularly in cases where hail is mixed with rain (Balakrishnan and Zrnić 1990a;

Giangrande and Ryzhkov 2008), or for long-term accumulations of light rain (e.g., Borowska et al. 2011b). Additionally, Sachidananda and Zrnić (1987) found that  $K_{DP}$  is almost linearly related to rainfall rate. Because the dependence on size of  $K_{DP}$  is smaller than that of  $Z_H$ , it is more sensitive to smaller drop sizes.

The normalized values of  $K_{DP}$  in rain are shown in Figure 2.15. In precipitation, the measured  $K_{DP}$  is inversely proportional to the radar wavelength; therefore, for a given precipitation echo, the measured  $K_{DP}$  at X band will be roughly 3.4 times larger than at S band and 1.7 times larger than at C band. Figure 2.15 also reveals that the dependence of C-band  $K_{DP}$  on temperature is much larger than at S or X bands.

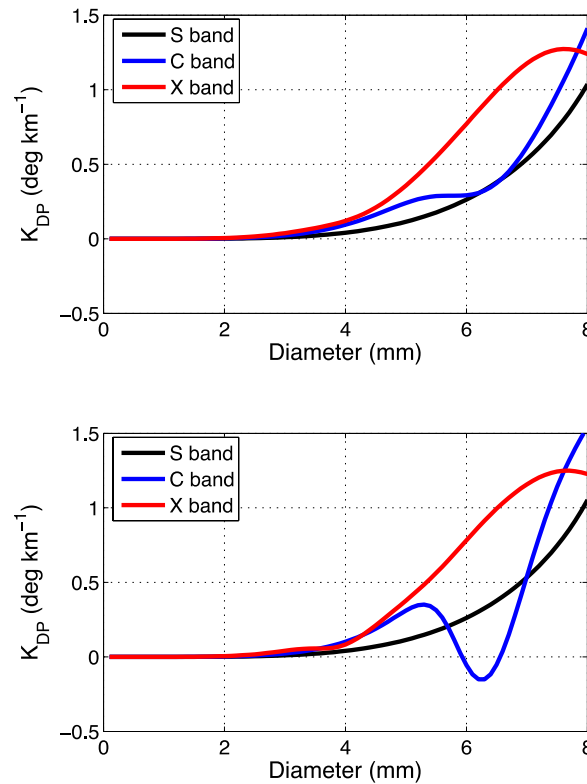


Fig. 2.15: Normalized specific differential phase ( $K_{DP}$ ) for raindrops, at S, C, and X bands (black, blue, and red curves). Shown for two temperatures: 0 °C (top) and 20 °C.



*b. Differential propagation phase shift in solid ice particles*

The normalized values of  $K_{DP}$  in small ice pellets are much smaller than in raindrops of the same size and shape (Fig. 2.16), owing primarily to the much smaller complex relative permittivity of ice compared to water. A secondary factor is the increased canting angle distribution width for frozen particles. For dry hailstones, however, the behavior of  $K_{DP}$  is rather complicated (Fig. 2.17), featuring large oscillations and both positive and negative values. These large fluctuations are a result of Mie scattering and indicate a “trading off” in the amount of phase shift acquired on propagation between the H and V polarization waves. In other words, negative values of normalized  $K_{DP}$  indicate that the V-polarization wave has “slowed” relative to the H-polarization wave, and positive values represent the opposite. These large oscillations are superposed on a general decreasing trend, which may lead to negative  $K_{DP}$  values in large hailstones. However, in practice, the presence of backscatter differential phase ( $\delta$ ) will likely obfuscate the “true”  $K_{DP}$ , as will the larger statistical fluctuations associated with a decrease in  $\rho_{hv}$ .

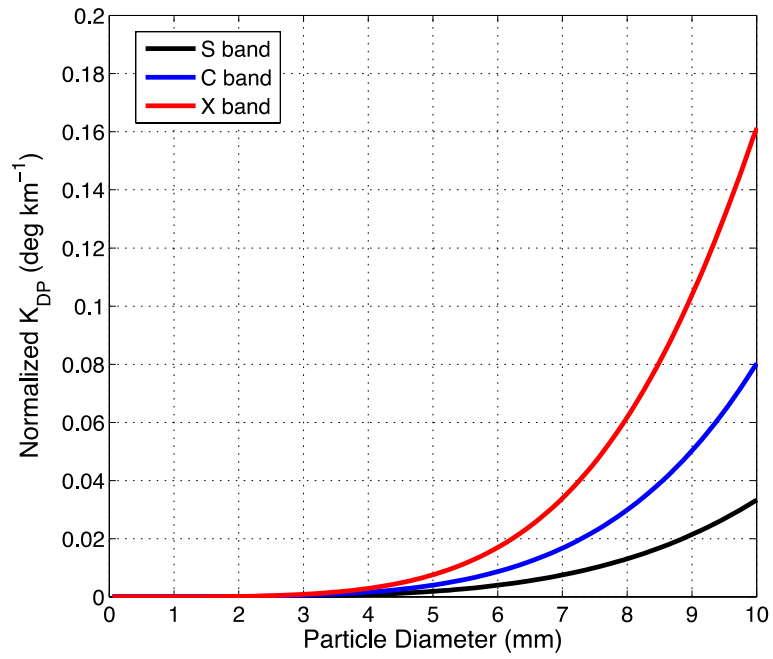


Fig. 2.16: Normalized specific differential phase ( $K_{DP}$ ) for ice pellets, at S, C, and X bands (black, blue, and red curves).

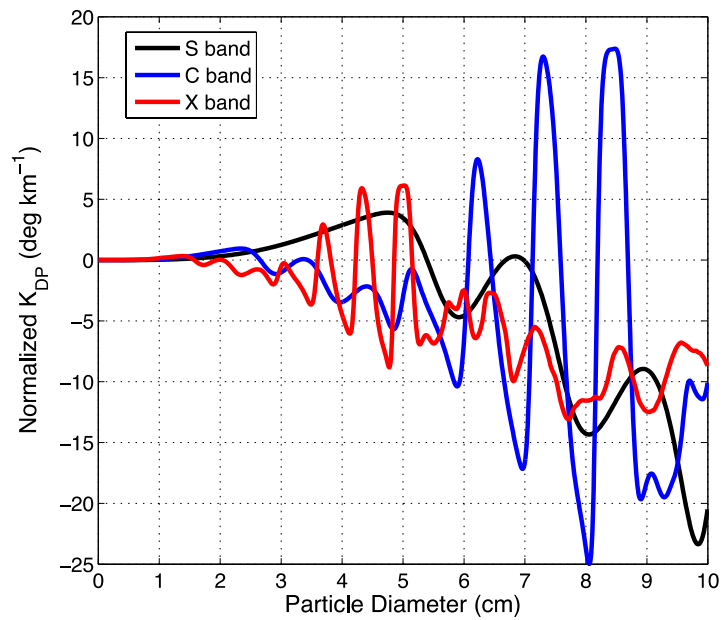


Fig. 2.17: Normalized specific differential phase ( $K_{DP}$ ) for dry hailstones, at S, C, and X bands (black, blue, and red curves).

*c. Differential propagation phase shift in dry snow*

As with  $Z_{DR}$ , the intrinsic  $K_{DP}$  in dry snow can vary widely depending on the crystal habit. Snow aggregates tend to have  $K_{DP}$  values near zero (i.e., are essentially “invisible” to the propagation phase shift), whereas pristine ice crystals can produce  $K_{DP}$  values on the order of  $0.5 \text{ deg km}^{-1}$  at S band (e.g., Ryzhkov and Zrnić 1998a; Ryzhkov et al. 1998; Kennedy and Rutledge 2011; Andrić et al. 2012), and even higher at shorter radar wavelengths. This can be useful in determining regions of ongoing secondary ice crystal production (Andrić et al. 2012) or dendrite growth (Kennedy and Rutledge 2011) in cases when the intrinsic large  $Z_{DR}$  of low- $Z_H$  pristine ice crystals is obfuscated by contributions from high- $Z_H$  aggregates, which have low intrinsic  $Z_{DR}$ . Strong electric fields within the upper portions of storms can cause an alignment of low-inertia columnar ice crystals, which can produce enhanced positive or negative  $K_{DP}$  (as well as signal depolarization; see Ryzhkov and Zrnić 2007, and Chapter 3). Measurements of  $K_{DP}$  in dry snow can be very noisy, owing to low variability of the radial slope of  $\Phi_{DP}$  with range. This especially inhibits use of  $K_{DP}$  at S band in dry snow in areas of low signal-to-noise ratio, where statistical fluctuations in  $\Phi_{DP}$  are larger.

*d. Differential propagation phase shift in mixed-phase particles*

As with  $Z_{DR}$ , an increase in liquid water content leads to larger  $K_{DP}$  values for a given particle size and shape (at least for small hydrometeors). Again, this is directly related to the much larger relative permittivity of water compared to ice. Because large,

wet snow aggregates can produce resonance scattering (even at S band), the addition of differential phase shift upon backscatter  $\delta$  can lead to problems estimating  $K_{DP}$ .

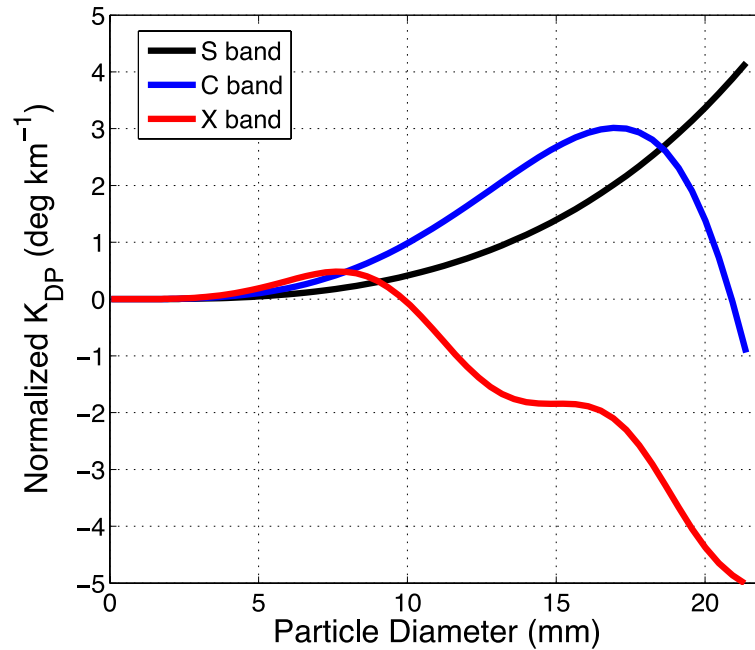


Fig. 2.18: Normalized specific differential phase ( $K_{DP}$ ) for melting snowflakes, at S, C, and X bands (black, blue, and red curves).

In melting hail, the normalized  $K_{DP}$  values (Fig. 2.19) display a complex behavior similar those in dry hail. Of note, the magnitudes of the oscillations at S band are larger than for dry hail, whereas those at C and X bands are comparatively smaller. Additionally, the same overall decrease in normalized  $K_{DP}$  with size is evident. Again, however, Mie scattering effects will likely render the measured  $K_{DP}$  values suspect in the case of large wet hail.

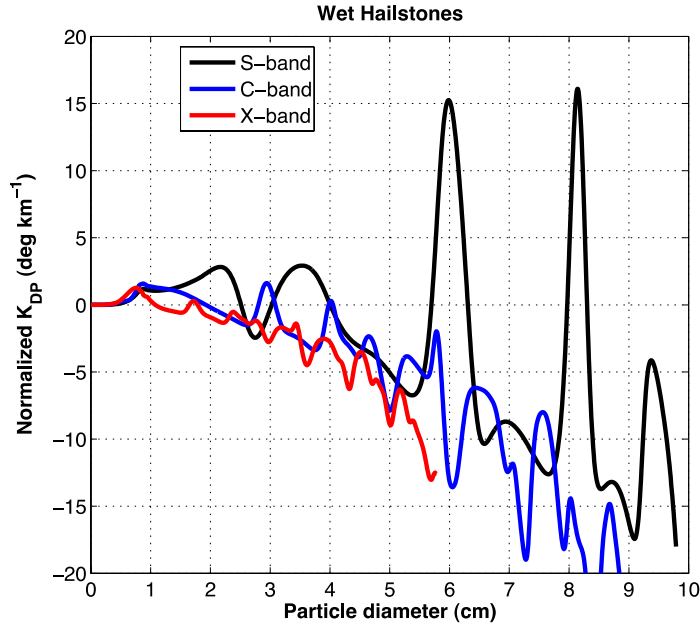


Fig. 2.19: Normalized specific differential phase ( $K_{DP}$ ) for wet hailstones, at S, C, and X bands (black, blue, and red curves).

#### 4. Co-polar cross-correlation coefficient

The co-polar cross-correlation coefficient  $\rho_{hv}$  is the correlation between the complex co-polar H and co-polar V backscattered signals, taken at zero lag time. [Biases in the polarimetric variables are possible in regions of low signal-to-noise ratio; thus, estimating the moments at lag one (e.g., Melnikov 2006; Melnikov and Zrnić 2007) is often adopted to mitigate such biases]. Because  $\rho_{hv}$  depends on the complex scattering functions and not just their magnitudes, it accounts for both power and phase of the returned signal. It can be thought of as a measure of similitude between the amplitude and phases of the returned signals at H and V polarizations; in other words, it can be considered a measure of diversity of the scatterers in the radar sampling volume. This diversity includes any physical characteristic of the hydrometeors that affects the returned signal and phase that varies within the sampling volume, including

composition or complex dielectric factor, shape, and orientation angle. Note that a diversity of sizes in the sampling volume does not affect  $\rho_{hv}$  *unless the shape of the particles varies across the spectrum*. In addition, variability of differential phase within the sampling volume can also reduce  $\rho_{hv}$ . Particles producing significant variations of the backscatter differential phase ( $\delta$ ) thus lead to reduced  $\rho_{hv}$ . Backscatter differential phase is described in the next section.

$\rho_{hv}$  is independent of absolute radar calibration, and is not affected by propagation effects including attenuation, differential attenuation, and signal depolarization (e.g., Zrníc and Ryzhkov 1999). In addition,  $\rho_{hv}$  is independent of the concentration of hydrometeors in the sampling volume. However,  $\rho_{hv}$  is not immune to noise bias (when taken at zero lag time), and it can be affected by nonuniform beam filling. Because of these qualities,  $\rho_{hv}$  can be an extremely important variable in hydrometeor classification schemes. For example, nonmeteorological scatterers tend to produce very low  $\rho_{hv}$ , exhibiting little overlap with values observed in precipitation. Such nonmeteorological scatterers include chaff (Zrníc and Ryzhkov 2004; Fig. 2.20), smoke and ash from fires (e.g., Melnikov et al. 2008, 2009; Fig. 2.21), biological scatterers such as birds, bugs, and bats (e.g., Ryzhkov et al. 2005a; Fig. 2.22), sea clutter (e.g., Ryzhkov et al. 2002a; Fig. 2.23), and tornadic debris (Ryzhkov et al. 2005c; Fig. 2.24).

#### *a. Co-polar cross-correlation coefficient in rain*

The co-polar cross-correlation coefficient exhibits high values ( $> 0.97$ ) in rain at S and X bands. Values are slightly less than unity owing to a change of particle shape

with size, and slight wobbling of drops as they fall. Because of the enhanced resonance effects for large raindrops at C band,  $\rho_{hv}$  at C band in pure rain can be as low as 0.93 (Ryzhkov and Zrnić 2005). In light rain and drizzle,  $\rho_{hv}$  should be close to 1.0 for all radar wavelengths and can serve as a measure of the quality of the radar system.

*b. Co-polar cross-correlation coefficient in solid ice particles*

Small ice pellets produce  $\rho_{hv}$  near 1.0 at all radar wavelengths. There are no resonance effects owing to the drastically smaller values of the complex dielectric factor of solid ice. Very slight reductions in  $\rho_{hv}$  are caused by the change of particle shape with size as in rain, and increased tumbling of particles (larger  $\sigma$ ) compared to raindrops of the same size and shape.

Large, nonspherical hailstones can produce reductions in  $\rho_{hv}$ , even if completely dry. This is because such particles produce nonzero backscatter differential phase shifts as a result of Mie scattering. Additional factors contributing to the decrease in  $\rho_{hv}$  of hailstones are enhanced tumbling, and possibly irregularities in shape such as lobes or spikes (e.g., Balakrishnan and Zrnić 1990b).

*c. Co-polar cross-correlation coefficient in dry snow*

Like  $Z_{DR}$ , the values of  $\rho_{hv}$  in dry snow can vary depending on the dominant crystal habit present. For instance, large, fluffy aggregates of snow produce  $\rho_{hv}$  very close to 1.0 (their very low density counteracts the wobbling effect and irregular shapes). On the other hand, pristine anisotropic crystals can produce a tangible decrease

in  $\rho_{hv}$  ( $< 0.96$ ) because the impact of a distribution of canting angles is accentuated with highly anisotropic particles.

*d. Co-polar cross-correlation coefficient in mixed phase particles*

The lowest observed values of  $\rho_{hv}$  in precipitation are produced by wet ice particles such as melting snow and melting hail. The addition of liquid water accentuates differences in shapes, wobbling, etc. The melting layer “bright band” in  $\rho_{hv}$  is unmistakable in stratiform precipitation, observed as a dramatic decrease in  $\rho_{hv}$  below values expected in pure rain or pure dry snow at S, C, and X bands (Fig. 2.25). Such pronounced signatures make  $\rho_{hv}$  reductions the basis of automated melting layer detection algorithms for polarimetric WSR-88D radars (Giangrande et al. 2005, 2008). This decrease in  $\rho_{hv}$  is caused by several factors, including a mixture of hydrometeor types and shapes (wet snow aggregates, pure liquid raindrops, etc.), wobbling of wet snowflakes, nonuniform beam filling, and (possibly) resonance scattering caused by the largest wet aggregates.

Wet hail can also produce anomalously low  $\rho_{hv}$  at all weather radar wavelengths, especially those sizes of resonance size. Within the updrafts of severe convective storms, very low  $\rho_{hv}$  caused by large hailstones undergoing wet growth is a commonly observed feature, often called the “ $\rho_{hv}$  hole” (e.g., Ryzhkov et al. 2005c; Kumjian and Ryzhkov 2008a; Picca and Ryzhkov 2012). Values below 0.85 are routinely observed at S band in such signatures, and Picca and Ryzhkov (2012) observed  $\rho_{hv} < 0.4$  at C band. Melting hailstones mixed with raindrops often produce depressed  $\rho_{hv}$  values beneath the melting layer; such observations prove a useful indicator of the presence of hail (e.g.,



Ryzhkov et al. 2005a,c; Heinselman and Ryzhkov 2006; Kumjian and Ryzhkov 2008a; Park et al. 2009).

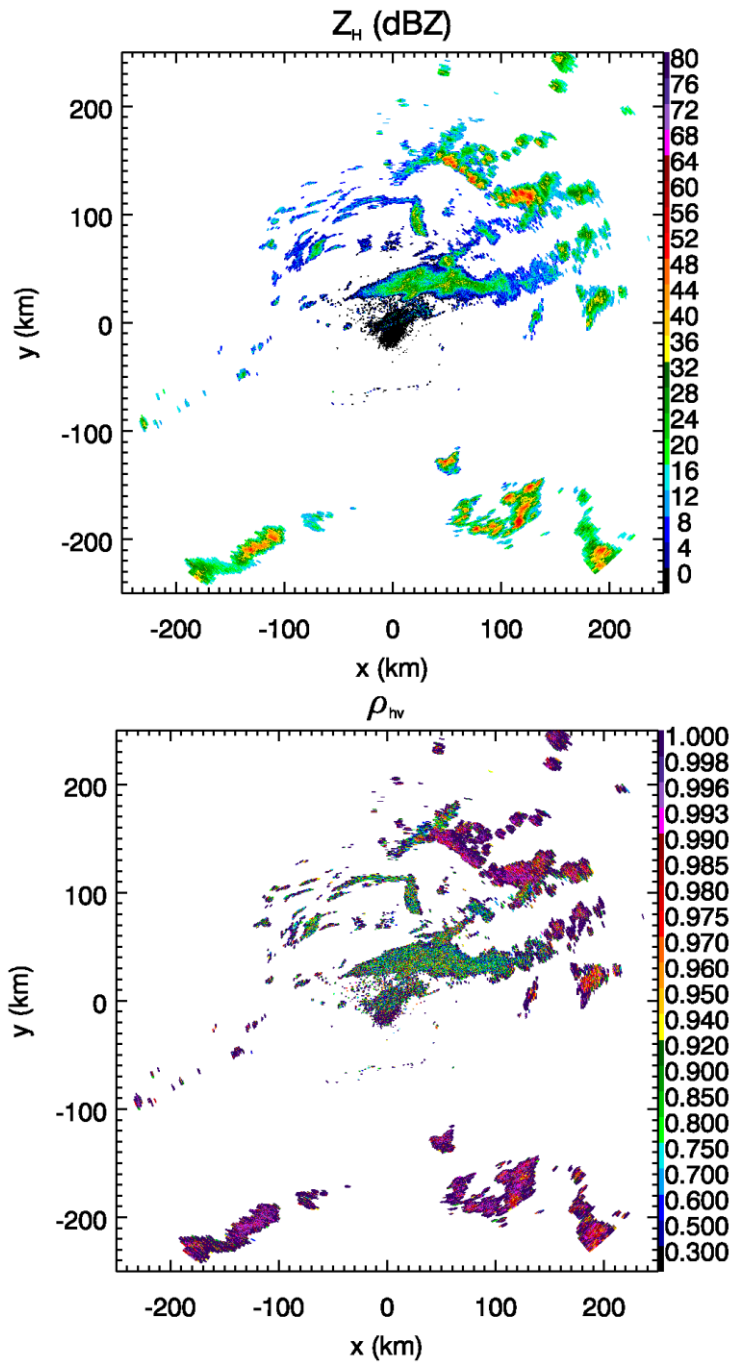


Fig. 2.20: Display of (top)  $Z_H$  and (bottom)  $\rho_{hv}$  from the polarimetric WSR-88D radar in Key West, Florida (KBYX) on 7 February 2012, at 2128 UTC. Data show chaff mixed with precipitation. The chaff is clearly identified by  $\rho_{hv}$  as bands of extremely low  $\rho_{hv}$  values ( $< 0.70$ ), whereas the precipitation has  $\rho_{hv}$  near unity.

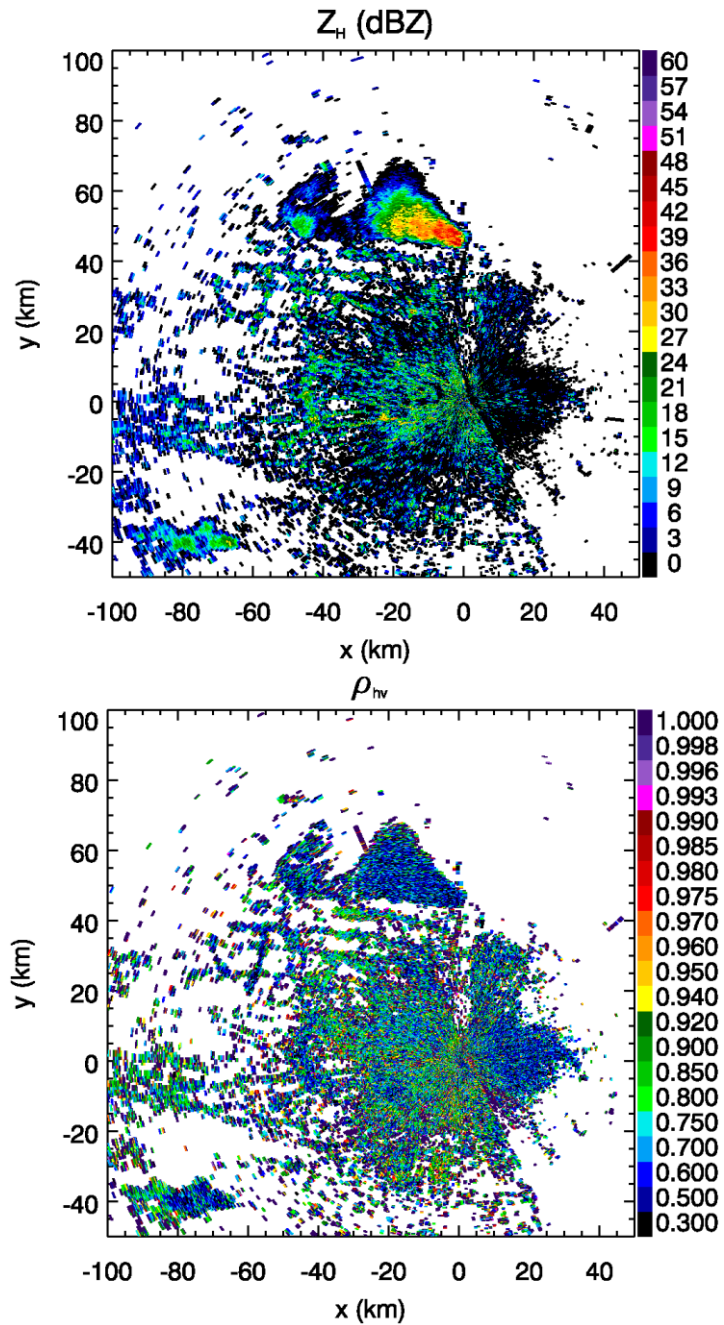


Fig. 2.21: Display of (top)  $Z_H$  and (bottom)  $\rho_{hv}$  from the polarimetric WSR-88D radar in Melbourne, Florida (KMLB) on 31 January 2012, at 2114 UTC. Data show a large grassfire north of the radar. The smoke and ash from the fire is clearly identified by  $\rho_{hv}$  values ( $< 0.50$ ), whereas the clouds have  $\rho_{hv}$  near unity.

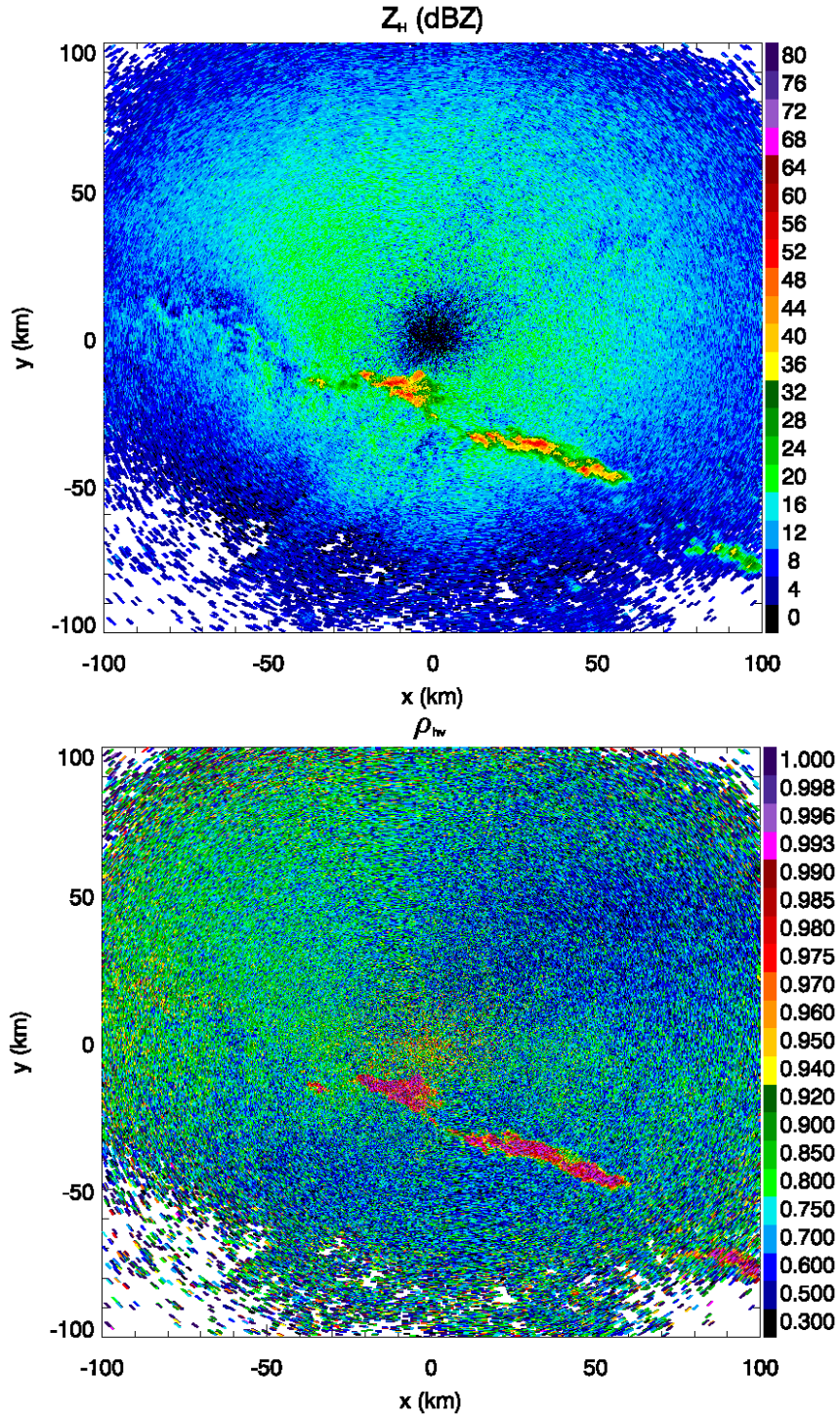


Fig. 2.22: Display of (top)  $Z_H$  and (bottom)  $\rho_{hv}$  from the polarimetric WSR-88D radar in Huntsville, AL (KHYX) on 3 March 2012, at 0545 UTC. Data show a widespread region of biological scatterers, including insects and birds as very low  $\rho_{hv}$ , as well as a few precipitation cells evident by  $\rho_{hv}$  near unity.

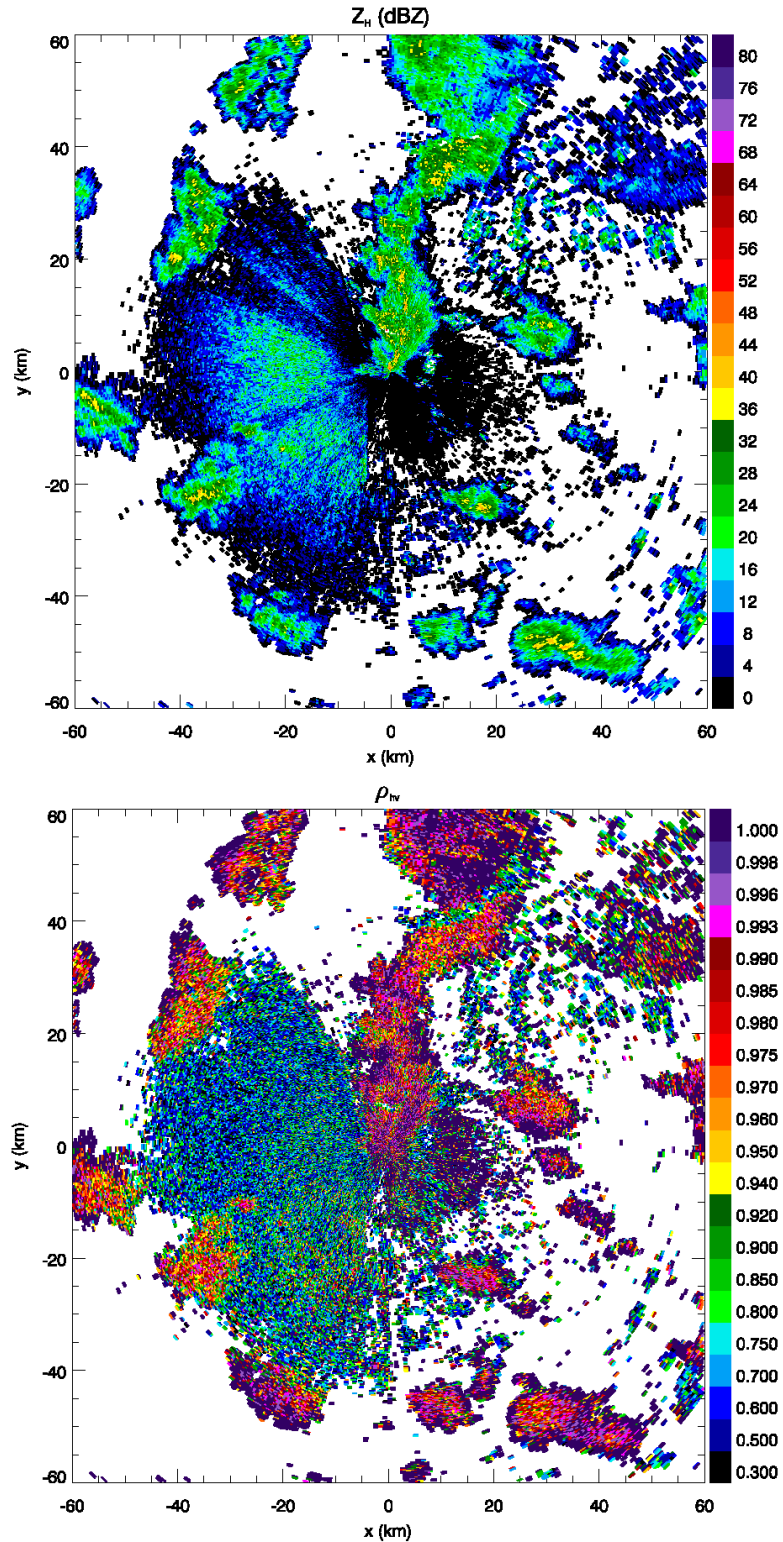


Fig. 2.23: Display of (top)  $Z_H$  and (bottom)  $\rho_{hv}$  from the polarimetric WSR-88D radar in Langley Hill, Washington (KLGX) on 7 February 2012, at 2242 UTC. Data show sea clutter mixed with precipitation. The sea clutter is clearly identified by  $\rho_{hv}$  values ( $< 0.70$ ), whereas the precipitation has much higher  $\rho_{hv}$  ( $> 0.90$ ).

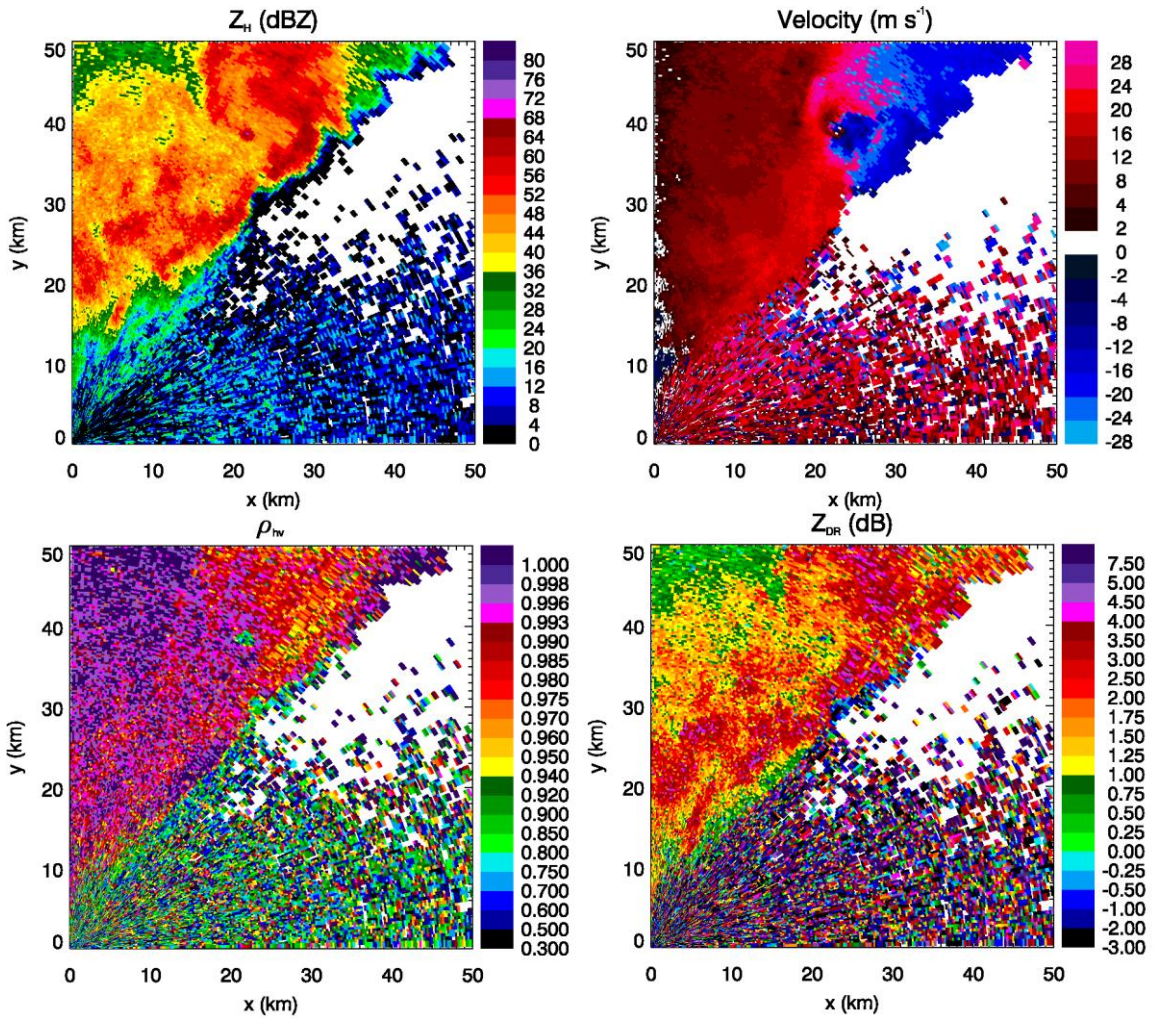


Fig. 2.24: Display of (top left)  $Z_H$ , (top right) Doppler velocity, (bottom left)  $\rho_{hv}$ , and (bottom right)  $Z_{DR}$  from the polarimetric WSR-88D radar in Springfield, Missouri (KSGF) on 29 February 2012, at 0605 UTC. Data show a tornadic debris signature, marked by high  $Z_H$ , low  $Z_{DR}$ , very low  $\rho_{hv}$  collocated with a vortex signature in the Doppler velocities, located at approximately  $x = 22$  km,  $y = 39$  km.

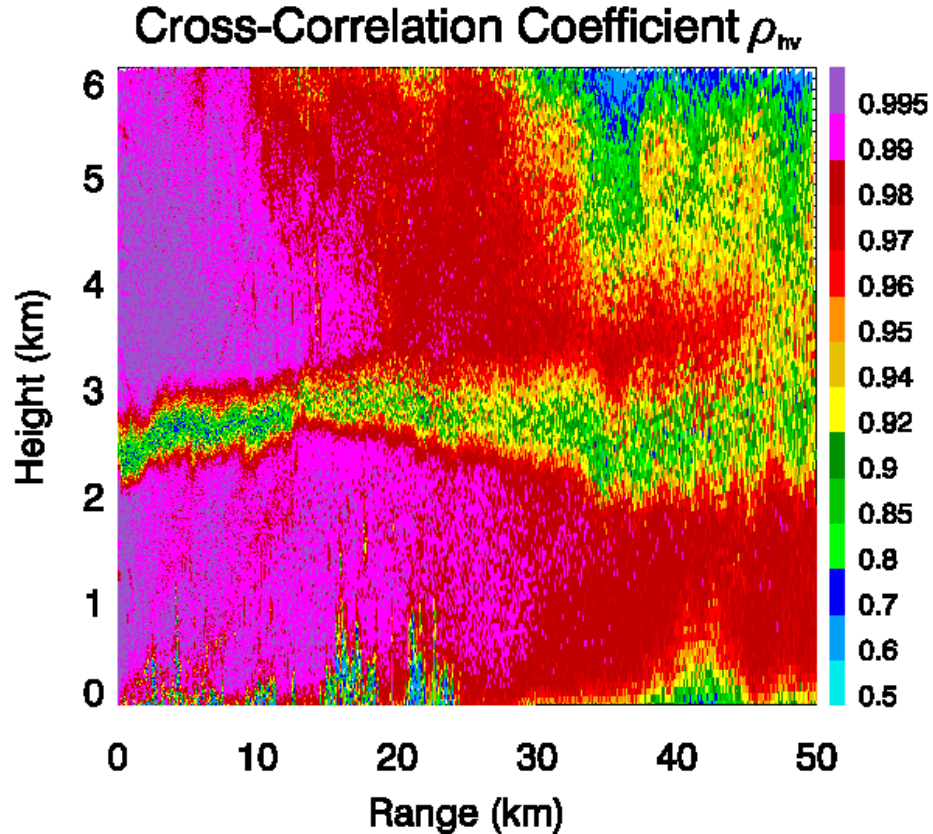


Fig. 2.25: Display of  $\rho_{hv}$  from the BOXPOL radar. Data are from the same scan as Figure 2.13. A dramatic decrease in  $\rho_{hv}$  is evident in the melting layer. The decrease in  $\rho_{hv}$  with range is a result of decreased signal-to-noise ratio.

### 5. Backscatter differential phase shift

In addition to the component of differential phase acquired as the H and V polarized waves propagate through an anisotropic medium, Mie scattering produces a component of differential phase on backscatter off nonspherical particles that are large compared to the radar wavelength. Known as the backscatter differential phase shift  $\delta$ , this additional phase shift can lead to a reduction in  $\rho_{hv}$  and is a tell-tale sign of Mie scatterers within the radar sampling volume. Additionally,  $\delta$  is superposed on the propagation differential phase shift  $\Phi_{DP}$ , leading to difficulty in estimating  $K_{DP}$ .

The backscatter differential phase shift is zero for spherical or randomly tumbling particles, and generally is larger for larger values of complex relative permittivity. There is no straightforward physical explanation for the cause of  $\delta$  because the physics of resonance scattering is extremely complicated. It may be thought of as a delay in excitation (and thus backscatter) of the H or V dipole of an illuminated particle owing to the particle's size and geometry, which is such that internal refraction and interference between the incident and excited waves occur.

*a. Backscatter differential phase shift in rain*

At S band,  $\delta$  is negligible for most raindrop sizes (Fig. 2.26). For shorter radar wavelengths,  $\delta$  becomes noticeable for resonance-sized drops (5 – 6 mm at C band; 3 – 4 mm at X band). There exists a temperature dependence that is most noticeable at C band, where warmer raindrops produce a larger variation in  $\delta$  over the resonance size band. For this reason alone, C-band  $\rho_{hv}$  values measured in pure rain can be lower than at S or X bands, reaching a theoretical minimum of about 0.93 (Ryzhkov and Zrníc 2005).

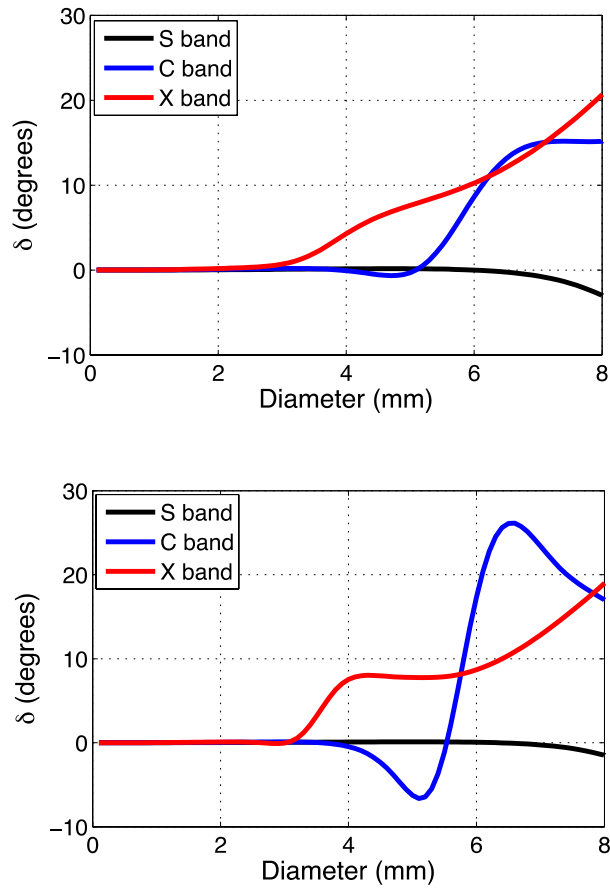


Fig. 2.26: Backscatter differential phase shift ( $\delta$ ) for raindrops, at S, C, and X bands (black, blue, and red curves). Shown for two temperatures: 0 °C (top) and 20 °C (bottom).

*b. Backscatter differential phase shift in solid ice particles*

Owing to the much smaller complex dielectric factor of ice than for water, the  $\delta$  for solid ice pellets is much smaller at all three radar wavelengths than for raindrops of the same size and shape (Fig. 2.27). For particles larger than 1 cm, however, the effects of resonance scattering are clear (Fig. 2.28), as  $\delta$  exhibits large fluctuations for large dry hailstones. The wavelength dependence is clear from Figure 2.28 as well, as the fluctuations start first at X band, then C band, and lastly at S band. Note that the patterns are the same for each wavelength, just shifted to smaller sizes for higher



frequencies. This indicates that the behavior of  $\delta$  as a function of size is produced entirely by the geometry of the particle, with a simple scaling between particle size and radar wavelength (for spheroidal particles of the same axis ratio, as in the modeled hail).

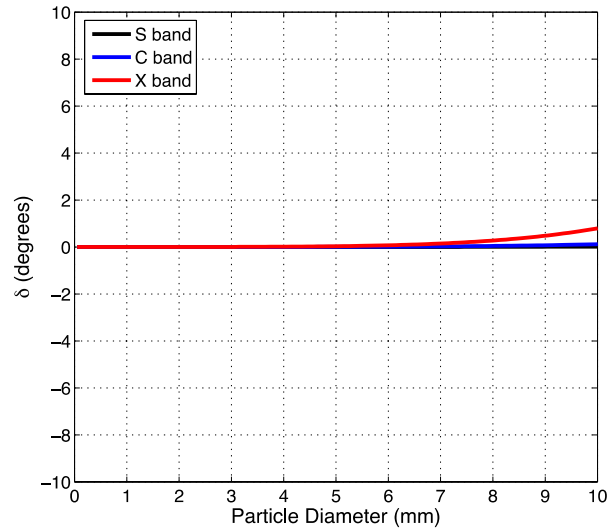


Fig. 2.27: Backscatter differential phase shift ( $\delta$ ) for ice pellets, at S, C, and X bands (black, blue, and red curves).

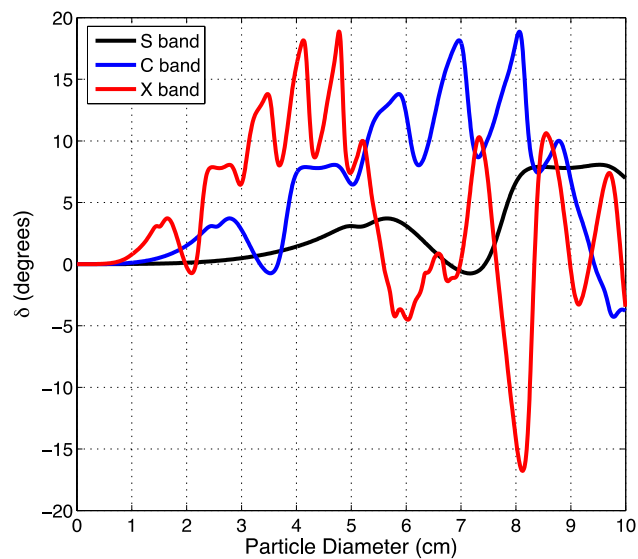


Fig. 2.28: Backscatter differential phase shift ( $\delta$ ) for dry hailstones, at S, C, and X bands (black, blue, and red curves).

*c. Backscatter differential phase shift in dry snow*

At all radar wavelengths, dry snowflakes produce negligible  $\delta$  owing to their low density (and thus very low values of complex dielectric). Even the complex geometry of large snow aggregates apparently is insufficient to produce appreciable values of  $\delta$ .

*d. Backscatter differential phase shift in mixed phase particles*

In contrast to dry snow, wet snow can produce resonance scattering effects, possibly even at S band. For individual snowflakes, (Fig. 2.29),  $\delta$  is most apparent at X band. However, the presence of large, wet aggregates at the bottom of the melting layer inferred from polarimetric data (e.g., Zrnić et al. 1993; Ryzhkov et al. 2008; Giangrande 2007) may be of sufficient size and wetness to cause nonzero  $\delta$  at S band, causing a decrease in  $\rho_{hv}$ . However, there remains uncertainty in quantifying the relative importance of  $\delta$  and of nonuniform beam filling (Ryzhkov 2007) in decreasing  $\rho_{hv}$ . Figure 2.30 is a display of  $\Phi_{DP}$  measured with the BOXPOL radar at the same time as the scan shown in Figure 2.13. The nonmonotonic behavior of  $\Phi_{DP}$  through the melting layer is clearly seen, indicating  $\delta$  possibly as high as  $5^\circ - 15^\circ$ . Note that such “bumps” in the radial profile of  $\Phi_{DP}$  are quite distinct from the monotonic increase in precipitation, which is evident at low levels farther downrange (annotated in the figure).  $K_{DP}$  estimation is difficult in the presence of  $\delta$  because of the negative slope of the measured  $\Phi_{DP}$  on the downrange side of the  $\delta$  bump, as shown schematically in Figure 2.31.

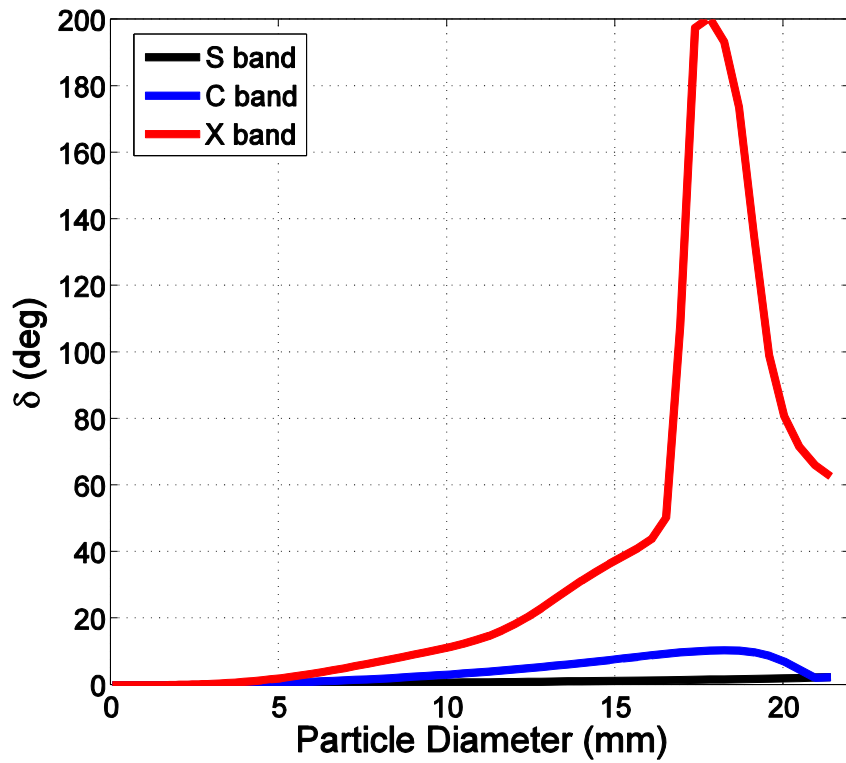


Fig. 2.29: Backscatter differential phase  $\delta$  for melting snowflakes at S, C, and X bands (black, blue, and red curves).

Melting hailstones can exhibit substantial  $\delta$  at all radar wavelengths (Figure 2.32). The large fluctuations over narrow size bands suggest that  $\rho_{hv}$  can be dramatically lowered in wet hail, as is typically observed.

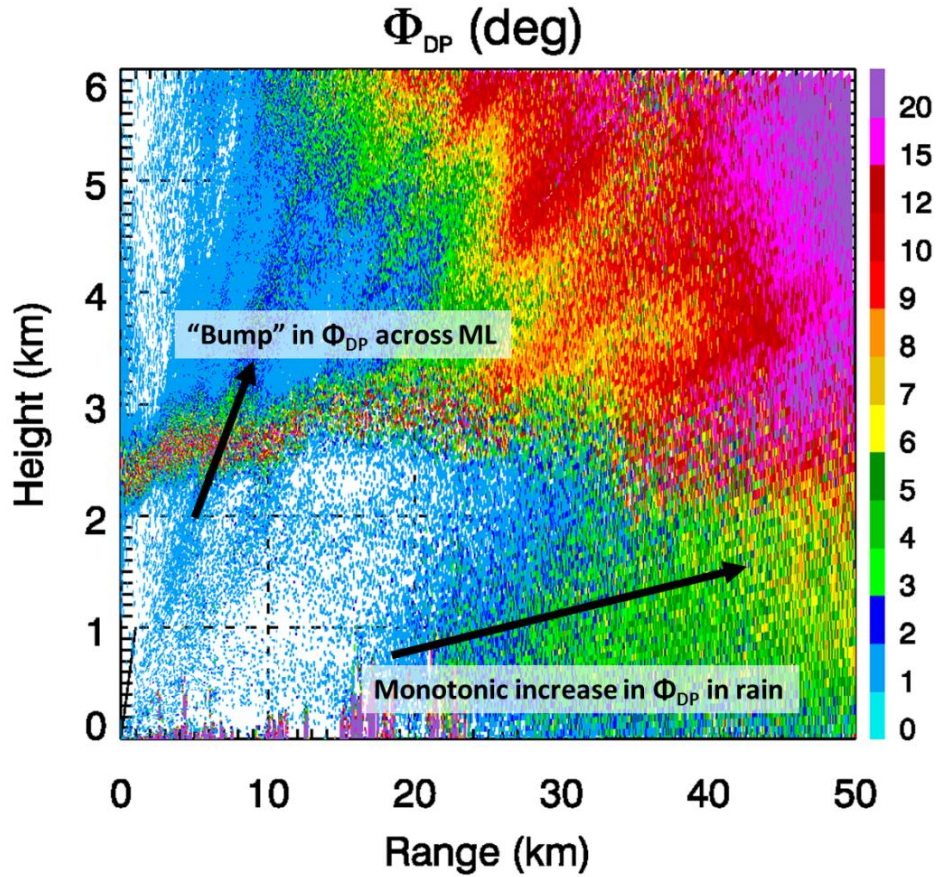


Fig. 2.30: As in Figure 2.13, but  $\Phi_{DP}$  is shown. Note the “bump” in  $\Phi_{DP}$  through the melting layer, a contribution to differential phase caused by backscatter off large, wet snow aggregates.

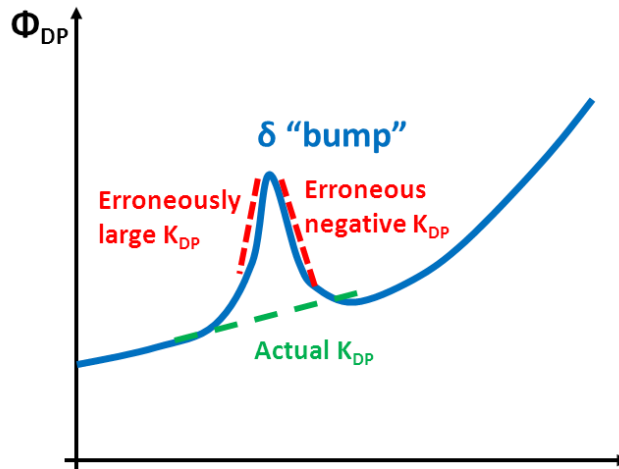


Fig. 2.31: Schematic illustrating the difficulty estimating  $K_{DP}$  (the slope of the dashed straight lines) in the presence of a  $\delta$  bump on the radial profile of the measured  $\Phi_{DP}$  (blue curve). Erroneously large positive and negative errors in the  $K_{DP}$  estimates are depicted in red, whereas the true  $K_{DP}$  is shown in green.

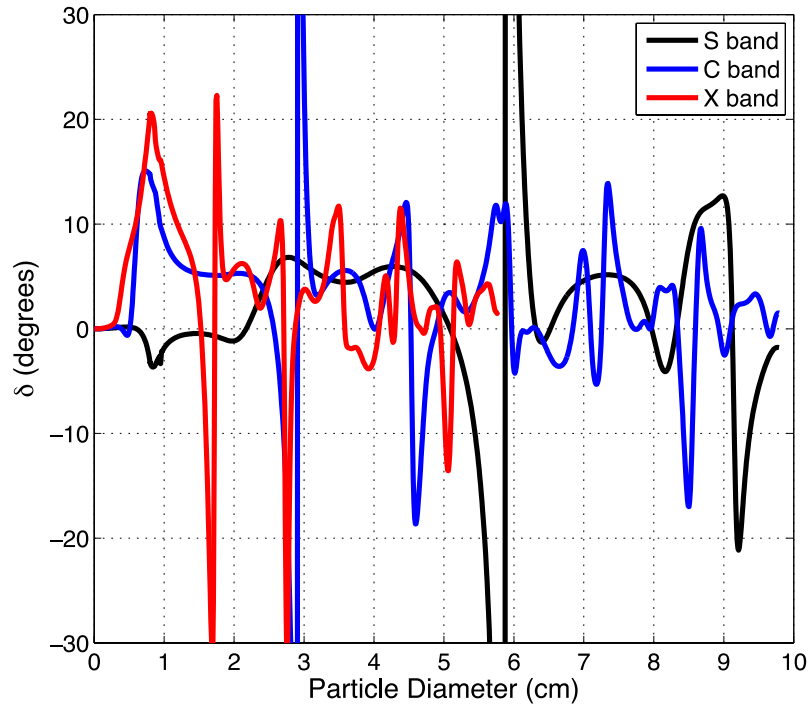


Fig. 2.32: Backscatter differential phase shift ( $\delta$ ) for melting hailstones, at S, C, and X bands (black, blue, and red curves).

## 6. Linear depolarization ratio

When electromagnetic radiation of a given polarization illuminates a hydrometeor canted in the plane of polarization, both dipoles are illuminated. This leads to the hydrometeor scattering radiation with components of *both* polarizations. The secondary radiation that has the same polarization as the incident radiation is called the co-polar component, whereas when the incident and scattered polarizations are different, the scattered radiation has a cross-polar component (and the hydrometeor is said to have *depolarized* the incident radiation). The concept of depolarization is shown schematically in Figure 1.6.

The linear depolarization ratio  $L_{DR}$  is a measure of the magnitude of the depolarized component of the backscattered signal normalized by the co-polar

component of the backscattered radiation. It is not available from radars that transmit and receive H and V polarization waves simultaneously. Because  $L_{DR}$  is a ratio (like  $Z_{DR}$ ), it is independent of absolute radar calibration and is independent of hydrometeor number concentration. However, it can be affected by noise bias and is not immune to propagation effects. For example, upon propagation of a radar signal through a depolarizing medium, the observed  $L_{DR}$  will exhibit an increasing trend. After emerging from the depolarizing medium, the signal retains the “memory” of depolarization and  $L_{DR}$  values remain elevated, even in a noncanted medium. Because the depolarized component of scattered radiation tends to be orders of magnitude smaller than the co-polar component, the measured  $L_{DR}$  is given in logarithmic units (dB) and is generally negative. For example, in the case of no depolarization on backscatter,  $L_{DR}$  is equal to negative infinity. However, limitations of the antenna (and other hardware) design typically limit the so-called “cross-polar isolation” to about -40 dB, which is generally about the lower limit of measurable  $L_{DR}$ .

$L_{DR}$  increases for irregularly shaped particles that are canted with respect to the polarization of the incident wave. Because most hydrometeors tend to have  $0^\circ$  mean canting angle (implying zero depolarization), it is the *width* of the canting angle distribution ( $\sigma$ ) that controls  $L_{DR}$ . In other words, increasing  $\sigma$  tends to increase  $L_{DR}$  for nonspherical particles.

#### *a. Linear depolarization ratio in rain*

$L_{DR}$  in rain tends to be very low, especially for smaller drops that have essentially spherical shape (Fig. 2.32). Though larger drops are oblate and can thus depolarize the

incident radiation if canted, the mean canting angle of raindrops tends to be  $0^\circ$  (e.g., Ryzhkov et al. 2002b). Thus, some of the lowest values of measured  $L_{DR}$  tend to be in rain.

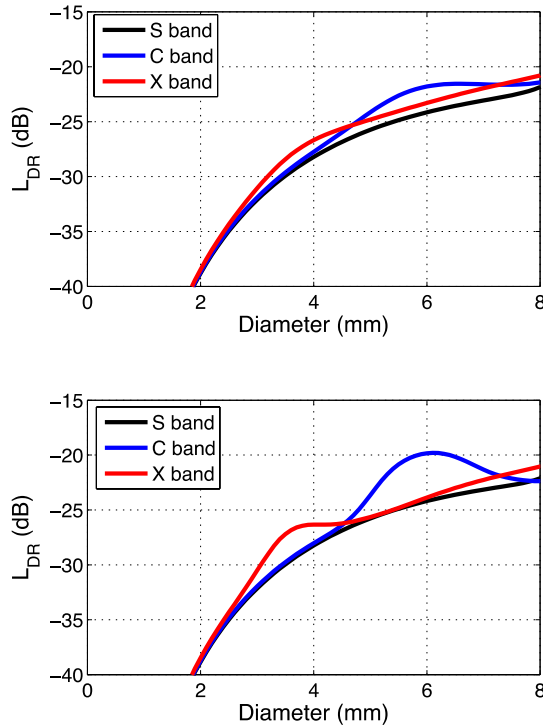


Fig. 2.33: Linear depolarization ratio ( $L_{DR}$ ) for raindrops, at S, C, and X bands (black, blue, and red curves). Shown for two temperatures:  $0^\circ\text{C}$  (top), and  $20^\circ\text{C}$  (bottom).

*b. Linear depolarization ratio in solid ice particles*

The  $L_{DR}$  in small ice pellets is lower than raindrops of the same size and shape (Fig. 2.34), indicating that the decreased complex dielectric factor of ice, which tends to decrease  $L_{DR}$ , dominates the effect of increased tumbling, which tends to increase  $L_{DR}$ . In contrast, the  $L_{DR}$  of dry hailstones can grow quite large at all radar wavelengths (Fig. 2.35). There is a large separation of  $L_{DR}$  values at S, C, and X bands for hailstones

smaller than about 5 cm, with the largest values at X band. This suggests the possibility of using dual-wavelength  $L_{DR}$  measurements to determine hail size.

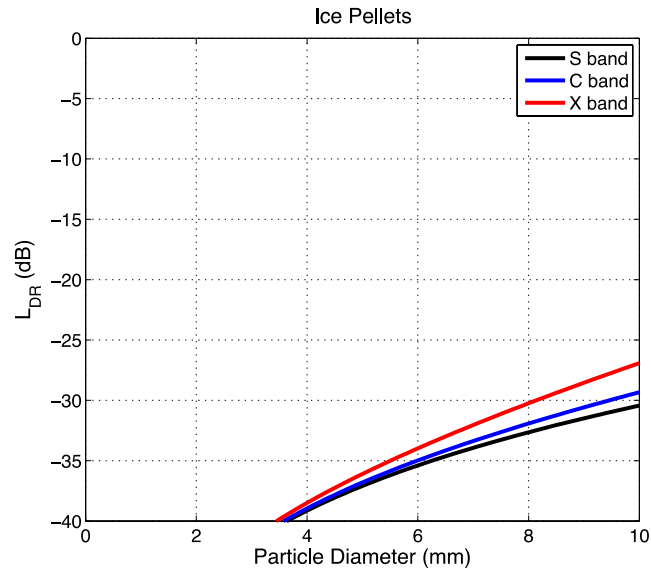


Fig. 2.34: Linear depolarization ratio ( $L_{DR}$ ) for ice pellets, at S, C, and X bands (black, blue, and red curves).

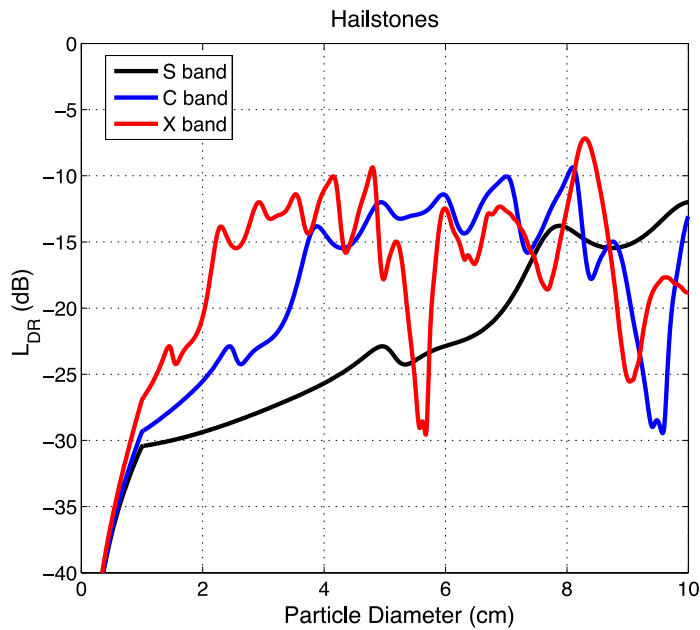


Fig. 2.35: Linear depolarization ratio ( $L_{DR}$ ) for dry hailstones, at S, C, and X bands (black, blue, and red curves).



*c. Linear depolarization ratio in dry snow*

For a given  $Z_H$ , the  $Z_{DR}$  in dry snow and light rain exhibits heavy overlap (e.g., Ryzhkov and Zrnić 1998a). Because of the increased wobbling of dry snowflakes, however,  $L_{DR}$  offers additional discriminatory power (Fig. 2.36) for detecting differences between depolarizing dry snowflakes and light rain in which depolarization is very small. This is especially true for smaller, higher-density snowflakes.

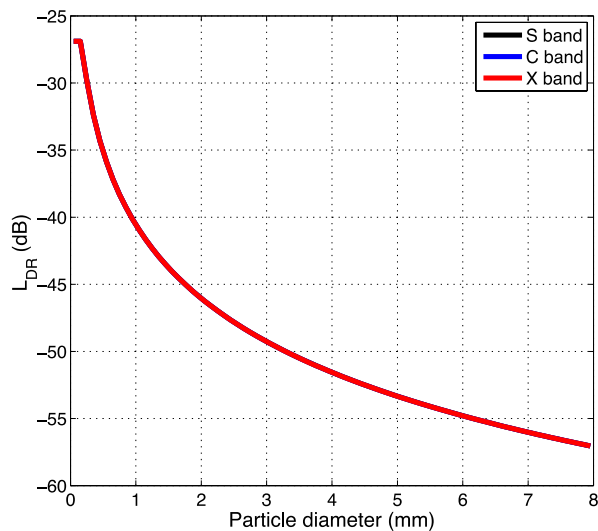


Fig. 2.36: Linear depolarization ratio ( $L_{DR}$ ) for dry snowflakes, at S, C, and X bands (black, blue, and red curves). Snowflakes considered as oblate spheroids (aspect ratio 0.7), with density decreasing as a function of size following Brandes et al. (2007). Complex scattering amplitudes were computed using the Rayleigh approximation. The canting angle distribution width  $\sigma = 40^\circ$ .

*d. Linear depolarization ratio in mixed phase particles*

In contrast to dry snow,  $L_{DR}$  can be quite large in melting snowflakes at all radar wavelengths (Fig. 2.37), making it an attractive variable for melting layer detection. The enhancement is due to large, wet, oblate snowflakes wobbling. An increase in liquid water content on a particle helps enhance the cross-polar component of the backscattered radiation, enhancing  $L_{DR}$ .

Wet hailstones produce much larger values of  $L_{DR}$  than pure rain (Fig. 2.38). This includes hailstones at low levels, or hail undergoing wet growth in convective storm updrafts aloft. The latter contributes to an observed enhancement of  $L_{DR}$  known as the “ $L_{DR}$  cap” (e.g., Jameson et al. 1996; Bringi et al. 1997; Hubbert et al. 1998; Kennedy et al. 2001).

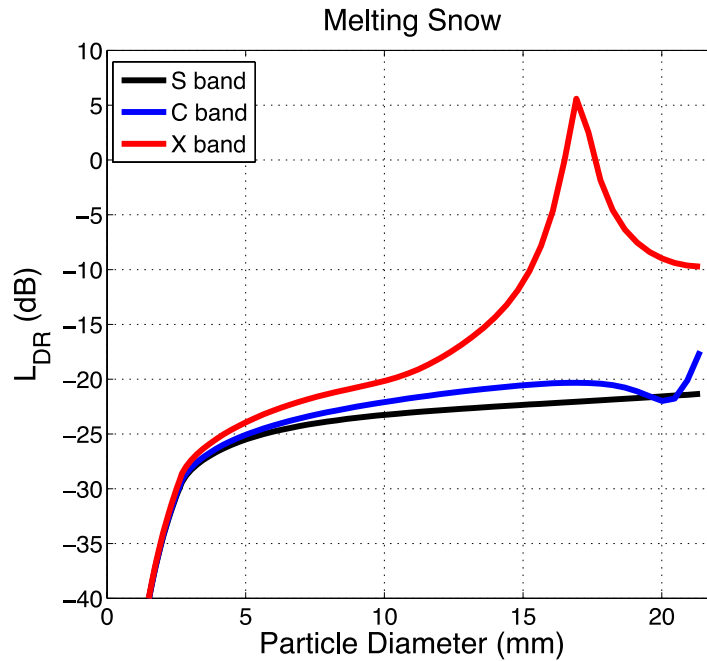


Fig. 2.37: Linear depolarization ratio ( $L_{DR}$ ) for melting snowflakes, at S, C, and X bands (black, blue, and red curves).

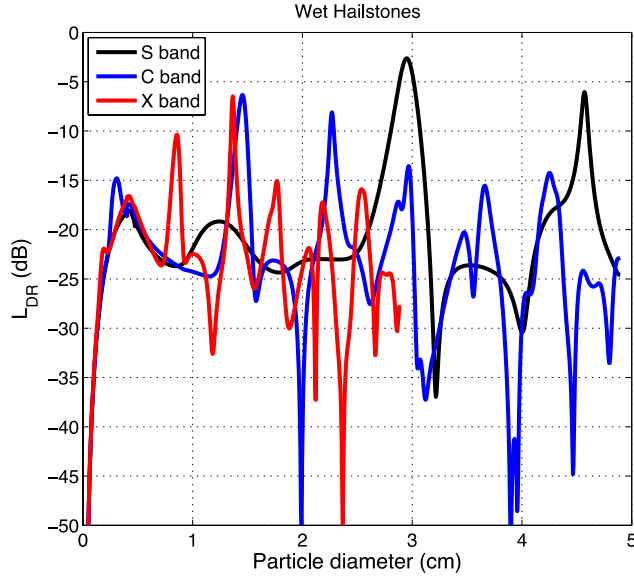


Fig. 2.38: Linear depolarization ratio ( $L_{DR}$ ) for wet hailstones, at S, C, and X bands (black, blue, and red curves).

## 7. Co-cross-polar correlation coefficients

Two of the least-explored polarimetric radar variables are the co-cross-polar correlation coefficients  $\rho_{xh}$  and  $\rho_{xv}$ , which measure the correlation between the cross-polarized and co-polarized components of the backscattered radiation. Ryzhkov (2001) provides a theoretical description of  $\rho_{xh}$  and  $\rho_{xv}$ , and the follow-up study by Ryzhkov et al. (2002b) provides some of the first measurements of these variables in precipitation. The co-cross-polar correlation coefficients  $\rho_{xh}$  and  $\rho_{xv}$  depend strongly on the orientation of the irradiated hydrometeors. For particles that are randomly oriented in the horizontal plane or entirely randomly oriented,  $\rho_{xh}$  and  $\rho_{xv}$  are identically zero. More commonly, however, hydrometeor orientations are described by an axisymmetric, two-dimensional, Gaussian distribution of canting angles. In this case, Ryzhkov (2001) demonstrates that  $\rho_{xh}$  and  $\rho_{xv}$  depend almost entirely on the mean canting angle  $\langle\alpha\rangle$  of hydrometeors within the resolution volume, and the width of the canting angle

distribution  $\sigma$ . (When  $\sigma$  is larger than  $\langle\alpha\rangle$ , which occurs for most hydrometeors, the magnitudes of the co-cross-polar correlation coefficients are proportional to the ratio  $\langle\alpha\rangle/\sigma$ ). As such, the co-cross-polar correlation coefficients are much more sensitive to changes in particle orientation than to variations in the particle size distribution. If the mean canting angle of particles within the sampling volume is  $\langle\alpha\rangle = 0$ , then  $\rho_{xh} = \rho_{xv} = 0$ . Measured nonzero values (about 0.2 – 0.3) of  $\rho_{xh}$  and  $\rho_{xv}$  in rain are a manifestation of  $\langle\alpha\rangle \neq 0$  in a given resolution volume (e.g., Ryzhkov et al. 2002b). The average  $\langle\alpha\rangle$  over a propagation path (defined as the “net” canting angle) needs to be only a few tenths of a degree to cause a visible trend in  $|\rho_{xh}|$  and  $|\rho_{xv}|$ . Such net canting of raindrops may be possible in cases of vertical wind shear (e.g., Brussard 1976). Ice crystals aloft oriented with strong electric fields (but not exactly in the vertical or the horizontal) have been observed to cause a strong increase in  $|\rho_{xh}|$  and  $|\rho_{xv}|$  with range. The lowest values of  $|\rho_{xh}|$  and  $|\rho_{xv}|$  occur in the melting layer, owing to increased wobbling of large, wet snow aggregates. Enhanced  $\sigma$  tends to decrease the importance of  $\langle\alpha\rangle$ .

The co-cross-polar correlation coefficients are independent of hydrometeor concentration and are independent of absolute radar calibration. However, they are affected by noise bias and are quite sensitive to propagation effects, especially depolarization on propagation. In fact, on propagation through a medium of nonspherical particles which are canted with respect to the plane of polarization (i.e., those that cause depolarization),  $|\rho_{xh}|$  and  $|\rho_{xv}|$  display a pronounced increase with range. After emerging from the depolarizing medium, the signal retains the “memory” of the depolarization and  $\rho_{xh}$  and  $\rho_{xv}$  maintain their enhanced values. Note that a noticeable trend of  $|\rho_{xh}|$  and  $|\rho_{xv}|$  in range can also signify radar system imperfections.

Whereas the magnitudes of  $\rho_{xh}$  and  $\rho_{xv}$  are directly related to the orientation parameters  $\langle\alpha\rangle$  and  $\sigma$ , the phases of  $\rho_{xh}$  and  $\rho_{xv}$  are related to the sign of  $\langle\alpha\rangle$  and the presence of non-Rayleigh scatterers in the resolution volume. For Rayleigh scatterers with small values of the imaginary part of the complex dielectric factor (including dry snow and ice crystals), the phase of  $\rho_{xh}$  and  $\rho_{xv}$  is 0 or  $\pi$ , depending on the sign of  $\langle\alpha\rangle$ . For particles with larger imaginary parts of the complex dielectric factor (or non-Rayleigh targets), the phases are nonzero and may contain information about the microphysical properties of the particles. Note that unlike the co-polar differential phase shift upon backscatter  $\delta$ , the so-called depolarization phases (see Chapter 1) are much less affected by particle shape; particles simply must be sufficiently nonspherical as to produce a depolarized component of the backscattered radiation.

## **8. Specific attenuation**

Though not directly measured, the specific attenuation  $A_{H,V}$  is an important polarimetric radar variable, especially at shorter radar wavelengths. It is the amount of attenuation of the co-polar H (or V) polarization signal as it propagates through a lossy medium, typically expressed in logarithmic units ( $\text{dB km}^{-1}$ ). In other words, it describes the amount that the measured reflectivity factor at H (or V) polarization  $Z_{H,V}$  decreases owing to attenuation. Integrating  $A_H$  or  $A_V$  over range along a radial provides the total attenuation of the signal along that radial. Specific attenuation is directly proportional to the imaginary part of the complex forward scattering amplitudes of a given hydrometeor, and thus depends on the particle's composition and size.

a. Specific attenuation in rain

The normalized  $A_H$  as a function of size for raindrops is shown in Figure 2.39. The proportionality to wavelength is clearly seen, as values are negligible for most drop sizes at S band, but become large for large raindrops at the shorter radar wavelengths. The temperature dependence is also quite evident, especially for the resonance sizes at C band. Because the specific attenuation values are insignificant for drops smaller than about 3 mm at all wavelengths, it is clear that only rain with  $> 3$  mm diameter drops can produce appreciable attenuation. Continental convective rain, for which numerous large drops are produced by melting small hail and graupel, thus can produce significant attenuation at the shorter radar wavelengths.

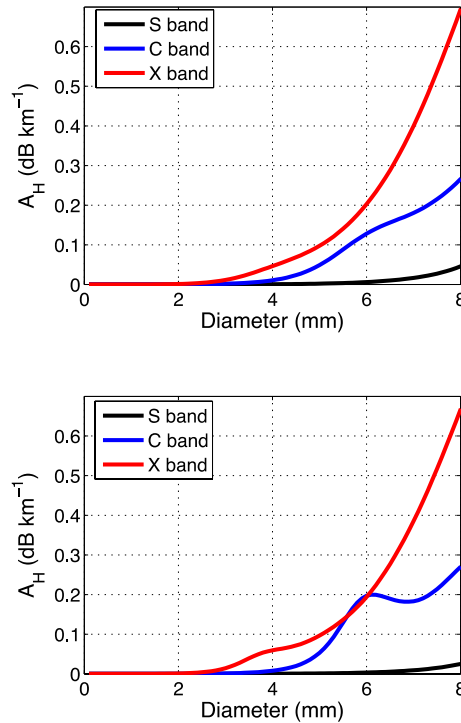


Fig. 2.39: Normalized specific attenuation ( $A_H$ ) for raindrops at S, C, and X bands (black, blue, and red curves). Shown for two temperatures: 0 °C (top), and 20 °C (bottom).

*b. Specific attenuation in solid ice particles*

Owing to the much smaller imaginary part of the complex dielectric factor of ice, attenuation in small ice particles is negligible compared to attenuation in raindrops of the same size and shape (Fig. 2.40). In contrast,  $A_H$  in large hailstones can be quite significant at all radar wavelengths (Fig. 2.41). Note that resonance-sized hailstones at S band ( $> 6$  cm) produce larger values of  $A_H$  than at C and X bands.

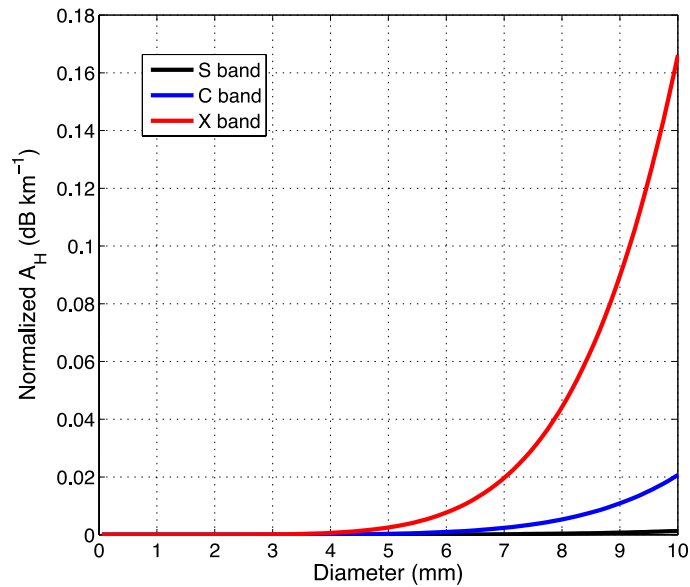


Fig. 2.40: Normalized specific attenuation ( $A_H$ ) for ice pellets, at S, C, and X bands (black, blue, and red curves).

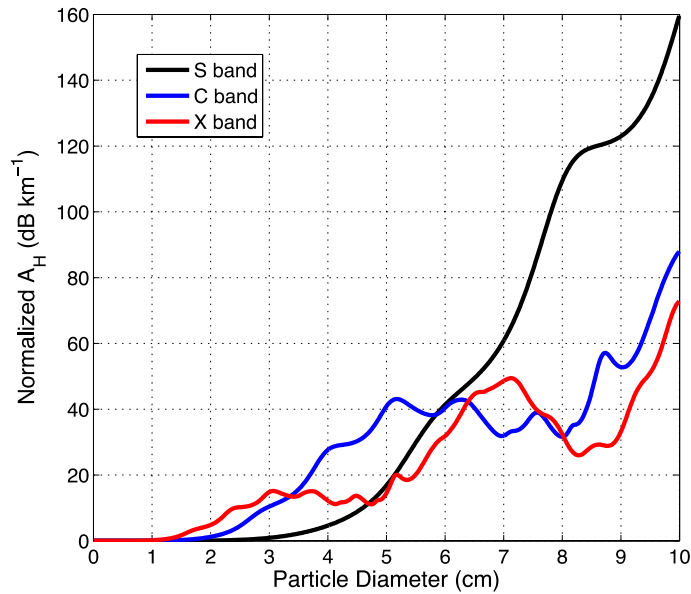


Fig. 2.41: Normalized specific attenuation ( $A_H$ ) for dry hailstones, at S, C, and X bands (black, blue, and red curves).

*c. Specific attenuation in dry snow*

Because of the very small imaginary part of the complex relative permittivity of dry snow, the specific attenuation in snow is negligible at S, C, and X bands.

*d. Specific attenuation in mixed-phase particles*

Though melting snow generally produces small values of  $A_H$  at S band, the attenuation at C and X bands can be quite large (Fig. 2.42). Wet hailstones can produce significant  $A_H$  at all three wavelengths (Fig. 2.43). Note that  $A_H$  for wet hail is generally smaller than for dry hailstones at all three weather radar wavelengths. Also, the values of  $A_H$  in wet hail are similar for S, C, and X bands.



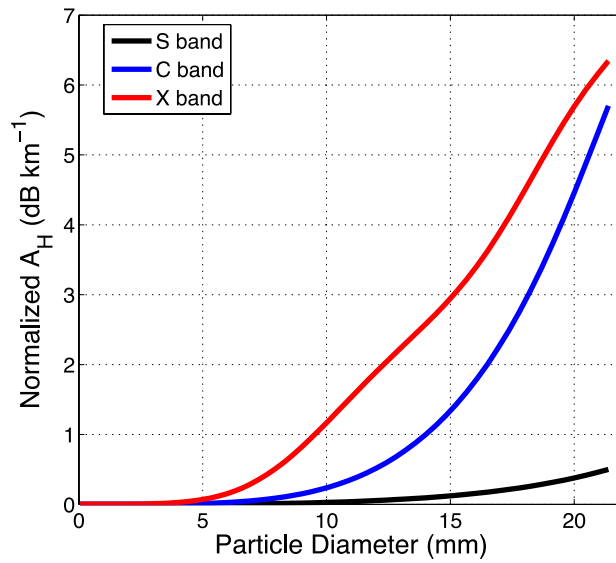


Fig. 2.42: Normalized specific attenuation ( $A_H$ ) for melting snow, at S, C, and X bands (black, blue, and red curves).

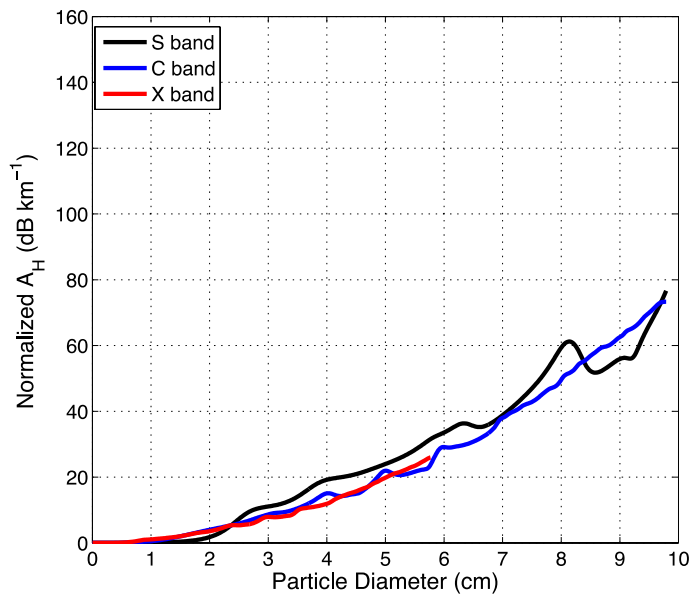


Fig. 2.43: Normalized specific attenuation ( $A_H$ ) for wet hail, at S, C, and X bands (black, blue, and red curves). Note that it is the same scale as for dry hailstones.

## 9. Specific differential attenuation

Whereas  $A_H$  and  $A_V$  describes the decrease in  $Z_H$  and  $Z_V$  owing to attenuation, their difference  $A_{DP} = A_H - A_V$  describes the decrease in  $Z_{DR}$ , called *specific differential attenuation*.  $A_{DP}$  is directly proportional to the difference between the imaginary parts of the complex forward scattering amplitudes at H and V polarizations, and thus depends on the particle's composition, shape, and size. Spherical particles have  $A_{DP} = 0$  by definition.

### *a. Specific differential attenuation in rain*

$A_{DP}$  is near 0 for smaller raindrops at all wavelengths because of their nearly spherical shapes (Fig. 2.44). Large drops produce large  $A_{DP}$  values at X band, and again, the temperature dependence is evident.

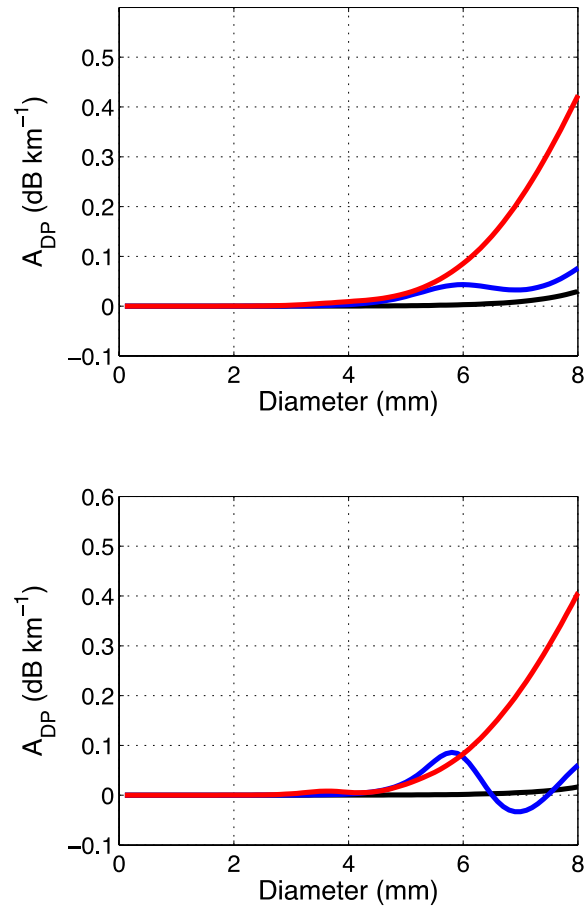


Fig. 2.44: Specific differential attenuation ( $A_{DP}$ ) for raindrops, at S, C, and X bands (black, blue, and red curves). Shown for two temperatures: 0 °C (top), and 20 °C (bottom).

*b. Specific differential attenuation in solid ice particles*

Specific differential attenuation is very small in ice pellets (Fig. 2.45), owing to the small imaginary part of the complex dielectric factor of ice at all three wavelengths. Large dry hailstones, however, can produce large  $A_{DP}$  (Fig. 2.46), assuming they are nonspherical. However, at C and X bands the large positive and negative fluctuations in  $A_{DP}$  are centered on zero; the integrated effect of a distribution of dry hailstones may indeed make  $A_{DP}$  near zero, even if such large hailstones are present. At S band,  $A_{DP}$

values tend to be positive (which would result in a decrease in  $Z_{DR}$ ) for oblate hailstones smaller than about 10 cm.

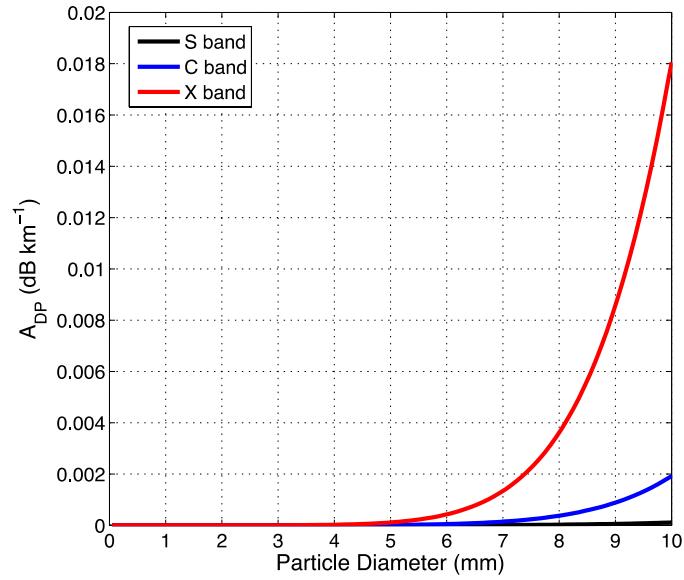


Fig. 2.45: Specific differential attenuation ( $A_{DP}$ ) for ice pellets, at S, C, and X bands (black, blue, and red curves).

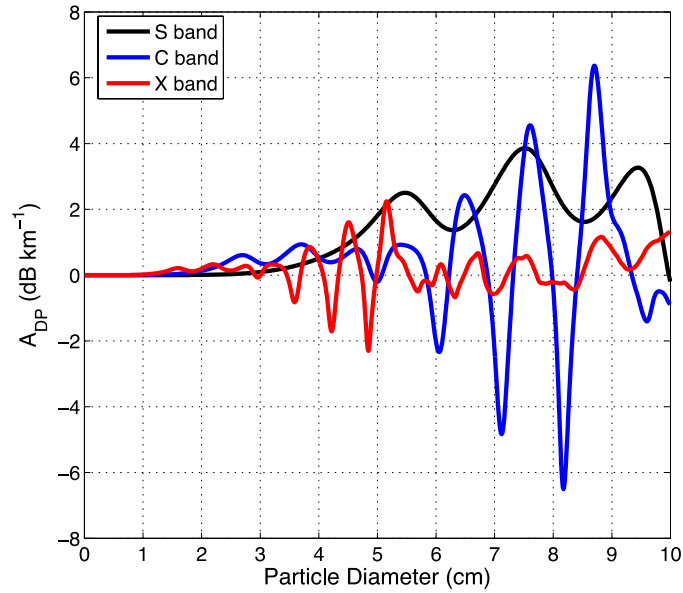


Fig. 2.46: Specific differential attenuation ( $A_{DP}$ ) for dry hailstones, at S, C, and X bands (black, blue, and red curves).

*c. Specific differential attenuation in dry snow*

The imaginary part of the complex dielectric factor of snow is very small; hence,  $A_{DP}$  in dry snow is insignificant at all three weather radar wavelengths.

*d. Specific differential attenuation in mixed-phase particles*

Melting snow can produce very large  $A_{DP}$  at C and X bands (Fig. 2.47). Differential attenuation is possible at S band when large, wet snow aggregates are present in the melting layer. An example of S-band differential attenuation in melting snow is provided in Figure 2.48, evident as a radial streak of slightly negative  $Z_{DR}$  emanating from the melting layer bright band starting at a range of about 50 km.

Wet hail produces very large differential attenuation (Fig. 2.49) at all three wavelengths. Unlike for dry hailstones,  $A_{DP}$  values tend to be positive for most hailstone sizes at all radar wavelengths, implying a decrease in  $Z_{DR}$  should be observed in melting hail (if it is sufficiently large). Also of note is that the  $A_{DP}$  values for S band in giant hail (> 5 – 6 cm) are larger than at C and X bands. Large differential attenuation at shorter wavelengths is routinely observed in convective storms, and correcting for such anomalous differential attenuation remains a challenging problem (e.g., Bringi et al. 1990; Snyder et al. 2010; Gu et al. 2011; Borowska et al. 2011a). At S band, differential attenuation in convective storms is less common, but is still observed (Figure 2.50).

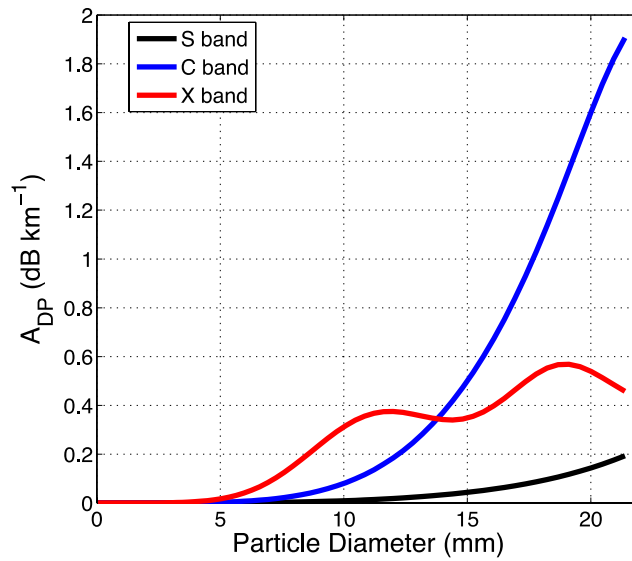


Fig. 2.47: Specific differential attenuation ( $A_{DP}$ ) in melting snowflakes at S, C, and X bands (black, blue, and red curves).

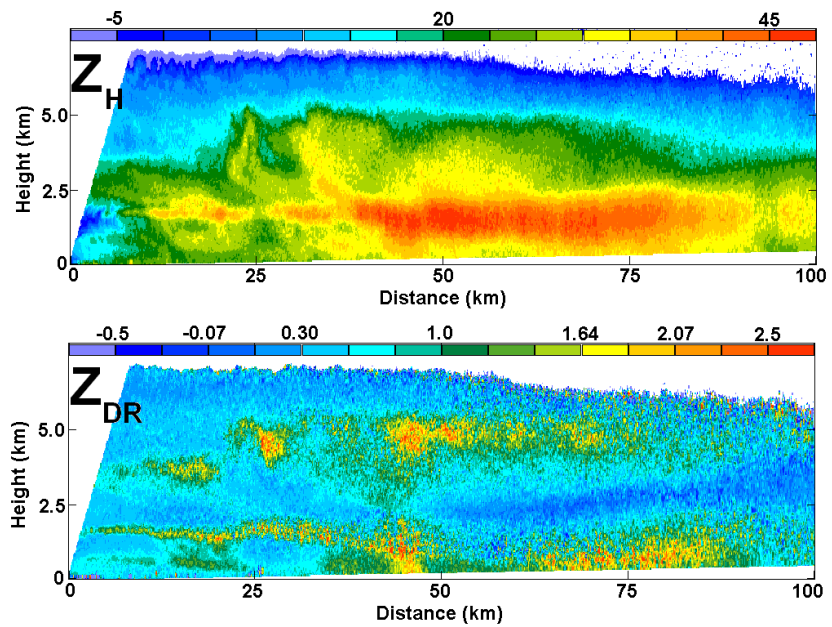


Fig. 2.48: Data from a vertical cross section through a winter stratiform precipitation event on 27 January 2009 at 2317 UTC, taken with the S-band KOUN along the  $181^\circ$  azimuth. The radial streak of negative  $Z_{DR}$  emanating from about 50 km range is caused by differential attenuation.

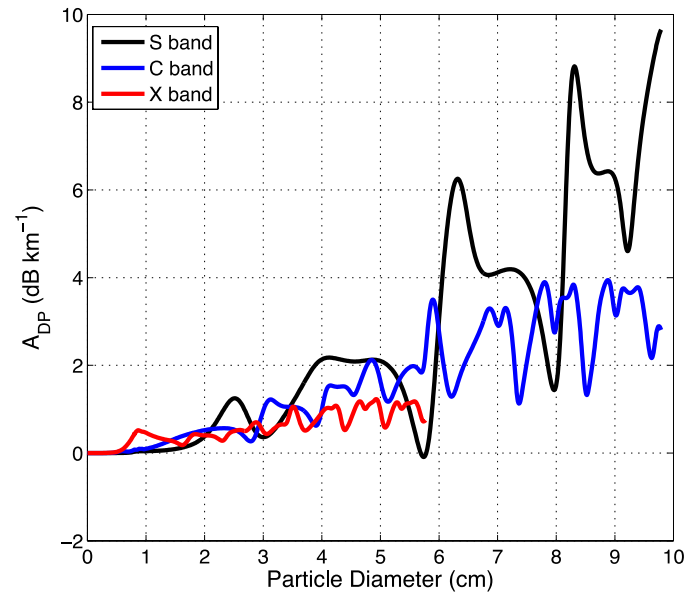


Fig. 2.49: Specific differential attenuation ( $A_{DP}$ ) in wet hailstones at S, C, and X bands (black, blue, and red curves).

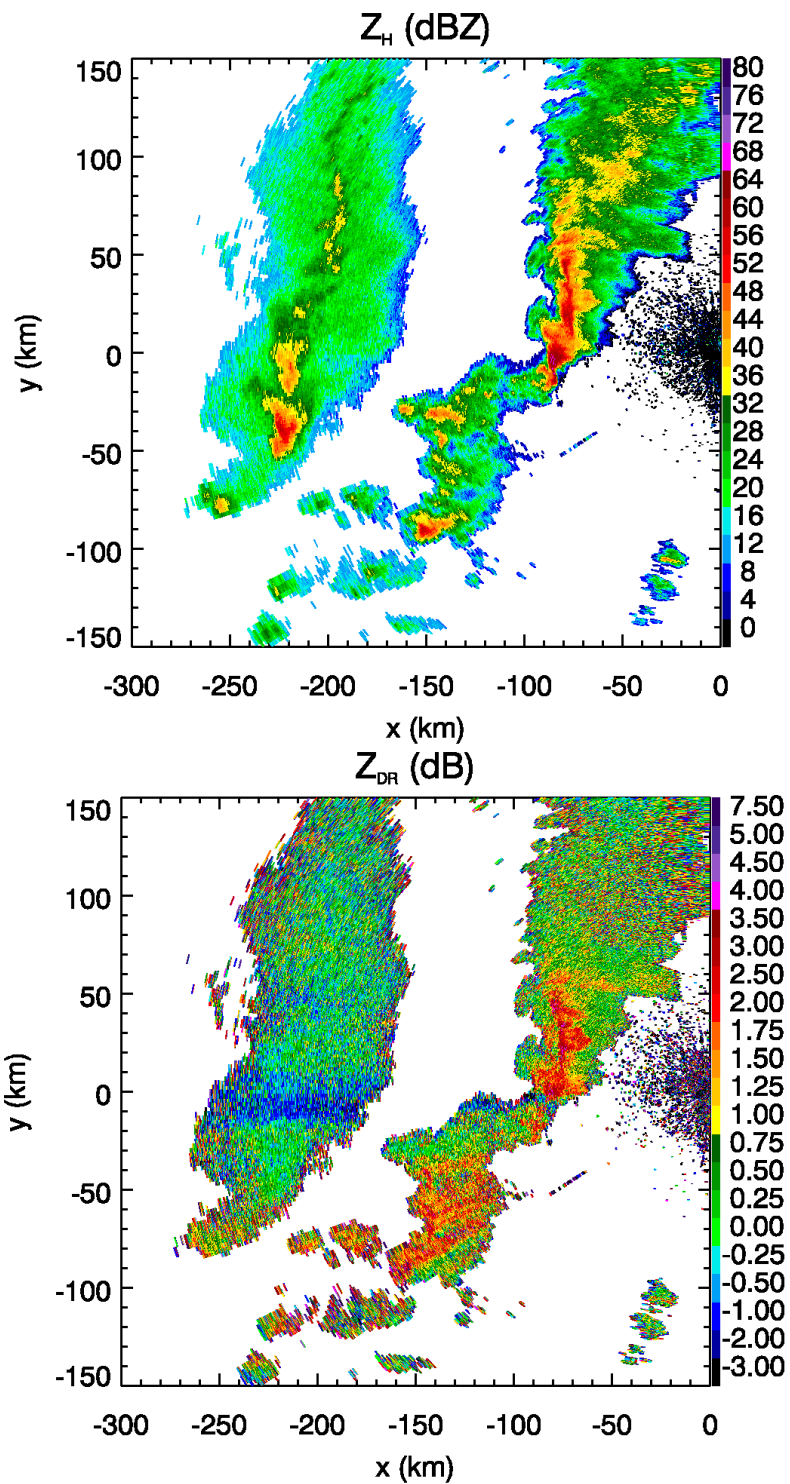


Fig. 2.50: Observations of (a)  $Z_H$ , and (b)  $Z_{DR}$  with the S-band polarimetric WSR-88D near Vance Air Force Base in Oklahoma (KVNX). Data are from  $0.5^\circ$  in elevation, on 3 February 2012, at 0335 UTC. The radial streaks of negative  $Z_{DR}$  are indications of differential attenuation.



### Chapter 3: Artifacts in dual-polarization radar data.

Dual-polarization radar data offer important new information regarding the type and size of precipitation particles within storms, as shown in the first two chapters. However, with this new technology comes a new collection of possible data artifacts. Proper identification and understanding of these potential problems will alleviate confusion in the interpretation and utilization of dual-polarization data. In this chapter, we discuss some of the most common artifacts present in dual-polarization data, their effect on data quality, and their possible uses.

#### 1. Attenuation / Differential Attenuation

Attenuation is the extinction of the transmitted signal as it propagates through a medium. Power is removed from the propagating signal and dissipated as thermal energy within the hydrometeors. The specific attenuation (in dB km<sup>-1</sup>) of the horizontally polarized signal by perfectly oriented hydrometeors is given by

$$A_H = 8.686\lambda \int_0^{\infty} \text{Im}\{f_b^{(0)}\} N(D) dD \quad , \quad (3.1)$$

and is a function of the imaginary part of the forward complex scattering amplitude  $f_b^{(0)}$ . In the Rayleigh approximation, recall that

$$f_b^{(0)} = f_b^{(\pi)} = \frac{\pi^2 D^3}{6\lambda^2} \frac{1}{L_b + \frac{1}{\epsilon - 1}} \quad . \quad (3.2)$$

Therefore,  $A_H \propto \lambda^{-1}$ . This inverse dependence on radar wavelength means that higher-frequency (shorter-wavelength) radar signals suffer from more attenuation in rain than lower-frequency (longer-wavelength) systems. A secondary reason that smaller-

wavelength radars suffer more attenuation is that the imaginary part of the complex dielectric function  $\varepsilon$  is larger for shorter wavelengths (at a given temperature; see Appendix A). The National Weather Service WSR-88D radar network operates at S band, or at about 11-cm wavelength, so attenuation and differential attenuation typically are not major concerns. However, it can be observed in some extreme cases, such as when the beam propagates through the supercell storm in Figure 1. Specific differential attenuation is the difference in attenuation between the horizontally- and vertically-polarized channels:

$$A_{DP} = 8.686\lambda \int_0^{\infty} \text{Im}\{f_b^{(0)} - f_a^{(0)}\} N(D) dD \quad . \quad (3.3)$$

Differential attenuation causes a decrease in  $Z_{DR}$ , and is especially noticeable in Fig. 3.1 as the down-range  $Z_{DR}$  values drop below -3 dB. Differential attenuation is also evident in Figure 3.2. Notice the increased differential propagation phase in this area; the propagation phase shift  $\Phi_{DP}$  is proportional to the real part of the complex forward scattering amplitudes. Thus, regions experiencing attenuation often exhibit large  $\Phi_{DP}$ . Because phase measurements are unaffected by attenuation,  $\Phi_{DP}$  is extremely useful for correction of attenuation and differential attenuation (e.g., Bringi et al. 1990; Testud et al. 2000; Snyder et al. 2010; Gu et al. 2011; Borowska et al. 2011a).

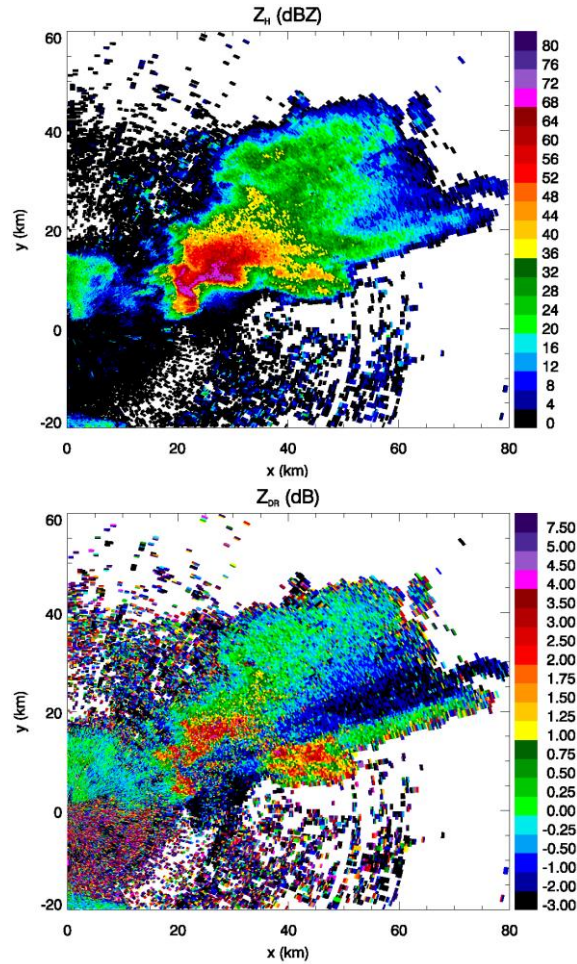


Fig. 3.1: Two-panel plot of  $Z_H$  (top) and  $Z_{DR}$  (bottom) from the polarimetric WSR-88D radar near Huntsville, AL (KHTX) collected on 2 March 2012, at 2254 UTC. Data were sampled at the  $0.5^\circ$  elevation angle. The example shows differential attenuation, evident as the swath of negative  $Z_{DR}$  values downrange of the supercell storm.

## 2. Nonuniform Beam Filling

Regions of differential attenuation are often coincident with regions of radially-oriented  $\rho_{hv}$  reductions (Fig. 3.2). Though often confused with attenuation<sup>3</sup>, this artifact is a result of nonuniform beam filling. Beam broadening with range can lead to inhomogeneous filling of the sampling volume (Fig. 3.3). In the event that there are large cross-beam gradients of  $\Phi_{DP}$  within the radar sampling volume,  $\rho_{hv}$  is reduced

<sup>3</sup> Recall that  $\rho_{hv}$  is not affected by attenuation.

(e.g., Ryzhkov 2007). This reduction in  $\rho_{hv}$  occurs because of the spread of  $\Phi_{DP}$  values within the sampling volume, which is analogous to the reduction in  $\rho_{hv}$  associated with the presence of Mie scatterers that produce nonzero differential phase shift upon backscatter ( $\delta$ ). Recall that a diversity of differential phase within the sampling volume reduces the correlation coefficient  $\rho_{hv}$ . In addition, large cross-beam gradients in  $Z_H$  or  $Z_V$  can lead to biases in  $Z_{DR}$ ,  $\Phi_{DP}$ , and  $\rho_{hv}$  (Ryzhkov 2007).

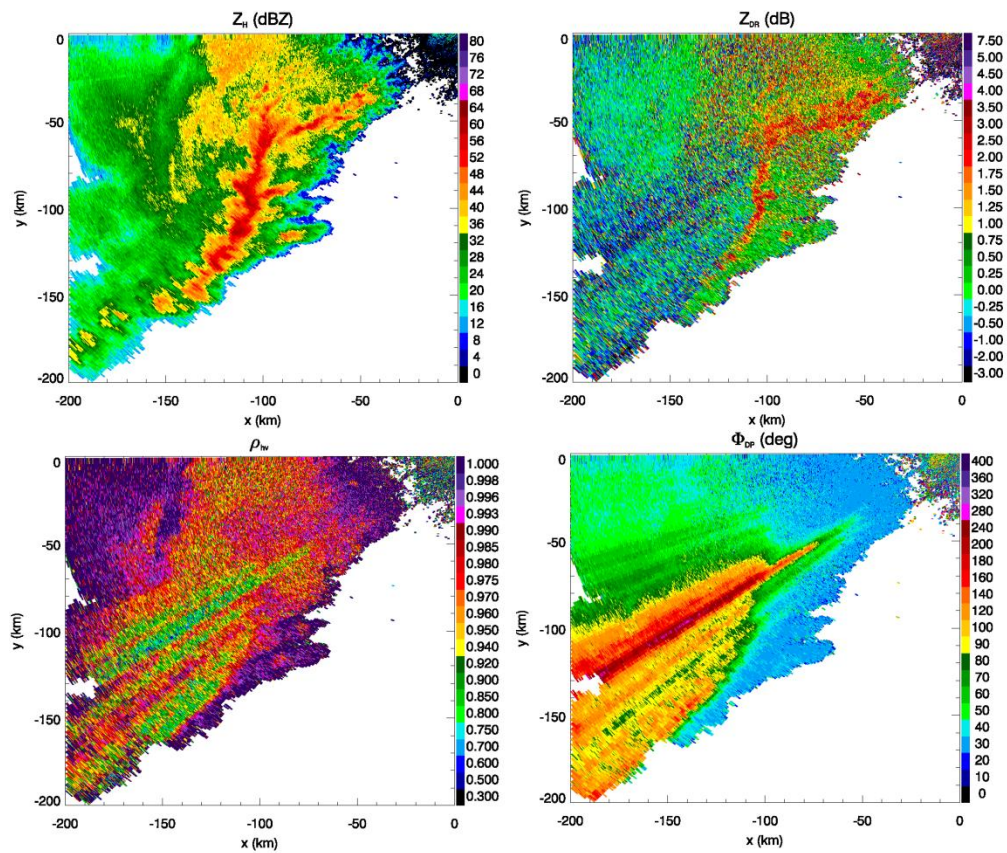


Fig. 3.2: Four-panel display of  $Z_H$  (top left),  $Z_{DR}$  (top right),  $\rho_{hv}$  (bottom left), and  $\Phi_{DP}$  (bottom right), collected with the polarimetric WSR-88D radar near Memphis, TN (KNQA) on 1 February 2012, at 2215 UTC. Data show the effects of nonuniform beam filling, especially in the radial streaks of reduced  $\rho_{hv}$ , as well as differential attenuation in  $Z_{DR}$ .

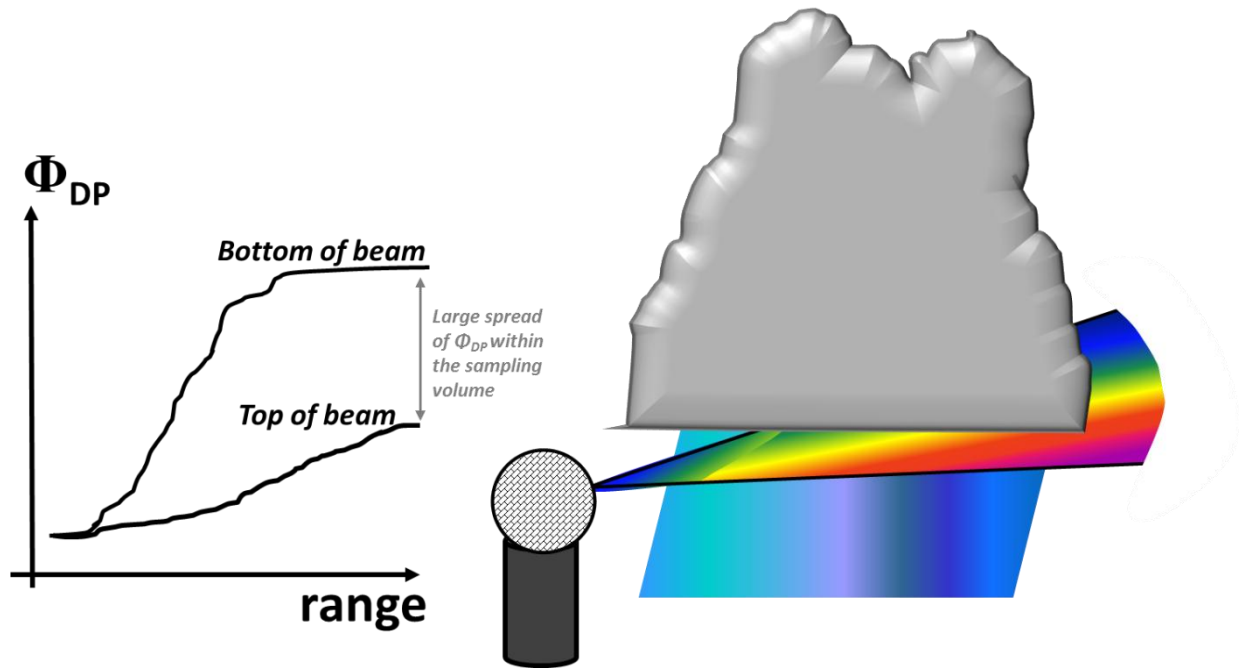


Fig. 3.3: Schematic illustrating nonuniform beamfilling (NBF). In this example, the bottom portion of the beam intercepts heavy rain characterized by large  $\Phi_{DP}$  values while the top of the beam intercepts ice-phase particles (with low  $\Phi_{DP}$ ) above the freezing level. This large spread of  $\Phi_{DP}$  results in a reduction of  $\rho_{hv}$ .

Nonuniform beam filling is common when convective storms occur at large distances from the radar. The reduction in  $\rho_{hv}$  causes increased statistical fluctuations in all polarimetric variables. The reduced data quality leads to a deterioration of quantitative precipitation estimates and hydrometeor classification. The latest version of the hydrometeor classification algorithm (Park et al. 2009) accounts for regions of reduced signal quality, but meteorologists should be aware of these areas when interpreting polarimetric radar measurements.

### 3. Depolarization streaks

In the presence of strong electric fields in the upper regions of storms, small ice crystals may align with the electric field. This phenomenon has been observed with

polarimetric radars that transmit circularly-polarized waves (e.g., Hendry and McCormick 1976; Kreihbel et al. 1996) and linearly-polarized waves (e.g., Caylor and Chandrasekar 1996; Metcalf 1997; Ryzhkov and Zrnić 2007; Hubbert et al. 2010b; Palmer et al. 2011). The common alignment of the crystals lasts until a lightning discharge substantially reduces the electric field intensity, whereupon the crystals return to more typical orientations (generally, with their larger dimension more-or-less aligned in the horizontal). Crystals aligned in an electric field that is neither purely horizontal or vertical in orientation can produce a peculiar artifact in polarimetric measurements made with radars operating in the simultaneous transmission and reception mode, such as the WSR-88D (Ryzhkov and Zrnić 2007; Hubbert et al. 2010a,b; Zrnić et al. 2010a). Polarimetric radars operating in a mode of alternating transmission and reception are immune to this type of artifact.

The artifact appears as radial “streaks” of positive or negative  $Z_{DR}$  (e.g., Figure 3.4) generally at higher elevation angle scans where the radar is sampling ice hydrometeors. These “depolarization streaks” are not visible in the  $\rho_{hv}$  fields, but are sometimes coincident with discernable increases in  $\Phi_{DP}$  (because of crystal anisotropy). A necessary condition for these streaks to appear is a nonzero phase  $\psi = \Phi_t + \phi_{dp}/2$ , where  $\Phi_t$  is the system phase upon transmission and  $\phi_{dp}$  is the intrinsic differential phase shift along the interceding medium. In many cases, the transmitted wave propagates through rain at lower altitudes before entering the ice-phase region, acquiring nonzero  $\phi_{dp}$ , so this condition is satisfied.

When the transmitted wave enters the depolarizing medium (i.e., the oriented ice crystals), the electromagnetic wave becomes progressively depolarized, as depicted in

the schematic in Figure 3.5. Once the signal is depolarized, the *remainder of the data* downrange of the point of depolarization is compromised. This artifact inhibits the usefulness of  $Z_{DR}$  for quantitative precipitation estimation and hydrometeor classification. However, these depolarization streaks, though a detriment to quantitative precipitation estimation and hydrometeor classification, can serve as a useful indicator of the presence of a relatively strong electric field (i.e., sufficiently strong to orient low-inertia crystals). Though the presence of such streaks does not always indicate an imminent lightning discharge, further research may determine their applicability as a lightning forecasting tool. Additionally, the generation of electric charge requires rimed particles, implying the presence of supercooled liquid water. Localization of areas of ongoing riming, especially in embedded convection within more widespread stratiform precipitation, may be useful to indicate conditions favorable for aircraft icing. These and other applications of depolarization streaks remain to be investigated.

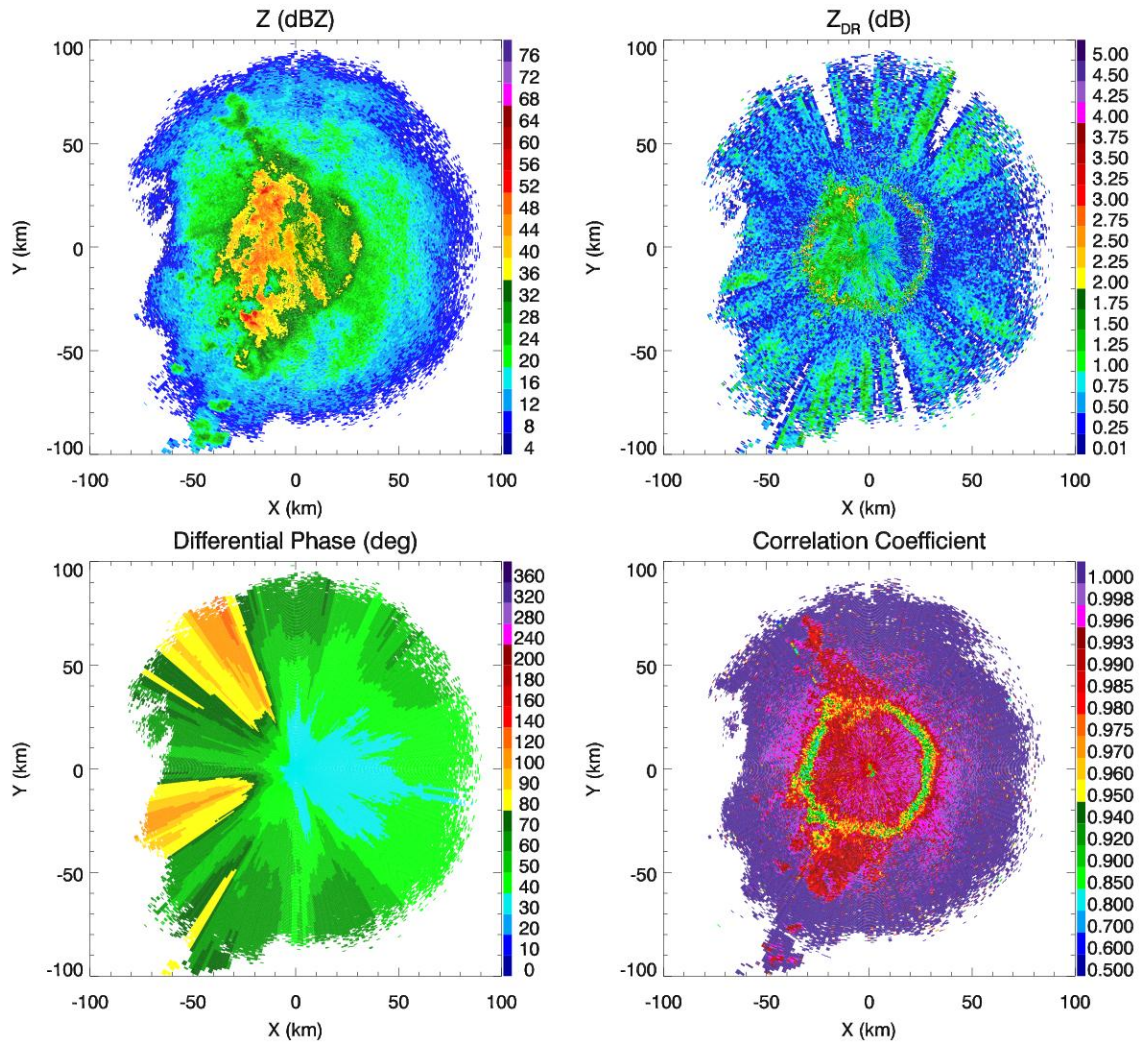


Fig. 3.4: Four-panel display of  $Z_H$  (top left),  $Z_{DR}$  (top right),  $\Phi_{DP}$  (bottom left), and  $\rho_{hv}$  (bottom right). Shown is an example of depolarization streaks, from Tropical Storm Erin (19 August 2007, 0856 UTC). Data were collected with the research WSR-88D radar (KOUN) in Norman, OK at  $8.0^\circ$  elevation.



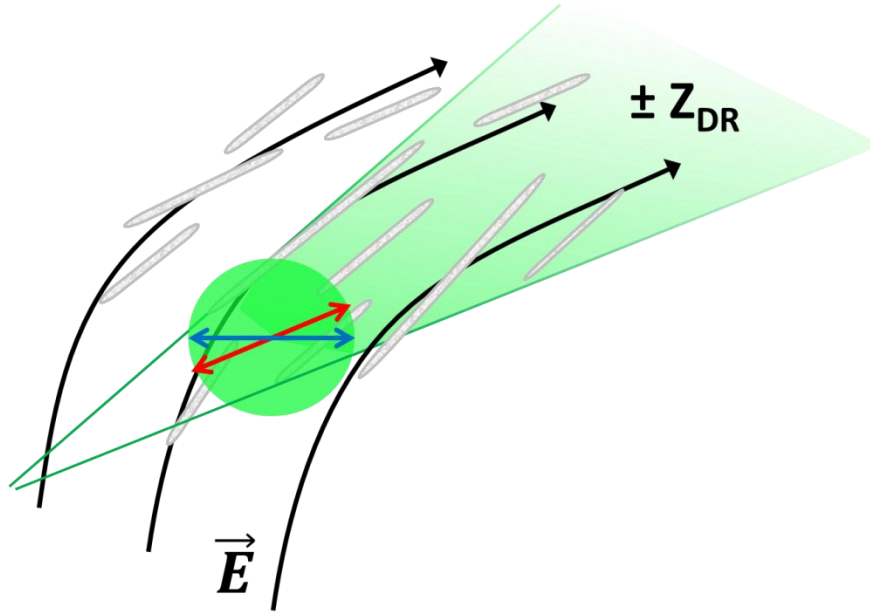


Fig. 3.5: Cartoon illustrating the depolarization of the signal by crystals oriented in an electric field ( $\vec{E}$ ). The original polarization of the transmitted wave (blue, only H-polarization is shown) is depolarized by the canted ice crystals, changing the polarization state of the propagating wave (red vector). From the moment of depolarization in the canted medium (green circle), the rest of the signal further along the radial is compromised, evident as a radial streak of positive or negative  $Z_{DR}$ . The sign of  $Z_{DR}$  depends on the accumulated  $\Phi_{DP}$  along the propagation path leading up to the canted crystals, the system differential phase upon transmission, and the orientation angle of the crystals (Ryzhkov and Znić 2007).

#### 4. Polarimetric Three-Body Scattering Signature (PTBSS)

The three-body scattering signature (TBSS; Znić 1987; Wilson and Reum 1988) in the  $Z_H$  field has been used to indicate the presence of hail (e.g., Lemon et al. 1998). The signature appears as a radially-oriented “spike” of weak  $Z_H$  protruding from the far side (relative to the radar) of the storm. It occurs when electromagnetic radiation scattered off hailstones reflects off the ground, then scatters again off the hailstones and towards the radar. In polarimetric radar observations, the near-storm portion of the TBSS is often observed to have extremely large  $Z_{DR}$  values ( $> 6$  dB) and very low  $\rho_{hv}$  ( $< 0.5$ ) whereas the downrange portion tends to have low  $\rho_{hv}$  and negative  $Z_{DR}$  (Fig. 3.6).

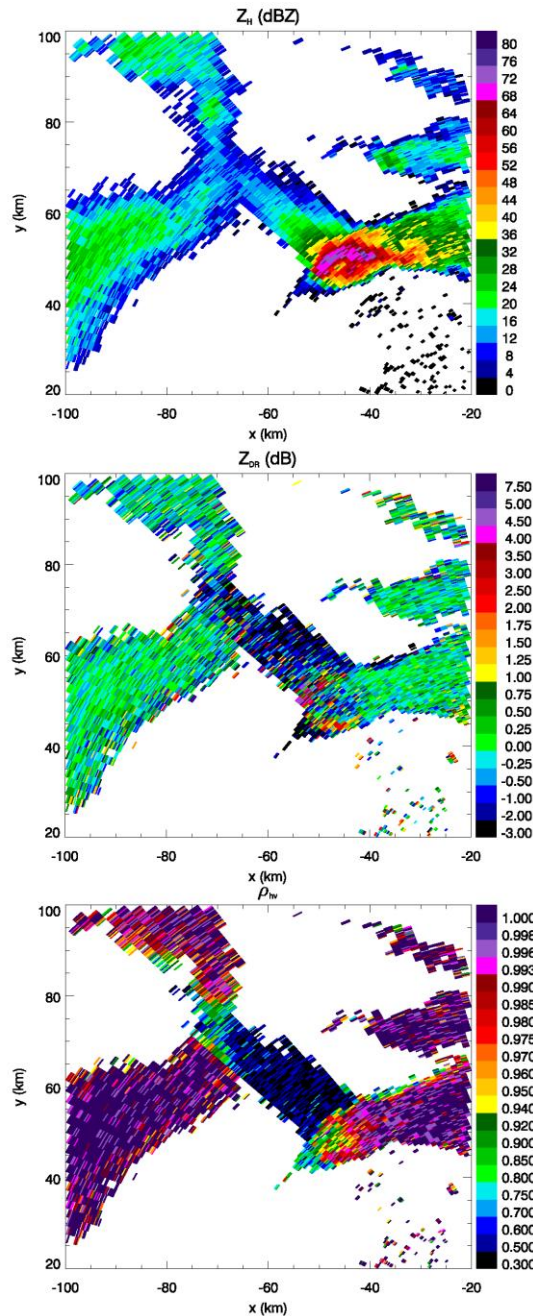


Fig. 3.6: Three-panel display of  $Z_H$  (top),  $Z_{DR}$  (middle), and  $\rho_{hv}$  (bottom) from the polarimetric WSR-88D radar near Knoxville, TN (KMRX). Shown is an example of a polarimetric three-body scattering signature (PTBSS), observed on 2 March 2012 at 2318 UTC, at elevation  $2.4^\circ$ . The PTBSS extends nearly 50 km behind the hail core. Note the large positive  $Z_{DR}$  ( $> 4$  dB) just beyond the hail core, followed by predominantly negative values downrange. Values of  $\rho_{hv}$  are extremely low ( $< 0.6$ ) throughout.

The cause of the large  $Z_{DR}$  associated with the PTBSS can be explained within the framework of simple scattering theory. The received  $Z_{DR}$  from the PTBSS can be considered the product of three factors, as explained by Picca and Ryzhkov (2012):

$$Z_{dr} \approx \frac{P_H}{P_V} \times \frac{\sigma_H}{\sigma_V} \times \frac{L_H}{L_V} \quad . \quad (3.4)$$

The first factor ( $P_H / P_V$ ) characterizes the difference between radiation patterns of the scatterer at H and V polarizations. The second factor ( $\sigma_H / \sigma_V$ ) is the ratio between radar cross-sections (at H and V polarizations) of the ground or underlying surface beneath the hail core. The third factor is a ratio of attenuation factors at H and V polarization ( $L_H / L_V$ ) that characterizes losses due to propagation through the hailstones as well as scatter off the ground or underlying surface. Note that each of these factors is a function of the angle  $\theta$  of the radiation path between the hail core and the ground (measured from nadir).

In the Rayleigh scattering approximation, a hailstone can modeled as horizontally- and vertically-oriented electric dipoles aligned with the major and minor axes of the particle, which is assumed to be spheroidal in shape. When illuminated by incident microwave radiation, the dipoles that are aligned with the incident radiation polarization vector are excited and emit secondary radiation. The radiation emitted by the excited horizontal (vertical) dipole is horizontally- (vertically-) polarized. In general, the radiation patterns at H and V polarizations are different. For example, the V dipole does not radiate in the downward direction, but only at oblique angles ( $\theta \neq 0^\circ$ ). In contrast, the H dipole does radiate directly downward (Fig. 3.7, part I). Thus, the radiation scattered in the nadir direction ( $\theta = 0^\circ$ ) has no vertically-polarized component, resulting in infinite  $Z_{DR}$  (Kumjian et al. 2010b).

In reality, of course, the PTBSS is produced by downscatter paths over a conical region (e.g., Zrnić 1987). Thus, V-polarized component of the downscattered signal is nonzero, though still much smaller than the H-polarized component. This produces large (but finite) bistatic  $Z_{DR}$  (e.g., Aydin et al. 1998). In contrast, at these downscattered paths close to nadir the ratio of ground cross sections  $\sigma_H / \sigma_V$  is close to one, assuming the absence of any interesting geological features (Fig. 3.7, part II). Similarly, the loss factor  $L_H / L_V$  is also near unity (Fig. 3.7, part III). Thus, the PTBSS  $Z_{DR}$  is determined primarily by the factor  $P_H / P_V$ , which is expected to be very large for the reasons explained above. Because the downscattered paths at angles near nadir are shorter than those at larger angles, the highest  $Z_{DR}$  is expected to be located nearest the hail core. Indeed, observations of PTBSSs reveal that the highest  $Z_{DR}$  signatures are separated from the presumed hail core (maximum in  $Z_H$ ) by ranges comparable to the height AGL of the sampled hail core (Kumjian et al. 2010b). Extended TBSSs indicate contributions from downscattered paths at larger  $\theta$ . At such larger  $\theta$ , the bistatic  $Z_{DR}$  (that is, the ratio  $P_H / P_V$ ) decreases (Aydin et al. 1998). Similarly, the ratios  $L_H / L_V$  and  $\sigma_H / \sigma_V$  decrease with increasing  $\theta$  (e.g., Ulaby et al. 1982; Hubbert and Bringi 2000; Picca and Ryzhkov 2012). This can lead to negative  $Z_{DR}$  values in the downrange portions of PTBSSs (Fig. 3.7).

The PTBSS can be especially useful for hail detection when the  $Z_H$  TBSS is obfuscated by the presence of other storms. However, the very large  $Z_{DR}$  values should not be mistaken for a  $Z_{DR}$  column. Though  $Z_{DR}$  columns can be coincident with reduced  $\rho_{hv}$ , the nonmeteorological values associated with the PTBSS can be used to discern between the two signatures. Also note that the PTBSS only appears on the rear

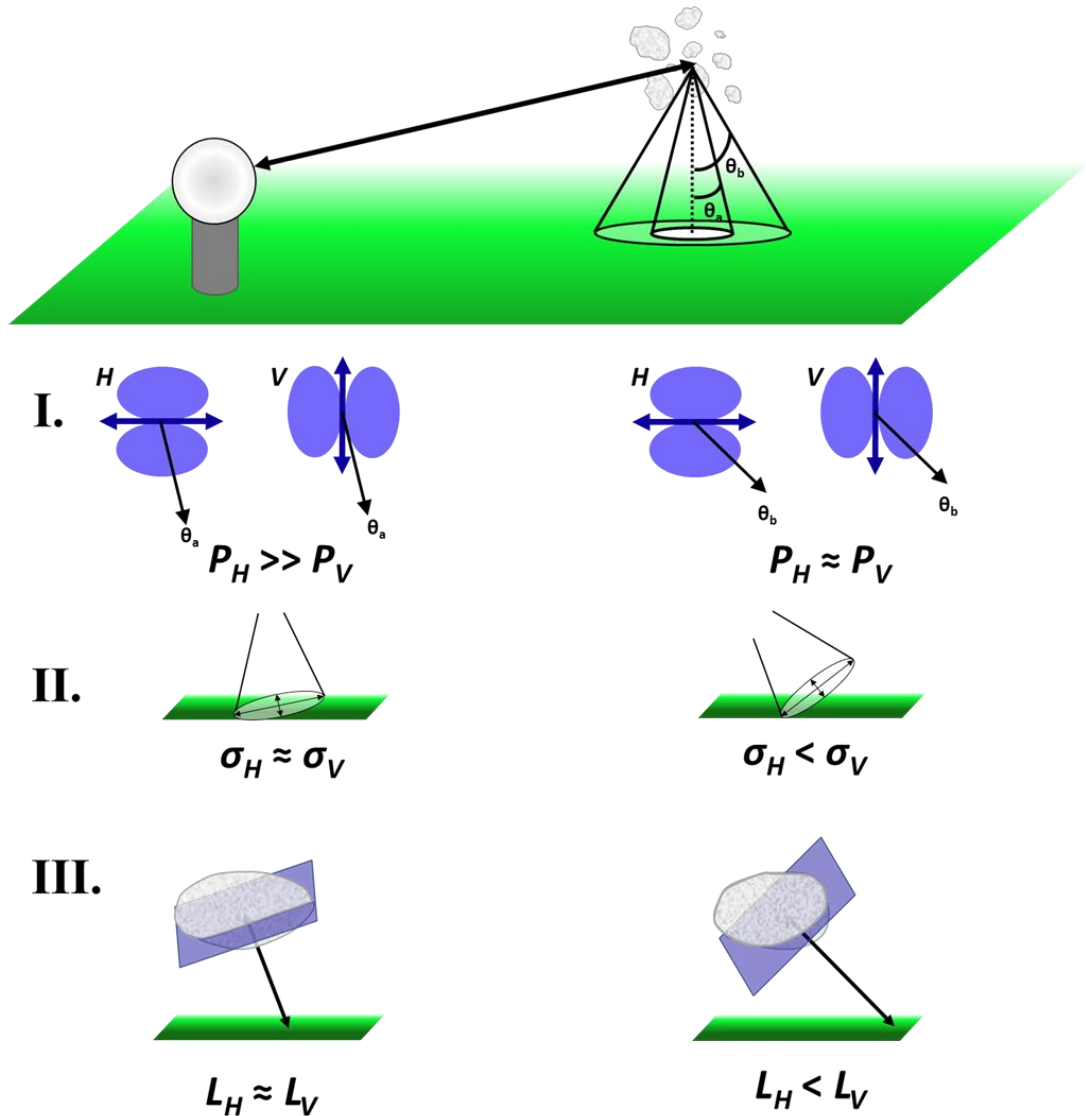


Fig. 3.7: Schematic illustrating the polarimetric TBSS. In the top panel, selected paths of electromagnetic radiation are shown. Radiation scatters off the hailstones and towards the ground at two off-nadir angles ( $\theta_a$  and  $\theta_b$ ). The measured  $Z_{DR}$  in the PTBSS is the product of three ratios: I. The “bistatic  $Z_{DR}$ ” (Aydin et al. 1998), which is the ratio of the powers of the radiation scattered downward by the hailstones ( $P_H/P_V$ ); II. The ratio of the ground backscattering cross section at H and V polarizations ( $\sigma_H / \sigma_V$ ); and a factor representing the differential attenuation suffered by the signal as it propagates through the hailstones and off the ground ( $L_H / L_V$ ). The left column schematically shows these three factors for  $\theta_a$ , close to nadir, whereas the right column shows the three factors for  $\theta_b > \theta_a$ . Adapted from Picca and Ryzhkov (2012), with changes.

side of the storm (i.e., the downrange side). It is unlikely that the PTBSS can be used as an indicator of hail *size*, just as the TBSS in  $Z_H$  is ambiguous (Zrnić et al. 2010b). The explanation above considered hailstone radiation patterns in the Rayleigh approximation. Even at S band, hailstones larger than about 2 – 3 cm in diameter are outside of the valid limits of the Rayleigh approximation, in which case their radiation patterns are produced by higher-order multipoles excited by the incident radiation. Thus, though larger hailstones may be able to downscatter more radiation, their intrinsic bistatic  $Z_{DR}$  is much lower than the smaller hailstones (that have radiation patterns more closely approximated by two dipoles aligned with their principle axes), as seen in Figure 3.8.

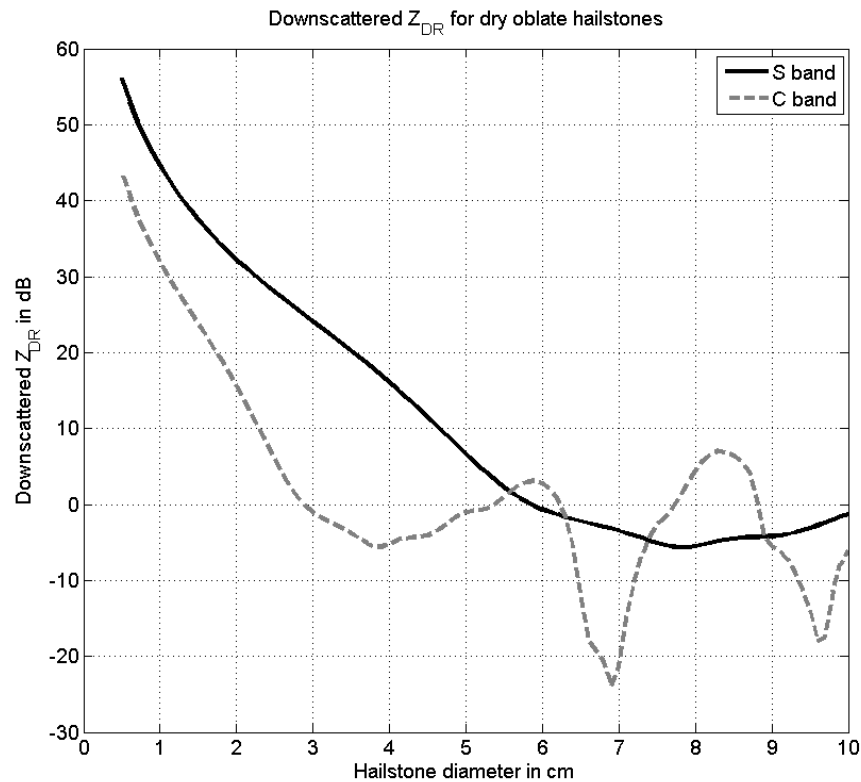


Fig. 3.8: Bistatic  $Z_{DR}$  produced by dry, oblate hailstones (axis ratio 0.8) for S and C bands (black solid and gray dashed lines, respectively). From Kumjian et al. (2010b).

## Chapter 4: The Impact of Raindrop Conduction and Temperature on the Polarimetric Radar Variables.

### 1. Introduction

We saw in the background sections that some of the dual-polarization radar variables are quite sensitive to the temperature of raindrops. If a temperature difference exists between a raindrop and the surrounding air, enthalpy is transferred between the drop and air in an attempt to minimize the temperature gradient. Because the air and the raindrop are in direct contact, such a diffusion of thermal energy is considered conduction.

In most electromagnetic scattering computations, the raindrop temperature is simply taken as the environmental temperature. This chapter presents a simple model of thermal conduction between the raindrops and the air to determine the temperature of raindrops as they fall in an environment characterized by a vertical gradient of temperature (i.e., lapse rate). Such a model can be used to efficiently provide a better estimate of raindrop temperature for electromagnetic scattering calculations, which could be especially relevant for shorter-wavelength radars.

### 2. Model description

The balance equation governing the transfer of thermal energy between a raindrop and its environment is given as (e.g., Pruppacher and Klett 1979):

$$\left. \frac{dq}{dt} \right|_{\text{conduction}} = 4\pi r k_a \bar{f}_h (T - T_{\text{drop}}), \quad (4.1)$$

where  $r$  is the drop radius,  $k_a$  is the thermal conductivity of air,  $\bar{f}_h$  is the ventilation coefficient for thermal energy transfer,  $T$  is the temperature of the ambient environment, and  $T_{drop}$  is the temperature of the surface of the raindrop. Expressions for the thermal conductivity and ventilation coefficient are provided in Chapter 6. If there are no other sources of heating or cooling of the raindrop (e.g., no evaporation/condensation), then we can express

$$\left. \frac{dq}{dt} \right|_{conduction} = \left. \frac{dq}{dt} \right|_{total} = mc_w \frac{dT_{drop}}{dt}, \quad (4.2)$$

where  $m$  is the mass of the drop and  $c_w$  is the specific heat capacity of liquid water (4186 J kg<sup>-1</sup> K<sup>-1</sup>). *If we assume the environmental temperature  $T$  does not change in time*, then we may include  $T$  in the right hand side of eqn. (4.2):

$$\left. \frac{dq}{dt} \right|_{conduction} = \left. \frac{dq}{dt} \right|_{total} = mc_w \frac{d}{dt} (T_{drop} - T). \quad (4.3)$$

Substituting eqn. (4.1) into eqn. (4.3),

$$mc_w \frac{d}{dt} (T_{drop} - T) = 4\pi r k_a \bar{f}_h (T - T_{drop}). \quad (4.4)$$

Re-arranging the terms and considering the raindrops as spheres such that

$$m = \frac{4}{3} \pi \rho_w r^3,$$

we arrive at a simple, separable ordinary differential equation for the temperature difference between the raindrop and its environment  $\Delta T = T_{drop} - T$ :

$$\frac{d \ln \Delta T}{dt} = - \frac{3k_a \bar{f}_h}{r^2 c_w \rho_w}. \quad (4.5)$$

Eqn. (4.5) can be easily integrated to obtain an expression for the temperature difference  $\Delta T$  as a function of time:



$$\Delta T(t) = \Delta T_0 \exp\left(-\frac{t}{\tau_c}\right), \quad (4.6)$$

where  $\Delta T_0$  is the initial temperature difference between the raindrop and its environment, and the relaxation time  $\tau_c$  is given by

$$\tau_c = \frac{r^2 c_w \rho_w}{3k_a \bar{f}_h}, \quad (4.7)$$

which is on the order of several seconds for most drop sizes. It can be seen that for  $t \gg \tau_c$ ,  $\Delta T \rightarrow 0$ . In the case of evaporation or condensation, the thermal energy balance equation for the drop contains an additional term describing the latent enthalpy of vaporization associated with mass diffusion. As shown in Pruppacher and Klett (1997), this additional term results in an equilibrium  $\Delta T$ ; stated mathematically, as  $t \rightarrow \infty$ ,  $\Delta T \rightarrow \kappa \neq 0$ . Thus, the case of simple conduction and no latent heating/cooling should be considered as the most conservative case, or minimum bound of the temperature difference between the raindrop and the surrounding environment.

The theoretical framework of Pruppacher and Klett (1997) considers a raindrop suddenly placed in an environment with ambient temperature  $T > T_{drop}$ . Though idealized, it is possible to relate this treatment to a physical analog in the real atmosphere. In cold microphysical processes, raindrops may originate from the melting of ice particles such as snow, graupel, or hail. As a particle is melting, it consists of liquid water and solid ice in some combination and has a temperature of 0 °C, as all external thermal energy is applied to latent heating associated with melting. Because the process of melting is of finite duration, the melting particle may fall to levels where  $T > 0$  °C before all ice has melted. The moment it becomes a purely liquid particle, the

raindrop temperature may begin to adjust to the environmental temperature through conduction, if such a temperature difference exists.

However, in most cases of raindrops falling in the atmosphere, the assumption of environmental temperature constancy is not valid. This is because of environmental vertical temperature gradients, which almost always exist. In the Lagrangian reference frame of the raindrop, this is equivalent to a time-varying environmental temperature. We can change the independent variable from time  $t$  to height  $z$  by dividing the equations by  $dz/dt = v_t$ , the terminal fallspeed of the raindrops. This provides an expression for drop temperature as a function of height,

$$\frac{dT_{drop}}{dz} = \frac{1}{v_t \tau_c} (T - T_{drop}). \quad (4.8)$$

Equation (4.8) is solved numerically in a simple one-dimensional bin model. The vertical resolution is 1.0 m. Independent calculations are made for each raindrop size bin, ranging from 0.5 to 8.0 mm in 0.1-mm increments. The drops start at the top of the domain at 0 °C, whereas the temperature is  $> 0$  °C at the top of the domain and increases towards the ground. The thermodynamic profiles can be prescribed based on an assumed lapse rate, or initialized with an observed sounding interpolated onto the model grid space.

### 3. Model Results

Figure 4.1 shows the results of an idealized simulation of the temperature of raindrops falling 2 km through an environment with a lapse rate of  $6.5$  °C  $\text{km}^{-1}$ . The initial drop temperature at the top of the domain is 0 °C, and the environmental temperature at the top of the domain is 3 °C. It is clear that the larger drops warm

slower than the smaller drops. Note that the smallest drop size shown (0.5 mm) adjusts to the environmental temperature essentially instantaneously, and thus the far left of the figure can be considered the environmental temperature as well.

The difference ( $\Delta T$ ) between the raindrop temperature and the environmental temperature (Figure 4.2) clearly shows the dependence of drop size. Whereas the smaller raindrops ( $< 2.5$  mm) fall slowly enough and are small enough in size to be able to adjust to the environmental temperature, large drops ( $> 5$  mm) are unable to “catch up” to the changing environmental temperature, maintaining a temperature at least 1.5 °C colder than their surroundings.

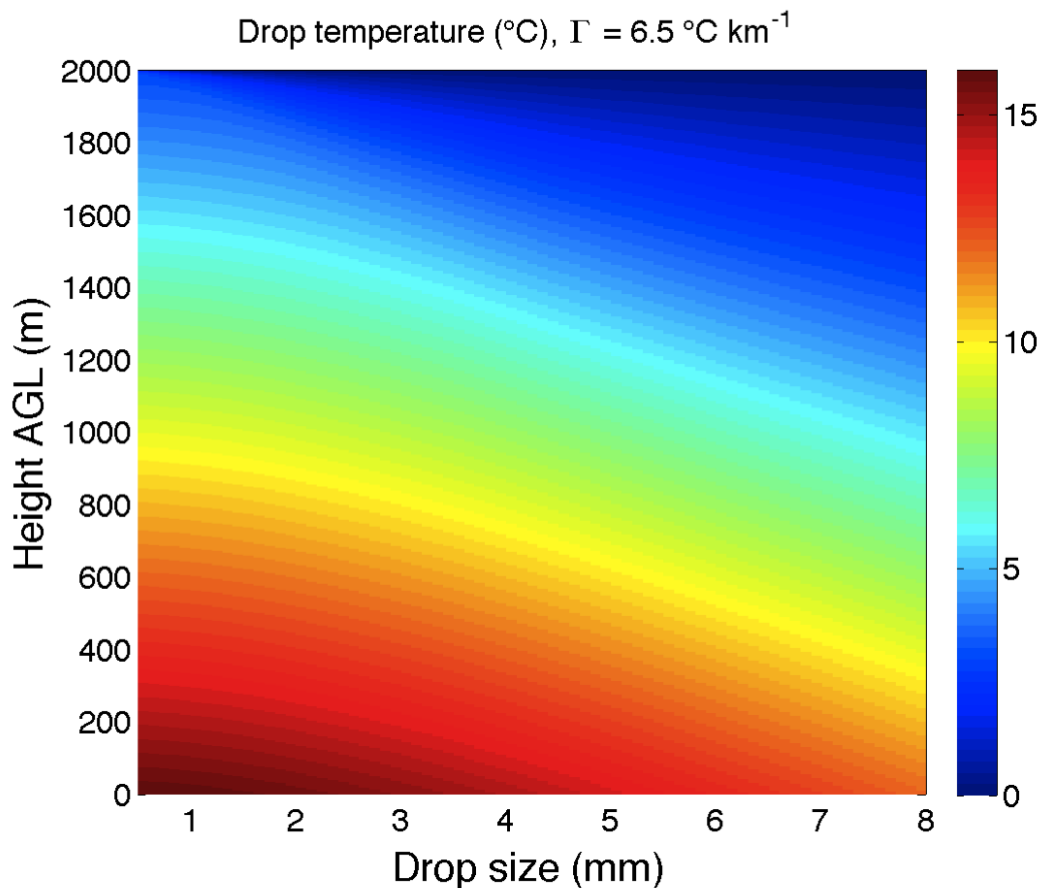


Fig. 4.1: Temperature of raindrops (°C, color shading) as a function of drop size (mm) and height (m AGL). Drops were initialized at the top of the domain with temperature 0 °C. The lapse rate ( $\Gamma$ ) is  $6.5 \text{ }^\circ\text{C km}^{-1}$ , with initial temperature 3 °C at the top of the domain.

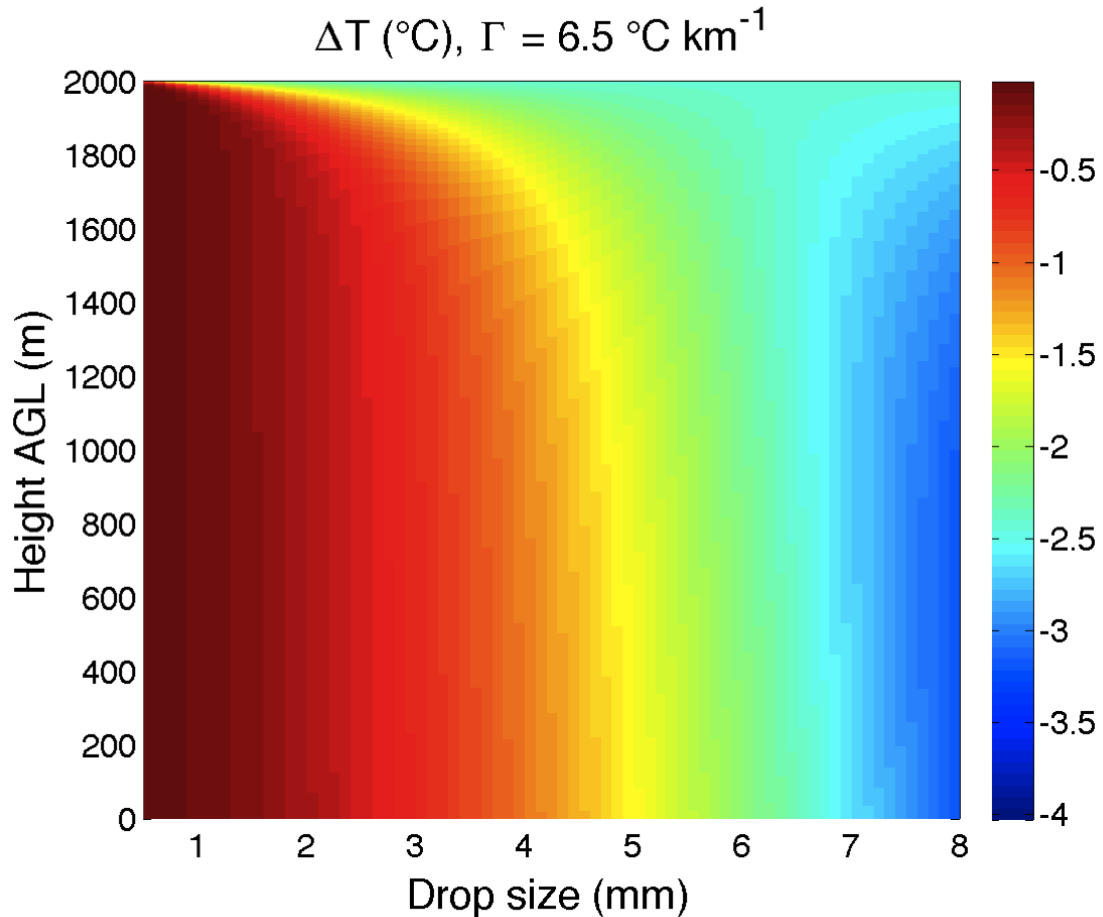


Fig. 4.2: As in Fig. 4.1, but the difference between the drop temperature and air temperature ( $\Delta T$ ) is shown. A negative difference indicates that the drops are colder than the ambient air at that level.

If allowed to fall about 2 km, all drop sizes attain an equilibrium temperature difference with respect to the ambient environmental temperature. This equilibrium temperature difference is independent of the initial temperature of the raindrops prescribed aloft (i.e., top boundary condition), but is a function of both the drop size and the environmental lapse rate. For a given environmental lapse rate, drops attain an equilibrium temperature difference  $\Delta T$  that increases in magnitude with lapse rate *and* drop size (Fig. 4.3). For drops smaller than about 2.5 mm in diameter, all realistic atmospheric lapse rates result in an equilibrium  $\Delta T$  of less than 1  $^{\circ}\text{C}$  in magnitude.

However, larger drops and steep lapse rates can combine to yield large values of equilibrium  $\Delta T$  ( $< -3$  to  $-6$  °C). Therefore, large raindrops are always *colder* than the environmental temperature (given that environmental temperature decreases with height).

Recall that these calculations ignore the effects of raindrop evaporation, which acts against the thermal energy transfer of conduction and therefore would *enhance the temperature differences*. Thus, these calculations can be considered *conservative estimates*<sup>4</sup> of the difference between raindrop temperature and the air temperature.

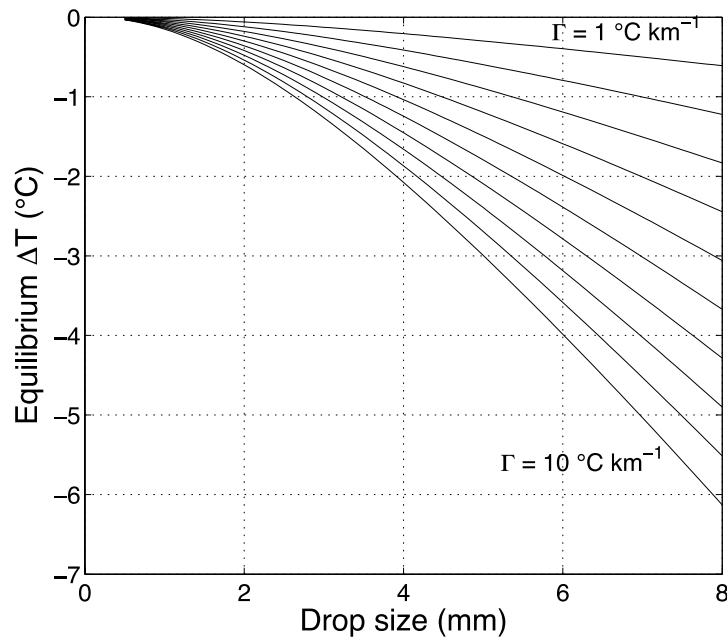


Fig. 4.3: Equilibrium temperature difference ( $\Delta T$  in °C) as a function of drop size (in mm) for lapse rates ( $\Gamma$  in °C km<sup>-1</sup>) between 1 and 10 °C km<sup>-1</sup>. All drop sizes attain their equilibrium temperature difference after free fall of about 2 km.

---

<sup>4</sup> Not to be misconstrued as politically conservative estimates about scientific issues, which are generally inaccurate enough as to be discarded.

#### 4. Impact of Temperature on Scattering

The temperature of a particle affects its scattering properties because its complex dielectric factor  $\epsilon$  is temperature (and wavelength) dependent (Fig. 4.4). Expressions for computing the complex dielectric function from Ray (1972) are found in Appendix A. Note that the real part of  $\epsilon$  has a larger dynamic range (as a function of temperature) for shorter radar wavelengths. For these smaller radar wavelengths, where resonances scattering effects are important for large raindrop sizes, these temperature effects can become significant (Fig. 4.5). The raindrop size assumed for calculations presented in Fig. 4.5 is 5.9 mm, which corresponds to the peak resonance in the  $Z_{DR}$  curve at C band. It is clear that  $Z_{DR}$  varies by several dB depending on the raindrop temperature. Similarly, the backscatter differential phase  $\delta$  changes by about 10 degrees in the temperature range shown. Because small raindrops have negligible  $\delta$  at C band, a given distribution of raindrops will produce lower  $\rho_{hv}$  for increased temperature, owing to a larger diversity of  $\delta$  within the radar sampling volume.

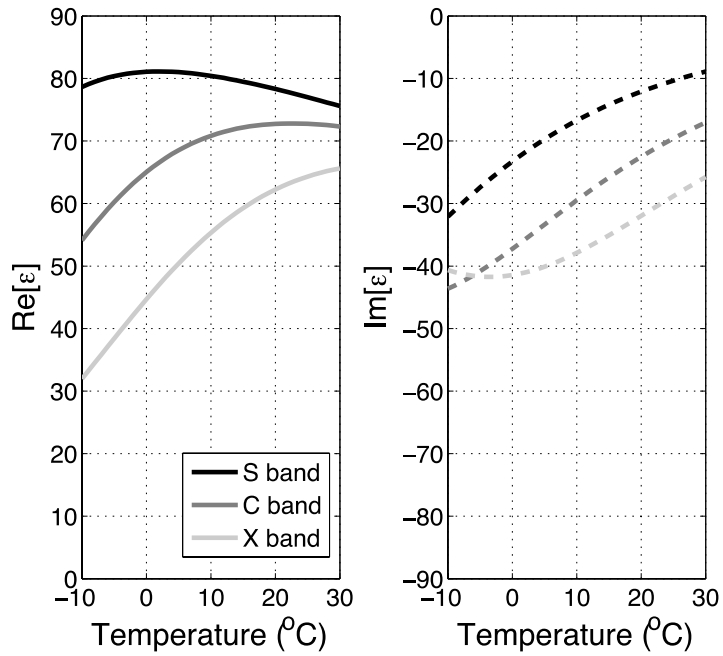


Fig. 4.4: Complex dielectric of liquid water drops as a function of temperature for three radar wavelengths: S, (black curves), C, (dark gray curves) and X (light gray curves). (left) Real part, in solid lines, and (right) imaginary part, in dashed lines.

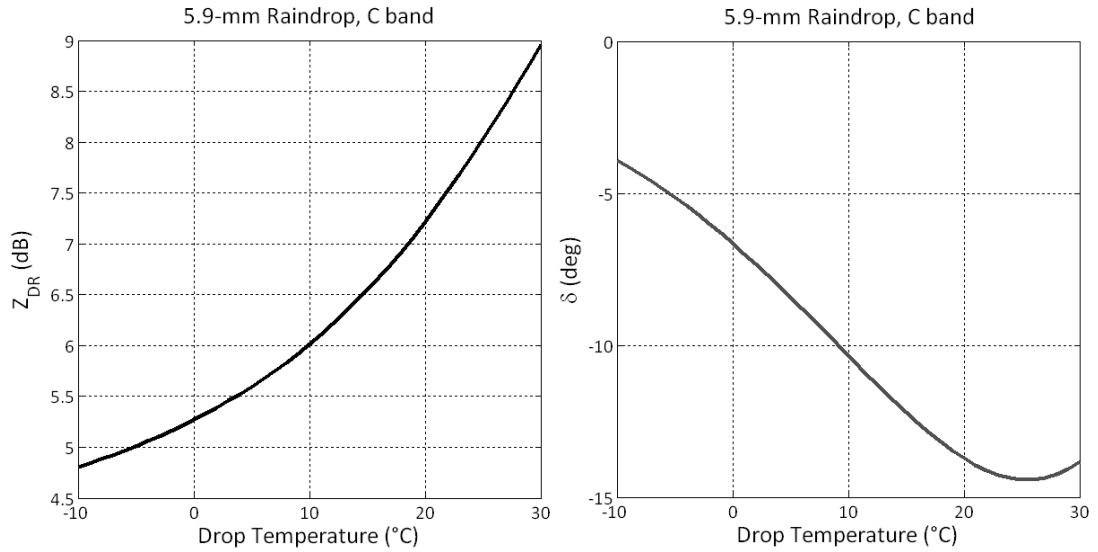


Fig. 4.5:  $Z_{\text{DR}}$  (left) and  $\delta$  (right) as a function of raindrop temperature, computed for a resonance-sized raindrop 5.9 mm in diameter at C band.

## Chapter 5: The Impact of Size Sorting on the Polarimetric Radar

### Variables

Material in this chapter comes from Kumjian and Ryzhkov (2012).

#### 1. Introduction

The onset of precipitation in clouds is the development of particles large enough to sediment relative to cloud droplets and ice crystals. The rate of descent of these precipitation particles is dependent on their mass: larger, heavier particles tend to fall faster than smaller, lighter particles in quiescent conditions. This fall speed difference leads to differential sedimentation of precipitating particles, which explains the frequent appearance of “big drops” beneath developing ordinary convective clouds preceding the onset of heavier precipitation.

Numerous microphysical processes affect the evolution of the raindrop size distribution (DSD) as the drops sediment, including coalescence, breakup, and evaporation. This chapter will focus on size sorting of raindrops; evaporation is treated in Chapter 6, and the collisional processes in Chapter 7. Consider a continuously precipitating cloud. If only hydrometeor fallout is considered, differential sedimentation is transient. This is because, after sufficiently long times, the smallest drops have reached the surface, and all drop sizes occupy all altitudes between the cloud and the ground, thereby eliminating any size sorting. However, in nature, various types of atmospheric flows can *maintain* this otherwise transient size sorting, resulting in prolonged regions of ongoing particle sorting in precipitating storms. For example,



consider the presence of a convective updraft. If upward vertical velocities are sufficiently strong, smaller raindrops may be lofted while larger drops are able to fall against the updraft and reach the ground. The presence of the updraft thus maintains the initial transient size sorting by completely removing the smallest particles from the distribution.

Though undetectable by single-polarization radars, size sorting can have an impact on dual-polarization radar observations. The differential reflectivity factor ( $Z_{DR}$ ), first introduced by Seliga and Bringi (1976), is the logarithmic ratio of received signal powers at horizontal and vertical polarizations. It provides bulk information about the power-weighted shape of scatterers in the radar sampling volume. Because raindrop oblateness increases with increasing size (e.g., Pruppacher and Pitter 1971; Brandes et al. 2004a, 2005),  $Z_{DR}$  in rain is a reflectivity-weighted measure of raindrop size in the sampling volume. Because DSDs altered by size sorting result in regions of the storm with large median drop sizes, polarimetric observations of these regions reveal large  $Z_{DR}$  values. However, in rainfall,  $Z_{DR}$  tends to increase with increasing radar reflectivity factor at horizontal polarization  $Z_H$  (e.g., Sachidananda and Zrnić 1987) because heavier rain tends to have larger concentrations of bigger drops that increase both  $Z_H$  and  $Z_{DR}$ . Thus,  $Z_{DR}$  values alone are not sufficient to diagnose regions of ongoing size sorting. Rather, owing to the narrowing effect of size sorting on DSDs (e.g., Rosenfeld and Ulbrich 2003),  $Z_H$  tends to be relatively low in cases of size sorting. Therefore, observations of relatively low  $Z_H$  and large  $Z_{DR}$ , indicating a DSD skewed to larger drop sizes in relatively low concentrations, may be indicative of ongoing size sorting. The importance of such features led to the inclusion of a “big

drops” category to the polarimetric hydrometeor classification algorithm to be implemented in the nationwide WSR-88D radar network dual-polarization upgrade (e.g., Straka et al. 2000; Park et al. 2009). Note that the regions of small drops “sorted out” also represent a skewed DSD that is a result of size sorting, but such small-drop-dominated distributions may not be as apparent in polarimetric radar data.

Size sorting by updrafts and other mechanisms, including strong vertical wind shear, has been recognized for several decades. One of the earliest works to realize the importance of wind shear on precipitation particle size sorting is that of Marshall (1953). He computed analytic trajectories of particles falling in a sheared flow, determining that linear vertical shear results in parabolic particle trajectories, and realized the importance of the particle’s rate of descent on the slope of the trajectory. Further, he stated “as the precipitation pattern moves past a fixed point on the ground, the first precipitation to arrive should be the fastest falling” (Marshall 1953). In the complete absence of vertical wind shear, Marshall (1953) demonstrated the absence of any continuous precipitation sorting (aside from the initial transient effect), even for vertically homogeneous winds of any magnitude.

Atlas and Plank (1953) also discuss the differential advection of particles in sheared flow and the importance of gravitational sorting of different sized particles. Gunn and Marshall (1955) computed the effect of wind shear sorting on radar reflectivity and rainfall rate. Their simplified computations produced patterns that bear a remarkable resemblance to those produced by the bin models in the present study shown below. In Gunn and Marshall (1955), the largest raindrops are shown at the leading edge of their modeled rain shaft, foreshadowing the impact of size sorting on

$Z_{DR}$  demonstrated herein. Atlas and Chmela (1957) explicitly mention that updrafts can cause additional size sorting of hydrometeors, in addition to wind shear, the latter of which is also mentioned in Hitschfeld (1960). Such conclusions are echoed in later works by Zawadzki and de Agostinho Antonio (1988) and Kollias et al. (2001), which are based on more sophisticated observations and analysis techniques, and that of Battan (1977), which emphasizes the deviation in the DSD from exponential caused by wind shear size sorting.

Sauvageot and Koffi (2000) indirectly hint at size sorting by wind shear as a factor in creating multimodal DSDs in some circumstances. However, their explanation of the appearance of large drops at the leading edge of squall lines invokes overlapping of rain shafts from several convective cells in various stages of growth, but such observations can be explained in much simpler terms by size sorting alone, as shown below. The review by Rosenfeld and Ulbrich (2003) briefly mentions the impact of size sorting on the DSD, as well as the possibility of updrafts affecting the observed DSD at the ground. It is unclear why their schematic indicates a *decrease* in the number of large drops associated with a substantial *increase* in the number of medium-sized drops; the narrowing effect of the DSD is exaggerated to the point of perhaps being inaccurate in their presentation.

Scientific curiosity about and focus on the issue of differential sedimentation and size sorting has been recently reignited by research in bulk microphysics parameterization schemes (e.g., Wacker and Seifert 2001; Milbrandt and Yau 2005a; Dawson et al. 2010; Mansell 2010; Milbrandt and McTaggart-Cowan 2010) and in polarimetric radar observations (e.g., Ryzhkov et al. 2005c; Kumjian and Ryzhkov

2008a, 2009). The purpose of this chapter is to review common size-sorting mechanisms and quantify the impact of such sorting on the polarimetric radar variables with the use of simplistic bin models. Additionally, the inability of simple one- and two-moment bulk microphysics parameterizations to reproduce realistic hydrometeor size sorting is discussed, and errors in the computed polarimetric radar variables owing to the assumptions in such bulk schemes are quantified.

## 2. Size Sorting in Bulk and Bin Model Configurations

Differential sedimentation of precipitation particles arises from differences in fallspeeds of particles of differing size. Observations of raindrops in free fall show that fall speed increases with increasing drop diameter, at least for drops smaller than about 6 mm (e.g., Gunn and Kinzer 1949; Pruppacher and Beard 1970; Fig. 5.1). The polynomial relation between drop size  $D$  (in mm) and fallspeed  $v_t$  ( $\text{m s}^{-1}$ ) presented in Brandes et al. (2002)

$$v_t = -0.1021 + 4.932D - 0.9551D^2 + 0.07934D^3 - 0.002362D^4 \quad (5.1)$$

best matches the historical observational data and more recent observations (e.g., Thurai and Bringi 2005). The other relations used in Fig. 5.1 are summarized in Table 5.1. Note the disagreement of the velocity relations for larger drops ( $> 6$  mm). The power law relation of Atlas and Ulbrich (1977), which was developed for ease of use in analytic and numerical computations, substantially overestimates the fall speed of drops larger than about 4 mm. On the other hand, the velocity relation used in some bulk microphysics parameterization schemes (e.g., Ferrier 1994; Milbrandt and Yau 2005b; originally from Umlinger 1981) slightly underestimates the fall speeds of the largest

drops. Note that other microphysics schemes use a variety of other different fall speed relations, but the present study will consider only those mentioned above.

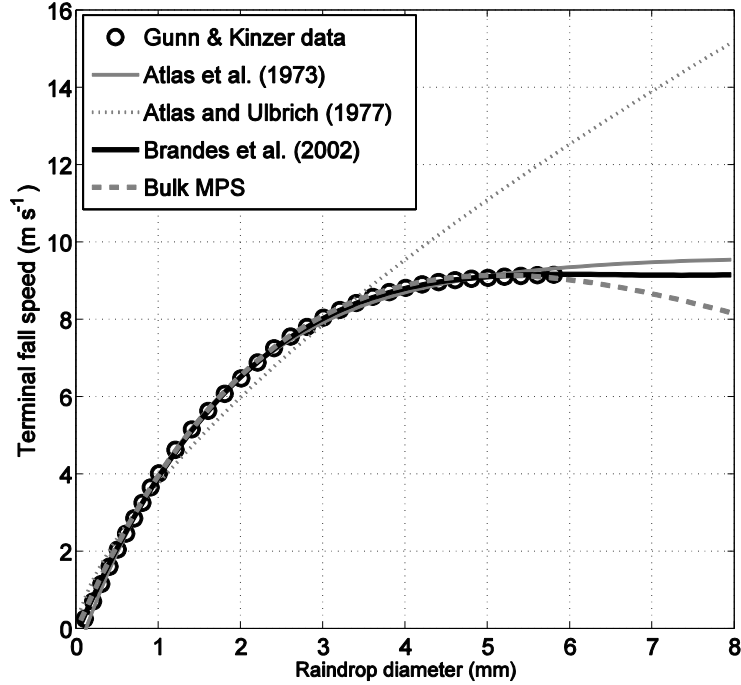


Fig. 5.1: Raindrop terminal fall speed as a function of diameter. Observations of Gunn and Kinzer (1949) are shown as open circle markers. The Atlas et al. (1973) exponential relation (gray solid curve), Atlas and Ulbrich (1977) power law relation (gray dotted line), Brandes et al. (2002) polynomial relation (eqn. 5.1; thick black line), and the functional relation used in bulk microphysics parameterization schemes (“Bulk MPS,” thick gray dashed line, from Uplinger 1981) are overlaid.

Source	Relation
Uplinger (1981); MY05b	$v_t(D) = 4854.0 D \exp(-0.195D)$
Atlas et al. (1973)	$v_t(D) = 9.65 - 10.3\exp(-0.6D)$
Atlas and Ulbrich (1977)	$v_t(D) = 3.78D^{0.67}$
Brandes et al. (2002)	Eqn. (5.1) in text

Table 5.1: Fall speed relations used in Fig. 5.1. In each equation, D is in mm and the fall speed is in m s<sup>-1</sup>.

In bulk schemes, the particle size distributions are assumed to have a shape described by an analytic function, generally the three-parameter gamma distribution (e.g., Ulbrich 1983):

$$N(D) = N_0 D^\alpha \exp(-\Lambda D) \quad (5.2)$$

where  $N_0$ ,  $\alpha$ , and  $\Lambda$  are the intercept, spectral shape, and slope parameters, respectively. The aforementioned studies have demonstrated that microphysics schemes with only one prognostic moment (usually mass mixing ratio) are unable to capture differential sedimentation. In contrast, double-moment microphysics schemes with a fixed spectral shape parameter produce unrealistically large differential sedimentation, often leading to excessively large particles and mean particle diameters (e.g. Wacker and Seifert 2001; Milbrandt and Yau 2005a, herein MY05a). Models employing spectral (or “bin”) microphysics are able to explicitly capture differential sedimentation, as each particle size bin is assigned its own fallspeed. Whereas bulk models with diagnostic (for two-moment schemes) or prognostic (for three-moment schemes) spectral shape parameters can better match the differential sedimentation from bin models after an extended amount of time, the initial match between the bulk scheme solutions and that of the bin model is often quite poor (MY05a). None of these studies has investigated the maintained size sorting possible by updrafts or vertical wind shear.

Recent investigations of supercell storms have revealed repetitive polarimetric radar signatures that are seemingly characteristic of such storms (Kumjian and Ryzhkov 2008b). Hypothesized explanations of several of these signatures (notably, the “ $Z_{DR}$  arc” and “ $Z_{DR}$  column”) invoke size sorting as a significant process contributing to their appearances (Kumjian and Ryzhkov 2008a, 2009). Evidence in support of the size-

sorting hypothesis has come from the use of Doppler spectra data (Yu et al. 2009), disdrometer observations (Carey et al. 2010), and numerical simulations with bulk microphysics schemes (Jung et al. 2010) as well as simplified bin models (Kumjian and Ryzhkov 2009). As shown below, size sorting occurs not just in supercell storms, but can appear in any precipitating system. The dilemma is then readily apparent: if size sorting has such a pronounced effect on dual-polarization observations, and bulk microphysics schemes widely used in operational numerical weather prediction models cannot adequately capture size sorting, then there exist serious problems for future attempts to utilize dual-polarization data in storm-scale numerical models (e.g., data assimilation).

The remainder of this chapter is devoted to quantifying the impact of size sorting on dual-polarization radar variables using simplified bin models applied to common size sorting mechanisms. Additionally, the errors in the radar variables computed based on assumptions in bulk microphysics schemes will be quantified.

### **3. Size sorting models**

For each subsection below, a model of a particular size sorting mechanism is developed and results are presented. Each mechanism is applied to both a bin model framework and to the assumptions of bulk schemes. The resulting DSDs are converted into S-band polarimetric radar variables as follows. For the bin models, drops are divided into 80 bins (0.05 mm to 7.95 mm in 0.1-mm increments). Calculation of the polarimetric radar variables from the bulk scheme profiles uses the same drop partitioning to discretize the moment integrals to ensure that differences in the

polarimetric variables are entirely because of differences in the explicit versus parameterized treatment of size sorting. The radar variables are then computed from scattering amplitude calculations using a T-Matrix code. Raindrops are assumed to be pure liquid water at a temperature of 20 °C, with mean canting angle of 0° with respect to the vertical, and a canting angle distribution root-mean square (rms) width of 10° (e.g., Ryzhkov 2001; Ryzhkov et al. 2002b). The corrected Brandes et al. (2004a,b, 2005) drop shapes are assumed. Such a formulation is analogous to recent polarimetric radar operators developed for bulk models (Jung et al. 2010) and for bin models (Ryzhkov et al. 2011).

*a. Pure sedimentation*

1) MODEL DESCRIPTION

Differential sedimentation of precipitation particles is the most basic mechanism of size sorting. Following the previously cited literature, a simple one-dimensional model of pure sedimentation is constructed. In this framework, a distribution of raindrops is prescribed at the top of the domain, and these drops begin falling at the initial time. The initial distribution is inverse exponential in shape (i.e., the spectral shape parameter  $\alpha = 0$ ), with raindrop mass mixing ratio  $q = 1 \text{ g kg}^{-1}$  and the Marshall-Palmer (1948) intercept parameter  $N_0 = 8000 \text{ m}^{-3} \text{ mm}^{-1}$ . Fresh drops are continuously replenished at the top of the domain (“cloud base”) at each time step, which is  $\Delta t = 0.5$  s. The domain is 3 km tall, with vertical grid spacing of 10 m. There are no changes in air density with height. A simple first-order forward in time upstream in space finite differencing scheme is used. It should be noted that such a scheme is numerically



diffusive, thereby smoothing the resulting “shockwaves” formed because of the quasi-linear advection equations used in the bulk schemes (e.g., Wacker and Seifert 2001). The fine grid spacing is intended to minimize the effects of the diffusive numerical scheme.

To simulate the sedimentation of drops in bulk schemes, moment-weighted fall speeds are calculated based on the prognostic moments of total number concentration ( $N_{TOT}$ , the zeroth moment), mass mixing ratio ( $q$ , proportional to the third moment), and Rayleigh reflectivity factor ( $Z$ , the sixth moment) :

$$\bar{V}_N = \int_0^{\infty} N(D)v_t(D)dD \Big/ \int_0^{\infty} N(D)dD \quad (5.3)$$

$$\bar{V}_q = \int_0^{\infty} N(D)v_t(D)m(D)dD \Big/ \int_0^{\infty} N(D)m(D)dD \quad (5.4)$$

$$\bar{V}_Z = \int_0^{\infty} N(D)v_t(D)D^6dD \Big/ \int_0^{\infty} N(D)D^6dD \quad (5.5)$$

where  $N(D)$  is the drop size distribution,  $v_t(D)$  is the MY05b fallspeed relation given in Table 5.1, and  $m(D)$  is the raindrop mass expressed in terms of diameter. By using such moment-weighted fallspeeds, bulk schemes assume *every drop size falls at the same speed* for given values of  $N_{TOT}$ ,  $q$ , and  $Z$ . The prognostic moments used above (0<sup>th</sup>, 3<sup>rd</sup>, and 6<sup>th</sup>) are selected because of their widespread use in operational numerical weather prediction models. Note that the choice of moments can produce significantly different results, as demonstrated by Wacker and Lüpkes (2009) and Milbrandt and McTaggart-Cowan (2010, herein MM10). For the single-moment (1M) case, the mass-weighted fallspeed is given by eqn. (5.4), with sedimentation of  $q$  governed by

$$\frac{\partial q}{\partial t} - \frac{1}{\rho_{air}} \bar{V}_q \frac{\partial}{\partial Z} (\rho_{air} q) = 0. \quad (5.6)$$

Both the mass- and number-weighted fallspeeds given by eqns. (5.3-5.4) are used for the double-moment (2M) case, with sedimentation of  $N_{TOT}$  given by

$$\frac{\partial N_{TOT}}{\partial t} - \bar{V}_N \frac{\partial}{\partial Z} (N_{TOT}) = 0. \quad (5.7)$$

Note that  $\bar{V}_q > \bar{V}_N$  for any shape parameter  $\alpha \geq 0$ , so mixing ratio  $q$  will always sediment faster than  $N_{TOT}$  (which is the cause of excessive “size sorting”, e.g., MY05a; MM10; Mansell 2010). For the three-moment (3M) scheme, sedimentation of  $Z$  is given by

$$\frac{\partial Z}{\partial t} - \bar{V}_Z \frac{\partial}{\partial Z} (Z) = 0. \quad (5.8)$$

The shape parameter  $\alpha$  is prognosed following the closure scheme of MY05a,b by implicitly solving for  $\alpha$  using the new values of  $Z$ ,  $q$ , and  $N_{TOT}$  (eqns. 5.6-5.8) at each level and timestep:

$$\frac{(6 + \alpha)(5 + \alpha)(4 + \alpha)}{(3 + \alpha)(2 + \alpha)(1 + \alpha)} - Z N_{TOT} \left( \frac{\pi \rho_w}{6 \rho_{air} q} \right)^2 = 0. \quad (5.9)$$

In the iterative solver,  $\alpha$  is determined to a precision of 0.05. Using the new  $\alpha$ , the slope and intercept parameters  $\Lambda$  and  $N_0$  are computed.

For the bin model, two drop velocity relations are used: the relation in eqn. (5.1), which is most accurate for larger drop sizes (Thurai and Bringi 2005), and the relation used in computing the moment-weighted fall speeds for the bulk schemes (Table 5.1; MY05b). The latter is used to make a fair comparison between the bulk and bin model

approaches, though it leads to slight underestimation of size sorting because it underestimates the fall speed of the largest raindrops by up to  $1 \text{ m s}^{-1}$ .

## 2) MODEL RESULTS

Figure 5.2a presents the modeled DSDs at  $t = 333$  seconds at a height of 1000 m above the ground from the bulk scheme simulations as well as the reference bin solutions. This time is selected because it captures the initial transient size sorting effect before the steady-state profiles have developed and the largest raindrops (in the bin framework) have just reached the ground, and the height level is selected because it is near the bottom of the bulk scheme rainshafts. Despite the initial inverse exponential DSD aloft, the resulting bin reference solution DSDs have narrowed, producing a deficit of smaller drops. The 1M scheme (with fixed  $N_0$  and  $\alpha$ ) accounts for decreasing mass at lower levels by *removing large drops*, doing “violence” to the actual physics (to borrow a phrase from Kessler 1969). The 2M scheme (with fixed  $\alpha$ ) produces a DSD with an extremely shallow slope, also in disagreement with the reference solution. MY05a and MM10 found similar results and proposed diagnostic relations for  $\alpha$ , allowing the 2M schemes to capture the narrowing distribution shape owing to size sorting. Alternatively, they demonstrate that 3M schemes (which prognose  $\alpha$ ) better approximate the narrowing DSD. The 3M scheme solution certainly provides a much better representation of the bin solutions, albeit imperfectly (Fig. 5.2). The difference in the two fall speed relations used in the bin reference solution is evident in the DSDs at the ground at  $t = 333 \text{ s}$  (Fig. 5.2b). The Brandes et al. (2002) velocity relation produces higher concentrations of the largest drops compared to the bulk scheme

relation (Uplinger 1981; Ferrier 1994; MY05b). There are no DSDs from the 1M and 2M bulk schemes in Fig. 5.2b because the sedimenting fields of  $q$  and  $N_{TOT}$  have not reached the ground by this time. In contrast, the 3M scheme produces a narrow DSD similar to the bin solutions.

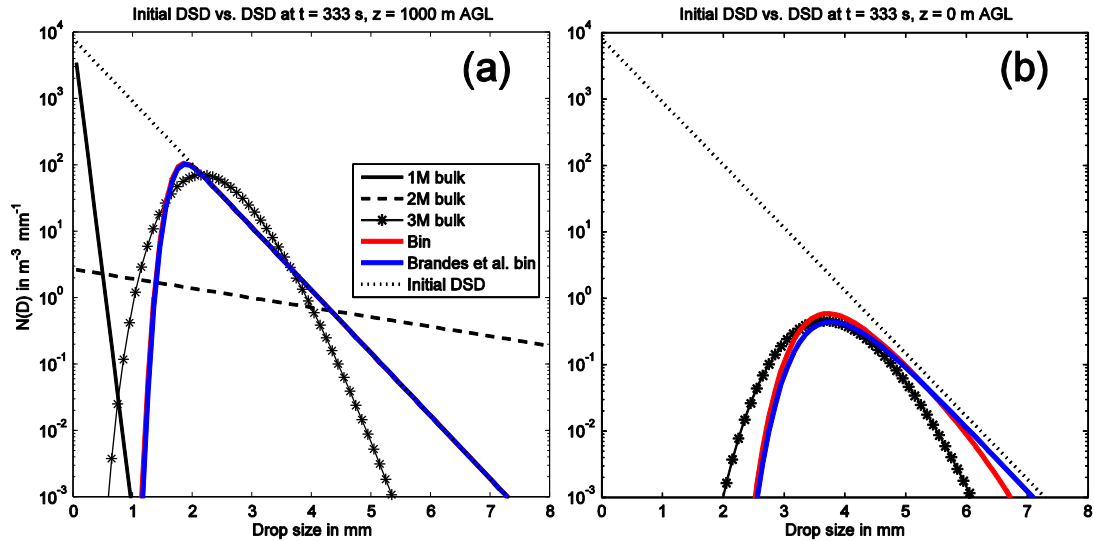


Fig. 5.2: DSDs from the sedimentation model. The initial DSD aloft is shown by the thin dotted line in both panels. (a) At  $t = 333$  s, at height level  $z = 1000$  m AGL, the one-moment bulk microphysics scheme (“1M bulk”) solution is given by the solid black line, the two-moment solution (“2M bulk”) is given by the dashed black line, and the three-moment (“3M bulk”) scheme solution is shown in the solid line with asterisk markers. The reference bin solutions are shown in solid red and blue lines, the difference being the assumed fall speed relation. (b) As in (a), but surface ( $z = 0$  m) DSDs at  $t = 333$  s from the reference bin solutions. Note that in (a), the bin solutions overlap.

As expected from the substantial disagreements in the simulated DSDs, the vertical profiles of the S-band polarimetric radar variables also differ significantly (Fig. 5.3). In the  $Z_H$  profile (Fig. 5.3a), neither the 1M or 2M bulk schemes’ rainshafts has reached the surface, whereas the surface  $Z_H$  from the bin solutions is about 36 dBZ. The 3M scheme provides a rather close agreement to the bin solutions, underestimating the  $Z_H$  by about 2 dBZ at the ground. At midlevels, the 2M scheme overpredicts  $Z_H$  by

nearly 10 dBZ, whereas the 1M and 3M schemes match well ( $< 1$  dBZ error). Predominantly, this difference is because of the excessive number of large drops (which strongly affect  $Z_H$ ) predicted by the 2M scheme. Note that where  $Z_H \leq 0$  dBZ, all radar variables have been censored to emulate a minimum detectable radar signal.

The profiles of  $Z_{DR}$  (Fig. 5.3b) are perhaps the most revealing. The 1M solution predicts an accurate profile down to about 1 km AGL, but is entirely wrong below 1 km, owing to a lack of any drops able to fall below that level. Thus,  $Z_H$  and  $Z_{DR}$  decrease sharply at the leading edge of this “shockwave.” The inability to capture the size sorting is due to the use of a single prognostic moment; all variables of interest are a single-valued function of  $q$ , and because  $q$  does not reach the ground,  $Z_{DR}$  (and all of the radar variables) follows the same pattern. In stark contrast, the 2M scheme produces excessive “size sorting,” resulting in an overprediction of  $Z_{DR}$  by over 2.5 dB (a relative error of 168%) at midlevels and towards the bottom of the rain shaft. The simulated  $Z_{DR}$  values reach the upper limit (about 4 dB) because of the truncated DSD used to calculate the polarimetric variables (maximum drop size is 8 mm); otherwise,  $Z_{DR}$  values could far exceed those observed at S band as unrealistically large (and presumably oblate) drops would be produced. The 3M scheme  $Z_{DR}$  profile is closer to the bin solutions, though still underestimates  $Z_{DR}$  by almost 0.5 dB (about 25% relative error). The 3M errors will be discussed in more detail below. Though the reference solutions are similar to one another, the Brandes et al. (2002) velocity relation predicts a surface  $Z_{DR}$  value 0.15 dB larger than the power-law relation used in bulk schemes. The increase in  $Z_{DR}$  at the surface over the initial value aloft is over 1.0 dB for both bin

solutions, illustrating the ability of size sorting to substantially enhance  $Z_{DR}$  values in rain.

The profiles of  $K_{DP}$  (Fig. 5.3c) produced by the bulk scheme solutions also show the shock wave problem, albeit smoothed by the diffusive finite differencing scheme used. The 2M scheme produces a midlevel relative maximum in  $K_{DP}$ , causing an overprediction compared to the bin solution (relative error of 217%), whereas the 1M scheme's maximum overprediction of  $K_{DP}$  is only about 10%. The 3M scheme overpredicts  $K_{DP}$  at midlevels, with a maximum relative error of 24%. The reference solution smoothly varies in height and both velocity relations produce nearly identical results. Though differences exist in the profiles of  $\rho_{hv}$  (Fig. 5.3d), the changes are small in magnitude at S band (all variations are  $< 0.01$ ) and likely are not measurable. At smaller radar wavelengths, resonance scattering associated with large raindrops (5-6 mm at C band, 3-4 mm at X band) could exacerbate the errors to the extent that they become measurable.

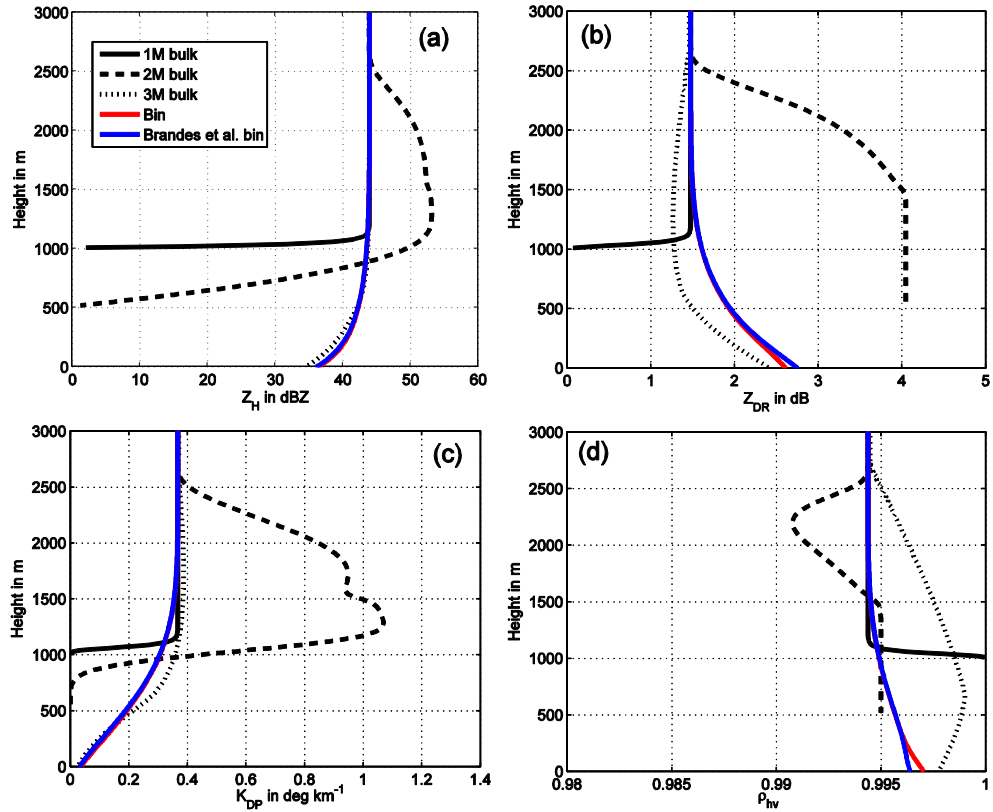


Fig. 5.3: Vertical profiles of the S-band polarimetric radar variables predicted by the sedimentation model at  $t = 333$  seconds. The solutions for the one-moment (solid black line), two-moment (dashed black line), and three-moment (dotted black line) bulk schemes are compared to the reference solutions (red and blue solid curves). Variables shown are calculated for S band: (a)  $Z_H$ , (b)  $Z_{DR}$ , (c)  $K_{DP}$ , and (d)  $\rho_{hv}$ . For the bulk schemes, all variables are censored where  $Z_H \leq 0$  dBZ.

During sedimentation of the sixth moment  $Z$  in the 3M scheme, the shape parameter  $\alpha$  can grow to unrealistically large values. Disdrometer observations generally do not reveal  $\alpha$  larger than about 15 – 20 (e.g., Zhang et al. 2001; Cao et al. 2008). The microphysics scheme of MY05b limits  $\alpha$  to a maximum of  $\alpha_{\max} = 40$  during sedimentation (D. Dawson, 2011 personal communication), which is used in the present study. Varying  $\alpha_{\max}$  changes the error characteristics, especially at the bottom of the rain shaft (Fig. 5.4). Whereas the magnitudes of the relative errors in  $Z_H$  are  $< 5\%$ , larger errors ( $> 20\%$ ) are possible in  $Z_{DR}$  and  $K_{DP}$ . Above about 1 km AGL,  $Z_{DR}$  errors

become increasingly negative towards the ground (Fig. 5.4b), indicating underestimations for all values of  $\alpha_{\max}$ . This is because narrowing the DSD by increasing  $\alpha$  leads to a decrease in the number of small drops (which is physically consistent with size sorting) *as well as* a decrease in the number of large drops (which is inconsistent; cf. Figure 5.2a). Thus,  $Z_{\text{DR}}$  is underestimated. Below 1 km, at the very bottom of the rain shaft, the ability of the 3M scheme to reproduce the “true”  $Z_{\text{DR}}$  profile depends on  $\alpha_{\max}$ . Limiting  $\alpha_{\max}$  to 10 results in an overprediction of  $Z_{\text{DR}}$  near the ground, because once the  $\alpha_{\max}$  is achieved, the additional size sorting is represented by decreasing the slope parameter  $\Lambda$ , as in the 2M scheme. The vertical profiles of relative errors in  $K_{\text{DP}}$  (Figure 5.4c) demonstrate similar behavior, but of opposite sign. The increasingly positive errors (overestimations) result from an artificial increase in the number medium-sized drops (cf. Fig. 5.2a). Based on the excessive narrowing of the DSD that occurs for large  $\alpha_{\max}$  demonstrated above, it is recommended to use more rigid constraints (e.g.,  $\alpha_{\max} = 20.0 - 30.0$ ) for the 3M scheme, especially for polarimetric radar applications.



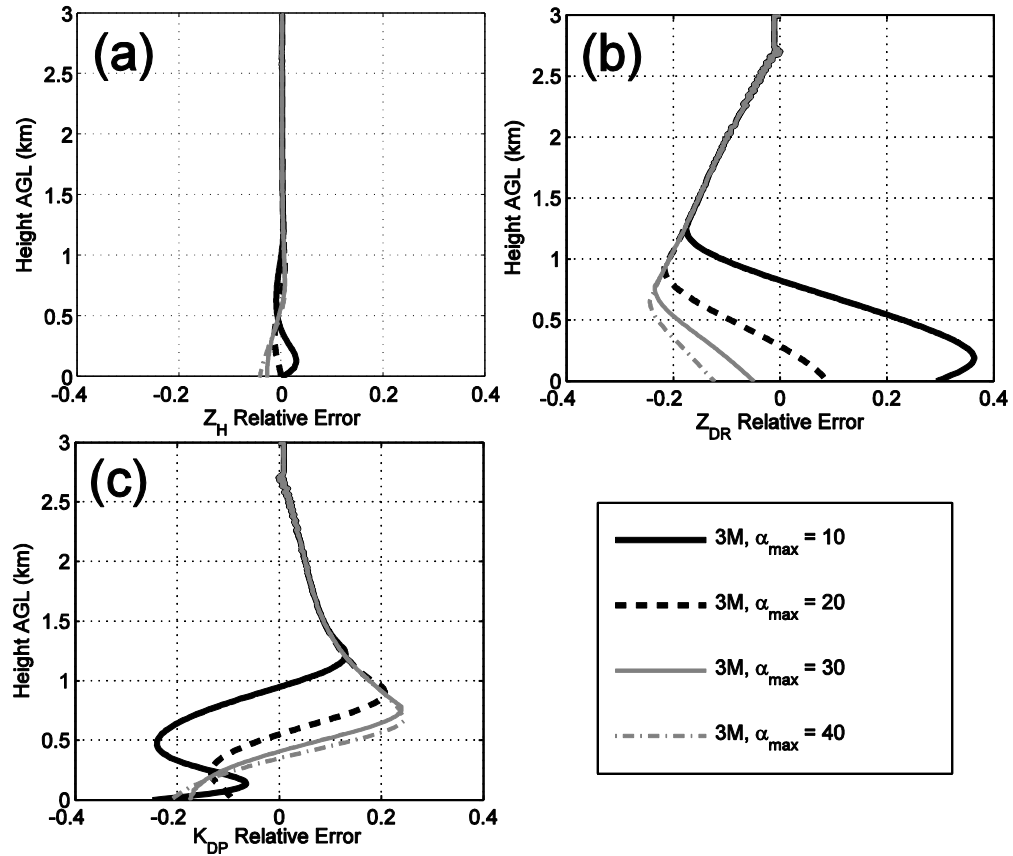


Fig. 5.4: Relative errors in the polarimetric variables computed from the three-moment scheme with different values of maximum shape parameter  $\alpha$ : 10 (black solid line), 20 (dashed black line), 30 (solid gray line), and 40 (dash-dot gray line). Variables shown are (a)  $Z_H$ , (b)  $Z_{DR}$ , and (c)  $K_{DP}$ . The Brandes et al. bin solution is considered “truth” for these error calculations. Positive errors correspond to overestimations by the 3M scheme, negative errors to underestimations.

### *b. Updraft*

#### 1) MODEL DESCRIPTION

Though the differential sedimentation modeled above is transient, such size sorting can be maintained by various influences. Perhaps the most frequently observed modifying influence is an updraft. Precipitation particles injected into an updraft (from above, for example) or developing within the updraft are subject to size sorting as the updraft’s vertical winds act in opposition to the particle terminal fallspeed. In the case

where the updraft speed is greater than the particle fallspeed, the particle is lofted. In contrast, faster-falling particles may fall “against” the updraft if their fallspeeds exceed the vertical velocity in the cloud. Beneath such an updraft, only the faster-falling, larger particles are able to fall. This process is probably responsible for the lower portions of observed “ $Z_{DR}$  columns,” where the largest particle fallout leads to enhanced  $Z_{DR}$  all the way to the ground beneath convective updrafts (Bringi and Chandrasekar 2001; Kumjian and Ryzhkov 2008a,b).

In a crude representation of an updraft, a one-dimensional fallout model such as the one described in the previous subsection can be utilized. Instead of using the terminal fallspeeds  $v_t$  of the drops, however, their vertical velocity is modified by the updraft speed  $w$  at a given level by taking  $v_t - w$ . In this way, drops with  $|v_t| < |w|$  are then lofted upwards and whisked out of the domain, removed from the distribution. Such a model framework was employed by MY05a, except hailstones were used rather than raindrops. In a steady-state version of such a model (i.e.,  $\partial/\partial t = 0$ ), the flux of drops at each height level is conserved:

$$\frac{\partial}{\partial z} [(v_t(D) - w)N(D)] = 0. \quad (5.10)$$

In the bulk configuration,

$$\frac{1}{\rho_{air}} \frac{\partial}{\partial z} [(\bar{V}_q - w)q\rho_{air}] = 0, \quad (5.11)$$

$$\frac{\partial}{\partial z} [(\bar{V}_N - w)N_{TOT}] = 0, \quad (5.12)$$

and

$$\frac{\partial}{\partial z} [(\bar{V}_Z - w)Z] = 0. \quad (5.13)$$

## 2) MODEL RESULTS

Barring any vertical variations in air density, the vertical profiles of all polarimetric variables beneath the updraft are constant in height (not shown). Stronger updraft speed  $w$  results in lower  $Z_H$  and increased  $Z_{DR}$  (Fig. 5.5). The decreased  $Z_H$  with increasing updraft is because of the steady-state assumption of the model: drop flux  $N(D)[v_t(D) - w]$  is conserved at each level, so larger ascent velocity  $[v_t(D) - w]$  corresponds to decreased concentration  $N(D)$  and thus smaller  $Z_H$ .  $Z_{DR}$  is enhanced because stronger updrafts loft drops of increasingly larger sizes, increasing the minimum drop size able to fall through the updraft. The maximal value of  $Z_{DR}$  beneath the updraft is dependent on the DSD initially injected into the updraft as well as the updraft speed. Because drops with diameters in excess of about 6 mm all fall at roughly the same speed, DSDs with “flatter” tails (i.e., small slope parameters and/or negative shape parameters) and thus relatively more big drops will produce larger  $Z_{DR}$  values.

In bulk schemes, the impact of the updraft entirely depends on the moment-weighted fallspeeds for  $Z, q$ , and  $N_{TOT}$  compared to the updraft speed. In a crude representation of an updraft such as a one-dimensional model, this can lead to cases where  $q$  is able to sediment but  $N_{TOT}$  is lofted, resulting in undefined DSDs. In more realistic treatments of convective updrafts (such as in high-resolution three-dimensional numerical models), the “sorting” effect is captured in two-moment schemes, leading to enhanced  $Z_{DR}$  within and beneath the updraft (e.g., Jung et al. 2010).

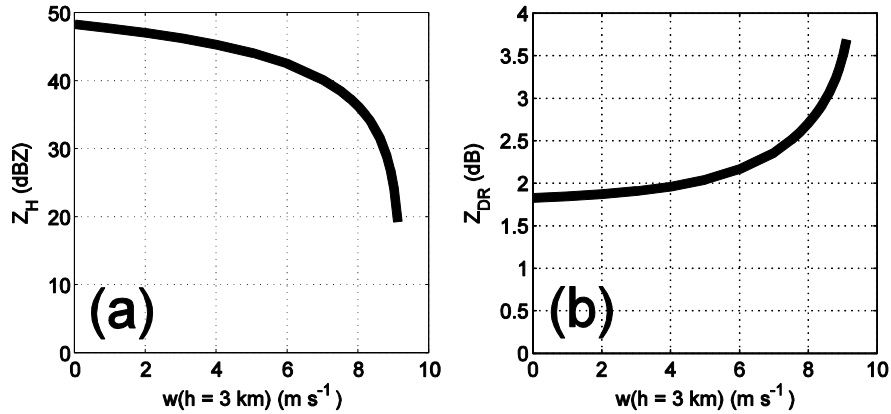


Fig. 5.5: Results from the 1D updraft model, showing the ground-level (a)  $Z_H$  and (b)  $Z_{DR}$  as a function of the updraft speed at the top of the domain  $w(h = 3 \text{ km})$ .

### c. Vertical Wind Shear

#### 1) MODEL DESCRIPTION

The effect of vertical wind shear is to provide non-zero storm-relative flow, allowing raindrops to be advected away from directly beneath the cloud. Because smaller drops fall slower than larger drops, the smaller drops encounter this storm-relative flow for longer periods of time and are thus transported farther downstream than the larger drops. This flavor of size sorting, along with that caused by convective updrafts described above, helps explain the enhancement of  $Z_{DR}$  (and narrow distribution of large drops) frequently observed at the leading edge of linear mesoscale convective systems (e.g., Ulbrich and Atlas 2007; Morris et al. 2009; Kumjian and Ryzhkov 2009; Teshiba et al. 2009).

A simple two-dimensional model is constructed to quantify the changes in polarimetric radar variables as a result of vertical wind shear. The model is similar to the previous one-dimensional versions, except a vertical wind profile is introduced. For the results shown below, the “storm”-relative winds increase linearly towards the

ground from  $0 \text{ m s}^{-1}$  at cloud base (3 km AGL) to  $20 \text{ m s}^{-1}$  near the surface (i.e., a sounding would show winds increasing from  $0 \text{ m s}^{-1}$  at the surface to  $20 \text{ m s}^{-1}$  at 3 km AGL). A 1-km wide precipitating “cloud” is placed at the top left portion of the domain. The cloud precipitation intensity pattern has a Gaussian distribution centered at the middle of the cloud ( $x = 1000 \text{ m}$ ), with maximum rainwater mixing ratio of  $q = 2.0 \text{ g kg}^{-1}$ , which corresponds to a rainfall rate of about  $50 \text{ mm hr}^{-1}$ , tapering towards the edges (distribution width is 300 m). The model configuration is shown schematically in Figure 5.6. The rain DSD (based on  $q$ ) is prescribed at the top of the domain as a Marshall-Palmer (1948) inverse exponential type. The slope parameter  $\Lambda$  of the DSD is determined by the Gaussian-distributed  $q$  profile, which results in a modulation of all polarimetric radar variables (larger  $Z_H$ ,  $Z_{DR}$ , and  $K_{DP}$ , and lower  $\rho_{hv}$  at the center of the cloud). Raindrop motion is determined purely by advection and sedimentation, governed by

$$u(z) \frac{\partial}{\partial x} [N(D)] + v_t(D) \frac{\partial}{\partial z} [N(D)] = 0 \quad (5.14)$$

in the bin model (assuming air density is constant in height). In other words, no momentum transfer between the air and raindrops (e.g., Shapiro 2005) is accounted for, and no other microphysical processes are considered. Horizontal resolution is 5 m, and vertical resolution is 75 m. Note that this model is steady state (no time dependence in eqn. 5.14), illustrating how such wind shear size sorting can maintain the transient effect of differential sedimentation. The bulk scheme configuration is governed by equations similar to (5.14), except the moment-weighted fallspeeds replace  $v_t$ , and  $Z$ ,  $q$ , and  $N_{TOT}$  replace  $N(D)$ .

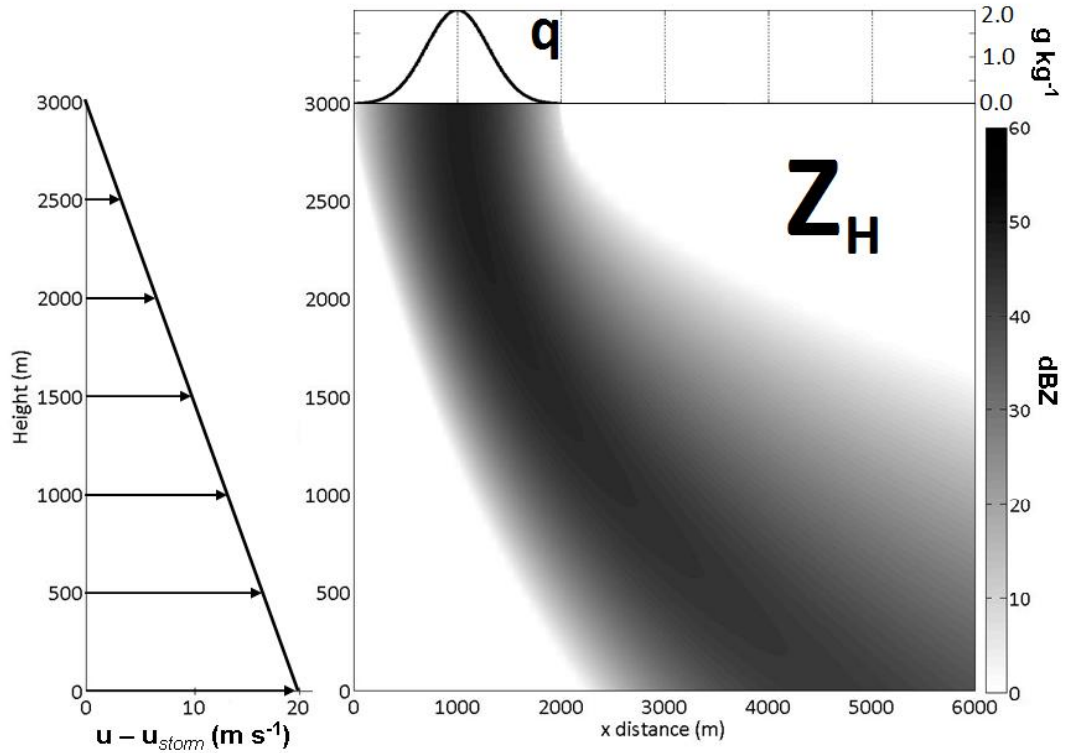


Fig. 5.6: Schematic of the two-dimensional wind shear model configuration. Storm-relative wind ( $u - u_{storm}$ ) profile is shown to the left. The domain and example resulting  $Z_H$  distribution (shaded in dBZ) is shown to the right. The “cloud” rainwater mixing ratio ( $q$ ) profile is shown above the domain ( $\text{g kg}^{-1}$ ).

## 2) MODEL RESULTS

The results of the bin model configuration are presented in Figure 5.7. Left-to-right advection of the precipitation is evident in all fields. Values of all polarimetric radar variables are removed where  $Z_H$  is less than 0 dBZ, as before. In  $Z_H$ , the largest values are confined to the center of the rainshaft (Fig. 5.7a). The  $Z_{DR}$  field (Fig. 5.7b) reveals where the impact of the size sorting is most readily apparent in the polarimetric variables: the highest values are found towards the ground and at the leading edge of the echo, along the gradient of  $Z_H$ . For the shear and initial model parameters used here, the maximal value of  $Z_{DR}$  near the surface is 36% larger than the maximal value in the cloud aloft, indicating the ability of wind shear size sorting to amplify the observed  $Z_{DR}$

in precipitating systems.  $K_{DP}$  (Fig. 5.7c) closely follows the  $Z_H$  pattern, as expected. The  $\rho_{hv}$  field (Fig. 5.7d) exhibits slightly decreased values towards the leading edge, though changes at S band are imperceptible to WSR-88D radars ( $< 0.01$ ).

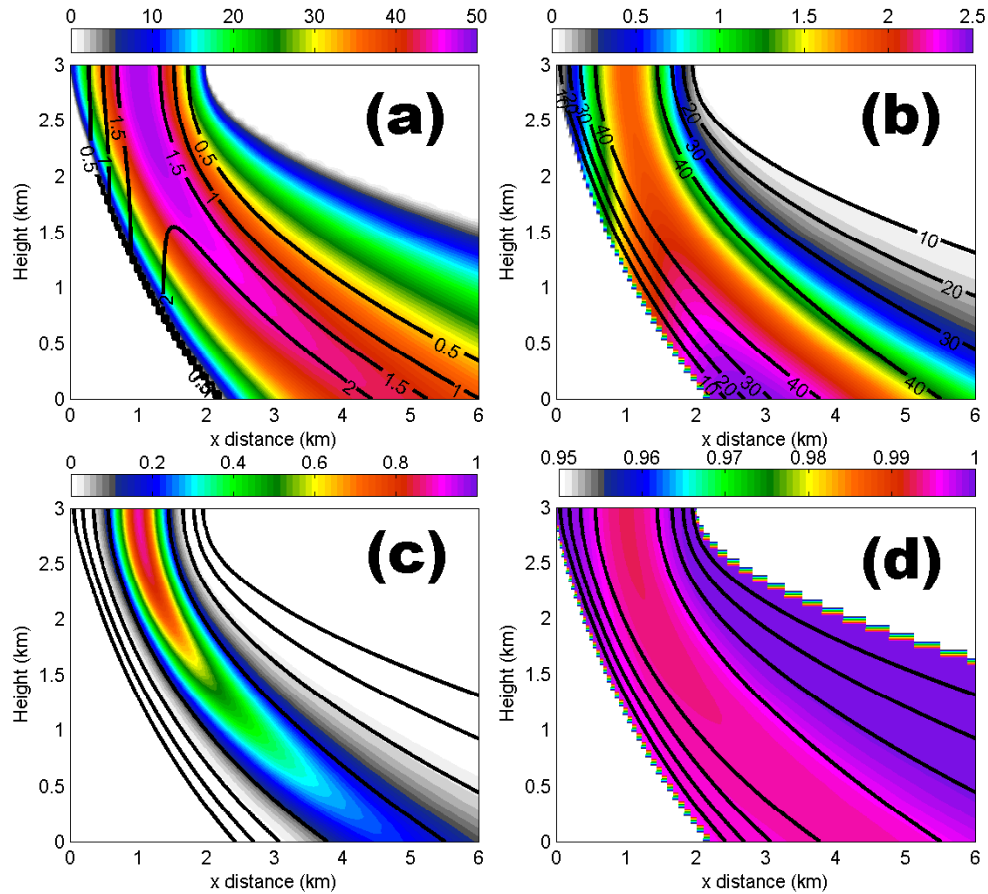


Fig. 5.7: Results from the two-dimensional wind shear model using the bin formulation. Panels show the two-dimensional fields of (a)  $Z_H$ , (b)  $Z_{DR}$ , (c)  $K_{DP}$ , and (d)  $\rho_{hv}$ . Overlaid on panel (a) is the  $Z_{DR}$  contours (0.5 – 2.5 dB in 0.5 dB increments), whereas panels (b)-(d) have  $Z_H$  contours 10 – 40 dBZ (in 10-dBZ increments) overlaid. For  $Z_H < 0$  dBZ, all fields are set to zero.

The 1M scheme reproduces  $Z_H$  fairly well, though the rainshaft is narrower at low levels (Fig. 5.8a). In terms of  $Z_{DR}$  (Fig. 5.8b), the 1M results are wholly unsatisfying, owing to the inability of 1M schemes to model size sorting; rather, there is a one-to-one correspondence between  $q$  and all other variables (including  $Z_H$  and  $Z_{DR}$ ).

Therefore, 1M schemes produce the maximum in  $Z_{DR}$  collocated with the maximum in  $Z_H$ . Similar to  $Z_H$ , the  $K_{DP}$  field (Fig. 5.8c) is reproduced well. Though slight differences are evident in the  $\rho_{hv}$  field (Fig. 5.8d), the overall changes in  $\rho_{hv}$  are too small to be measured at S band.

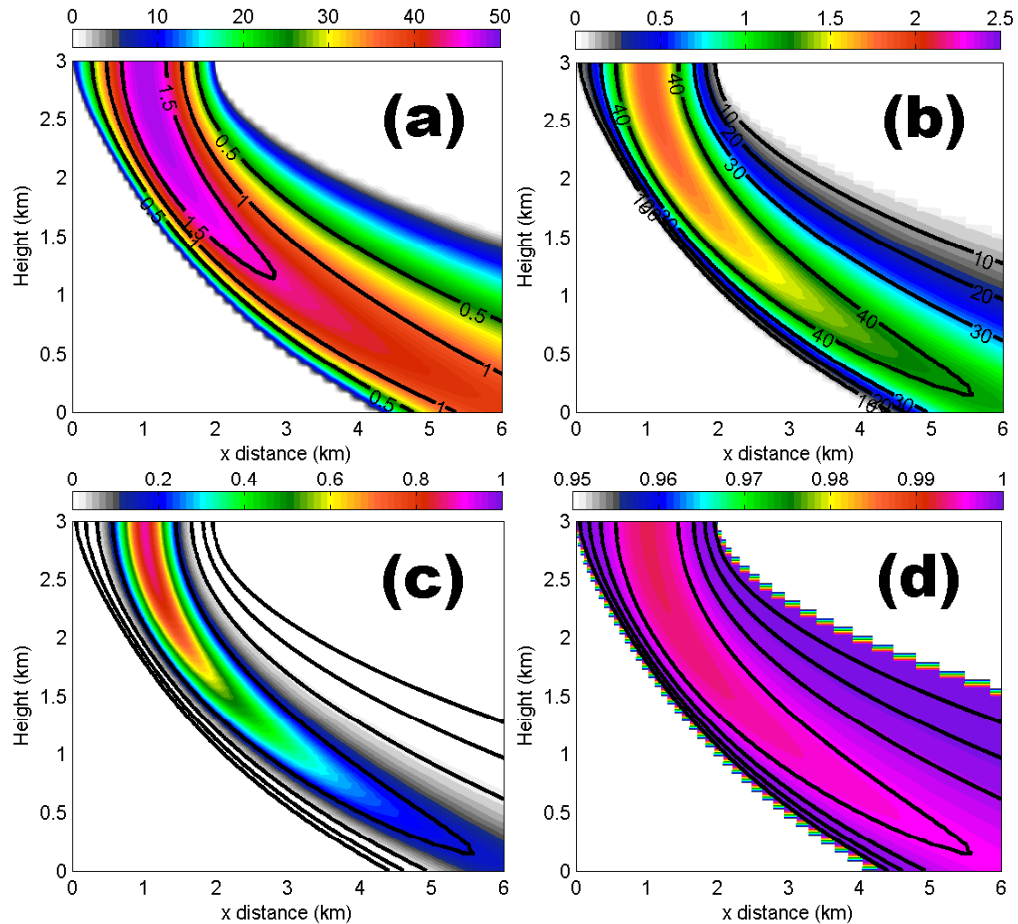


Fig. 5.8: As in Fig. 5.7, except the results are from the single-moment bulk scheme configuration.

Results from the 2M scheme are presented in Figure 5.9. Though the width of the rainshaft closer matches the bin model solution, the  $Z_H$  values (Fig. 5.9a) are incorrectly enhanced by about 10 dBZ in the middle of the echo below about 2.5 km.



The same overprediction of  $Z_H$  is evident in the pure sedimentation model (cf. Fig. 5.3a) and is a result of the increased number concentration of larger drops, which significantly contribute to the overall  $Z_H$  signal (at S band,  $Z_H$  is proportional to  $D^6$ ). The excessive amount of larger drops is caused by a combination of the decreased intercept parameter  $N_0$  (owing to substantially decreased total number concentration  $N_{TOT}$ ) and a decreased slope parameter  $\Lambda$  (flattening of the distribution shape to account for the still-appreciable rainwater mixing ratio  $q$ ). These differences are caused by the different sedimentation rates of  $N_{TOT}$  and  $q$ , owing to the weighted fallspeed differences discussed above. Figure 5.10 depicts the modeled  $q$  and  $N_{TOT}$  fields, which clearly demonstrate the impact of the different weighted fallspeeds on the advection and sedimentation of precipitation modeled in the 2M bulk scheme. The  $N_{TOT}$  field, which has a lower fallspeed characteristic of the smaller raindrops, is quickly blown downstream, while the  $q$  field is advected less rapidly owing to its larger characteristic fallspeed (more heavily weighted by the large drops).

The excessive overprediction of large drops and underprediction of smaller drops yields excessive  $Z_{DR}$  over much of the rainshaft (Fig. 5.9b):  $Z_{DR}$  reaches its maximum value at S band. Whereas the 1M scheme produces no size sorting at the leading edge of the precipitation echo, the 2M scheme exaggerates the size sorting (and thus  $Z_{DR}$ ). Similar to  $Z_H$ ,  $K_{DP}$  (Fig. 5.9c) is enhanced in the center of the echo, overpredicted by  $0.6 - 0.8 \text{ deg km}^{-1}$ . This enhancement can also be attributed to the overprediction of large drop sizes and the strong dependence of  $K_{DP}$  on drop size ( $K_{DP} \sim D^{4.5}$ ). The minimum values of  $\rho_{hv}$  (Fig. 5.9d) run along the gradient of  $Z_{DR}$ , similar to the bin model results, though again these variations across the precipitation shaft are

imperceptible to S-band radars. Note that the overprediction of large drops, which are resonance scatterers at C- and X-band frequencies, will substantially lower the  $\rho_{hv}$  in regions of high  $Z_{DR}$ .

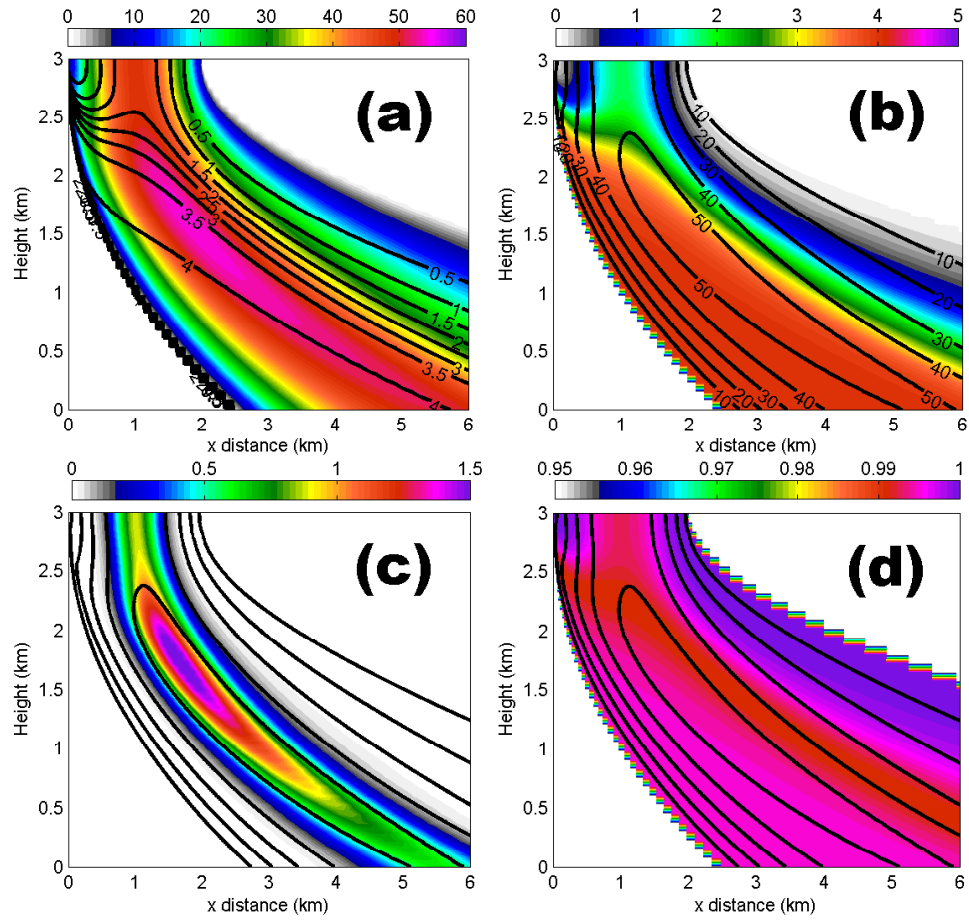


Fig. 5.9: As in Figs. 5.7 and 5.8, except the results from the two-moment bulk scheme configuration are shown. Note the changes in the color scales of  $Z_H$ ,  $Z_{DR}$  and  $K_{DP}$ .

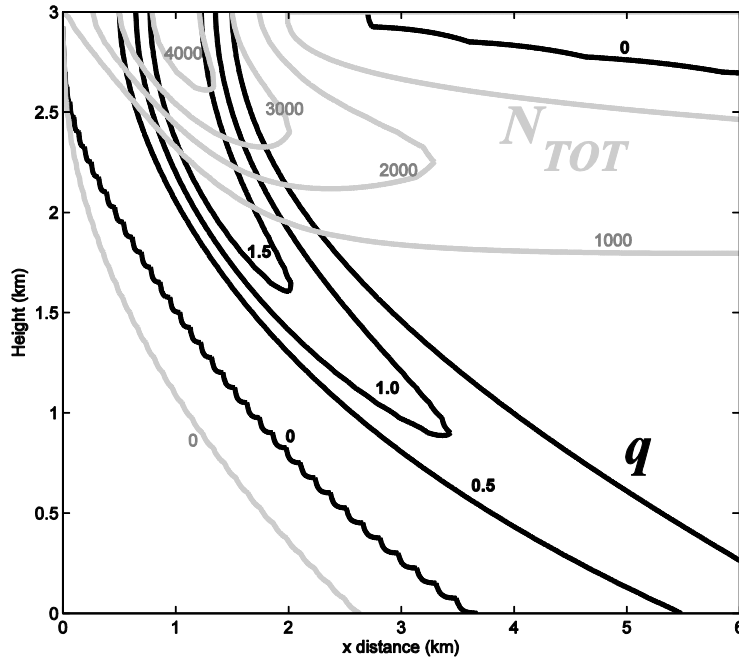


Fig. 5.10: Fields of rainwater mixing ratio ( $q$ , in  $\text{g kg}^{-1}$  and contoured in black) and total number concentration ( $N_{TOT}$ , in  $\text{m}^{-3}$  and contoured in gray) from the two-dimensional wind shear model run using the two-moment scheme shown in Fig. 5.9.

In contrast to the 1M and 2M schemes, the 3M results (Fig. 5.11) closely resemble the bin model solution. Whereas the  $Z_H$  field is nearly indistinguishable from the bin model (Fig. 5.11a), the 3M scheme underestimates the maximum  $Z_{DR}$  at the leading edge by nearly 0.5 dB (Fig. 5.11b). The 2-dB contour of  $Z_{DR}$  only reaches a height of about 0.5 km AGL in the 3M scheme, whereas the same contour extends above 1.5 km AGL in the bin solution (cf. Figs. 5.7a and 5.11a). Also,  $K_{DP}$  values are slightly overestimated in the 3M scheme at low levels (Fig. 5.11c). As demonstrated in the 1D sedimentation model, the overestimation in  $K_{DP}$  occurs because of an overprediction of smaller and medium-sized drops.

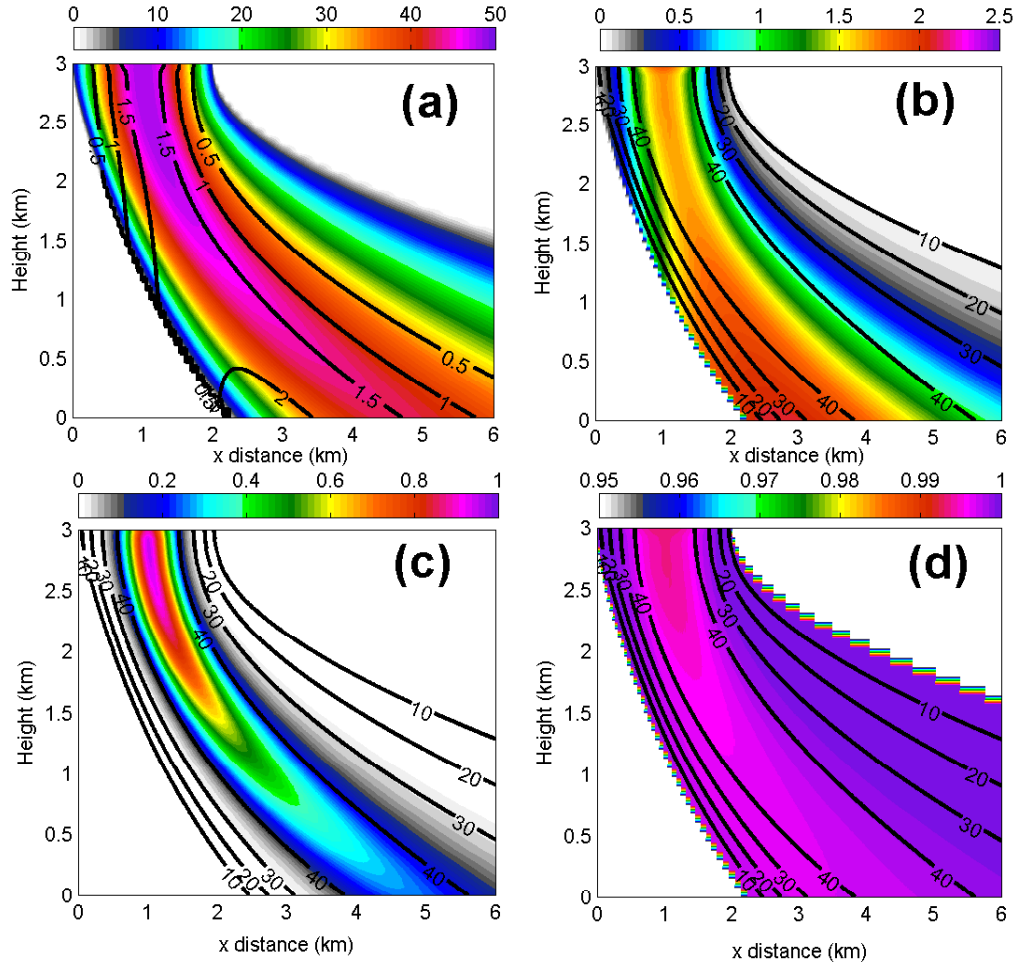


Fig. 5.11: As in Figs. 5.7 – 5.9, except results from the three-moment bulk scheme configuration are shown.

The difference fields in  $Z_{DR}$  between the bin model solution and those of the bulk schemes are illustrated in Fig 5.12. The 1M scheme substantially underpredicts  $Z_{DR}$  nearly everywhere (Fig. 5.12a), especially towards the ground where size sorting is most pronounced in the bin model results. Underpredictions are nearly 2 – 3 dB through a considerable depth of the rainshaft. The region of slightly negative differences aloft illustrates where the highest  $q$  (and thus highest  $Z_H$  and  $Z_{DR}$  in the 1M scheme) is offset from the region of enhanced  $Z_{DR}$  in the bin model results. In contrast, large overpredictions of  $Z_{DR}$  (>2 dB) are evident in the 2M scheme (Fig. 5.12b). The

narrow region of positive differences at the leading edge is caused by the difference in location of the front edge of the echo. Though the largest drops heavily weight the fallspeed of  $q$ , the smaller drops still have an impact (eqn. 5.4), which causes  $\bar{V}_q$  to be slightly less than the true fallspeed of the largest drops. Thus, the  $q$  field is advected slightly farther downstream than the actual edge of large drops determined by the bin model. Differences in the 3M scheme (Fig. 5.12c) are no more than 0.5 dB in magnitude, with slight underestimations over much of the rain shaft. These comparatively small errors are a result of excessive narrowing of the DSD, resulting in undercounting of the largest drops. These errors increase in magnitude towards the ground and towards the leading edge of the shaft because of the increasingly narrow DSD simulated by the 3M scheme's treatment of size sorting.

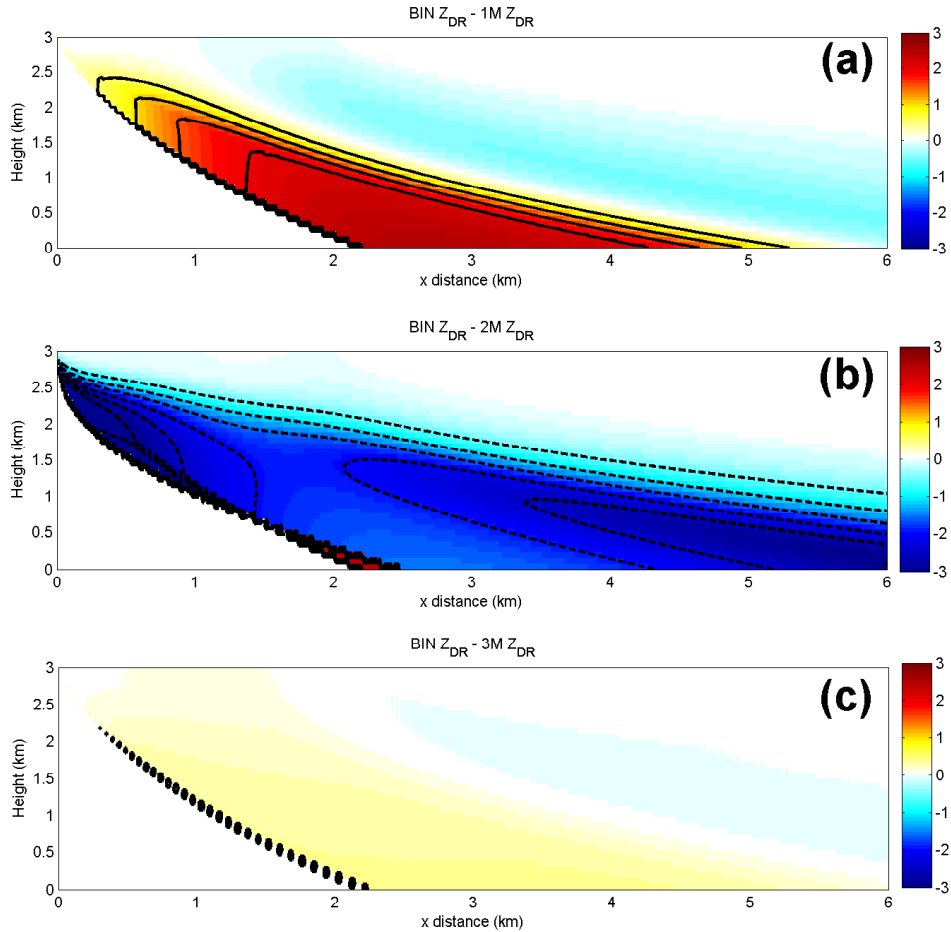


Fig. 5.12:  $Z_{DR}$  difference fields between (a) the bin model and the 1M bulk scheme, (b) the bin model and the 2M bulk scheme, and (c) the bin model and the 3M bulk scheme. Contours in 0.5-dB intervals are overlaid (solid lines for positive differences, dashed lines for negative).

As expected, changes in the magnitude of the vertical wind shear affect the maximal  $Z_{DR}$  found at low levels in the bin model. Increasing the maximum storm-relative winds further increases the maximum  $Z_{DR}$  values near the ground, as well as the vertical depth and width of a given  $Z_{DR}$  contour. The relative increase in maximal ground-level  $Z_{DR}$  increases approximately logarithmically with vertical wind shear (not shown). Additionally, the DSD aloft controls the relative change in  $Z_{DR}$ , as initial DSDs characterized by larger  $Z_{DR}$  produce smaller relative changes at the ground (i.e.,

size sorting acting on DSDs that begin with significant contributions from large drops will produce comparatively smaller low-level  $Z_{DR}$  enhancements).

The simulations above consider the case of unidirectional vertical wind shear. It is worth mentioning that size sorting by *directional* wind shear can produce unique polarimetric radar signatures. Using a simplified three-dimensional bin model of precipitation fallout and advection, Kumjian and Ryzhkov (2009) showed that size sorting is capable of explaining the observed “ $Z_{DR}$  arc” signature along the forward flank precipitation echo of supercell storms. The strong directional and speed shear common in supercell inflow environments sorts raindrops in such a manner to reproduce the observed shape and alignment of the  $Z_{DR}$  arc signature. Further, Kumjian and Ryzhkov (2009) found a positive correlation between the simulated magnitude of the maximum  $Z_{DR}$  in the simulated signature and the storm-relative environmental helicity in the inflow environment. Thus, unidirectional shear alone can provide enhancements of  $Z_{DR}$  at low levels, but the addition of directional shear can also alter the alignment of the observed  $Z_{DR}$  enhancement.

#### **4. Polarimetric Radar Observations**

As demonstrated in the preceding simulations, size sorting leads to an increase in  $Z_{DR}$  coincident with a decrease in  $Z_H$  (and  $K_{DP}$ ). Often, the enhancement of  $Z_{DR}$  is located along a gradient of  $Z_H$ . Indeed, polarimetric radar observations (particularly in convective storms) routinely reveal such patterns of  $Z_H$  and  $Z_{DR}$  that may be attributed to size sorting. For example, Figure 5.13 is a genuine RHI (or vertical cross-section) through a mesoscale convective system that demonstrates the impact of size sorting on

the observed polarimetric variables at a snapshot in time. Along the leading edge of the squall line, large values of  $Z_{DR}$  collocated with modest  $Z_H$  are found starting at a range of about 65 km through about 80 km. The highest values of  $Z_{DR}$  ( $> 4$  dB) are found at the base of a developing convective core (evident by the enhanced  $Z_H$  aloft). The  $Z_{DR}$  enhancement owing to size sorting is a result of some combination of transient differential sedimentation and the updraft, the extent of which is unknown owing to the lack of vertical velocity measurements in the storm.  $Z_{DR}$  values of 2 – 4 dB for  $Z_H < 30$  dBZ represent a significant departure (1 – 3 dB) from what is expected in typical rain DSDs in Oklahoma (e.g., Cao et al. 2008), demonstrating the efficiency of the size sorting process at substantially altering the DSD.

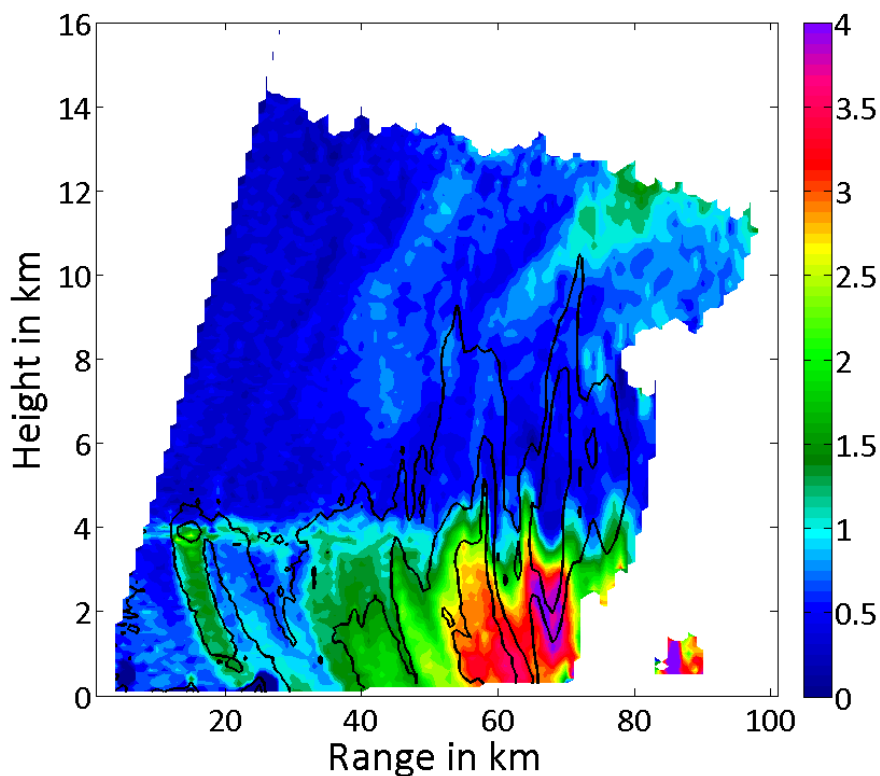


Fig. 5.13: Observations from 17 June 2005, at 0544 UTC, along the azimuth  $191^\circ$ .  $Z_{DR}$  (in dB) is shaded, with  $Z_H$  contours of 30, 40, and 50 dBZ overlaid. The abscissa is range (distance) from the KOUN radar. The high  $Z_{DR}$  region near the ground at a range of about 85 km is from biological scatterers (i.e., insects and/or birds).



The  $Z_{DR}$  arc signature in supercell storms (Fig. 5.14) is a unique example of size sorting by wind shear, characterized by large  $Z_{DR}$  along the gradient in  $Z_H$ . Indeed,  $Z_{DR}$  values in excess of 4 dB are present outside the 30-dBZ  $Z_H$  contour, indicating a sparse concentration of large drops. The size sorting mechanism hypothesized to produce the  $Z_{DR}$  arc signature is the strong wind shear (both directional and speed) in supercell environments (Kumjian and Ryzhkov 2008b, 2009). As such, it contains potentially useful information regarding the type of environmental wind shear available to the storm and can serve as an indicator of storm severity (Kumjian and Ryzhkov 2009).

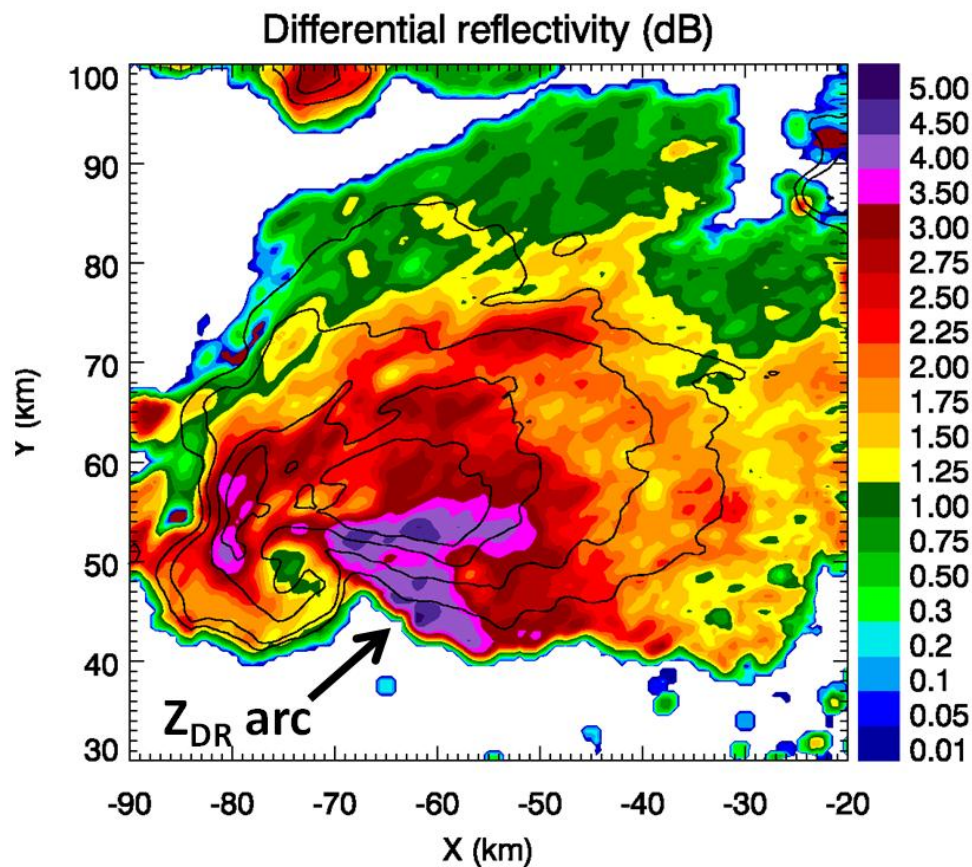


Fig. 5.14: Example PPI from 30 May 2004 at  $0.5^\circ$  elevation, at 0044 UTC. The color shading is  $Z_{DR}$  (dB), with the 30-, 40-, 50-, and 55-dBZ contours of  $Z_H$  overlaid. Distances are relative to the location of the KOUN radar.

Deep convective storms are not the only situations in which size sorting is observed. Figure 5.15 is a genuine RHI scan from near Bonn, Germany, taken on 22 June 2011 with the Bonn X-band Polarimetric radar (BOXPOL), operated by the Meteorological Institute of the University of Bonn. The scan captures an isolated cell producing light to moderate rain falling into an environment with vertical wind shear. The observed fields of  $Z_H$  and  $Z_{DR}$  beneath the melting layer are qualitatively similar to the modeled rainshaft in Fig. 5.7. Namely, the highest  $Z_{DR}$  is located at the leading edge of the shaft along a gradient in  $Z_H$  (located at about 29 km in range), whereas the higher  $Z_H$  is offset and coincident with lower  $Z_{DR}$  (30 – 31 km in range). A vertical profile of the Doppler velocities extracted from a range of 29 km (Fig. 5.16) illustrates the vertical shear, as inbound (negative) velocities become increasingly negative with height. The shear is strongest in the layer near 1 km AGL, where magnitudes reach  $\sim 0.02 \text{ s}^{-1}$ .

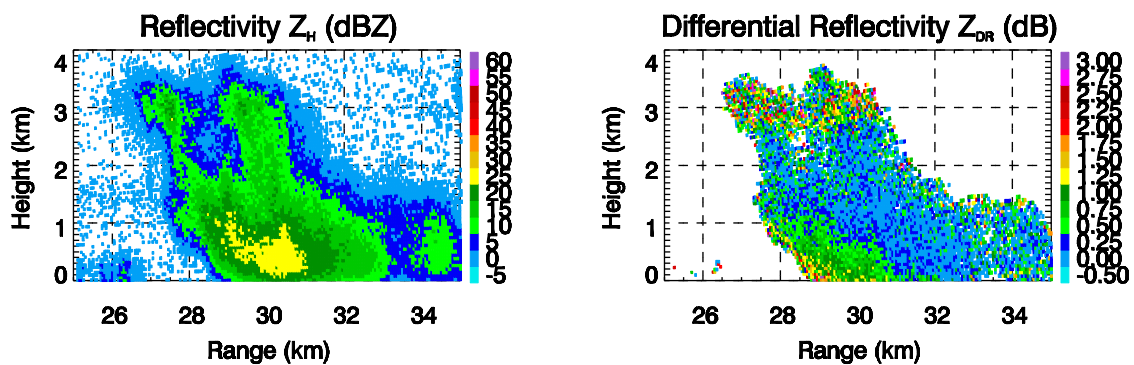


Fig. 5.15: RHI scans of  $Z_H$  (left) and  $Z_{DR}$  (right), taken at 0404 UTC 22 June 2011 from the Bonn X-band Polarimetric radar (BOXPOL) operated by the Meteorological Institute at the Universität Bonn (Germany). Data are from the  $309.5^\circ$  azimuth.

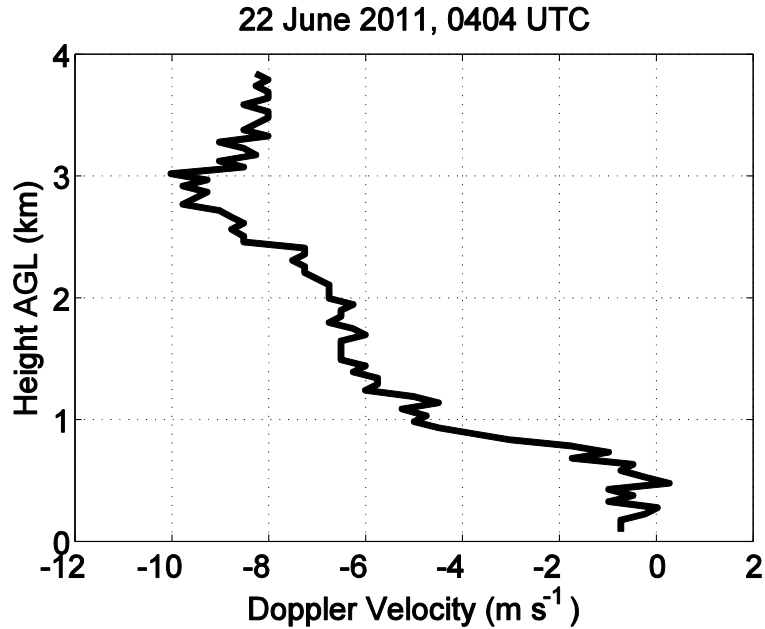


Fig. 5.16: Vertical profile of Doppler velocity extracted from the RHI shown in Figure 15, at a range of 29 km.

Figure 5.17 depicts a different scenario on the same day, when widespread stratiform precipitation was present. At 0944 UTC (Fig. 5.17, top panels), a distinct melting layer “bright band” is evident between 2.5 and 3.0 km AGL in both  $Z_H$  and  $Z_{DR}$ . At this time, the majority of the rain has not fully reached the ground, evident in the lack of  $Z_H > 20$  dBZ below 1 km AGL (strong echoes near the surface are from ground clutter). Enhanced  $Z_{DR}$  is observed at the lower portions of the rain curtains, in the gradient of  $Z_H$ . The next RHI taken 5 minutes later reveals that all rain has reached the ground (Fig. 5.17, bottom panels), and the inverse correlation between  $Z_H$  and  $Z_{DR}$  is no longer found everywhere along the base of the shafts. This transient effect of differential sedimentation is reminiscent of the 1D model in section 3a.

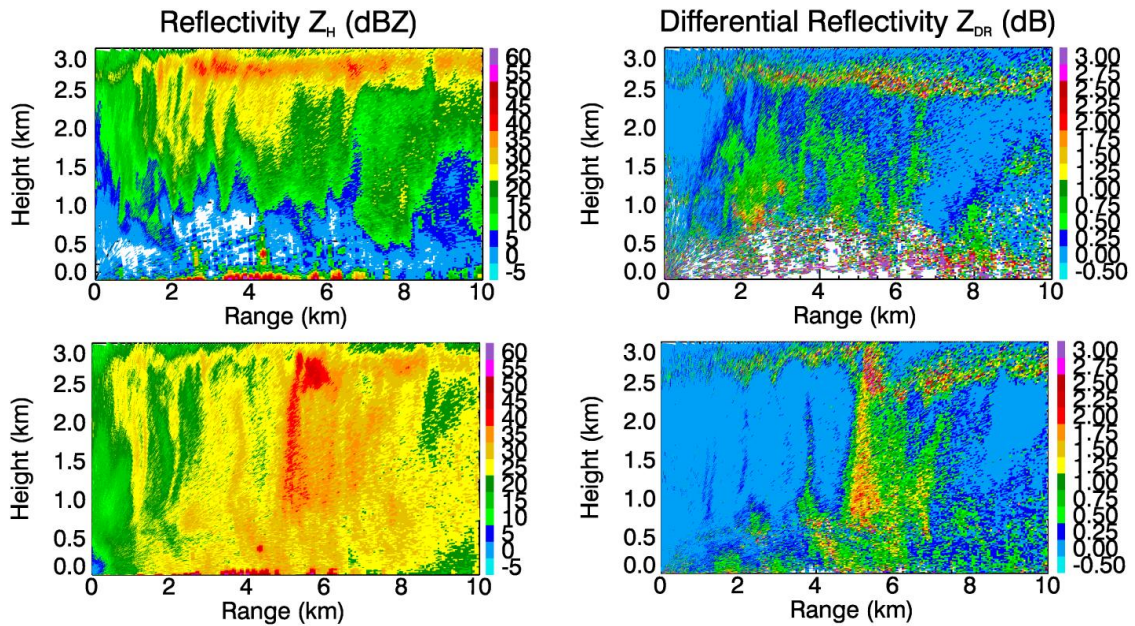


Fig. 5.17: As in Fig. 5.15, but from 0944 UTC (top panels) and 0949 UTC (bottom panels) on 22 June 2011. Data from BOXPOL, operated by the Meteorological Institute at the Universität Bonn (Germany).

Finally, Figure 5.18 is an illustrative example of several cells in various stages of development. The elevated cell located at about 11 km range has the highest  $Z_{DR}$  at the bottom of the rain shaft, along a gradient of  $Z_H$ , again indicative of the differential sedimentation flavor of size sorting. The cell at 13 km range again reveals high  $Z_{DR}$  at the lower portion of the rainshaft; however, this time, the  $Z_H$  values *also* increase towards the ground. Rather than indicating ongoing size sorting, the radar observations indicate that the vertical evolution of the DSD in this cell is dominated by some other process, such as raindrop growth by coalescence. Such an example demonstrates that one must assess  $Z_{DR}$  *and*  $Z_H$  to detect regions of ongoing size sorting. The example observations from Germany were all collected on the same day, demonstrating that while size sorting is often transient in nature, it is widespread in many types of precipitating systems.

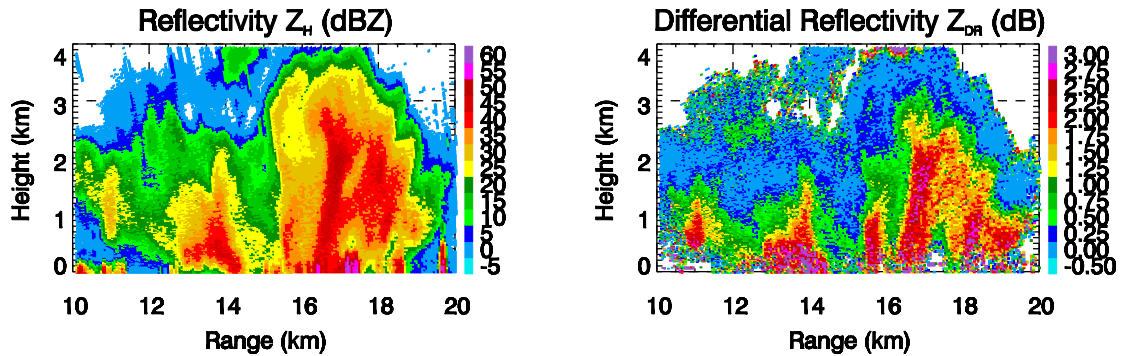


Fig. 5.18: As in Figs. 5.15 and 5.17, but from 1454 UTC on 22 June 2011. Data from BOXPOL, operated by the Meteorological Institute at the Universität Bonn (Germany).

## 5. Discussion

In nature, precipitation formation in continental deep convective storms is generally dominated by ice microphysical processes (e.g., Dye et al. 1974; Rosenfeld and Ulbrich 2003, among others). Thus, melting of graupel and small hail particles often is responsible for the production of large raindrops. A notable exception is in tropical convection, where large raindrops forming from efficient coalescence growth in the absence of ice processes are also possible (e.g., Rauber et al. 1991; Szumowski et al. 1997; Hobbs and Rangno 2004). As a consequence of shedding of excess meltwater (Rasmussen and Heymsfield, 1987), small hail and graupel of sizes between approximately 8 – 14 mm melt into large raindrops of about 8 mm in size, producing a relative excess of larger drops (Ryzhkov et al. 2009). Such an enhancement of the concentration of the largest drops can amplify the size sorting effect by producing larger  $Z_{DR}$  values. This enhancement is probably important for attaining maximal  $Z_{DR}$  values, because although  $Z_{DR}$  increases monotonically for increasing raindrop size (at S band), the fallspeed of drops larger than about 6 mm is essentially the same, according to the

Brandes et al. (2002) relation. This leveling-off of the fall speeds thereby inhibits further sorting. Further observations of large drop fall speeds through video disdrometer measurements is critical for better understanding the sorting potential of the largest drop sizes.

As demonstrated above, rain DSDs altered by size sorting tend to be narrow with large median drop sizes (e.g., Battan 1977; Zawadzki and de Agostinho Antonio 1988; Rosenfeld and Ulbrich 2003; MY05a). Narrowing of the DSD is at the expense of the smaller drops, which are sorted out of the distribution. The effect of this process on the DSD is analogous to evaporation (e.g., Rosenfeld and Ulbrich 2003), which also preferentially depletes the smaller drops. Observations of  $Z_{DR}$  enhancements are sometimes explained by invoking evaporation as a significant contribution (e.g., Jung et al. 2010). However, Kumjian and Ryzhkov (2010) quantified the impact of evaporation on the polarimetric radar variables in rain and demonstrated that the enhancement of  $Z_{DR}$  owing to evaporation (no more than 0.1 – 0.2 dB at S band, even in extreme cases) is completely dominated by enhancements in  $Z_{DR}$  owing to size sorting. Size sorting is more efficient at narrowing the DSD than evaporation.

In bulk microphysics parameterization schemes with fixed shape parameter ( $\alpha$  in eqn. 5.2), such substantial narrowing of the DSD by size sorting (represented by increased  $\alpha$ ) obviously is not captured. To address this shortcoming, MY05a and MM10 propose a diagnostic shape parameter, or one that is allowed to vary as a function of the other two prognostic moments. In the most common configuration for bulk microphysics schemes, the two prognostic moments are the mass mixing ratio  $q$  and the total number concentration  $N_{TOT}$ , which are proportional to the 3<sup>rd</sup> and 0<sup>th</sup>

moments ( $M_3$  and  $M_0$ , respectively). A useful parameter characterizing the DSD is the mean-mass diameter, defined as

$$D_m = \left(\frac{M_3}{M_0}\right)^{1/3} = \left(\frac{6\rho_{air}q}{\pi\rho_w N_{TOT}}\right)^{1/3} = \left[\frac{\Gamma(4 + \alpha)}{\Gamma(1 + \alpha)} \frac{1}{\Lambda^3}\right]. \quad (5.15)$$

In multi-moment bulk microphysics schemes, size sorting is represented by  $N_{TOT}$  having a smaller sedimentation velocity than  $(\bar{V}_q > \bar{V}_N)$ . Therefore,  $N_{TOT}$  is reduced (“sorted”) more than  $q$ , resulting in larger  $D_m$ . Larger values of  $D_m$  are analogous (but not equivalent) to the larger median diameters observed in situations of ongoing size sorting. Thus, MM10 suggest the following diagnostic relation for the shape parameter  $\alpha$  (with prognostic moments  $M_3$  and  $M_0$ )<sup>5</sup>

$$\alpha = 11.8(D_m - 0.7)^2 + 2.0, \quad (5.16)$$

where  $D_m$  is given in mm. For  $D_m > 0.7$  mm, the shape parameter increases quadratically with  $D_m$ . Thus, size sorting is parameterized by dramatically narrowing the DSD with increasing  $D_m$ , an approach similar to those adopted in MY05a and Seifert (2008). Note that the minimum shape parameter allowed by this parameterization is 2.0.

Another relation between DSD parameters is suggested in Cao et al. (2008), based on disdrometer observations:

$$\alpha = -0.0201\Lambda^2 + 0.902\Lambda - 1.718, \quad (5.17)$$

where the slope parameter  $\Lambda$  is expressed in  $\text{mm}^{-1}$ . This relation was derived semi-empirically based on thousands of disdrometer measurements in central Oklahoma and is similar to earlier work by Zhang et al. (2001) and Brandes et al. (2004a,b) based on

---

<sup>5</sup> Note that the diagnostic relation proposed in MM10 is generalized such that any two moments may be used. Here,  $M_3$  and  $M_0$  are shown because of their common use, and for subsequent comparisons.

disdrometer observations in Florida, both of which are verified by polarimetric radar measurements.

Note that negative values of shape parameter are allowed in Eqn. (5.17), in contrast to the relation in Eqn. (5.16). These negative shape parameters (*which are observed in real DSDs*) are usually associated with small slope parameters, indicating a rather broad, flat DSD commonly observed in convective storms. Such DSDs are usually characterized by large median diameters (and thus  $Z_{DR}$ , and  $D_m$ ). The disagreement is obvious (Fig. 5.19): in cases of large  $D_m$ , Eqn. (5.16) suggests a very large positive  $\alpha$ , whereas Eqn. (5.17) suggests a negative value for  $\alpha$  (Fig. 5.19b).

Why the disagreement? Size sorting such as differential sedimentation tends to narrow the distribution, as shown in numerous previous studies as well as the results presented above. However, disdrometer measurements of Cao et al. (2008) generally do not show values of  $\alpha$  in excess of about 15 or 20 at the ground.



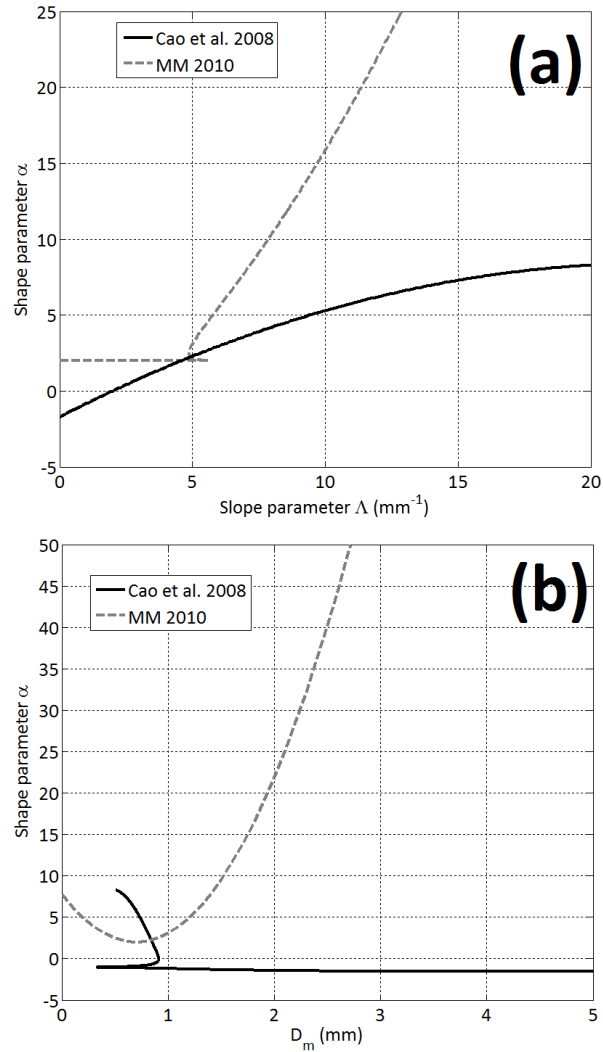


Fig. 5.19: Comparison of relations between DSD parameters by Cao et al. (2008), indicated by the solid black line, and Milbrandt and McTaggart-Cowan (2010; MM 2010), indicated by the dashed gray line. (a) The relation between DSD slope parameter  $\Lambda$  and shape parameter  $\alpha$  is shown. (b) The relation between mean-mass diameter  $D_m$  and shape parameter  $\alpha$  is shown. Relations were determined by Eqns. (5.16-5.17).

Consideration of sampling issues partly resolves the disagreement. Disdrometer observations in Cao et al. (2008) used only 1-minute DSDs with more than 50 drops counted. According to Cao et al. (2008) and others, the 2D video disdrometer has a sampling area on the order of  $\sim 0.01 \text{ m}^2$ . For a “big drop” DSD that forms as a result of size sorting, the characteristic drop velocity is about  $8 - 9 \text{ m s}^{-1}$ . Using  $9 \text{ m s}^{-1}$ , the

characteristic sampling volume of the disdrometer is about  $5.4 \text{ m}^3$ . Using the 1D sedimentation model (section 3a of this chapter), one can calculate the total number concentration of drops by simply summing the bin model DSD at each height level. Thus, we can determine where the disdrometer would sample less than 50 drops, assuming a sampling volume of  $5.4 \text{ m}^3$ . For the time shown in Figure 5.2, the total number of drops sampled in one minute is about 3.3. However, the hypothetical sampling volume would begin sampling  $> 50$  drops when the DSD located at about 400 m AGL reaches the surface (Fig. 5.20). At  $9 \text{ m s}^{-1}$ , that height corresponds to about 45 seconds. Therefore, only about the first 45 – 60 seconds of the “size sorting” DSD during fallout will be sampled by the 2D video disdrometer in the case of our 1-D fallout model.

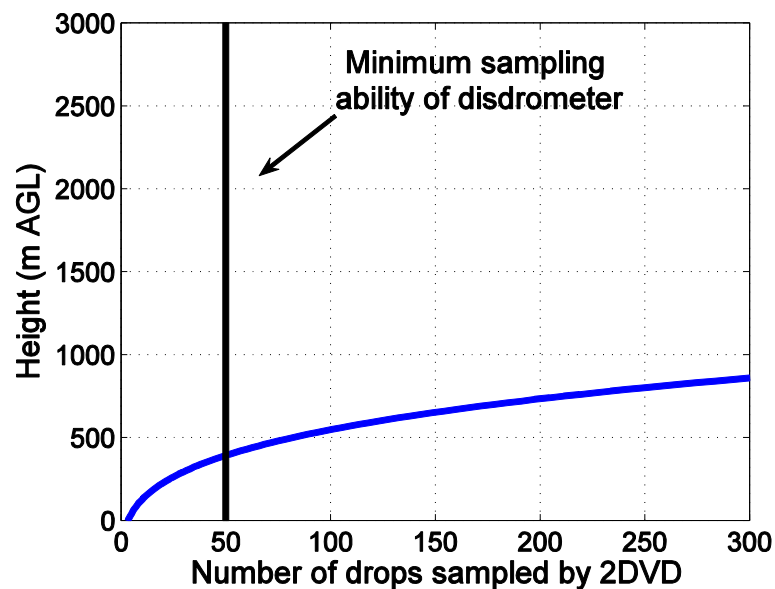


Figure 5.20: Number of drops sampled by the 2D video disdrometer. The vertical axis indicates height AGL of the DSD at the time shown in Figure 5.2 (this can be thought of as roughly corresponding to time). The vertical bar at 50 drops indicates the minimum sampling ability of the disdrometer. Calculations performed on the DSDs simulated by the bin solution of the 1D fallout model (Fig. 5.2).

If we apply the same type of calculations to the 2D wind shear model (section 3c), the first ~1 km of the rain shaft leading edge are not sampled by the 2D video disdrometer; in other words, the disdrometer would not sample 50 drops until the point at  $x = 3$  km in the 2D rain shaft in Figure 5.7. In conclusion, such a threshold ( $> 50$  drops) would obviously remove some situations where size sorting is a dominant process, such as at the onset of precipitation and at the leading edge of storms in sheared environments. Undercatchment of large drops is also a well-known sampling issue for disdrometers (e.g., Tokay et al. 1999; Williams et al. 2000; Schuur et al. 2001; Cao et al. 2008, among others). Thus, cases where size sorting is dominant likely do not contribute to the statistical analyses that produce the DSD parameter relations based on disdrometer observations. Cao et al. (2008) formulated a correction for this by identifying where their relation (eqn. 5.17) is likely to produce errors with dual-polarization radar measurements; namely, in areas of size sorting characterized by large  $Z_{DR}$  and relatively low  $Z_H$ .

The incompatibility of the relations is a two-way street, though. As demonstrated by observations, most DSDs characterized by large median drop sizes (and/or  $D_m$ ) are *not* the result of size sorting. Thus, applying a relation such as Eqn. (5.16) everywhere and at all times may not be appropriate. Similar to the refinement of the  $\alpha - \Lambda$  relation by Cao et al. (2008), the relation in Eqn. (5.16) may need to be corrected in cases where large  $D_m$  is the result of processes that produced a broader, flatter spectrum. An analogy can be made with polarimetric measurements: high  $Z_{DR}$  by itself does not necessarily mean size sorting; one must consider *both*  $Z_H$  and  $Z_{DR}$  to

determine areas where size sorting is possible. Such considerations may become especially important in future attempts to assimilate polarimetric radar data directly into numerical models with bulk microphysics schemes.

The results demonstrating the deficiencies of bulk microphysics parameterizations in simulating the polarimetric radar variables in situations of ongoing size sorting have implications for attempts to assimilate polarimetric data. Because of the inability of 1M schemes to produce size sorting, assimilation of  $Z_{DR}$  into a model using such a scheme will likely increase analysis errors in cases of size sorting (e.g., Jung et al. 2010). This is because, in the framework of a 1M scheme, there is a one-to-one correspondence between the assimilated observation ( $Z_{DR}$ ) and the predicted model variable (e.g., rain mass mixing ratio  $q$ ). Thus, regions of high  $Z_{DR}$  would correspond to larger  $q$ . In the case of observed size sorting, the model would adjust to the high- $Z_{DR}$  observation by incorrectly increasing rain mass at that location, which is exactly opposite of the physical situation. The incorrect inclusion of additional water mass can affect other processes such as evaporation, which has ramifications for the development and strength of cold pools (e.g., Dawson et al. 2010). Therefore, if using 1M microphysics schemes in assimilation experiments where size sorting may be prevalent (e.g., supercells or other deep moist convection), it is best *not* to use  $Z_{DR}$  data.

2M schemes with fixed shape parameter ( $\alpha$ ) suffer from excessive size sorting. For this reason, diagnostic- $\alpha$  (e.g., MY05b; MM10) and other techniques (e.g., Mansell 2010) were developed. In MY05 and MM10,  $\alpha$  increases with increasing mean-mass diameter  $D_m$  to reflect the narrowing of DSDs undergoing size sorting.  $Z_{DR}$  offers an attractive observation that can be related to  $D_m$ ; of course, high  $Z_{DR}$  (and large  $D_m$ )

alone does not necessarily mean size sorting is occurring. Therefore, it may be desirable to “flag” areas of the storm where size sorting may be occurring using  $Z_H$  and  $Z_{DR}$  observations, thereby limiting the use of such diagnostic- $\alpha$  relations only to regions where they are necessary. Such a flagging system could make use of predetermined  $Z_H$  and  $Z_{DR}$  thresholds, or locations in which the  $Z_H$  and  $Z_{DR}$  data exhibit a strong negative correlation.

Though size sorting may not be widespread throughout all precipitating systems, it can be most pronounced and sustained in deep moist convective storms (DMCS), especially supercells. Many storm-scale data assimilation studies focus on such DMCS, both in observing system simulation experiments (OSSEs; e.g., Snyder and Zhang 2003; Tong and Xue 2005; Jung et al. 2008; Yussouf and Stensrud 2012) as well as real-data experiments (e.g., Hu et al. 2006a,b; Aksoy et al. 2009; Lim and Sun 2010; Schenkman et al. 2011a, 2011b; Dowell et al. 2011; Snook et al. 2011). Thus, the challenges associated with assimilating polarimetric radar data in cases of vigorous size sorting may be encountered in future endeavors when DMCS are investigated in high-resolution numerical models.

## **6. Summary**

This chapter has reviewed size sorting of precipitation particles by the most frequently-observed mechanisms, including differential sedimentation, updrafts, and vertical wind shear. Simple bin models were constructed to quantify the impact of size sorting by sedimentation, an updraft, and vertical wind shear on the polarimetric radar variables:  $Z_H$ ,  $Z_{DR}$ ,  $K_{DP}$ , and  $\rho_{hv}$ . Additionally, the treatment of size sorting by bulk

microphysics parameterizations was discussed, and errors in the simulated polarimetric radar variables were quantified.

The following summarizes the key points:

1. Size sorting of raindrops in the simplified bin models has a significant impact on the polarimetric radar variables, most notably leading to an increase in  $Z_{DR}$  along a gradient of  $Z_H$ . These results are in agreement with previous observational studies (e.g., Ryzhkov et al. 2005c; Kumjian and Ryzhkov 2008a,b, 2009).
2. The initial transient effect of differential sedimentation has been explored thoroughly by the modeling community. However, the transient effect can be *maintained* by updrafts and vertical wind shear. These size sorting mechanisms have not been investigated widely in the framework of bulk microphysics schemes, but are explored here.
3. Single-moment parameterizations are incapable simulating size sorting, in agreement with many previous studies (e.g., Wacker and Seifert 2001; MY05a; among others). This inability to reproduce size sorting results in large errors in  $Z_{DR}$  computed from the resulting DSDs. Also in agreement with earlier studies, double-moment schemes with fixed shape parameters can suffer from excessive “size sorting.” This leads to dramatic overestimation of  $Z_{DR}$  (by several dB),  $Z_H$ , and  $K_{DP}$  in large parts of a simulated rainshaft encountering wind shear, as well as beneath newly-precipitating clouds. Use of a diagnosed shape parameter in a two-moment scheme or a prognosed shape parameter in a three-moment scheme largely

mitigates the errors associated with size sorting. However, excessive narrowing of the DSD may occur if the shape parameter is allowed to grow to unrealistic values. Limiting the maximum value of the shape parameter to 20.0 – 30.0 reduces the errors.

4. Though size sorting is most apparent in deep convective storms, examples from other precipitation regimes (including stratiform rain and isolated shallow convection) demonstrate that size sorting is widespread in occurrence and is possible in any precipitating system.
5. Special care must be taken in attempts to assimilate polarimetric radar data into numerical weather prediction models, especially  $Z_{DR}$  in cases of ongoing size sorting. Problems may arise because of the fundamental disconnect between the physical process of size sorting (which strongly affects  $Z_{DR}$ ) and the parameterization of the process in bulk schemes, which in some cases does not resemble reality.

## **Chapter 6: The Impact of Raindrop Evaporation on the Polarimetric Radar Variables.**

The material in this chapter is derived from Kumjian and Ryzhkov (2010).

### **1. Introduction.**

As rain falls from a precipitating cloud, the distribution of mass amongst different sized drops is governed by several microphysical processes. The evolution of this drop size distribution (DSD) is a complex problem that has received considerable attention in the literature over the past few decades. The dominant microphysical processes governing the evolution of the DSD as drops descend towards the ground include differential sedimentation or size sorting, spontaneous breakup, collisional breakup, coalescence, and growth or decay by vapor diffusion (i.e., condensation or evaporation). Early works by Young (1975), Srivastava (1978), and Johnson (1982) determined that spontaneous breakup is relatively unimportant compared to collisional breakup, especially for larger rainwater contents. Laboratory studies by Low and List (1982a) and Beard and Ochs (1995) have improved our understanding of collisional processes such as coalescence and breakup. Based on their experimental data, Low and List (1982a,b) developed coalescence efficiencies and a parameterization for the fragment size distribution of particles resulting from the collisional breakup of raindrops in the so-called filament, sheet, and disk modes. These and similar parameterizations have been widely analyzed, improved, and utilized in zero-dimensional box models and one-dimensional rainshaft models (e.g., Gillespie and List



1976, 1978; List and Gillespie 1976; Low and List 1982b; Brown 1986, 1987; List and McFarquhar 1990, among others). Evaporation beneath the cloud base was included in the models by List et al. (1987), Tzivion et al. (1989), Brown (1993, 1994), Hu and Srivastava (1995), and Seifert (2008).

These studies and others have found that the collisional processes of coalescence and breakup tend to dominate the evolution of the DSD shape. These processes tend to drive an arbitrary initial DSD towards a family of equilibrium shapes which are related through simple multiplicative factors (List et al. 1987; Brown 1987, 1993; Hu and Srivastava 1995). The latter authors found that DSD evolution can be categorized into two phases: (1) collisional processes dominate the evolution of the spectrum as it approaches equilibrium, followed by (2) evaporation dominates the spectral evolution, smoothing maxima and decreasing the overall mass (while only slowly changing the shape of the distribution). If the initial drop size distribution is already close to its equilibrium shape, Hu and Srivastava (1995) found that the first stage does not occur. Note that some of the equilibrium DSDs in the aforementioned works are the result of artifacts in the original Low and List (1982a,b) parameterization; the parameterization by McFarquhar (2004) based on the Low and List data alleviates some of these shortcomings and produces equilibrium distributions that are quite different than those found in the previous studies.

The collisional processes themselves do not contribute to or deplete liquid water content in the sub-cloud layer: they simply redistribute mass to different sizes. However, net evaporation (the diffusion of water vapor away from drops) depletes the total rainwater content, which has significant implications for quantitative precipitation

estimation. In addition, the generation of negative buoyancy via evaporational cooling plays an important role in storm evolution, including the production of severe downdrafts (e.g., Srivastava 1985, 1987) and even possibly affecting a supercell storm's likelihood of producing a tornado (e.g., Markowski et al. 2002, 2003; Grzych et al. 2007). Despite the many studies that quantify the impact of environmental conditions on the rate of evaporation and how evaporation affects the rainfall rate, DSD, downdrafts, and radar reflectivity factor (e.g., Srivastava 1985, 1987; Rosenfeld and Mintz 1988; Hu and Srivastava 1995), there is a paucity of studies investigating how evaporation is manifested in the polarimetric variables. A notable exception is Li and Srivastava (2001), who quantified the impact of evaporation on differential reflectivity  $Z_{DR}$ . In contrast, this chapter quantifies the sensitivity of all polarimetric radar variables to various environmental thermodynamic conditions, and variations in DSDs for light rainfall rates, as well as to formulate recommendations to aid in hydrometeorological rainfall estimation. As such, this work should not be viewed as an attempt to investigate DSD evolution; rather, the goal is to quantify the impact of evaporation on the polarimetric radar variables as a preliminary step in determining the polarimetric fingerprints of warm rain microphysical processes.

The following section will describe the physics of raindrop evaporation. The qualitative impact of evaporation on the polarimetric variables will be conceptualized to provide a framework for the quantitative analysis conducted in the remainder of the paper. This quantification will be done using an explicit microphysics model that is described in section 3. Section 4 details the results of model sensitivity tests meant to explore the parameter space, and of simulations of different evaporation scenarios. The

impact of evaporation on rainfall estimation is explored in the discussion section 5, followed by a brief comparison with an observational study in section 6. Section 7 is a summary of the important conclusions.

## 2. Physics of Evaporation

Liquid drops in clouds can grow by the diffusion of water vapor from the ambient environment if the ambient vapor density ( $\rho_v$ ) is greater than the vapor density at the droplet's surface ( $\rho_{vr}$ ). On the other hand, if the vapor density at the surface of the drop exceeds the vapor density in the ambient environment, vapor is diffused away from the drop (evaporation). These scenarios are depicted in Figure 6.1.

The rate of mass diffusion from a *falling* drop can be written as

$$\frac{dm}{dt} = 4\pi r \bar{f}_v D_v (\rho_v - \rho_{vr}), \quad (6.1)$$

where  $r$  is the radius of the drop,  $\bar{f}_v$  is the ventilation coefficient for vapor diffusivity to account for the ventilation effects of a drop falling,  $D_v$  is the molecular diffusion coefficient of water vapor in air, and  $\rho_v$  and  $\rho_{vr}$  are the vapor density of the ambient environment and at the surface of the drop, respectively. Following Pruppacher and Klett (1978) and Rogers and Yau (1989), one can derive an approximate expression describing the time rate of change of the drop radius undergoing growth or decay by vapor diffusion:

$$r \frac{dr}{dt} = \frac{S - 1}{F_K + F_D}. \quad (6.2)$$

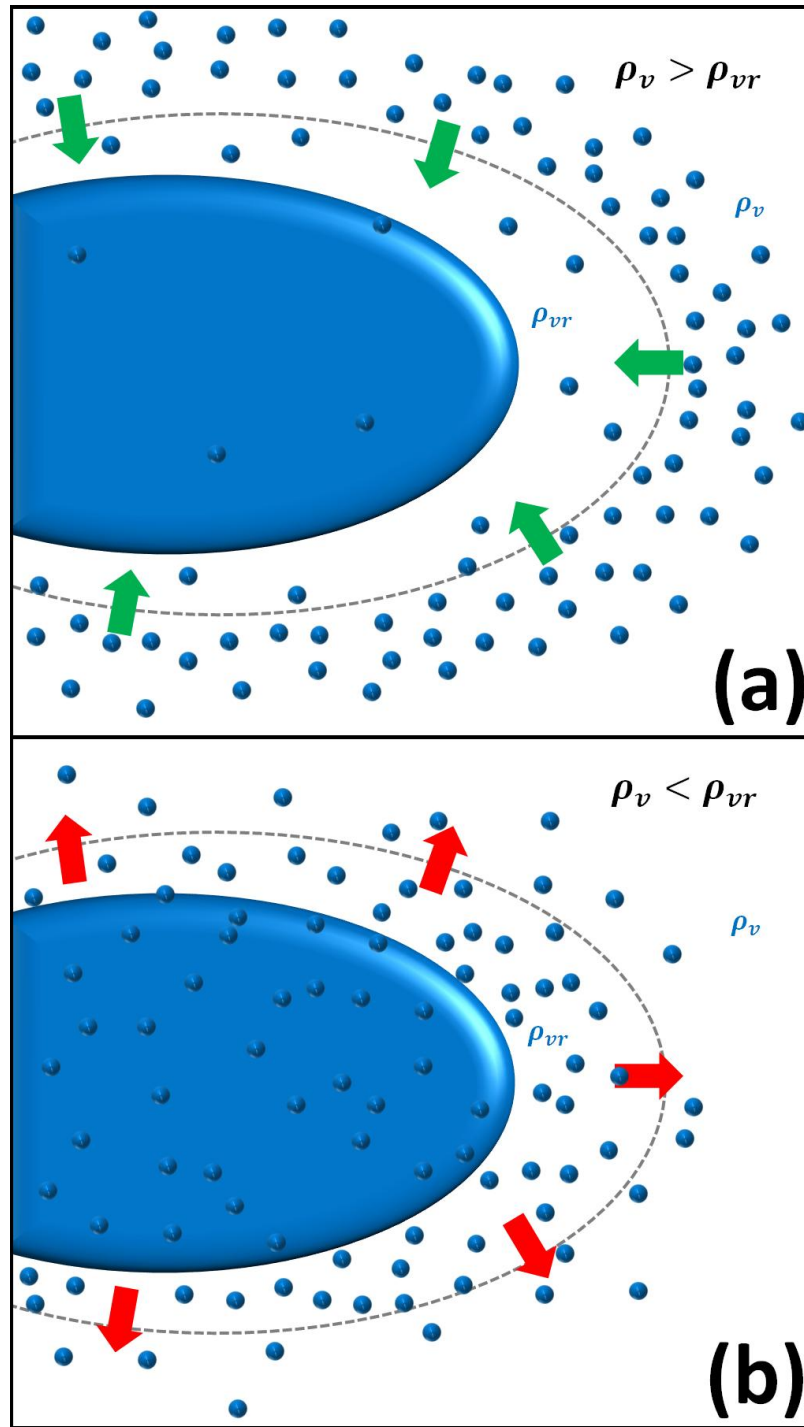


Fig. 6.1: Cartoon illustrating net vapor diffusion (a) onto a drop from the ambient environment (condensation), and (b) away from a drop into the ambient environment (evaporation). The dashed gray line represents a volume around the drop demarcating the near-drop environment and the ambient environment.

In eqn. (6.2),  $S$  is the saturation ratio, and  $F_K$  and  $F_D$  are terms related to heat conduction and vapor diffusion, respectively:

$$F_K = \left( \frac{L_v}{R_v T} - 1 \right) \frac{L_v \rho_w}{\bar{f}_h k_a T} \quad (6.3)$$

and

$$F_D = \frac{\rho_w R_v T}{\bar{f}_v D_v e_s(T)}. \quad (6.4)$$

In the above terms,  $L_v$  is the latent heat of vaporization,  $R_v$  is the gas constant for water vapor,  $T$  is the air temperature,  $\rho_w$  is the density of liquid water,  $k_a$  is the thermal conductivity of air,  $e_s(T)$  is the saturation vapor pressure of air as a function of temperature. The ventilation coefficients for vapor and heat are defined as

$$\bar{f}_v = 0.78 + 0.308 N_{Sc}^{1/3} N_{Re}^{1/2} \quad (6.5)$$

and

$$\bar{f}_h = 0.78 + 0.308 N_{Pr}^{1/3} N_{Re}^{1/2} \quad (6.6)$$

as in Pruppacher and Klett (1978) and Rasmussen and Heymsfield (1987). The ventilation coefficients are functions of the Schmidt ( $N_{Sc}$ ), Reynolds ( $N_{Re}$ ), and Prandtl ( $N_{Pr}$ ) numbers. The temperature dependencies of the thermodynamic quantities follow Rasmussen and Heymsfield (1987), but are provided in SI units here for convenience. The latent enthalpy of vaporization (in  $\text{J kg}^{-1}$ ) as a function of temperature (in K) is given as

$$L_v = 2.499 \times 10^6 \left( \frac{273.15}{T} \right)^\gamma, \quad (6.7)$$

where the exponent  $\gamma$  is

$$\gamma = 0.167 + (3.67 \times 10^{-4})T. \quad (6.8)$$

The thermal conductivity of air (in  $\text{J m}^{-1} \text{s}^{-1} \text{K}^{-1}$ ) is expressed as

$$k_a = (0.441635 + 0.0071T) \times 10^{-2}. \quad (6.9)$$

Similarly, diffusivity of water vapor in air ( $\text{m}^2 \text{s}^{-1}$ ) is expressed as

$$D_v = 2.11 \times 10^{-5} \left( \frac{T}{273.15} \right)^{1.94} \left( \frac{p_0}{p} \right), \quad (6.10)$$

where  $p_0$  is the reference level pressure, taken as 1000 hPa. Saturation vapor pressure (in hPa) as a function of temperature is approximated following Rogers and Yau (1989):

$$e_s(T) = 2.53 \times 10^9 \exp\left(-\frac{5420}{T}\right). \quad (6.11)$$

In order to calculate the Schmidt, Prandtl, and Reynolds numbers, the kinematic viscosity of the air ( $\nu_a$ ) is required. The kinematic viscosity (in  $\text{m}^2 \text{s}^{-1}$ ) is dependent on the dynamic viscosity of the air ( $\eta_a$ ) as well as the air density,  $\rho_{air}$ :

$$\nu_a = \eta_a / \rho_{air}. \quad (6.12)$$

The dynamic viscosity of air ( $\text{kg m}^{-1} \text{s}^{-1}$ ) for temperatures above freezing is assumed to be

$$\eta_a = (0.379565 + 0.0049T) \times 10^{-5}, \quad (6.13)$$

and the air density is calculated from the environmental thermodynamic profiles via the ideal gas law.

For now, we focus on a qualitative interpretation of (6.2). For subsaturated environments (where  $S < 1$ ), raindrop radius will decrease, indicating decay through evaporation. Also, because  $dr/dt$  is inversely proportional to drop radius, the radii of smaller drops will decrease more rapidly during evaporation than larger drops. A simple thought experiment (“*gedankenexperiment*”) suggests that the preferential depletion of smaller drops will result in a decrease in observed  $Z_H$  and  $K_{DP}$  with an *increase* in the

observed  $Z_{DR}$ . The observed decrease in  $Z_H$  has been well documented and is intuitive. Decreasing drop diameters across the spectrum and a decrease in the concentration of smaller drops (those that are totally evaporated) will result in a decreased magnitude of backscattered signal. Recall that  $K_{DP}$  is less sensitive than  $Z_H$  to large drops, and as a corollary, more sensitive to changes in the lower end of the drop size spectrum. Therefore, one can expect evaporation to affect  $K_{DP}$  more substantially than  $Z_H$ .

The expected increase in  $Z_{DR}$  is less intuitive because all drops are losing mass (size). However, because  $Z_{DR}$  is a measure of the median drop size in a distribution, a preferential depletion of smaller drops (which generally have a large concentration) causes an *increase* in the median drop size of a given DSD. This effect is shown schematically in Figure 6.2. At S band, the change in  $\rho_{hv}$  owing to evaporation in pure rain is not expected to be significant for reasons discussed in a later section. The magnitude of changes in all polarimetric variables should be dependent on the relative contributions of small drops and large drops and thus is strongly dependent on the DSD.

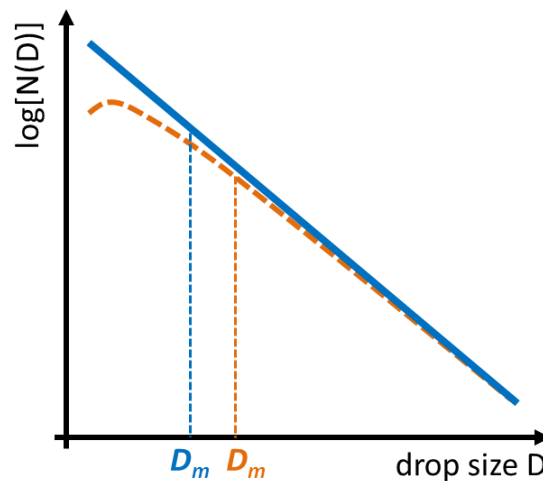


Fig. 6.2: Cartoon illustrating how evaporation can cause an increase in the median drop size  $D_m$  of a distribution. The solid blue line indicates the drop size distribution (DSD) before evaporation occurs; the dashed orange line represents the modified DSD owing to evaporation.

### 3. Model Description

In an effort to quantify the impact of evaporation on the polarimetric variables under different conditions and assumptions, a simple numerical model is constructed. The idealized one-dimensional model explicitly computes the change in size of raindrops falling through subsaturated air. The model domain can be thought of as the sub-cloud layer, with 100-m vertical resolution. Eighty initial drop sizes are considered, ranging from 0.05 mm to 7.95 mm in 0.1-mm increments. Each drop size “bin” is tracked independently in order to isolate the effects of evaporation. Hence, no drop interactions such as collisions, coalescence, or breakup are taken into account. Note that coalescence and breakup significantly contribute to the evolution of the drop size spectrum, as found in the numerous theoretical and modeling studies mentioned above. These collisional processes become increasingly important in heavier rainfall. On the other hand, evaporation tends to only change the slope of the DSD slowly, instead mainly affecting the total water content (e.g., Srivastava 1978; Hu and Srivastava 1995). For rainfall estimation, evaporation is important because it is the only sub-cloud process that directly affects the *total* mass of rainwater reaching the ground. The relative contributions to depletion of total water content from combinations of coalescence, breakup, and evaporation have been investigated previously (e.g., Hu and Srivastava 1995; Seifert 2008). Hu and Srivastava (1995) found that the effects of coalescence and breakup on the depletion of water content tend to approximately balance. In their model, total rainwater mass depletion in simulations that employed full microphysics (coalescence, breakup and evaporation) was similar to those in which only evaporation was considered. Thus, only including evaporation in this model,



although inherently limiting its applicability towards simulating the evolution of the DSD, is justifiable to improve computational efficiency given our focus on the radar measurements and associated rainfall estimation.

At the top of the domain, or at “cloud base,” any DSD model can be prescribed. In the sub-cloud domain, any vertical profile of temperature and relative humidity can be administered. The feedback on the environmental thermodynamic profiles due to evaporation may be turned on or off. The feedback adjustment scheme is described below. At the initial time, drops begin to fall into the top of the domain, as in many rainshaft models. After numerous tests, the time step was selected to be 0.25 seconds, maximizing computational efficiency while maintaining stable solutions.

We are interested in the vertical profiles of the polarimetric variables, so we convert eqn. (6.2) into an expression for the change in drop radius with height. This is accomplished by dividing eqn. (6.2) by the fall speed of raindrops as a function of size,  $v_t(D)$ . To simplify the ensuing integration, the empirical power law fall speed relation suggested by Atlas and Ulbrich (1977) is used for the terminal velocity of the raindrops

$$v_t(D) = \alpha D^\beta \left( \frac{\rho_0}{\rho_{air}} \right)^{0.4}, \quad (6.14)$$

where  $\alpha = 3.78 \text{ m s}^{-1} \text{ mm}^{-0.67}$ ,  $\beta = 0.67$ , and the equivalent spherical diameter  $D$  is given in mm. The multiplicative factor  $(\rho_0/\rho_{air})^{0.4}$  is a density correction, where  $\rho_0$  is the surface reference density value following Foote and duToit (1969) and Beard (1985). Though eqn. (6.14) is less accurate for large drops than more recent empirical models (e.g., Brandes et al. 2002), it well represents the fall speeds of smaller drops (< 5 mm) for which evaporation effects are most significant. Thus, performing the change of variables in eqn. (6.2) and using the velocity relation (6.14) yields an analytic

expression for the change in diameter of a raindrop with initial size  $D_0$  as a function of height

$$D(z) = \left[ D_0^{\beta+2} + \frac{4(\beta+2)}{\alpha} \int_{z_0}^z \xi(z') \left( \frac{\rho_{air}(z')}{\rho_0} \right)^{0.4} dz' \right]^{(1/\beta+2)}, \quad (6.15)$$

where we have defined  $\xi$  as the right hand side of eqn. (6.2):

$$\xi = \frac{S-1}{F_K + F_D}. \quad (6.16)$$

To numerically integrate this expression,  $\xi$  and  $\rho_{air}$  are assumed to be constant over each height step  $\Delta z = z_i - z_{i+1}$  (where  $z_{i+1} < z_i$ ). For sufficiently small height steps (100 m is used in this study), we obtain

$$D(z_{i+1}) = \left[ D(z_i)^{\beta+2} + \frac{4\xi(z_i)(\beta+2)}{\alpha} \left( \frac{\rho_{air}(z_i)}{\rho_0} \right)^{0.4} \Delta z \right]^{(1/\beta+2)}. \quad (6.17)$$

In this way, the simple expression (6.17) is used to calculate what a given initial drop size should be at any height beneath the cloud base for given thermodynamic profiles, assuming the drops are falling at terminal velocity.

In many of the aforementioned modeling studies, the mass concentration of raindrops  $n(m)$  is governed by the following equation

$$\frac{\partial}{\partial t} [n(m)] + \frac{\partial}{\partial z} [v_t n(m)] + \frac{\partial}{\partial m} \left[ \frac{dm}{dt} n(m) \right] = B + C. \quad (6.18)$$

The first term on the left hand side is the Eulerian time rate of change of the mass concentration of the drops, and the second term is the change in drop concentration owing to differential sedimentation. The third term describes the change in concentration of drops of mass  $m$  due to growth or decay by vapor diffusion,  $dm/dt$  (i.e., the time rate of change of the drop mass due to condensation or evaporation). On

the right hand side, the terms  $B$  and  $C$  account for the collisional processes of breakup and coalescence, respectively; these will be omitted herein. For the calculation of radar variables, it is more convenient to work in terms of drop diameter,  $D$ . Thus, we seek to express eqn. (6.18) in terms of  $N(D)$ , where  $N(D)dD$  is the number of raindrops of size  $D$  to  $D + dD$ . The mass and size distributions are related by

$$n(m) = N(D) \frac{dD}{dm}. \quad (6.19)$$

Assuming spherical symmetry of the raindrops,  $m = (\pi/6)\rho_w D^3$ , and thus

$$\frac{dD}{dm} = \frac{2}{\pi\rho_w D^2}. \quad (6.20)$$

When computing the polarimetric radar variables, drop shape is important and must be dealt with appropriately. However, assuming a spherical shape of drops does not significantly impact computations of evaporation (Straka and Gilmore 2006). Thus, the inconsistency with treating drop shape will not affect the results of this study. The mass diffusion term must be written in terms of  $D$ :

$$\frac{dm}{dt} = \frac{d}{dt} \left[ \frac{\pi}{6} \rho_w D^3 \right] = \frac{\pi}{2} \rho_w D^2 \frac{dD}{dt}. \quad (6.21)$$

Thus, substituting eqns. (6.19) – (6.21) into eqn. (6.18), and making use of the change of variables

$$\frac{\partial}{\partial m} = \frac{dD}{dm} \frac{\partial}{\partial D}$$

yields the governing equation in terms of drop diameter  $D$ :

$$\frac{\partial}{\partial t} [N(D)D^{-2}] = -\frac{\partial}{\partial z} [v_t(D)N(D)D^{-2}] - D^{-2} \frac{\partial}{\partial D} \left[ \frac{dD}{dt} N(D) \right]. \quad (6.22)$$

For the most general case in a 1D rainshaft model, the drop concentration is a function of diameter, height, and time, i.e.,  $N = N(D, z, t)$ . For brevity, the functional

dependence of  $N$  and  $v_t$  will herein be omitted. Thus, applying the chain rule to expand the derivatives in eqn. (6.22) results in

$$\frac{\partial N}{\partial t} = \frac{2N}{D} \frac{dD}{dt} - \frac{\partial}{\partial z} (v_t N) + \frac{2N v_t}{D} \frac{\partial D}{\partial z} - \frac{\partial}{\partial D} \left( \frac{dD}{dt} N \right). \quad (6.23)$$

For drops falling at terminal velocity  $v_t$ ,

$$v_t \frac{\partial D}{\partial z} = \frac{dz}{dt} \frac{\partial D}{\partial z} = \frac{dD}{dt}.$$

So, eqn. (6.23) becomes

$$\frac{\partial N}{\partial t} = - \frac{\partial}{\partial z} (v_t N) - \frac{\partial}{\partial D} \left( \frac{dD}{dt} N \right) - \frac{4N}{D} \frac{dD}{dt}, \quad (6.24)$$

which governs the time rate of change of the raindrop size distribution. Using eqn. (6.14) for terminal velocity and noting that  $dD/dt = 4\xi D^{-1}$ , we can write eqn. (6.24) in discrete form

$$N_{j,k}^{i+1} = N_{j,k}^i - \frac{\Delta t}{\Delta z} \left( A_{j-1,k}^i [D_{j-1,k}^i]^\beta N_{j-1,k}^i - A_{j,k}^i [D_{j,k}^i]^\beta N_{j,k}^i \right) - \frac{4\Delta t}{D_{j,k}^i \Delta D} \left( \xi_{j,k+1}^i N_{j,k+1}^i - \xi_{j,k}^i N_{j,k}^i \right) + \frac{20\Delta t}{[D_{j,k}^i]^2} \xi_{j,k}^i N_{j,k}^i \quad (6.25)$$

for each time step  $i$ , height level  $j$ , and drop size bin  $k$ . Note that the density correction factor and constant  $\alpha$  have been absorbed into the variable  $A$ .

As raindrops begin to evaporate in subsaturated air, the thermodynamic properties of the air within the rainshaft are affected. Specifically, the shaft moistens and cools with time, thereby decreasing subsaturations and limiting the amount of evaporation that occurs. The decrease in temperature and precipitation loading contribute to negative buoyancy relative to the surrounding precipitation-free air, which forces a localized downdraft. The downdraft also serves to limit evaporation because it

can transport drops downwards faster than they would otherwise descend, decreasing the amount of time available for evaporation.

To simulate the local cooling and moistening effect, we utilize equation (6.1) as well as the equation governing thermal conduction towards the drop

$$\frac{dQ}{dt} = 4\pi r \bar{f}_h k_a (T_r - T), \quad (6.26)$$

where  $T_r$  is the temperature of the drop's surface. For simplicity, we assume the raindrop temperature to be in equilibrium at each level, neglecting the brief relaxation period towards their equilibrium temperature. Recently, Tardif and Rasmussen (2010) have investigated the validity of the equilibrium assumption and found that it may not hold if drops experience thermodynamic changes on time scales comparable to the equilibrium relaxation time. In our study, the height step (100 m) ensures that the drops remain within one grid box (in which thermodynamic conditions are constant) over the relaxation time scale, which tends to be on the order of 4-5 s for most drop sizes. A more accurate treatment of drop temperature is presented in Chapter 4. Using the total amount of mass evaporated at each level, and assuming that all latent enthalpy from the environment contributes directly to cooling the drop's surface (which immediately cools the surrounding air), the incremental change in air temperature is calculated at each time step. Similarly, the entire mass of liquid water lost due to evaporation goes directly into vapor, increasing the ambient air vapor density. Using the new temperature and vapor density, and the ideal gas law for water vapor, the new relative humidity can be calculated.

This environmental feedback scheme may be turned on or off in the model. Because the model is one-dimensional and is not tied to any dynamics, we have omitted

the generation of a downdraft. The velocity relation in eqn. (6.14) overestimates the fall speeds of the moderate and large drops already, which may partially account for the errors introduced when neglecting a downdraft. Also, to be realistic and dynamically consistent, the generation of a downdraft would require some parameterization of entrainment; without this entrainment, the shaft moistens and cools until it becomes saturated, halting further evaporation.

The change in diameter of the drop size bins at each height level and the calculated concentration of drops at each level are used to compute the vertical profiles of polarimetric variables according to the T-Matrix method (e.g., Mishchenko 2000). For raindrop shapes, we assume the relation suggested by Brandes et al. (2002; corrected in 2005):

$$\frac{D_a}{D_b} = 0.9951 + 0.02510D - 0.03644D^2 + 0.005303D^3 - 0.0002492D^4, \quad (6.27)$$

where  $D$  is in mm. See Brandes et al. (2002) for a discussion of the differences between this relation and others that are used frequently in the literature. The raindrops are assumed to have a mean canting angle of  $0^\circ$  with respect to the vertical, with a canting angle distribution width of  $20^\circ$ . In general,  $20^\circ$  is too high for typical rainfall; a standard deviation of  $10^\circ$  is more appropriate (e.g., Ryzhkov 2001; Ryzhkov et al. 2002). However, the higher value was chosen to increase the effect of evaporation on  $\rho_{hv}$ . The impact of this wider distribution of canting angles is to dampen the effects of evaporation on the other variables very slightly.

The evaporation model calculations will be separated into two groups: sensitivity studies, which will focus on the exploration of parameter space, and simulations, which will model vertical profiles of the polarimetric radar variables using

observed thermodynamic soundings from different climate regions. The *sensitivity studies* are designed to test the model sensitivity as well as the sensitivity of the polarimetric radar variables to different thermodynamic conditions, DSD models, and rainfall rates. The *simulations* are intended to illustrate potential variations in vertical profiles of polarimetric variables in different regions of the United States that may be observed following the ongoing nationwide weather radar upgrade to polarization diversity. For the experiments, the gradual moistening and cooling feedback mechanism has been turned off in order to create “snapshots” of the profiles of polarimetric variables. For applied simulations, the mechanism should be turned on to avoid overaggressive evaporation.

#### 4. Model Results

##### *a. Sensitivity Studies*

Because of the aforementioned differences in drop size dependency for each of the polarimetric variables, sensitivity to selection of the DSD is expected. To address this, each model sensitivity experiment is repeated using different initial DSDs. The three-parameter gamma model (e.g., Ulbrich 1983) is used:

$$N(D) = N_0 D^\mu \exp(-\Lambda D). \quad (6.28)$$

The rainfall rate for each DSD is fixed at the top of the domain. For the special case of the exponential DSD ( $\mu = 0$ ), the Marshall-Palmer DSD (herein MP) relation is used. Note that the intercept parameter most often used with the MP distribution,  $N_{00} = 8000 \text{ m}^{-3} \text{ mm}^{-1}$ , is calculated for use at sea level. Because we are using fixed rainfall rates

aloft, we must use a density-corrected version:  $N_0 = N_{00}(\rho(z_0)/\rho_0)^{0.4}$ . For the MP distribution, we can use the velocity relation (14) to calculate the slope parameter  $\Lambda$ :

$$\Lambda = \left( \frac{\pi}{6} \alpha N_0 \Gamma(4 + \beta) \right)^{1/4.67} R^{-(1/4.67)}. \quad (6.29)$$

Though the gamma model has three parameters, observational and modeling studies suggest that two of the parameters are constrained and thus not independent (e.g., Zhang et al. 2001, 2006; Brandes et al. 2004b; Cao et al. 2008; Seifert 2008). For Oklahoma precipitation, Cao et al. (2008) found an empirical relation between the shape parameter  $\mu$  and the slope parameter  $\Lambda$  based on disdrometer measurements:

$$\mu = -0.0201\Lambda^2 + 0.902\Lambda - 1.718, \quad (6.30)$$

applicable for  $0 \leq \Lambda \leq 20$ . Despite some debate over the validity of such relations (e.g., Moisseev and Chandrasekar 2007), the constrained gamma model is used. Shape parameter  $\mu$  is varied between -1 and 5 in our calculations. These values encompass the bulk of observations in Oklahoma rain (e.g., Cao et al. 2008). A slightly broader range of values of  $\mu$  was found in rain in Florida (Zhang et al. 2001), so there is some dependence on climate region. Because  $\Lambda$  is determined from the pre-selected  $\mu$  values using eqn. (6.30) and we have fixed the rainfall rate

$$R = \frac{\pi}{6} \int_0^{\infty} D^3 N(D) v_t(D) dD, \quad (6.31)$$

the intercept parameter  $N_0$  can be determined by solving (6.31) using (6.28):

$$N_0 = \frac{R}{\frac{\pi}{6} \alpha \left( \frac{\rho_0}{\rho_{air}} \right)^{0.4} \frac{\Gamma(\mu + 4 + \beta)}{\Lambda^{\mu+4+\beta}}}. \quad (6.32)$$



It is evident that a variety of DSD shapes have been selected (Fig. 6.3), covering a broad spectrum of precipitation regimes. Note that in Oklahoma precipitation, the negative shape parameters are most often associated with convective precipitation events, so the relatively high concentration of larger drops makes physical sense. Also note the similarities between the MP DSD (corresponding to  $\mu = 0$ ) and the  $\Gamma, \mu = 1$  distribution, which nearly overlap for all drop sizes except at the small drop end of the spectrum.

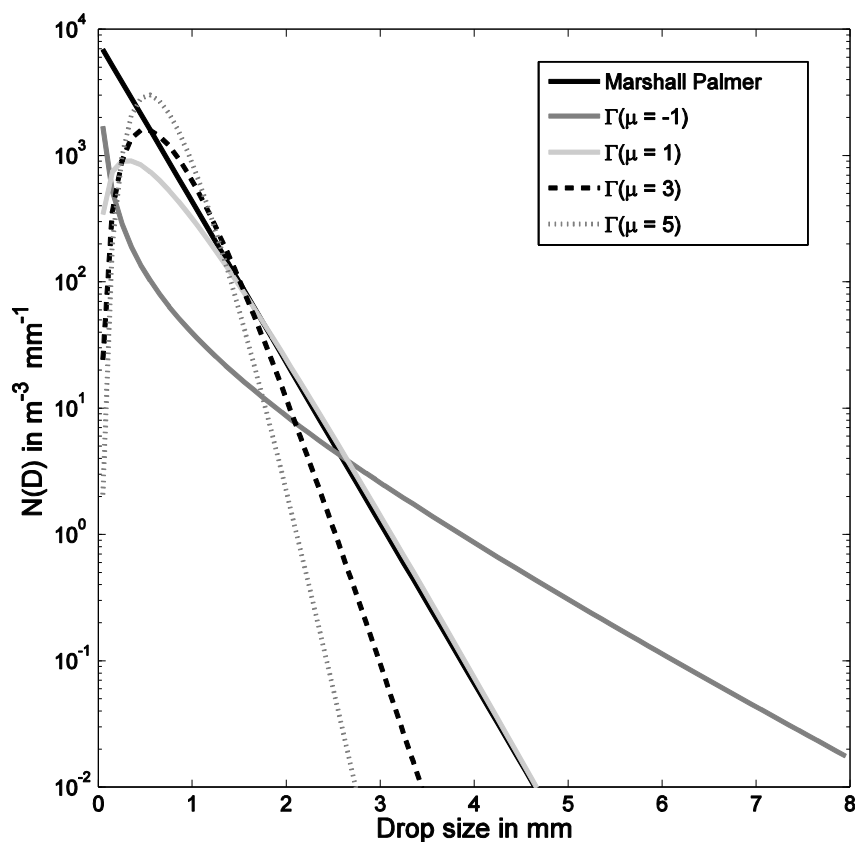


Fig. 6.3: DSD models used for the simulations. The Marshall-Palmer exponential distribution (solid black line); the  $\mu = -1$  gamma model (solid dark gray line); the  $\mu = 1$  gamma model (solid light gray line); the gamma model with  $\mu = 3$  (dashed black line); and the model with  $\mu = 5$  (dashed dark gray line). All models are for rainfall rates of 5 mm hr<sup>-1</sup>.

For each set of model runs the polarimetric radar variables are calculated for both S (10.9-cm wavelength) and C (5.4-cm wavelength) bands. In the first set of experiments, idealized isothermal layers 2-km deep are considered. The temperature is fixed at 20 °C, and relative humidity (RH) is set constant in height but varies from 10% to 95% in each experiment. Though not necessarily realistic, these experiments simply explore the parameter space of the model. In the second set of sensitivity runs, a dry adiabatic lapse rate is prescribed with a surface temperature of 30 °C. The RH profile is assumed to increase linearly from the given surface value to 100% at the cloud base (top of the domain, taken to be 3 km). The surface values are varied from 55% to 95% in 5%-increments. These idealized well-mixed boundary layer cases apply to warm season precipitation events. Simulations using observed thermodynamic profiles, including both warm and cool season events, are explored in section 5. In these two sets of sensitivity tests, each of the DSD models is used. The final set of sensitivity tests varies R from 0.1 mm hr<sup>-1</sup> to 20 mm hr<sup>-1</sup> using the MP DSD for a dry adiabatic environment with a surface RH of 75% and a surface temperature of 30 °C.

At the onset of precipitation, transient differential sedimentation occurs. As discussed in Chapter 5, the reason for this is simply the difference in terminal velocity of the large drops versus the smaller drops; the large drops fall faster and thus reach the ground before the smaller drops. Once enough time has elapsed, all drops that do not evaporate reach the ground, and the observable effects of differential sedimentation disappear. Note that the impact of differential sedimentation on the radar variables dominates any signal from evaporation, which produces more subtle changes in the vertical profiles of the polarimetric variables (Fig. 6.4). Thus, for the remainder of the

sensitivity studies and experiments where we quantify the effects of evaporation, the calculations are carried out for long times (equivalently, waiting for the profiles to attain steady-state solutions where the environmental feedback mechanism has been turned off).

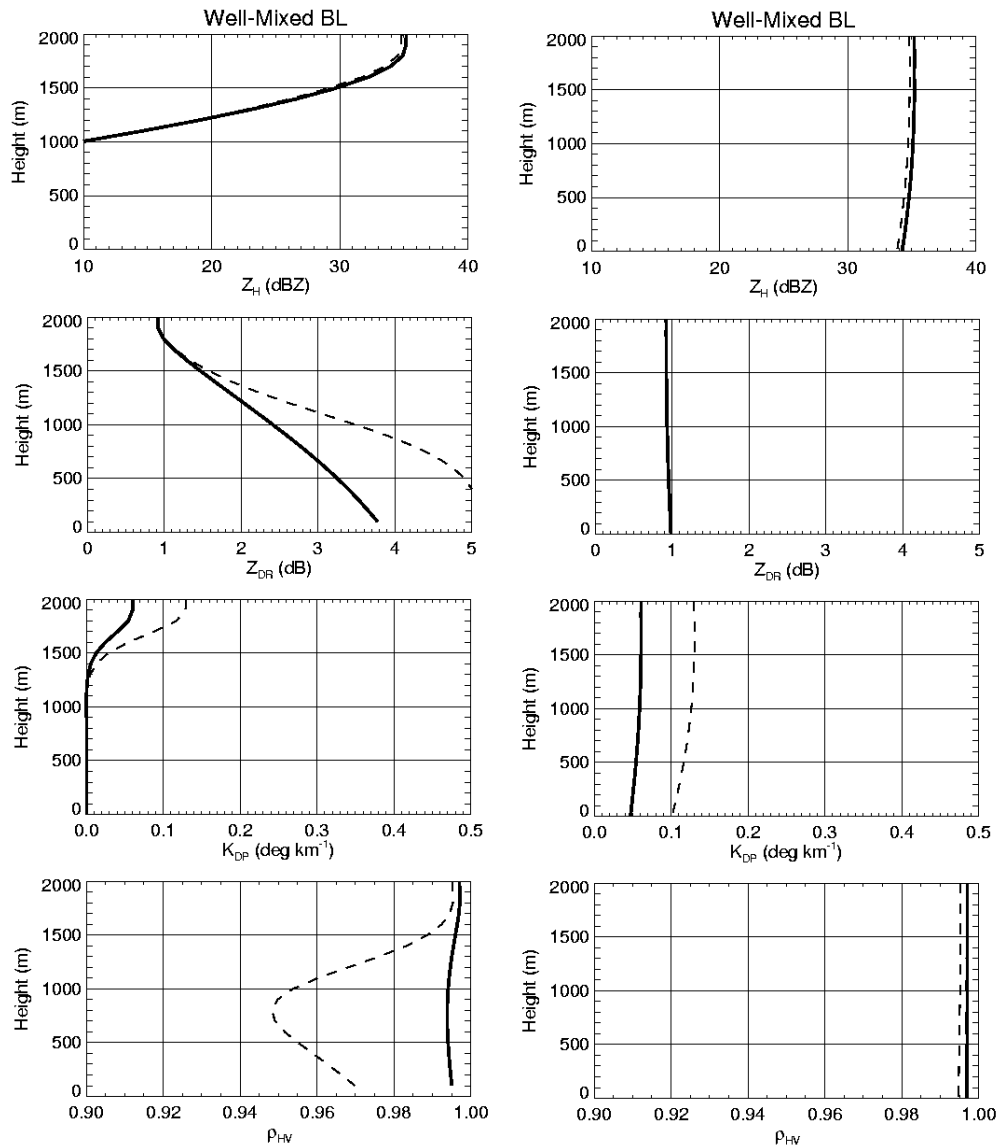


Fig. 6.4: Example simulation in a well-mixed boundary layer of 3 km depth, with surface temperature of 30 °C and surface relative humidity of 70%. The simulation uses the MP DSD aloft with a rainfall rate of 5 mm hr<sup>-1</sup>. The left column is after 60 seconds, showing the transient effect of differential sedimentation in vertical profiles of each of the polarimetric variables. The right column shows the steady-state profiles for the same environment. Solid lines are for S band, dashed lines indicate C-band values.

It is convenient to define the “evaporative change” in the polarimetric variables over the depth of the model domain, which is simply the value of the polarimetric variable at the ground minus its initial value aloft<sup>6</sup>. The evaporative change will be denoted as a  $\Delta$  before the variable. As discussed above, evaporation will produce negative  $\Delta Z_H$  and  $\Delta K_{DP}$  (indicative of a decrease towards the ground) and a positive  $\Delta Z_{DR}$  (indicative of an increase towards the ground). To make a more meaningful comparison between  $\Delta Z_H$  and  $\Delta K_{DP}$  the evaporative change in  $K_{DP}$  will be converted into logarithmic units

$$\Delta K_{DP}(dB) = 10 \log_{10} \left[ \frac{(K_{DP})_{ground}}{(K_{DP})_{aloft}} \right]. \quad (6.33)$$

Recall that the logarithmic differences for  $Z_H$ ,  $Z_{DR}$ , and  $K_{DP}$  can be converted into relative changes (for example, a 3-dB decrease corresponds to about a 50% reduction from its original value).

The results from the first set of experiments (considering isothermal layers) are summarized in Figs. 6.5 and 6.6 for S band and C band, respectively. It is clear that all of the variables are sensitive to the relative humidity in the layer, but perhaps more importantly the results are sensitive to the initial DSD model selected. The  $\Gamma, \mu = 5$  model exhibits much greater evaporative change in  $Z_H$  and  $K_{DP}$  than the other models (Figs. 6.5a,c; 6.6a,c). This is explained by two factors. First, the distribution contains a large concentration of small drops, which are preferentially evaporated, resulting in a substantial decrease in mass. Second, the  $\Gamma, \mu = 5$  DSD has fewer large drops than any other distribution. These large drops, which do not evaporate as efficiently as smaller

---

<sup>6</sup> In all cases, the changes in polarimetric variables due to evaporation are not constant in height and depend on the environmental thermodynamic profiles as expressed by the variable  $\xi(z)$ .

drops, tend to overwhelm the contribution to the observed  $Z_H$  (and to a lesser extent,  $K_{DP}$ ) for the other DSD models, which all exhibit lower magnitudes of  $\Delta Z_H$  and  $\Delta K_{DP}(\text{dB})$ .

Because  $Z_{DR}$  is more sensitive to drop size than  $Z_H$ , it follows that the large  $\Delta Z_{DR}$  values occur for the DSDs with relatively large concentrations of big drops. However, also playing an important role in producing the significant  $\Delta Z_{DR}$  values is a large concentration of small drops. The preferential evaporation of a significant portion of the spectrum will substantially increase the median drop size of the spectrum. This is why the MP model has the highest  $\Delta Z_{DR}$  (Figs. 6.5b, 6.6b): it has the highest concentration of small drops and a comparatively large concentration of big drops. Also note that the  $\Delta Z_{DR}$  at C band (Fig. 6.6b) is somewhat higher for all DSD models owing to resonance scattering effects of large drops.

At S band,  $\Delta \rho_{hv}$  magnitudes are quite small ( $< 0.002$  even for extreme evaporation) for all DSD shapes, at least for the electromagnetic scattering model employed in this study (Fig. 6.5d). Such small changes are insignificant and likely within the uncertainty of the WSR-88D measurements, or about  $\pm 0.005$  to  $0.01$ . At C band, the evaporative changes in  $\rho_{hv}$  are slightly larger in magnitude and negative for all models (Fig. 6.6d). For modest evaporation rates, changes in  $\rho_{hv}$  at both radar wavelengths are insignificant and probably difficult to detect operationally.

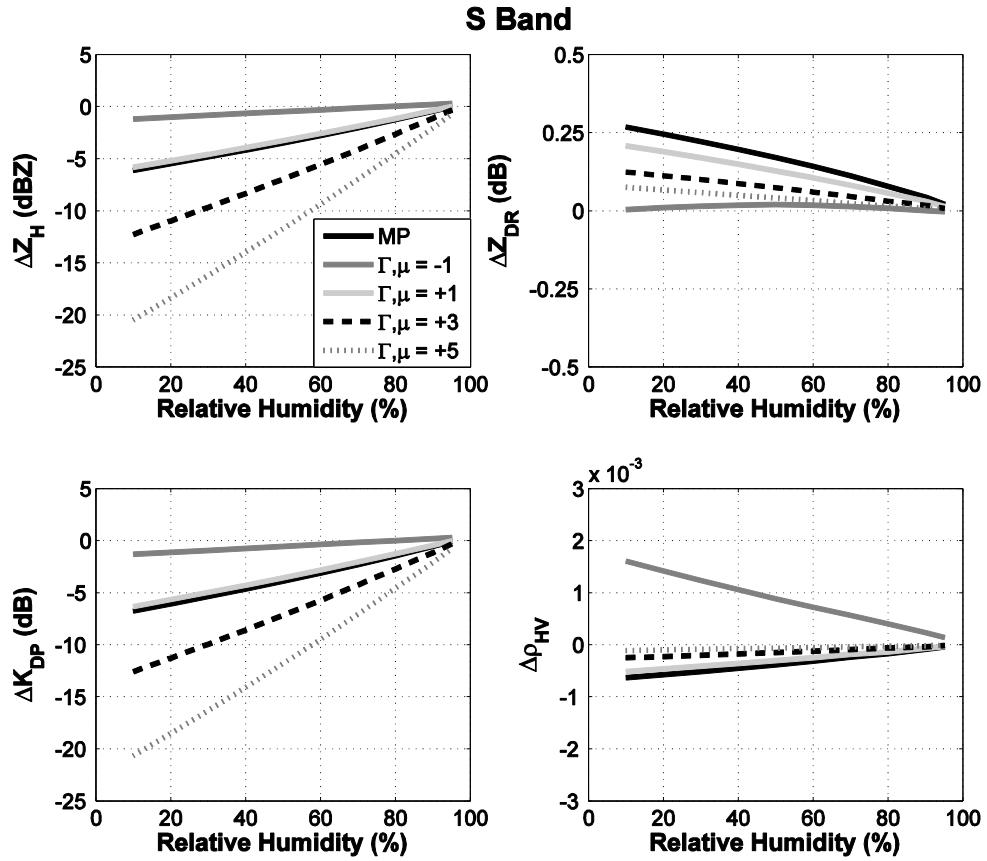


Fig. 6.5: Sensitivity of the evaporative change in the S-band dual-polarization variables to various constant relative humidity profiles for the 5 DSD models. The domain depth is 2 km and isothermal at 20 °C. The plotting convention for the DSD models is the same as in Fig. 6.2. The panels display evaporative changes in (a)  $Z_H$ , (b)  $Z_{DR}$ , (c)  $K_{DP}$ , and (d)  $\rho_{HV}$ .

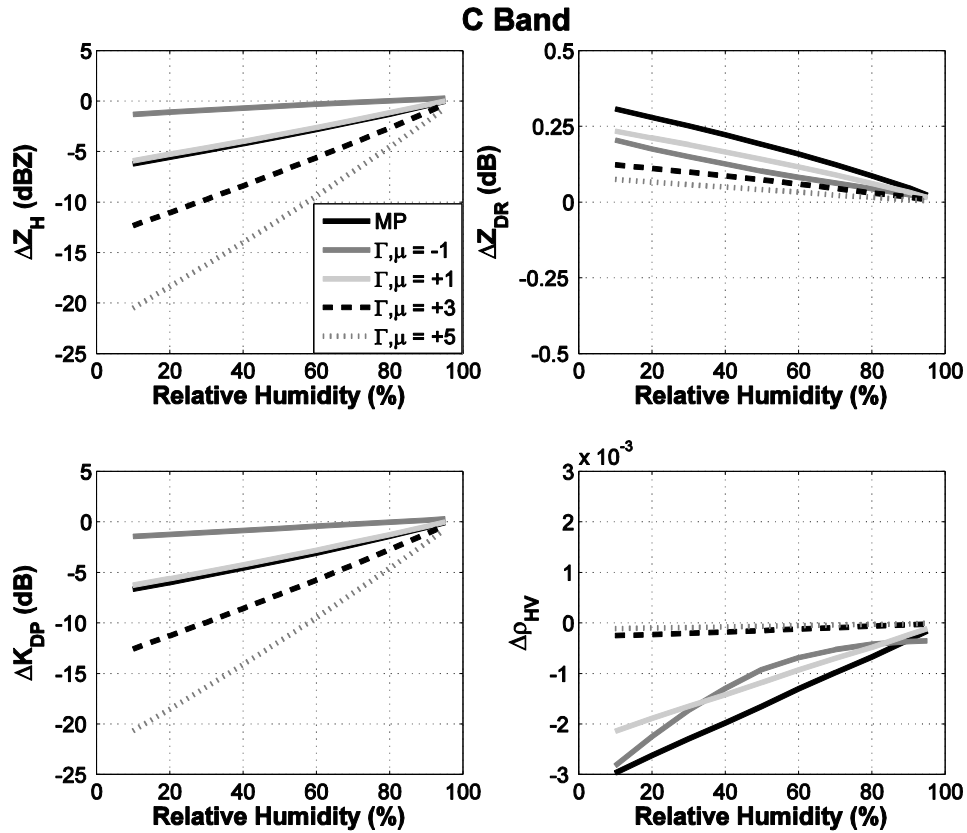


Fig. 6.6: As in Fig. 6.5, but for C band.

Next, idealized 3-km deep mixed layers are considered for the calculations. The results for S and C bands are summarized in Fig. 6.7. The resulting  $\Delta Z_H$  and  $\Delta K_{DP}$  are dependent on the surface RH and the DSD prescribed aloft, as expected. However, a feature of note is that  $\Delta Z_H$  and  $\Delta K_{DP}$  reverse sign for three of the DSD models (MP;  $\Gamma, \mu = -1$ ; and  $\Gamma, \mu = 1$ ) for large values of surface RH. This is because the relatively cool and moist conditions beneath cloud base do cause enough evaporation to counteract the effect of “raindrop convergence,” a result of the drops encountering increasing air density as they fall towards the ground. In the absence of any evaporation, the concentration of drops increases slightly with decreasing height, which

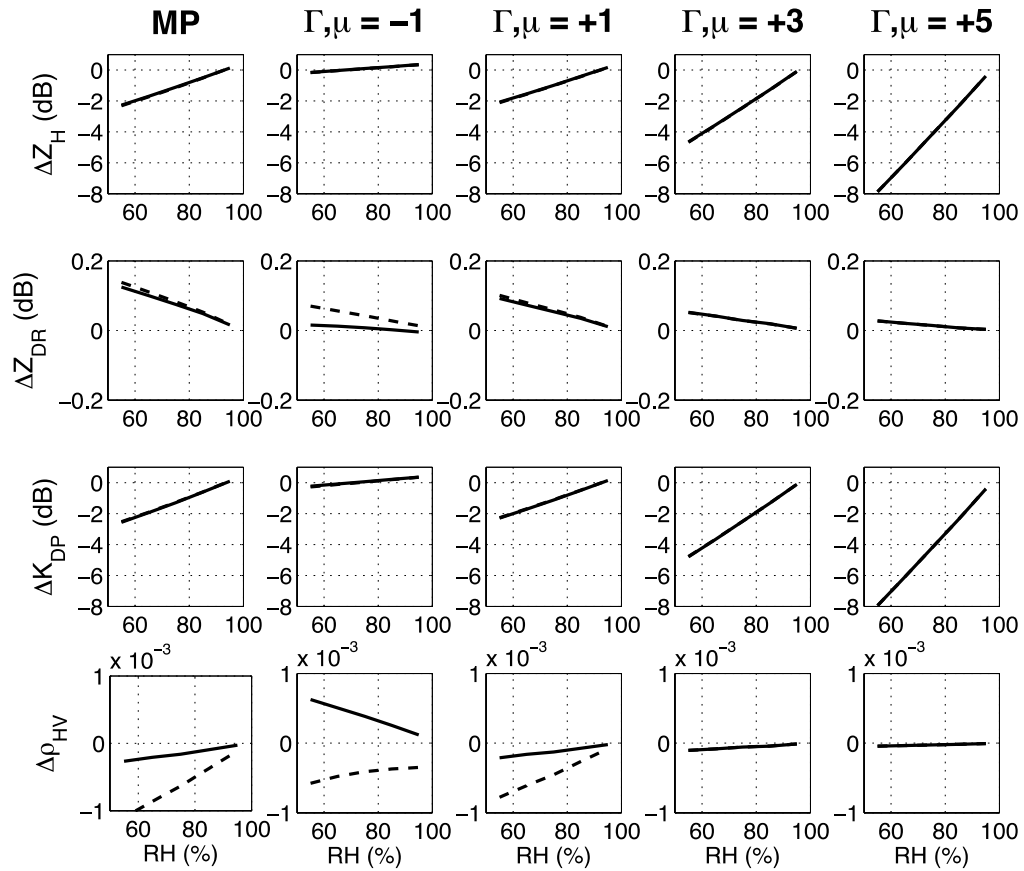


Fig. 6.7: Calculations of the evaporative changes in each of the polarimetric variables (each row is a variable) based on a 3-km deep idealized well-mixed layer, with a surface temperature of 30 °C. The surface relative humidity (RH) values are shown along the abscissa. Each column represents a DSD model, as indicated. The solid lines represent S-band values and the dashed lines represent C-band values.

affects  $Z_H$  and  $K_{DP}$ , but not  $Z_{DR}$  or  $\rho_{hv}$ . Also of note is that the difference between the S- and C-band values of  $\Delta Z_{DR}$  and  $\Delta \rho_{hv}$  increases with higher concentrations of large drops, a result of the resonance scattering effects prevalent in big drops at C band.

The results of varying the rainfall rate  $R$  are provided in Figure 6.8. For the higher rainfall rates considered, one should expect a greater change in  $K_{DP}$  for a given amount of evaporation than is observed in  $Z_H$ . At both S and C bands,  $\Delta \rho_{hv}$  is insignificant for all rainfall rates with the MP model. For the S-band calculations,  $\Delta Z_{DR}$



decreases with increasing rainfall rate whereas the  $\Delta Z_{DR}$  at C band increases slightly. The difference in behavior may be attributable to the enhanced resonance scattering effects at C band.

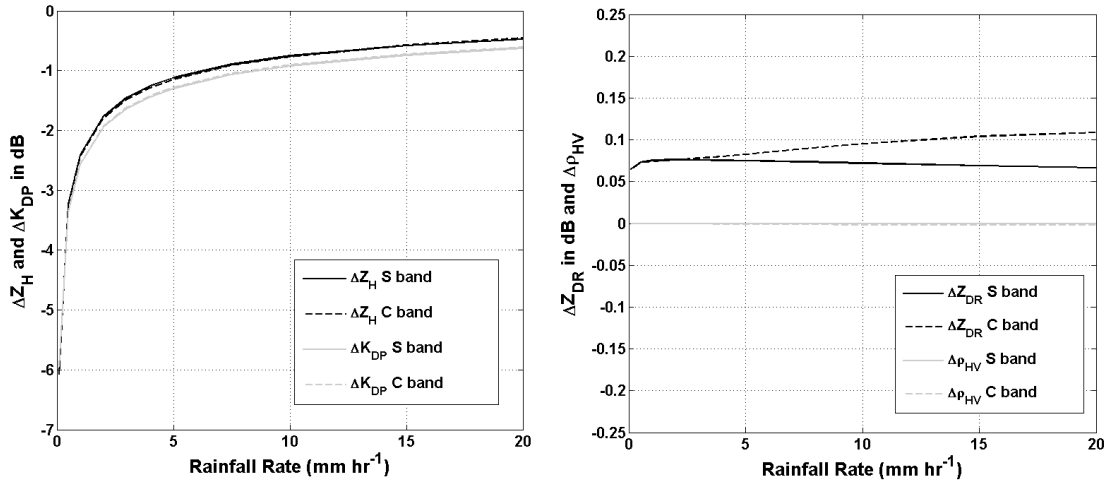


Fig. 6.8: Sensitivity of the evaporative change in the polarimetric variables to rainfall rate for the exponential DSD. The 3-km deep domain has a dry adiabatic temperature (surface temperature of 30 °C) with a surface relative humidity of 75%. S-band values are shown in solid lines and C-band values are in dashed lines. In the left panel,  $\Delta Z_H$  (black) and  $\Delta K_{DP}$  (gray) are shown, both in dB. In the right panel, black represents  $\Delta Z_{DR}$  and gray represents  $\Delta \rho_{HV}$ .

The sensitivity experiments have shown for given thermodynamic conditions, the largest  $\Delta Z_H$  and  $\Delta K_{DP}$  occur for the  $\Gamma, \mu = 5$  DSD model, with the  $\Gamma, \mu = -1$  model producing the smallest evaporative changes. These results are directly related to the shape of the DSD. Smaller concentrations of large ( $> 4$  mm) drops produce larger evaporative changes in  $Z_H$  and  $K_{DP}$ . The logarithmic changes in  $K_{DP}$  are slightly greater in magnitude than those of  $Z_H$  because  $K_{DP}$  is less dependent on drop diameter than  $Z_H$ . Because  $Z_H$  typically is displayed in logarithmic units (dBZ), whereas  $K_{DP}$  generally is displayed in  $\text{deg km}^{-1}$ ,  $\Delta K_{DP}$  may be more obvious to operational meteorologists. For example, an equivalent evaporative change of 3 dB for  $Z_H$  (e.g., 33 dBZ to 30 dBZ)

“appears” less significant than a 3 dB relative change in  $K_{DP}$  (e.g.,  $1.0 \text{ deg km}^{-1}$  to  $0.5 \text{ deg km}^{-1}$ ). However, it should be noted that for the relatively light rainfall rates considered in this study and at S band,  $K_{DP}$  can be noisy and difficult to estimate. At shorter radar wavelengths,  $K_{DP}$  estimates will be less noisy as the  $K_{DP}$  values will be larger (recall from Chapter 1 that  $K_{DP}$  is inversely proportional to radar wavelength). This suggests that evaporative changes may be easier to detect operationally with C- and X-band polarimetric radars.

For given conditions, the largest values of  $\Delta Z_{DR}$  occur for the MP DSD, and the smallest values are produced by the  $\Gamma, \mu = -1$  DSD. The changes depend on relative contributions from both the small- and large-drop ends of the size spectrum. Having the largest concentration of big drops of any of the DSDs used in this study, the  $\Gamma, \mu = -1$  DSD resulted in the smallest  $\Delta Z_{DR}$ . This is because of the comparatively low concentration of small drops ( $< 2 \text{ mm}$ ). With fewer small drops being depleted, there is a smaller shift in the median drop size. Coupled with this is the fact that the substantial concentrations of big drops, which are not as affected by evaporation, dominate the contributions to the backscattered signal.

#### *b. Simulations with Observed Soundings*

It is informative to look at real cases in an attempt to see the types of variations in vertical profiles of the polarimetric variables that may be observed in different evaporation scenarios. To accomplish this, we have selected three soundings from different regions that display different thermodynamic characteristics. These observed temperature and relative humidity profiles are used to initialize the model.

The three soundings are shown in Figure 6.9. The first sounding comes from Albuquerque, New Mexico on 16 August 2007 at 0000 UTC (Fig. 6.9a) and represents the summer season in the western United States with a deep, dry well-mixed layer. Light precipitation echoes were observed on the Albuquerque WSR-88D radar about the time of the sounding. Next is a spring sounding (Fig. 6.9b), taken from Norman, Oklahoma on 24 May 2008 at 1800 UTC and may be said to represent an atmosphere primed for severe weather: a cyclic tornadic supercell developed north of Oklahoma City in the afternoon, producing at least 10 tornadoes. The third sounding (Fig. 6.9c) comes from Wallops Island, Virginia on 7 October 2009 at 0000 UTC and represents a cool, moist boundary layer in which light rain was observed throughout the day. Note that the environmental feedback mechanism has been turned off for these simulations.

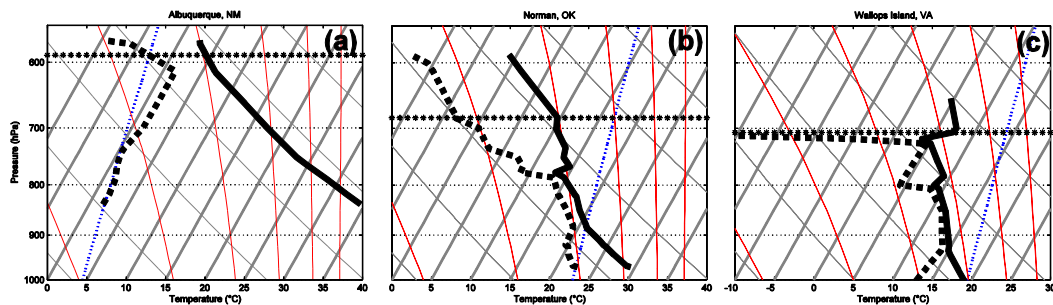


Fig. 6.9: Observed low-level (surface to approximately 3 km AGL) soundings used for the evaporation model simulations, representing three different evaporation scenarios: (a) Albuquerque, New Mexico on 16 August 2007 at 0000 UTC; (b) Norman, Oklahoma on 24 May 2008 at 1800 UTC, and (c) Wallops Island, Virginia on 7 October 2009 at 0000 UTC. Thick black solid (dashed) line indicates the temperature (dewpoint temperature) profile. The horizontal line with asterisk markers at the top of each sounding indicates the 3-km AGL height.

The MP distribution with a  $5 \text{ mm hr}^{-1}$  rainfall rate aloft is used in the simulations. The MP model is employed because it is perhaps the most widely known DSD model and provides intermediate magnitudes of evaporative changes. As

previously demonstrated, the choice of DSD model can have a significant impact on the evaporative changes of the polarimetric variables. This should be considered when interpreting the outcome of the simulations and the computed vertical profiles of polarimetric variables presented herein. Nonetheless, the purpose of these simulations is to illustrate the potential variations in vertical profiles of polarimetric observables that may occur in different climate regions and seasons throughout the United States.

Figure 6.10 displays the vertical profiles of polarimetric variables for the Albuquerque sounding (Fig. 6.9a). For both radar wavelengths,  $\Delta Z_H$  is less than -6 dB. The  $\Delta Z_{DR}$  is nearly 0.3 dB at S band, which may be detectable by the WSR-88D radars, and greater than 0.3 dB at C band. The magnitude of the change in  $\rho_{hv}$  is negligible at S band. At C band, the  $\Delta\rho_{hv}$  is about -0.003, which may be observable with very high-quality radar systems. The evaporative changes in all polarimetric variables for each of the simulated soundings are summarized in Table 6.1.

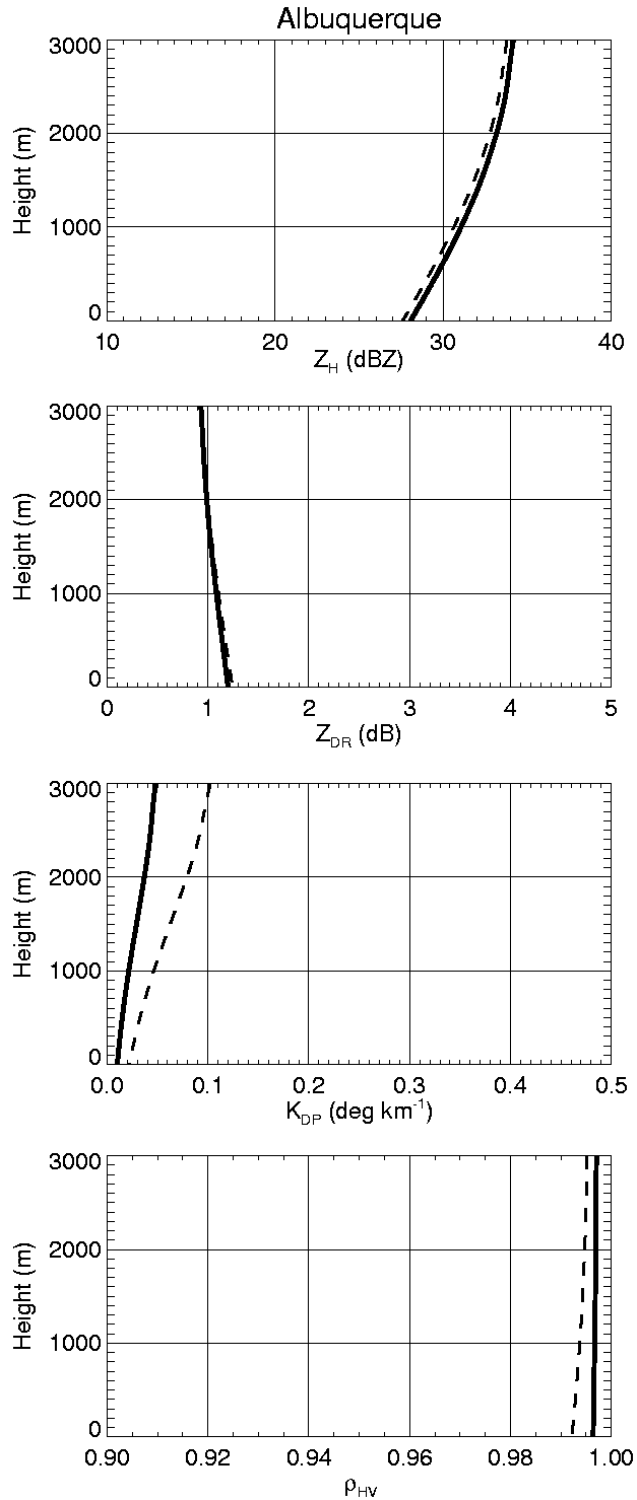


Fig. 6.10: Simulated vertical profiles of polarimetric variables for the Albuquerque sounding (Fig. 6.9a). The solid line indicates S band and the dashed line indicates C band. Variables shown are (a)  $Z_H$ , (b)  $Z_{DR}$ , (c)  $K_{DP}$ , and (d)  $\rho_{HV}$ . The MP DSD model is used at the cloud base, with a rainfall rate of 5 mm hr<sup>-1</sup> aloft.

	Albuquerque, NM	Norman, OK	Wallops Island, VA
$\Delta Z_H - S$ band	-6.23 dB	-2.29 dB	-1.25 dB
$\Delta Z_H - C$ band	-6.32 dB	-2.33 dB	-1.28 dB
$\Delta Z_{DR} - S$ band	0.27 dB	0.13 dB	0.09 dB
$\Delta Z_{DR} - C$ band	0.32 dB	0.14 dB	0.09 dB
$\Delta K_{DP}(\text{dB}) - S$ band	-6.88 dB	-2.59 dB	-1.45 dB
$\Delta K_{DP}(\text{dB}) - C$ band	-6.80 dB	-2.56 dB	-1.43 dB
$\Delta \rho_{hv} - S$ band	-0.0006	-0.0003	-0.0002
$\Delta \rho_{hv} - C$ band	-0.0031	-0.0011	-0.0007

Table 6.1: Results of simulated evaporative changes in the polarimetric variables at S and C bands from the three soundings in Fig. 6.9. Simulations used the MP distribution with a rainfall rate aloft of  $5 \text{ mm hr}^{-1}$ .

Because of the uncertainty involved with the choice of initial DSD, the same simulations are performed with the  $\Gamma, \mu = -1$  distribution as well as the  $\Gamma, \mu = 5$  DSD. These models were selected for a comparison since they encompass the extremes for evaporative changes in the different polarimetric variables (Table 6.2). The  $\Gamma, \mu = -1$  distribution exhibits much smaller magnitudes of  $\Delta Z_H$  and  $\Delta K_{DP}$  than the MP simulations. Also note that  $\Delta \rho_{hv}$  changes sign with the  $\Gamma, \mu = -1$  model depending on radar wavelength. In contrast, the  $\Gamma, \mu = 5$  DSD produces the most significant  $\Delta Z_H$  and  $\Delta K_{DP}$  values and very small changes in  $Z_{DR}$  and  $\rho_{hv}$ . These simulations can be viewed as the approximate quantitative bounds on the possible changes in polarimetric characteristics of light rain due to evaporation in differing environments.

	Albuquerque, NM	Norman, OK	Wallops Island, VA
$\Delta Z_H - S$ band	-1.22, -21.0 dB	-0.12, -8.06 dB	+0.16, -4.86 dB
$\Delta Z_H - C$ band	-1.32, -21.0 dB	-0.13, -8.07 dB	+0.15, -4.86 dB
$\Delta Z_{DR} - S$ band	0.00, 0.08 dB	0.02, 0.03 dB	0.01, 0.02 dB
$\Delta Z_{DR} - C$ band	0.21, 0.08 dB	0.07, 0.03 dB	0.05, 0.02 dB
$\Delta K_{DP}(\text{dB}) - S$ band	-1.32, -21.2 dB	-0.18, -8.14 dB	+0.12, -4.91 dB
$\Delta K_{DP}(\text{dB}) - C$ band	-1.44, -21.2 dB	-0.24, -8.14 dB	+0.08, -4.91 dB
$\Delta \rho_{hv} - S$ band	+0.0016, -0.0001	+0.0006, $\approx 0$	+0.0004, $\approx 0$
$\Delta \rho_{hv} - C$ band	-0.0030, -0.0001	-0.0006, $\approx 0$	-0.0004, $\approx 0$

Table 6.2: As in Table 1, but the  $\Gamma, \mu = -1$  and  $\Gamma, \mu = 5$  distributions are used, respectively, the values resulting from each DSD model separated by a comma in the table. Magnitudes of  $\Delta \rho_{hv}$  less than  $10^{-4}$  are indicated as  $\approx 0$ .

## 5. Rainfall Rate Estimation

In addition to calculating vertical profiles of the polarimetric radar variables, we calculate the vertical profiles of rainfall rate using the true value based on the DSD itself (eqn. 6.31) as well as radar relations developed for S-band rainfall estimation from the Joint Polarization Experiment (JPOLE; Ryzhkov et al. 2005a; also see Giangrande and Ryzhkov 2008):

$$R(Z_H) = 0.017(Z_h^{0.714}) \quad (6.34)$$

$$R(K_{DP}) = 44.0|K_{DP}|^{0.822}\text{sgn}(K_{DP}) \quad (6.35)$$

and based on DSD simulations by Bringi and Chandrasekar (2001)

$$R(Z_H, Z_{DR}) = 0.0067(Z_h^{0.927})(Z_{dr}^{-3.43}) \quad (6.36)$$

where R is given in  $\text{mm hr}^{-1}$  and the lowercase subscripts for  $Z_h$  and  $Z_{dr}$  indicate values in linear units. Understanding how radar-estimated rainfall rates may change in height

due to evaporation is important for QPE, especially far from the radar or in regions of complex terrain where low levels may not be adequately sampled (e.g., Maddox et al. 2002). Computing rainfall rates based on accepted algorithms (eqns. 6.34 – 6.36) and comparing these estimates to the actual rainfall rate demonstrates the performance of each of the algorithms in situations where the DSD is changing with height through evaporation.

Vertical profiles of rainfall rate are plotted in Fig. 6.11. A MP distribution is assumed at the top of the domain with a rainfall rate of  $5 \text{ mm hr}^{-1}$ . In all cases, the true rainfall rate changes more rapidly than any of the estimates. Note that the initial large decrease in  $R$  in the Wallops Island simulation is a consequence of the dry layer near 700 hPa (see Fig. 6.9c). At the top of the domain, the  $R(Z_H, Z_{DR})$  estimate is closest to the actual  $R$ , but as the raindrops evaporate, the  $R(K_{DP})$  better matches the true  $R$ . It should be noted, however, that actual measurements of  $K_{DP}$  can be noisy in light rain, so  $R(K_{DP})$  is not necessarily the best estimate for operational use in the case of evaporation and light rain, unless rainfall accumulations are taken over long times (e.g., Borowska et al. 2011b). The evaporative changes at the ground using different rainfall rate estimates are summarized in Table 6.3. Overall, the  $R(Z_H, Z_{DR})$  relation best captures the change in rainfall rate with height (i.e., it is least sensitive to the change in DSD at low rainfall rates, which was frequently claimed as an advantage of the polarimetric radar estimates), though all relations underestimate the change as calculated from the actual DSD. It is clear that substantial decreases in rainfall rate are possible in dry environments, and even in the moist Wallops Island environment the true rainfall rate



decreased by almost  $3 \text{ mm hr}^{-1}$ . If the rainfall rate at low levels is not adequately estimated based on radar measurements, this error can accumulate with time.

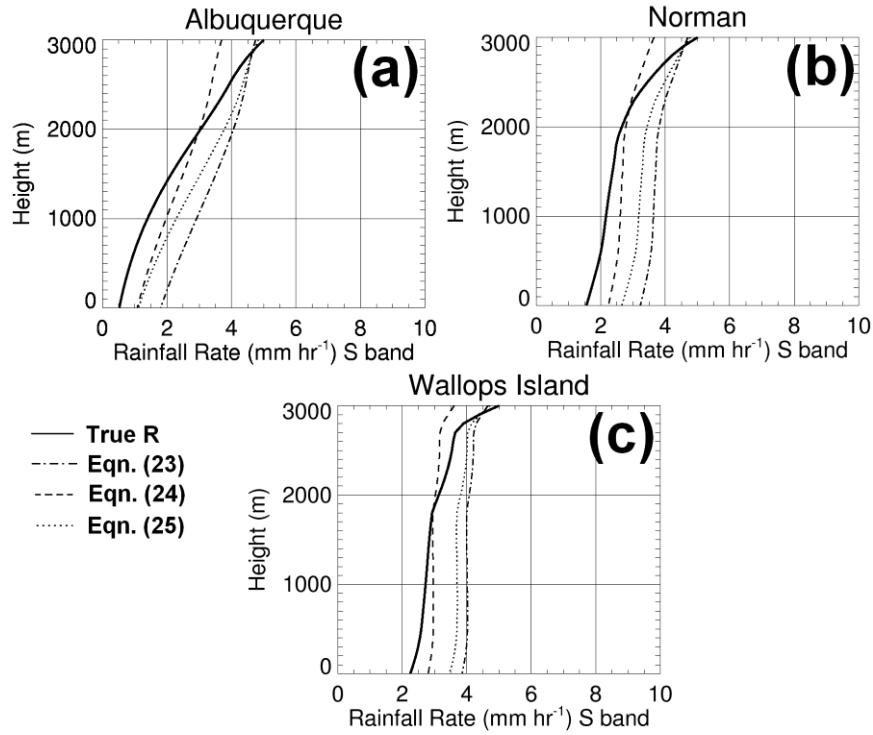


Fig. 6.11: Vertical profiles of rainfall rates for the three soundings. The thick solid line is the actual  $R$  determined from the DSD at each level. The dash-dot line is  $R(Z_H)$  (eqn. 6.34), the dashed line is  $R(K_{DP})$  (eqn. 6.35), and the dotted line is  $R(Z_H, Z_{DR})$  (eqn. 6.36). At cloud base, the MP model is used for these simulations, with a rainfall rate of  $5 \text{ mm hr}^{-1}$  aloft.

	Albuquerque, NM	Norman, OK	Wallops Island, VA
$\Delta R(Z_H)$ in $\text{mm hr}^{-1}$	-3.05	-1.48	-0.87
$\Delta R(K_{DP})$ in $\text{mm hr}^{-1}$	-2.70	-1.42	-0.87
$\Delta R(Z_H, Z_{DR})$ in $\text{mm hr}^{-1}$	-3.82	-2.13	-1.34
$\Delta R$ (true)	<b>-4.55</b>	<b>-3.46</b>	<b>-2.86</b>

Table 6.3: Evaporative change in rainfall rate for each of the three soundings for the three rainfall algorithms  $R(Z_H)$ ,  $R(Z_H, Z_{DR})$ , and  $R(K_{DP})$  (eqns. 6.34 – 6.36, respectively) based on the MP DSD along with the “true” rainfall rate calculated from the actual DSD.

There are numerous  $R(Z_H, Z_{DR})$  relations suggested in the literature (see Ryzhkov et al. 2005c for a review). For comparison, the calculations are reproduced comparing the  $R(Z_H, Z_{DR})$  relation from eqn. (6.36) to the one recommended by Giangrande and Ryzhkov (2008):

$$R(Z_H, Z_{DR}) = 0.0142(Z_h^{0.770})(Z_{dr}^{-1.67}) \quad (6.37)$$

and the relation of Brandes et al. (2002),

$$R(Z_H, Z_{DR}) = 0.00746(Z_h^{0.945})(Z_{dr}^{-4.76}) \quad (6.38)$$

The relations in eqns. (6.36) and (6.38) produced similar results and outperform the relation in eqn. (6.37) in gauging the decrease in rainfall rate due to evaporation. This is likely due to the stronger dependence of  $R$  on  $Z_{DR}$  in eqns. (6.36) and (6.38): the subtle changes in shape of the DSD are not captured by  $Z_H$ , whereas  $Z_{DR}$  does provide some information about the shape of the DSD.

Reproducing the calculations with the  $\Gamma, \mu = -1$  DSD, the relative errors (between the estimates of evaporative change in rainfall rate and the true evaporative change in rainfall rate) depend on the sounding but are all within  $2 \text{ mm hr}^{-1}$  of the true  $\Delta R$ . In contrast, these errors are minimized with the  $R(Z_H, Z_{DR})$  relation for the  $\Gamma, \mu = 5$  and MP models. The difficulty for operational forecasters is to determine the initial DSD aloft. There are rigorous methods for DSD retrieval based on polarimetric radar measurements, such as the procedures described in Zhang et al. (2001, 2006), and Brandes et al. (2002, 2004). These methods mainly rely on  $Z_H$  and  $Z_{DR}$  measurements.

Using the idealized well-mixed layer environments, and initializing the model with a variety of constrained gamma DSD models with varying rainfall rates ( $0.1 - 20 \text{ mm hr}^{-1}$ ) and shape parameters ( $-1 \leq \mu \leq 5$ ), the relation between the initial  $Z_H$  and  $Z_{DR}$

aloft and the evaporative change in rainfall rate over the domain (in this case, 3 km) is explored. With the constrained gamma DSD models, the *relative change in rainfall rate due to evaporation* ( $\Delta R/R$ ) is independent of the initial  $Z_H$  aloft. Thus,  $\Delta R/R$  is a function of the environment (including temperature, RH, and depth of the sub-cloud layer) and the initial  $Z_{DR}$  aloft. Observations of  $Z_H$  and  $Z_{DR}$  at cloud base can be used to identify the initial rainfall rate aloft. Obviously, these parameters may be a function of time in evolving storms, but for quantitative precipitation estimation one must assume a steady state for at least the duration of a radar volume scan. Next, the relative humidity (or another moisture variable) and temperature profiles in the layer beneath the radar horizon can be determined from observations or numerical weather prediction model output (e.g., the Rapid Update Cycle, or RUC; e.g., Benjamin et al. 1991, 1994, 2004). In this manner, environmental conditions and the observed  $Z_{DR}$  (which does not change much with height) can be utilized efficiently to estimate  $\Delta R/R$  (Figs. 6.12, 6.13). Such a process may aid in quantitative precipitation estimates, especially in regions far from the radar or in the case of poor low-level radar coverage.

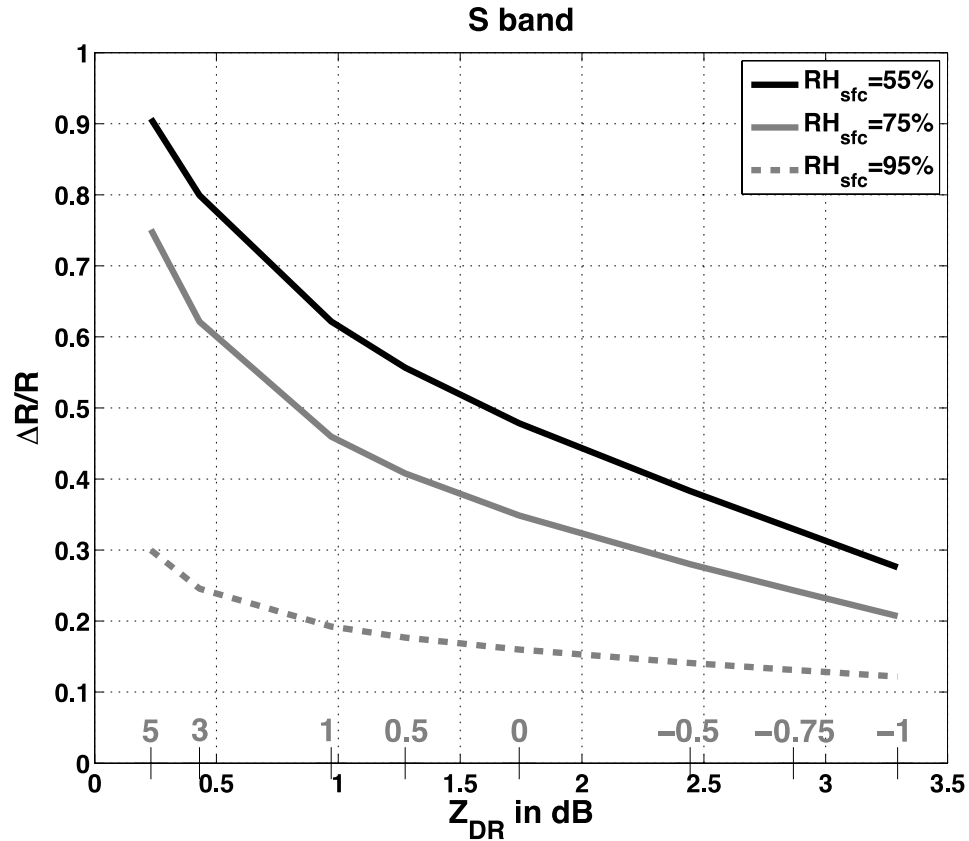


Fig. 6.12: The dependence of relative change in rainfall rate  $\Delta R/R$  on S-band  $Z_{DR}$  aloft and surface relative humidity. Results are of calculations using a 3-km deep idealized well-mixed layer with surface temperature of 30 °C. Each curve corresponds to a different value of surface relative humidity (solid black line for 55%, solid gray line for 75%, and dashed gray line for 95%). Only constrained gamma models (with 5 mm hr<sup>-1</sup> rainfall rate) are used in the calculations, where  $\Delta R/R$  is independent of  $Z_H$  aloft. The gray numbers along the abscissa correspond to the shape parameter ( $\mu$ ) values associated with the given  $Z_{DR}$ .

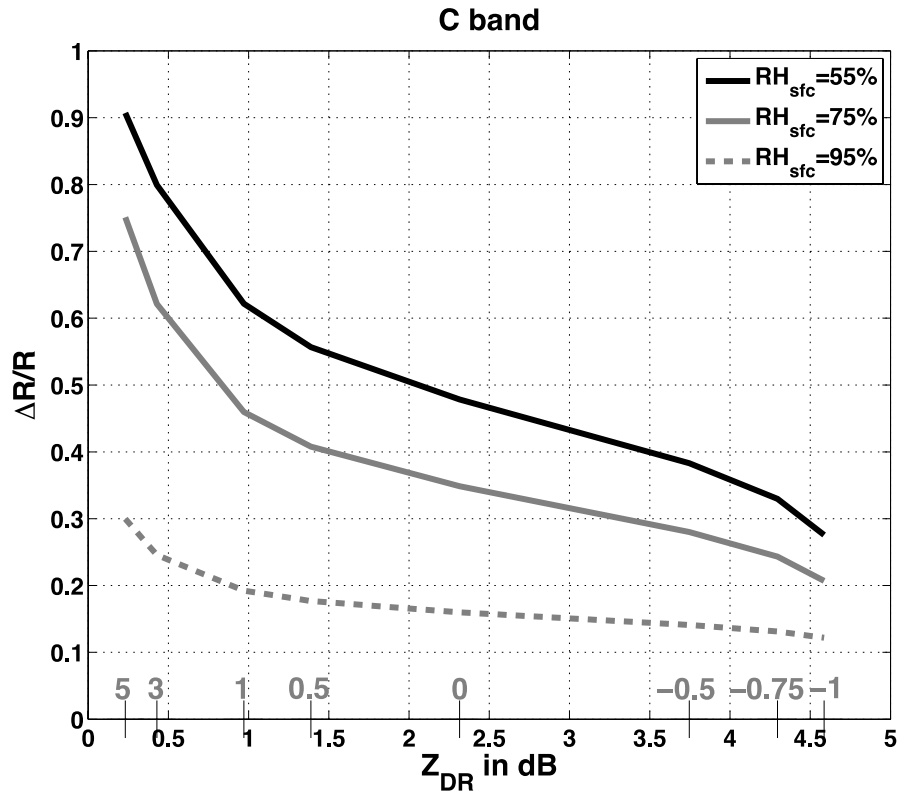


Fig. 6.13: As in Figure 6.12, except here C-band values are shown.

## 6. Comparison with Observations

A recent study by Borowska et al. (2011b) investigated the accumulation of light rainfall over a one-month period in Bonn, Germany. Their results are in agreement with the theoretical model described here. Notably, they found that  $Z_{DR}$  was larger at lower elevations, although it corresponded to a smaller rainfall rate. This inverse correlation between trends in  $Z_{DR}$  and rainfall rate towards the ground can also be caused by size sorting (see Chapter 5); however, because their observations spanned one month, the transient effects of size sorting can be safely ruled out. Borowska et al. (2011b) also applied the evaporation model to median conditions in Bonn: surface RH = 87%,  $T = 7.6$  °C, and sub-cloud depth of 1 km. The model predicts a 22% decrease in  $K_{DP}$  over

the 1 km depth, using the  $\Gamma, \mu = 5$  DSD with an initial rainfall rate of  $3 \text{ mm hr}^{-1}$ . Their measurements indicate a 20% average decrease in  $K_{DP}$  over that layer, in quite good agreement with the theoretical predictions offered by the simple model. This limited set of observations suggests that the evaporation model captures the essential physics in light rain.

## 7. Summary of Conclusions

In this chapter we have investigated and quantified the impact of evaporation on the polarimetric radar variables that will be available following the national upgrade of the WSR-88D radar network:  $Z_H$ ,  $Z_{DR}$ ,  $K_{DP}$ , and  $\rho_{hv}$ . Evaporation can produce significant decreases in  $Z_H$  and  $K_{DP}$  and subtle increases in  $Z_{DR}$ , with no significant change in  $\rho_{hv}$  at S band. At C band, changes in  $K_{DP}$ ,  $Z_{DR}$ , and  $\rho_{hv}$  are amplified for a given amount of evaporation. The change in true rainfall rate due to evaporation is dependent on the initial shape of the DSD aloft, which exemplifies the importance of using polarimetric radar observations to reduce this uncertainty. To test the sensitivity of the polarimetric variables to thermodynamic conditions in the sub-cloud environment, initial DSD aloft, and rainfall rate, a simple explicit bin microphysics model is constructed and numerous experiments were conducted. Because it neglects raindrop collisional processes, the model is limited to relatively light rainfall rates and should not be used to simulate DSD evolution. However, comparison with an observational study by Borowska et al. (2011b) demonstrates good agreement between the theoretical predictions of the model and the observational data. To summarize the main conclusions:

- 1) As expected, warmer and/or drier environments produce more evaporation and thus more substantial changes in the polarimetric radar variables as well as the rainfall rates inferred from these variables.
- 2) The resulting vertical profiles of polarimetric variables from the simplistic model are sensitive to the initial DSD aloft, which is of considerable uncertainty in various precipitation regimes. Thus, polarimetric radar measurements ( $Z_H$ ,  $Z_{DR}$ ) aloft are needed to diminish the uncertainty due to DSD variability. Drop size distributions with large concentrations of smaller drops ( $< 2$  mm) and relatively low number concentrations of big drops ( $> 4$  mm) exhibit the largest evaporative changes in  $Z_H$  and  $K_{DP}$ . This is because the small drops are preferentially evaporated, while the backscattered signals are not overwhelmed by contributions from a large number of big drops. Distributions with a comparatively large concentration of big drops and a sufficiently high concentration of smaller drops (such as the MP model) will exhibit the largest increase in  $Z_{DR}$ . Evaporative changes in  $\rho_{hv}$  are generally quite small in magnitude and likely unobservable at both S and C bands.
- 3) When the evaporative changes are converted into logarithmic units, the difference in  $K_{DP}$  is larger in magnitude than that of  $Z_H$ . This is because  $K_{DP}$  is less sensitive to large drops than  $Z_H$ . Since  $K_{DP}$  is generally displayed in linear units ( $\text{deg km}^{-1}$ ), evaporative changes may be more evident in  $K_{DP}$  than in  $Z_H$ , especially at shorter radar wavelengths. It is important to note that estimates of  $K_{DP}$  at S band can be noisy, especially in light rain as

considered in this study. The relative changes of  $K_{DP}$  are about the same at S and C bands.

- 4) Except for evaporative changes in  $Z_{DR}$  at C band, the changes in polarimetric variables become less significant with increasing rainfall rate. For rainfall rates larger than about  $10 \text{ mm hr}^{-1}$ , the effects of evaporation on the evolution of the drop size spectrum as well as the vertical profiles of polarimetric variables is less significant than other microphysical processes such as coalescence and breakup. These collisional processes should be considered dominant in heavy rain and should be included in more general applications.

Additionally, the use of observed soundings to initialize the model produces realistic vertical profiles of polarimetric variables. Different environments produce different degrees of evaporation that are in principle measurable by operational S- and C-band polarimetric radars. Quantitative bounds to the evaporative changes in polarimetric variables are suggested using the extremes in variations in DSD shape. However, we should again emphasize the limitations of the model. Because drop coalescence and breakup are ignored, the model is applicable only to relatively light rain. To more accurately model sub-cloud microphysics for more general applicability, these effects must be considered. Also, the moistening and cooling of the shaft must be turned “on” for simulation studies, especially when coupled with dynamical models.

In situations where low levels are unobserved by radar, modeling based on thermodynamic information from soundings or numerical weather prediction models such as the RUC may provide guidance for precipitation estimates, allowing for



adjustments to be made to observed rainfall rates aloft. Assuming the DSD can be described by a constrained gamma model, the relative change in rainfall rate due to evaporation  $\Delta R/R$  is independent of  $Z_H$  aloft. Thus,  $Z_{DR}$  (together with the environmental thermodynamic profiles) can be used in a simple evaporation model to estimate  $\Delta R/R$ . This method differs from conventional statistical or climatological techniques because the simple modeling approach in this study is physically based. The use of polarimetric measurements provides crucial information that is not available with single-polarization radar measurements of  $Z_H$ . Such adjustments to conventional techniques may improve estimates of rainfall rates at the surface, benefiting hydrology models and forecasts.

## **Chapter 7: The Impact of Coalescence on the Polarimetric Radar**

### **Variables.**

Material from this chapter comes from a conference paper (Kumjian et al. 2012b). The results and method presented herein should be considered more preliminary than the other chapters (which derive material from published articles).

#### **1. Introduction.**

Precipitation growth via the “warm rain processes” does not involve ice particles, as the name implies. Instead, cloud droplets grow by condensation until they become sufficiently large as to sediment relative to the other droplets. Once such sedimentation occurs, droplet growth quickly continues by accretion of other cloud droplets different in size (and thus fall speed), whereupon the collecting droplet rapidly grows in size to a raindrop. Apparently, only 1 droplet in  $10^6$  must attain sufficiently large size to initiate the production of precipitation (e.g., Rogers and Yau 1989; Pruppacher and Klett 1997).

As the precipitation particles fall to the ground, the evolution of the DSD beneath cloud base is governed by four main processes: growth of large drops (and subsequent depletion of small drops) by coalescence, depletion of large drops (and increase in concentration of smaller drops) by collisional breakup, size sorting of drops, and a decrease of drop sizes across the spectrum (and depletion of the smallest drops) by evaporation. Size sorting and evaporation were discussed in Chapters 5 and 6, respectively. The remaining two warm-rain processes (coalescence and breakup) are

considered the “collisional” processes and are discussed herein. The equation governing the evolution of number density  $n$  in time by the collisional processes can be written following Gillespie and List (1978) and Brown (1995, among others) as:

$$\begin{aligned}
\frac{\partial n(m, t)}{\partial t} = & \int_{\frac{m}{2}}^{\infty} \int_0^{\mu} n(\mu, t) n(\mu_1, t) f(\mu, \mu_1) [1 - E(\mu, \mu_1)] Q(m; \mu, \mu_1) d\mu_1 d\mu \\
& - \int_0^{\infty} n(m, t) n(\mu_1, t) f(m, \mu_1) [1 - E(m, \mu_1)] d\mu_1 \\
& + \int_0^{m/2} n(\mu, t) n(m - \mu, t) f(\mu, m - \mu) E(\mu, m - \mu) d\mu \\
& - \int_0^{\infty} n(m, t) n(\mu, t) f(\mu, m) E(\mu, m) d\mu \quad . \quad (7.1)
\end{aligned}$$

The first two terms on the right hand side of eqn. (7.1) represent drop breakup, and the latter two terms represent drop coalescence. Here,  $E(\mu, \mu_1)$  is the coalescence efficiency for drops of masses  $\mu$  and  $\mu_1$ ,  $Q(m; \mu, \mu_1)\Delta m$  is the average number of drop fragments with mass  $m$  to  $m + \Delta m$  produced by collision and subsequent breakup of drops with masses  $\mu$  and  $\mu_1$ , and  $f(\mu, \mu_1)$  is the collision kernel for drops with masses  $\mu$  and  $\mu_1$ . The collision kernel is given by

$$f(\mu, \mu_1) = \pi (r_{\mu} + r_{\mu_1})^2 E_{col}(\mu, \mu_1) |V_{\mu_1} - V_{\mu}|, \quad (7.2)$$

where  $r_{\mu}$  is the radius of a drop with mass  $\mu$ ,  $E_{col}$  is the collision efficiency of drops with masses  $\mu$  and  $\mu_1$ , and  $V_{\mu}$  is the falling velocity of a drop with mass  $\mu$ .

Obviously, the governing equation (7.1) is rather complex. As such, there have been many studies of this equation, methods for solving it, and its parameterizations

(Low and List 1982a,b; Brown 1986, 1987, 1993, 1994; List et al. 1987; List and McFarquhar 1990; Seifert et al. 2005). In contrast, there have been relatively few studies of these processes in nature, such as remote sensing-based retrievals of changes in the DSD owing to these processes. Dual-polarization radar is particularly well suited for such a study, as the polarimetric radar variables are sensitive to changes in the overall shape of the rain DSD, especially the large-drop end of the size spectrum. This sensitivity is particularly pronounced at shorter radar wavelengths (C and X bands).

Because of the aforementioned complexity of the governing equation, this chapter takes a different approach. Instead of a one-dimensional column model, vertical profiles of the polarimetric radar variables in warm-rain precipitation are investigated, and microphysical retrievals are performed. These retrievals include DSD parameters, which are used to explore the vertical evolution of the DSD in ongoing coalescence.

## **2. Physics of Coalescence: a *Gedankenexperiment*.**

Before embarking on the microphysical retrievals, it is instructive to consider a simple thought experiment, or *gedankenexperiment*. Consider two identical drops with mass  $m_1$  and diameter  $D_1 = (6m_1/\pi\rho_w)^{1/3}$ , where  $\rho_w$  is the density of liquid water. A collection of  $N_1$  of these drops would result in a radar reflectivity factor (in the Rayleigh approximation) of  $Z_1 = N_1 D_1^6$ . Consider now that these two drops collide and coalesce to form one larger drop of mass  $m_2 = 2m_1$ . It follows that the diameter  $D_2$  of the new big drop is given by  $D_2 = 2^{1/3} D_1$ , and the concentration of the big drop  $N_2 = 0.5N_1$ . Thus, we can calculate the Rayleigh radar reflectivity factor of the new big drop:

$$Z_2 = N_2 D_2^6 = 0.5N_1 (2^{1/3} D_1)^6 = 2N_1 D_1^6 = 2Z_1 \quad .$$

In other words, the new reflectivity factor is 3 dBZ larger than before the two drops coalesce. We can perform the same analysis for  $K_{DP}$ , which is dependent on drop diameters as  $D^4$  to  $D^6$ , depending on the rainfall rate. It is clear that for the smaller dependence on diameter, the change in  $K_{DP}$  is less. (If we assume, for the sake of argument, that  $K_{DP} \propto D^5$ , then  $K_{DP2} \approx 1.6K_{DP1}$ ). Thus, we can conclude that coalescence affects  $K_{DP}$  (in general) less than  $Z$ . Because drop oblateness monotonically increases with increasing drop size, it follows that coalescence of two smaller drops tends to increase  $Z_{DR}$  (as a result of the increased oblateness and size of the new big drop).

Using the simple power-law relation of Atlas and Ulbrich (1977) for the relation between drop size and terminal velocity ( $v \propto D^{0.67}$ ), the same analysis reveals that rainfall rate  $R$  increases for coalescence, owing to the larger drop sizes:

$$R_2 = N_2 D_2^3 v_2 \sim N_2 D_2^{3.67} = 0.5 N_1 (2^{1/3} D_1)^{3.67} \approx 1.167 R_1 .$$

It is clear that only those quantities proportional to  $D^x$  for  $x > 3.0$  are *increased* by the process of coalescence, which includes Rayleigh reflectivity factor  $Z$ ,  $K_{DP}$ ,  $Z_{DR}$ , and rainfall rate. Liquid water content  $M$  is proportional to the third moment of the DSD and thus is not changed during pure coalescence. In other words, the total amount of liquid water mass is conserved during coalescence; it is simply redistributed among the drop sizes. That  $M$  is conserved during pure coalescence will be a fundamental assumption of the microphysical retrievals in the following sections.

### 3. Observed Data.

Data from the Bonn X-band Polarimetric (BOXPOL) radar in Bonn, Germany are presented here. Genuine RHIs were collected with  $0.1^\circ$  spacing in elevation, affording high spatial resolution. The precipitation event occurred on 22 June 2011, in which several warm-rain storms were observed (e.g., Figure 7.1). Ten vertical profiles are extracted from this RHI between 13 and 14 km range. The median of these profiles is then constructed (Figures 7.2-7.3). The data reveal a distinct, well-pronounced increase in both  $Z_H$  and  $Z_{DR}$  towards the ground, indicative of increasingly larger drops present closer to the ground. Note that this differs from the signatures of differential sedimentation and evaporation, where  $Z_H$  *decreases* as  $Z_{DR}$  increases (see Chapters 5 – 6). Differential sedimentation is seen in the developing cell at 11 km range. Instead, the profiles in Figures 2-3 provide a clear indication of raindrop growth. We hypothesize that the radar signal and drop growth are being dominated by coalescence. Collisional breakup (which tends to decrease  $Z_{DR}$ ) is undoubtedly occurring, but it is not enough to balance the overall contribution of coalescence to the radar signal.  $Z_H$  increases by over 20 dBZ in 2 km depth. Likewise,  $Z_{DR}$  increases by about 2.5 dB. Note that the data below about 600 m in height are contaminated by ground clutter and have been censored from Figures 7.2 and 7.3. The next sections present a method of retrieving microphysical information (section 4) as well as preliminary results from this method (section 5). The goal is to test the hypothesis that coalescence growth of raindrops is the dominant process ongoing at the times of the radar scans in Figures 7.2 – 7.3, and that it is the microphysical fingerprint of coalescence that is observed in the data.

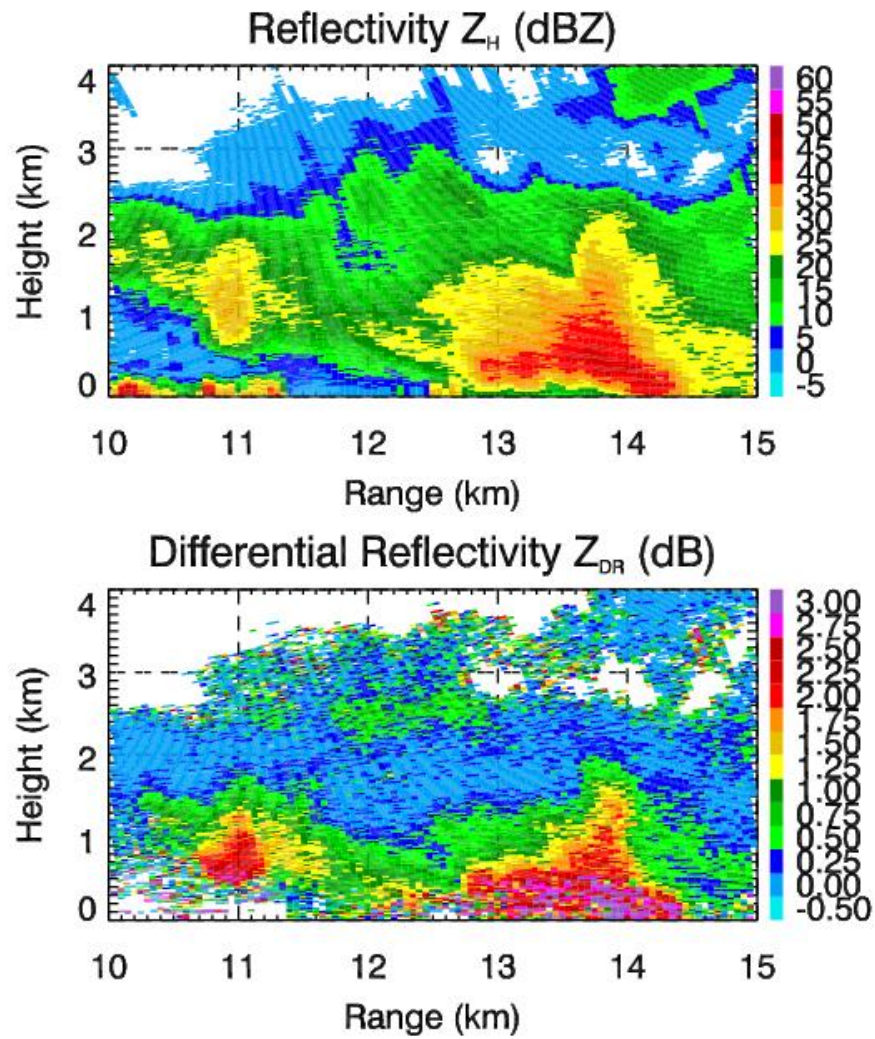


Fig. 7.1: Genuine RHI scan collected with BOXPOL on 22 June 2011 at 1454 UTC, along the  $309.5^\circ$  azimuth. Polarimetric radar variables shown are (top)  $Z_H$ , and (bottom)  $Z_{DR}$ . The cell of interest is located between 13 and 14 km range.

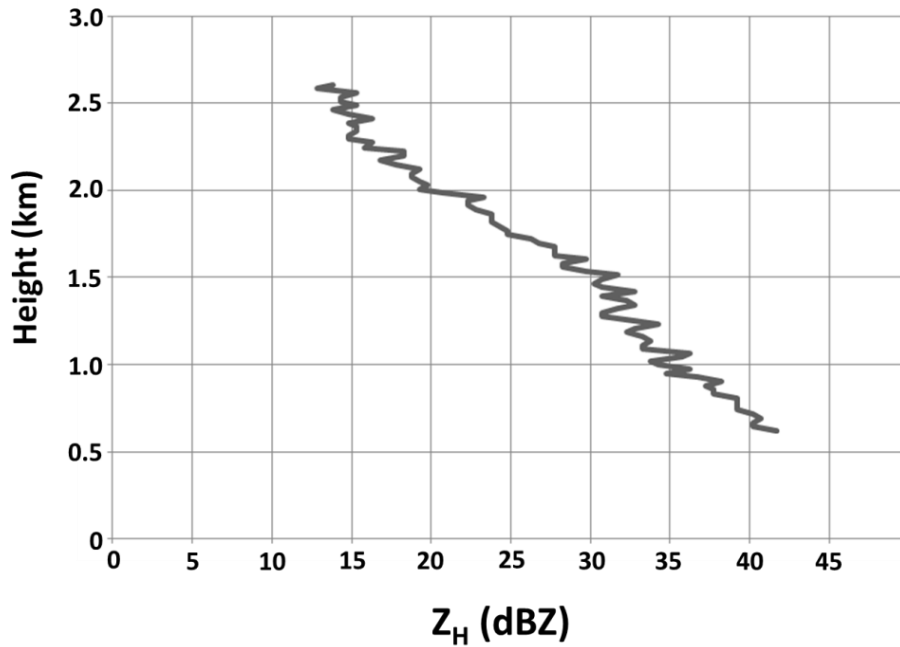


Fig. 7.2: Median vertical profile of  $Z_H$  through the storm in Figure 7.1, constructed from 10 extracted vertical profiles at ranges 13 – 14 km.

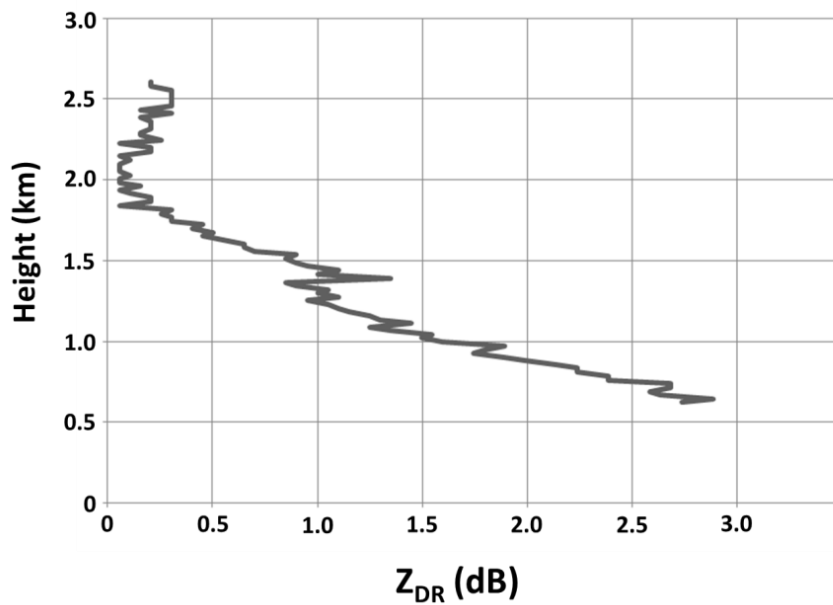


Fig. 7.3: Median vertical profile of  $Z_{DR}$  through the storm in Figure 7.1, constructed from 10 extracted vertical profiles at ranges 13 – 14 km.



#### 4. Microphysical Retrievals: Methods.

Dual-polarization radar observations have the unique capability of being used to retrieve information about the rain DSD shape (e.g., Zhang et al. 2001; Brandes et al. 2002, 2004a,b). For this chapter, calculations of the dual-polarization radar variables for a wide range of DSDs found in nature are modeled by the constrained-gamma relation (e.g., Zhang et al. 2001, 2003)

$$N(D) = N_0 D^\mu \exp(-\Lambda D) \quad . \quad (7.3)$$

The constrained gamma DSD is constrained by an assumed relation between shape parameter  $\mu$  and slope parameter  $\Lambda$ , which has been observed in natural DSDs (e.g., Cao et al. 2008):

$$\mu = -0.0201\Lambda^2 + 0.902\Lambda - 1.718, \quad (7.4)$$

where here  $\Lambda$  is in  $\text{mm}^{-1}$ . The constrained-gamma relation is convenient in that there exists a relation between the DSD slope parameter  $\Lambda$  and  $Z_{\text{DR}}$  (Fig. 7.4). The T-matrix method (Mischenko 2000) was used to compute the complex scattering amplitudes of raindrops at X band with a temperature of  $15^\circ \text{C}$ , from which the polarimetric variables were computed following Ryzhkov (2001) and Ryzhkov et al. (2011). The  $\mu$ - $\Lambda$  relation from Cao et al. (2008) is used to determine the  $Z_{\text{DR}}$  for a given slope parameter  $\Lambda$ . Though some controversy exists about the physical nature of this relation (e.g., see Zhang et al. 2003; Moisseev and Chandrasekar 2007; Seifert 2008), it is clear from Figure 7.4 that it lies within the natural range of values. The observed  $Z_{\text{DR}}$  profile is compared to the  $\Lambda$ - $Z_{\text{DR}}$  relation to determine the best match for  $\Lambda$ . Then, the retrieved profile of  $\Lambda$  is used with eqn. (7.4) to retrieve the vertical profile of  $\mu$  (Fig. 7.5). A vertical profile of  $Z_{\text{DR}}$  is computed based on the retrieved  $\Lambda$  and  $\mu$  values (remember

that  $Z_{DR}$  is independent of concentration and thus does not depend on  $N_0$ ). Obviously, one should expect this retrieved  $Z_{DR}$  to agree very well with the observed profile; this step is performed as a “sanity check” for the retrievals of  $\Lambda$  and  $\mu$ .

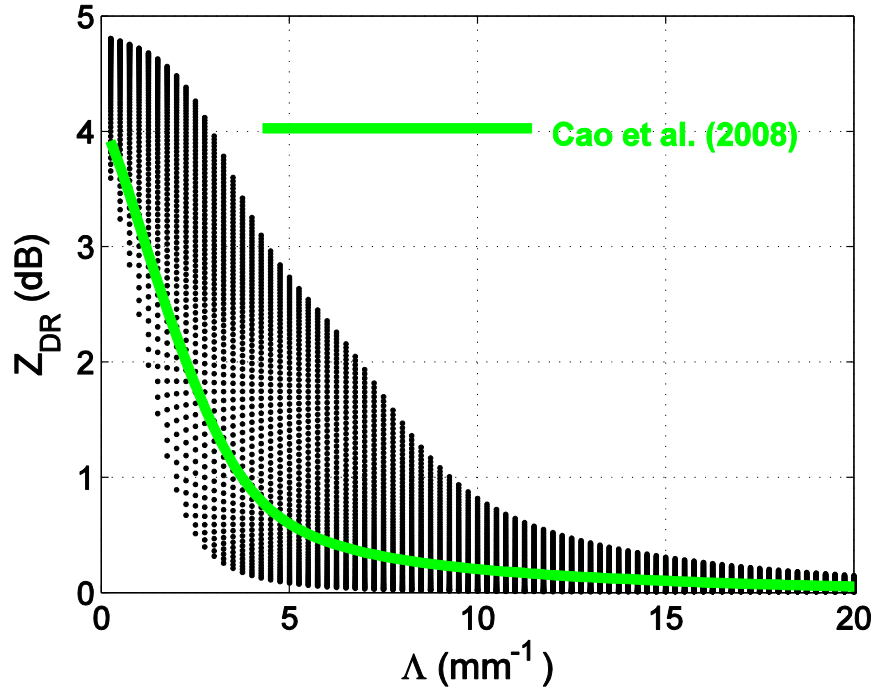


Fig. 7.4: Scatter of the range of  $\Lambda$ - $Z_{DR}$  points observed in nature (black points), overlaid with the  $Z_{DR}$  from the Cao et al. (2008) relation (green). Calculations made at X band, for raindrops with temperature = 15 °C.

At the bottom of the profile, total liquid water content  $M$ ,

$$M = \frac{\pi}{6} \rho_w \int_0^{\infty} N(D) D^3 dD \quad (7.5)$$

is determined (rather subjectively) based on what provides best match of the observed profiles of the polarimetric radar variables. From this height, *the flux of liquid water mass content  $M$  is assumed to remain constant with height*

$$Mv = M_{ref} v_{ref} = \text{constant} . \quad (7.6)$$

In other words, it is assumed that no water mass is lost owing to evaporation; rather, liquid water mass is simply redistributed from one size bin to another<sup>7</sup>, and is affected by the change in raindrop fallspeed with height owing to changes in air density. Air density is determined from the 12 UTC sounding on 22 June 2011 from Essen, Germany (Fig. 7.6), located roughly 90 km to the north-northwest of Bonn. Using  $M$ ,  $\mu$ , and  $\Lambda$  at each height, intercept parameter  $N_0$  is determined by solving eqn. (7.5):

$$N_0 = \frac{6M\Lambda^{4+\mu}}{\pi\rho_w\Gamma(4+\mu)}, \quad (7.7)$$

where  $\Gamma$  is the gamma function. The retrieved DSD at each level is then determined by equation (7.3). Note that  $Z_H$  is not used to determine the DSD parameters; rather, the  $Z_H$  calculated from the *retrieved* DSD will be compared to observations as a test of the methods and assumptions.

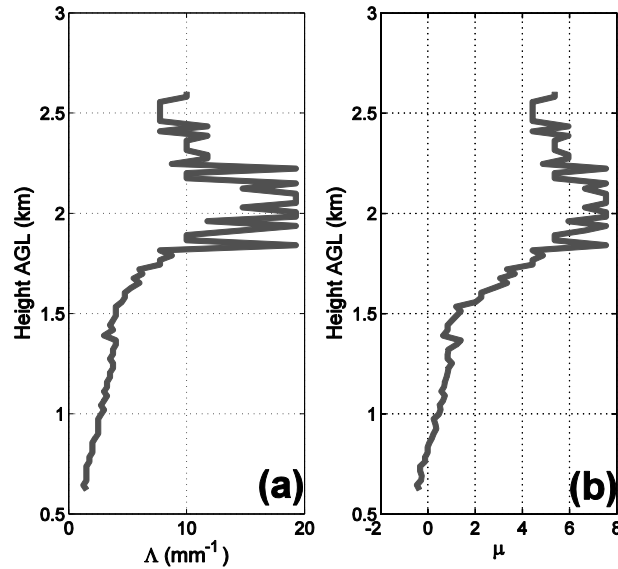


Fig. 7.5: Vertical profiles of (a) slope parameter  $\Lambda$  and (b) shape parameter  $\mu$ , retrieved from polarimetric radar measurements.

<sup>7</sup> Because coalescence causes a shift of mass from smaller drops to larger drops, it is analogous to conservative fiscal policy favoring the wealthy. In contrast, breakup can be thought of as a redistribution of mass from large drops to small drops, analogous to social democratic fiscal policy.

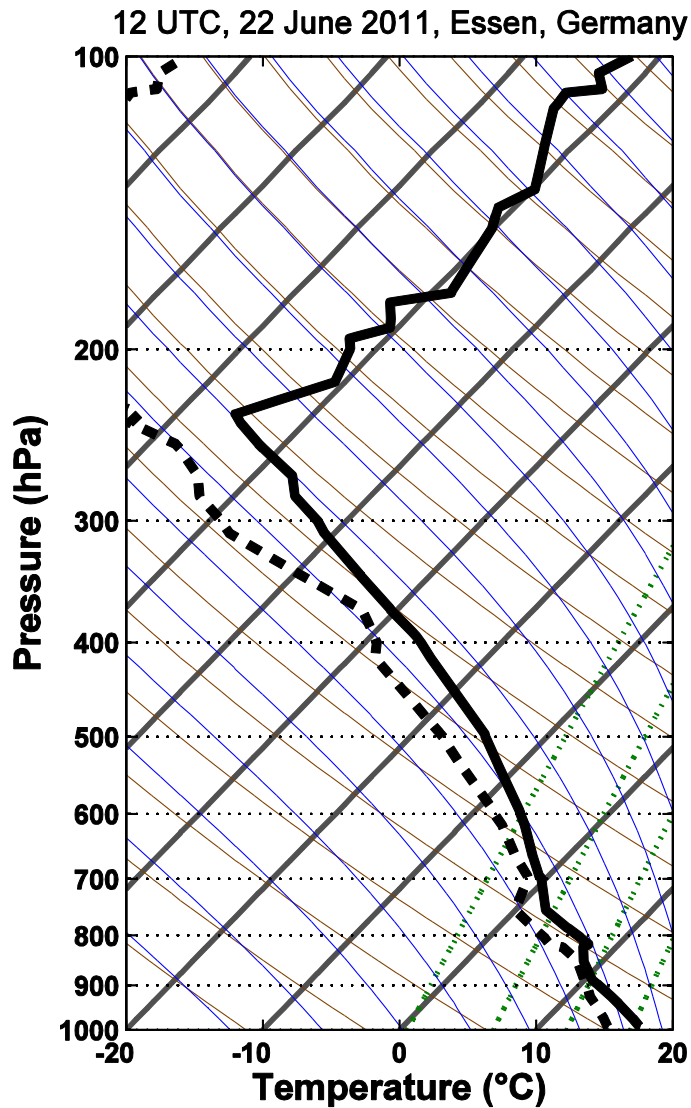


Fig. 7.6: Observed sounding from Essen, Germany, on 22 June 2011 at 12 UTC.

### 5. Microphysical Retrievals: Results.

The vertical profiles of polarimetric radar variables  $Z_H$  and  $Z_{DR}$  are calculated from the retrieved DSD at each level. Figure 7.7 compares the retrieved  $Z_{DR}$  profile to the observed  $Z_{DR}$  profile. As expected, there is very good agreement over all height levels. This is because the  $Z_{DR}$ - $\Lambda$  relation was used as an input to the retrieval. Figure

7.8 shows the retrieved vertical profile of  $Z_H$  compared to the observations. Recall that  $Z_H$  is under the constraint that the flux of the mass water content is conserved at each level. The surprisingly good agreement below about 2 km indicates that this assumption is likely valid. In other words, the analysis provides evidence in favor of our hypothesis that coalescence likely is the dominant process below this height. Indeed, relative errors (Fig. 7.9) in the retrieved  $Z_H$  (compared to the observed  $Z_H$ ) below 2 km AGL are within  $\pm 10\%$ . The disagreement between retrieved and observed  $Z_H$  above about 2 km is also informative. It demonstrates that the assumption of constant  $M$  flux is not valid in this height interval. We can infer this because the  $Z_{DR}$  profiles match very well, implying that the overall shape of the DSD ( $\mu$  and  $\Lambda$ ) are rather close to reality. In other words, there is likely a change in  $M$  with height above about 2 km. Because the retrieved profile has larger values of  $Z_H$  above 2 km than the observed profile, but matches below 2 km, one can infer that  $M$  is being *generated* or added at levels above 2 km, owing to activation of more drops (e.g., within an updraft) or accretion of cloud water droplets.

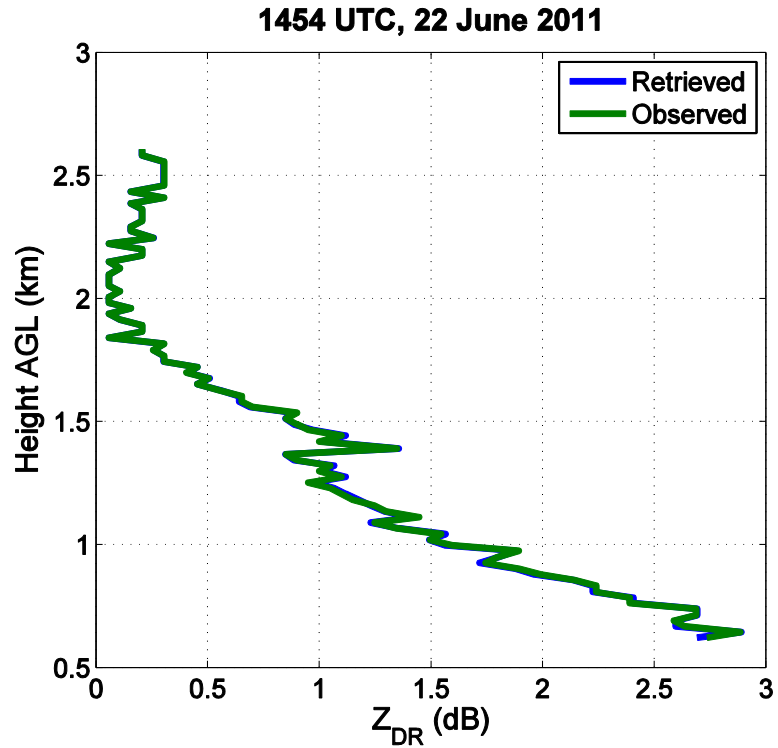


Fig. 7.7: Retrieved  $Z_{DR}$  (blue curve) and the observed  $Z_{DR}$  (green curve) profiles as a function of height.

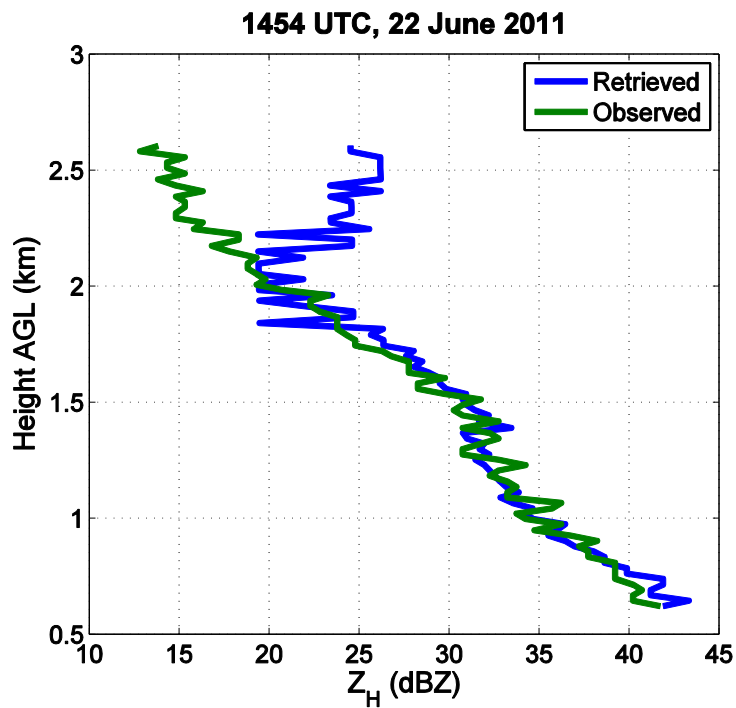


Fig. 7.8: As in Figure 7.7, but the retrieved (blue) and observed (green)  $Z_H$  profiles are shown.

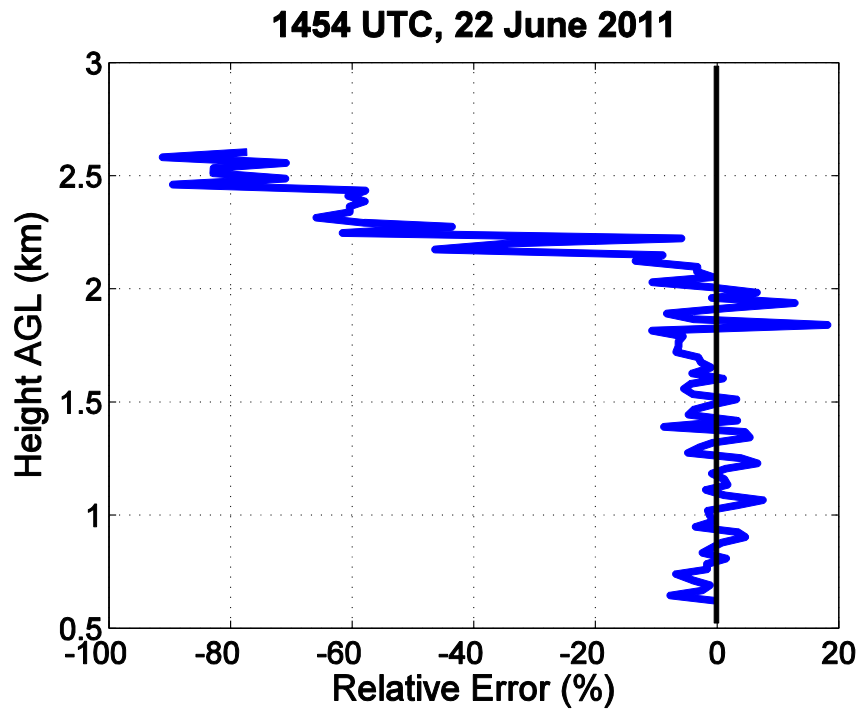


Fig. 7.9: Relative error (%) of the retrieved  $Z_H$  profile for 1454 UTC on 22 June 2011.

The DSDs retrieved at each level (Figure 7.10) reveal the evolution of DSDs undergoing assumed pure coalescence. It is important to emphasize that we do not attempt to perfectly retrieve the actual DSD; rather, the retrieval provides a *plausible* look at the evolution of the DSD in height affected by pure coalescence. Indeed, disagreement between the retrieved profiles and the observations is also instructive, as illustrated above. Moving towards the ground (colors in Figure 7.10 transition from black to blue to red) the concentration of smaller drops ( $< 1.5 \mu\text{m}$ ) decreases substantially as the concentration of large drops increases and the DSD broadens. Note that this effect is retrieved solely from our assumptions and polarimetric data; no physical parameterization of coalescence has been implemented.

These retrieved DSDs can be used to compute the other polarimetric radar variables  $K_{DP}$  and  $\rho_{hv}$  (Fig. 7.11). Note the increase in  $K_{DP}$  towards the ground; similar to  $Z_H$ , this implies that the increase in particle size overcomes the decrease in particle concentration. This result also agrees well with the *gedankenexperiment* described earlier: if converted to logarithmic units, the increase in  $K_{DP}$  is about 12 dBZ, which is less than the increase in  $Z_H$  (closer to 20 dBZ). The decrease in the retrieved  $\rho_{hv}$ , though small in magnitude, is consistent with the broadening of the DSD depicted by Figure 7.10.

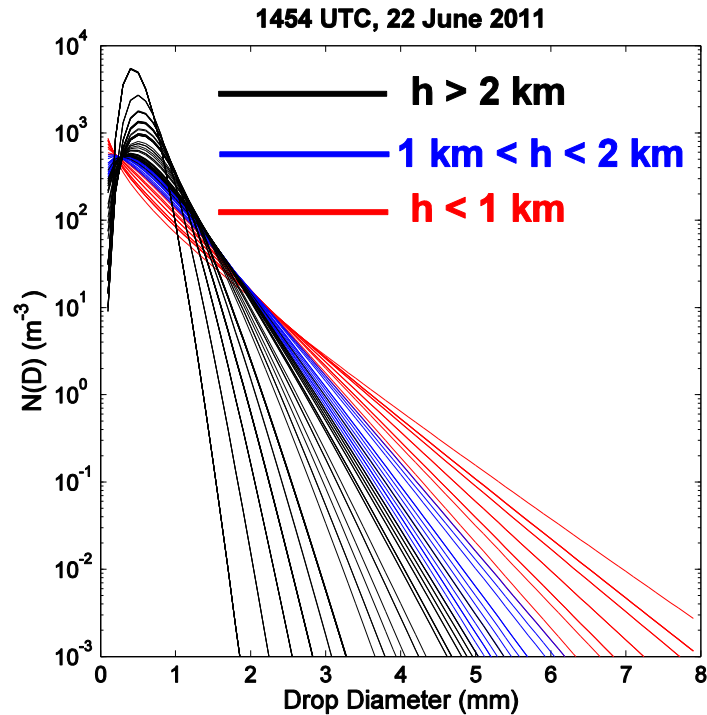


Figure 7.10: Retrieved DSD at each height level, with each color indicating a certain depth. As expected with coalescence growth, the initially narrow DSD broadens and acquires a shallower slope, indicative of an increase in concentration of large drops and a decrease in concentration of small drops (sizes < 2 mm).



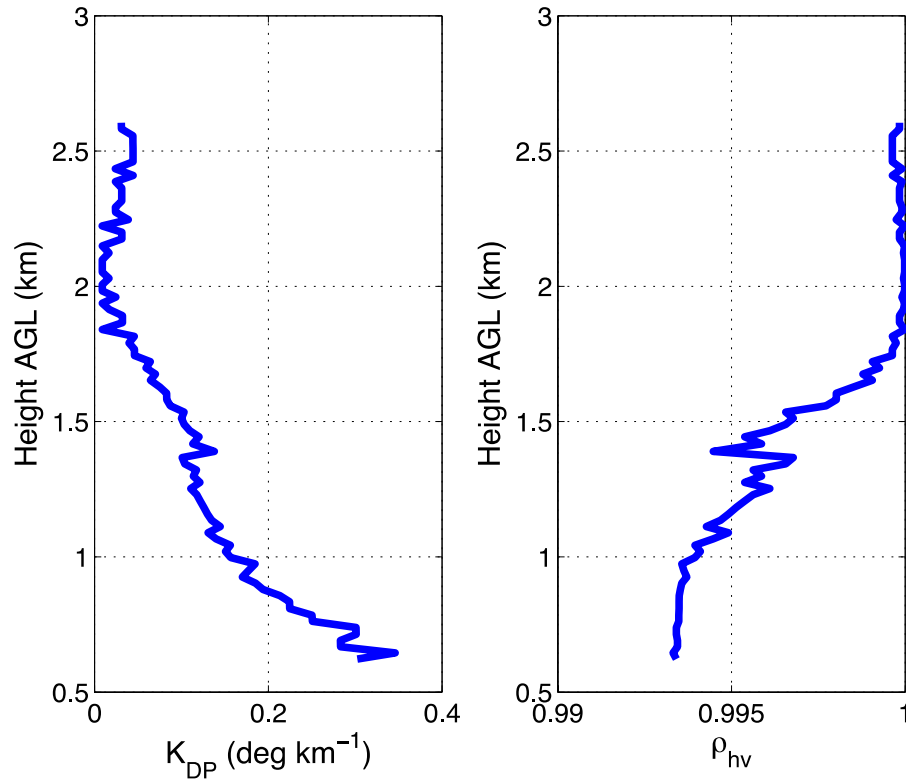


Fig. 7.11: Retrieved profiles of  $K_{DP}$  (left panel) and  $\rho_{hv}$  (right panel) from 22 June 2011, 1454 UTC.

## 6. Discussion and Conclusions.

Though the *gedankenexperiment* and microphysical analysis presented above deal with coalescence, in principle the same approach can be employed to explore the other collisional process: drop breakup. Based on the *gedankenexperiment*, we can expect breakup to produce a fingerprint in the polarimetric radar variables that is opposite in sign of that of coalescence. In other words, whereas coalescence leads to an increase in  $Z_H$ ,  $Z_{DR}$ , and  $K_{DP}$ , and a decrease in  $\rho_{hv}$ , breakup should cause a decrease in  $Z_H$ ,  $Z_{DR}$ , and  $K_{DP}$ , and an increase in  $\rho_{hv}$ . Note that the magnitudes may be different, depending on the number of drop fragments generated by the breakup of a single large drop; in many cases, it will be larger than 2 (e.g., Low and List 1982a,b). Microphysical

retrievals based on the same principle of conserved water mass flux could be performed. However, it is unlikely that examples of breakup-dominated rain will be found. In all likelihood, coalescence and breakup are occurring simultaneously in heavy rain. However, because coalescence tends to *increase* the larger drops that dominate the backscattered signal, the signal of coalescence is far more likely to be observed than a signal from breakup. If there is no clear change in the polarimetric radar variables with height (i.e., no pronounced increase in  $Z_{DR}$  or  $K_{DP}$ )<sup>8</sup>, one may speculate that coalescence growth and breakup are “in balance.”

In summary, an overview of the physics of drop coalescence was provided, describing the impacts on the polarimetric radar variables based on a simple thought experiment. In addition, a method for retrieving microphysical information was presented. In the case of coalescence, fundamental physical assumptions (namely, the conservation of liquid water mass flux) lead to testable predictions about the changes in the polarimetric radar variables, which are validated by the observations. Such retrievals provide experimental evidence that can be used for comparison with various models and parameterizations of the warm-rain physical processes. Additionally, they provide a basis for better understanding of how such microphysical processes affect rainfall rate beneath cloud base, which can be used to improve the accuracy of remote quantitative precipitation estimation.

---

<sup>8</sup> Note that an increase in  $Z_H$  and  $K_{DP}$  still occurs in the absence of any particle growth because of conservation of drop flux in an environment in which density increases towards the ground.

## Chapter 8: The Impact of Freezing on the Polarimetric Radar

### Variables.

Material in this chapter comes from Kumjian et al. (2012a), submitted to the *Journal of the Atmospheric Sciences*.

#### 1. Introduction

Within warm-season deep convective mid-latitude storms, both warm and cold microphysical processes occur that can be important for determining the precipitation characteristics of such storms. Warm-rain generated liquid drops can be carried above the environmental 0 °C level by the storm's updraft, where they subsequently freeze into ice pellets. These frozen drops can grow further via accretion of supercooled liquid cloud water (riming), transforming them into graupel. The graupel and frozen drops can serve as an important source of hailstone embryos (e.g., Knight and Knight 1970; 1974; 2001; Federer and Waldvogel 1978; Knight 1981; Ziegler et al. 1983; Nelson 1983). Graupel particles are also known to play an important role in lightning production through charge transfer and separation (e.g., MacGorman and Rust 1998, and references therein). Therefore, accurate representation of the freezing process in storm-scale numerical weather prediction models is important, including for short-term forecasts of hail and lightning hazards in severe convective storms.

Dual-polarization radar observations in convective storms routinely reveal columnar regions of enhanced differential reflectivity ( $Z_{DR}$ ) that extend above the environmental freezing level, in some cases by as much as 2 km or more. Such " $Z_{DR}$

columns” (Fig. 8.1) are indicative of wet, oblate hydrometeors being lofted above the freezing level by the convective storm updraft. Since the first observations of such signatures (Hall et al. 1984; Illingworth et al. 1987; Caylor and Illingworth 1987; Tuttle et al. 1989), they have been widely documented (e.g., Meischner et al. 1991; Herzegh and Jameson 1992; Conway and Zrnić 1993; Höller et al. 1994; Brandes et al. 1995; Hubbert et al. 1998; Kennedy et al. 2001; Loney et al. 2002; Ryzhkov et al. 2005c; Kumjian and Ryzhkov 2008a). At the top of  $Z_{DR}$  columns, polarimetric radar observations typically reveal a sharp decrease in  $Z_{DR}$  owing to a substantial decrease in the complex dielectric constant and increased tumbling of hydrometeors as they freeze into solid ice pellets. Coincident with this freezing zone is a decrease in the co-polar cross-correlation coefficient ( $\rho_{hv}$ ), which is sometimes called the  $\rho_{hv}$  hole (e.g., Kumjian and Ryzhkov 2008a). For radars operating in the mode of alternate transmission and reception of horizontally- and vertically-polarized waves, the hydrometeors and processes contributing to the  $\rho_{hv}$  hole are observed as a pronounced increase in linear depolarization ratio ( $L_{DR}$ ), called the  $L_{DR}$  “cap” (e.g., Jameson et al. 1996; Bringi et al. 1997; Hubbert et al. 1998; Kennedy et al. 2001). Though large changes in  $\rho_{hv}$  and  $L_{DR}$  at the summit of  $Z_{DR}$  columns have been associated with the wet growth of graupel and hail (e.g., Herzegh and Jameson 1992; Jameson et al. 1996; Kennedy et al. 2001; Picca and Ryzhkov 2012), changes that are smaller in magnitude may be explained by the increased tumbling and diversity of particle species present during the freezing process (Bringi et al. 1997; Hubbert et al. 1998). These signatures have been implicated in the role of hail formation and development (e.g., Kennedy et al. 2001; Picca and Ryzhkov 2012), and thus studying them may reveal important practical information.

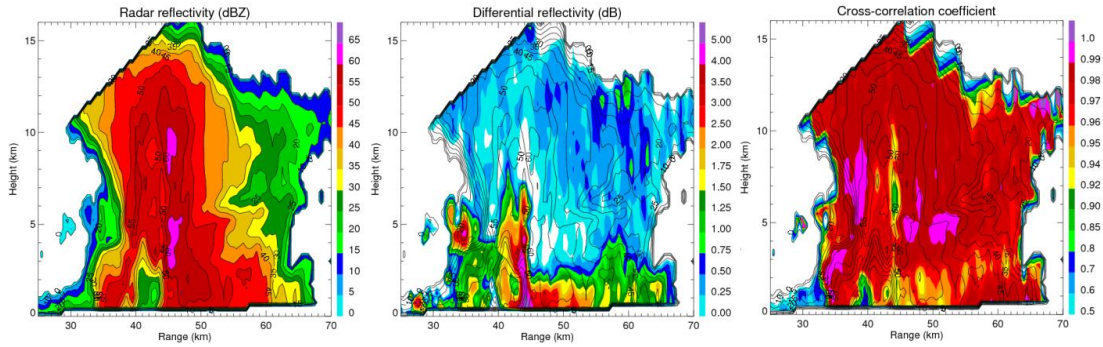


Fig. 8.1: Example of polarimetric data presented as a vertical cross-section through a supercell storm on 10 May 2003, at 0346 UTC, observed with the S-band polarimetric WSR-88D in Norman, Oklahoma. From left-to-right, panels show  $Z_H$ ,  $Z_{DR}$ , and  $\rho_{hv}$ . A  $Z_{DR}$  column is evident at about 44 km range. Note that the environmental melting level is at 4.2 km above the ground, and the updraft-perturbed melting level is near 5.2 km, assuming a surface-based parcel.

The evolution of  $Z_{DR}$  columns and their capping signatures can also provide insight into the storm's behavior. For example, the evolution of  $Z_{DR}$  columns has been recently investigated (Picca and Ryzhkov 2010; Picca et al. 2010) and has proven useful in the short-term forecast of severe convective storms and hail fall. These preliminary studies found strong positive lagged correlations between changes in the integrated volume of positive  $Z_{DR}$  values above the environmental freezing level (“ $Z_{DR}$  column volume”) and changes in the surface reflectivity factor ( $Z_H$ ) 60-dBZ to 40-dBZ ratio on timescales of about 15-20 minutes. Picca and Ryzhkov (2012) also found that a deeper minimum in the  $\rho_{hv}$  hole atop the  $Z_{DR}$  column was followed by an increase in hail size at the surface. Analogously, Kennedy et al. (2001) found that  $L_{DR}$  maxima aloft preceded the largest hail at the surface.

Aircraft penetrations through  $Z_{DR}$  columns confirm the inferences based on polarimetric radar data: that  $Z_{DR}$  columns comprise liquid raindrops and small, wet graupel and hailstones (e.g., Brandes et al. 1995; Smith et al. 1999; Loney et al. 2002; Schlatter 2003; Clabo et al. 2009). These observations demonstrate the existence of

liquid or mixed-phase hydrometeors at subfreezing temperatures in clouds. The presence and distribution of liquid water on or in a particle substantially alter its scattering characteristics, particularly at shorter radar wavelengths. Therefore, an accurate representation of such hydrometeors is crucial for applications of radar (especially polarimetric radar) data and for model-observation intercomparisons. Unfortunately, many bulk microphysics parameterization schemes do not allow for such mixed-phase particles at subfreezing temperatures. A notable exception is Thériault and Stewart (2010), whose winter microphysics scheme includes a “slush” category for partially-frozen/melted hydrometeors. Instead, many schemes convert liquid raindrops directly into ice pellets once they are lofted above the freezing level to sufficiently cold temperatures (e.g., Wisner et al. 1972; Ziegler 1985; Milbrandt and Yau 2005b), representing instantaneous freezing. Because of this, some bulk microphysics parameterization schemes struggle to reproduce realistic  $Z_{DR}$  columns (e.g., Jung et al. 2008; 2010). Such model inadequacies may limit the utility of numerical investigations of the possible prognostic capabilities of  $Z_{DR}$  columns: namely, the link between their evolution and storm behavior that has been recently revealed (e.g., Picca et al. 2010; Picca and Ryzhkov 2010).

To fully explore and understand these apparent links between  $Z_{DR}$  column evolution and storm behavior, we must first understand the physics governing the appearance of the columns. To do this, a one-dimensional explicit bin microphysics and electromagnetic model is developed and used to quantify the polarimetric radar variables. Though lacking the generality of full three-dimensional full-physics models, this type of simplified modeling approach allows for a better understanding of the

impact of the freezing process on the polarimetric radar variables in isolation from other processes. As mentioned above, bulk microphysics parameterization schemes often used in more general numerical weather prediction models inadequately describe the complete nucleation and freezing process, limiting their utility in investigations of  $Z_{DR}$  columns. The layout of the rest of the chapter is as follows. Section 2 provides an overview of the physics of raindrop freezing. The microphysics and electromagnetic model are described in section 3. Section 4 presents results of the model, including sensitivity tests and comparisons with observations. The chapter closes with a discussion and brief summary (section 5) of the main results.

## **2. Overview of the Physics of Freezing Drops**

In the atmosphere, supercooled liquid drops typically undergo heterogeneous nucleation because of the presence of impurities in the liquid water or aerosols in the air. Pruppacher and Klett (1997; herein PK97) describe four modes of heterogeneous nucleation: deposition, condensation, immersion, and contact. When the air is supersaturated with respect to ice, water vapor can be deposited directly as ice on the surface of a particle at temperatures below 0 °C in the deposition mode. For situations where saturation with respect to water is attained, subfreezing ice nuclei may act as cloud condensation nuclei, where freezing occurs at some later stage during condensation. In the immersion mode, the foreign particle is submersed in the liquid drop at temperatures above 0 °C, whereupon freezing occurs when the drop becomes sufficiently cold. In the contact mode, ice nuclei initiate nucleation instantaneously upon contact with a supercooled drop. The latter two modes are of interest for drop

freezing in convective storms.

Heverly (1949), Bigg (1953a,b), Langham and Mason (1958), Barklie and Gokhale (1959), Pitter and Pruppacher (1973), and Vali (1971, 1994) among others have showed through observations that the median nucleating temperature  $T_m$  of a population of drops is a function of the drop volume,  $V_d$ . This can be expressed in terms of the supercooled median nucleating temperature  $T_{sm} = T_0 - T_m$  (where  $T_{sm} > 0$  and  $T_0 = 0$  °C):

$$T_{sm} = A - B \ln(V_d) \quad , \quad (8.1)$$

where  $A$  and  $B$  are constants determined by the sample of water and its immersed foreign particles or impurities. There are two schools of thought on the process of how this freezing is initiated (PK97). In the “stochastic hypothesis,” it is assumed that at a given temperature, all equal-sized ice embryos formed in a population of equal-sized supercooled drops will have an equal probability of reaching the critical size for freezing, as a result of random fluctuations among the water molecules. Immersed nuclei will enhance the freezing potential, but otherwise not affect the stochastic nature of freezing. In the other view, called the “singular hypothesis,” heterogeneous drop freezing is attributed entirely to the immersed nucleus with the warmest characteristic freezing temperature. In addition, the number of ice germs formed in a particular drop depends on the number of immersed nuclei in the drop that are activated. Though both hypotheses have some elements of experimental evidence supporting them, neither is complete by itself (PK97). Because the singular hypothesis requires knowledge of the number concentration of immersed nuclei in each drop (which is generally not known), the stochastic hypothesis is used in this study.



The freezing process occurs in two stages. The first stage generally is assumed to happen instantaneously upon nucleation, wherein dendritic ice crystal growth occurs in the core of the liquid drop, converting only a small portion of the liquid water into ice. The amount of ice formed depends on the environmental temperature as described quantitatively in the next section. The subsequent freezing occurs from the outside in, as an ice shell forms around the droplet and grows inward (e.g., Fig. 8.2, from Johnson and Hallett 1968; PK97). The latter stage can take up to several minutes for the largest drop sizes (Fig. 8.3).

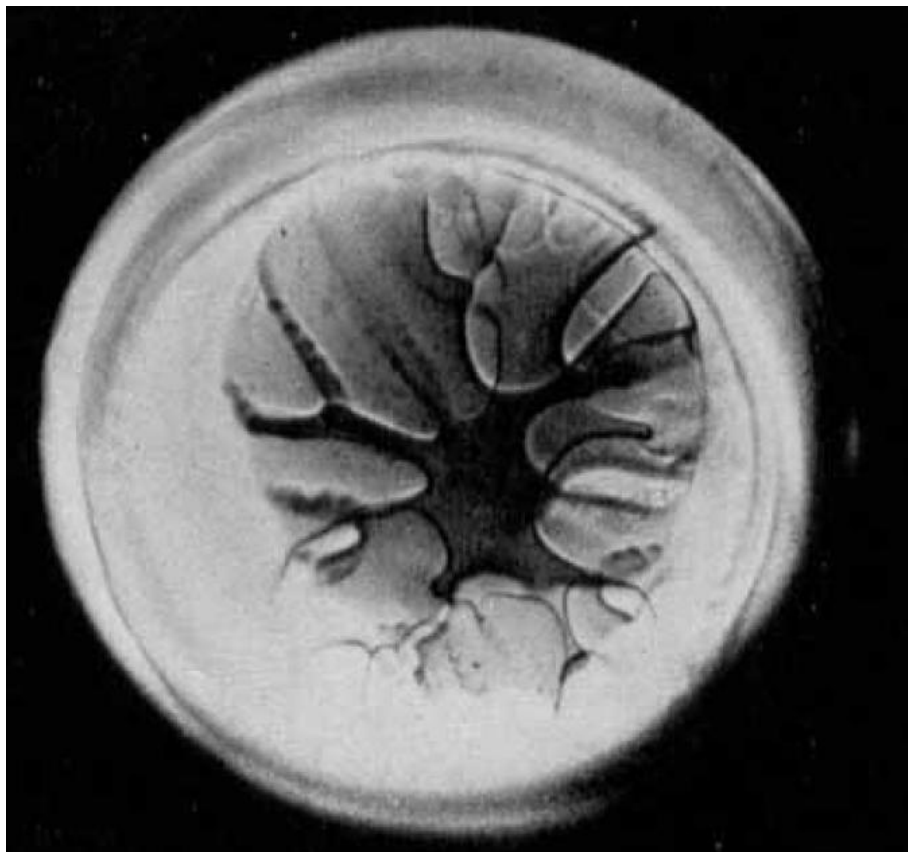


Fig. 8.2: Photograph of a 1-mm drop, from Johnson and Hallett (1968). The outer ice shell has just begun to form, and dendritic growth is evident in the drop core. The photograph was taken 10 seconds after nucleation, and complete freezing took another 40 seconds.

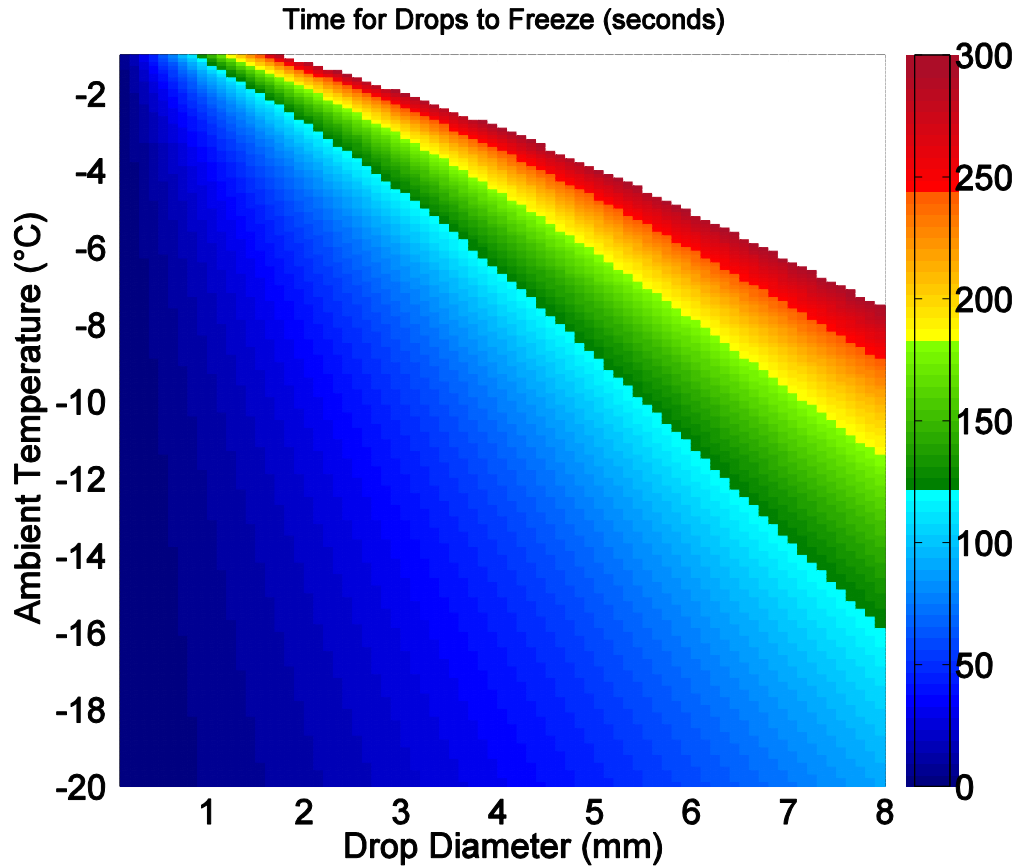


Fig. 8.3: Time for raindrops to freeze (color shading in seconds), following the assumptions and calculations of PK97. The drops are assumed to be nucleated and remain at a given ambient temperature. Calculations are based on PK97's eqn. (16-36). White shading indicates times over 300 seconds.

Smith et al. (1999) investigated the freezing of supercooled raindrops atop the  $Z_{DR}$  column in a convective storm. The authors hypothesized that the drop freezing contributed to the  $L_{DR}$  cap signature but did not show computations of the polarimetric radar variables. Though drop nucleation was treated in an overly simplistic manner, the study included the effects of accretion of supercooled water onto the freezing drops, conditions more realistic in convective storm updrafts. The heating of a particle due to accretion tends to prolong the freezing process. The authors also point out that remaining liquid water on the outside of freezing or frozen drops would also contribute to the

increase in  $L_{DR}$  frequently observed in polarimetric radar data. The upgrade of National Weather Service WSR-88D network will equip the radars with polarization diversity, but the radars will operate in the mode of simultaneous transmission and reception of horizontally and vertically polarized waves. Therefore,  $L_{DR}$  measurements will not be available. Instead,  $\rho_{hv}$  is measured; this variable will be reduced (analogously to an enhancement of  $L_{DR}$ ) for the same reasons as described by Smith et al. (1999). A diversity of hydrometeor types (ice pellets, partially-frozen drops, and pure liquid drops) will also contribute to reducing  $\rho_{hv}$  atop  $Z_{DR}$  columns. In severe convective storms, Picca and Ryzhkov (2012) argue that significant reductions in  $\rho_{hv}$  atop  $Z_{DR}$  columns in the temperature region between  $-10\text{ }^{\circ}\text{C}$  and  $-20\text{ }^{\circ}\text{C}$  indicate wet growth of giant ( $> 5\text{ cm}$  diameter) hailstones, owing to strong non-Rayleigh scattering effects. For the sake of simplicity, however, the current study will only consider the freezing of raindrops.

### **3. The Model**

#### *a. Freezing Model Physics and Equations*

The model simulates the freezing of raindrops in a simplified, steady-state one-dimensional column “updraft.” Previous studies have computed the polarimetric variables for idealized freezing drops without treatment of microphysics (e.g., Bringi et al. 1997; Hubbert et al. 1998), or have treated the microphysics in a simplified manner without showing computations of the radar variables (e.g., Smith et al. 1999). Here, we couple an explicit microphysics model with electromagnetic scattering calculations to compute vertical profiles of the polarimetric radar variables. The impact of the stochastic nucleation and deterministic freezing processes on the polarimetric radar

variables are of interest in this study. Thus, we neglect the growth of frozen particles by accretion and its associated contributions to the heat budget. Growth by accretion tends to prolong the freezing process and may contribute to the  $L_{DR}$  “cap” observed atop  $Z_{DR}$  columns (e.g., Jameson et al. 1996; Smith et al. 1999), but is not needed to explain it according to Bringi et al. (1997) and Hubbert et al. (1998). Additionally, collisions between particles of different sizes, a process which expedites freezing, are neglected. The temperature profile is prescribed as moist adiabatic to emulate in-cloud conditions, following a pseudoadiabat from a typical warm-season sounding in Norman, Oklahoma. At the first grid level, which corresponds to a height level of about 5.1 km MSL and a pressure level of about 552 hPa on the sounding, the temperature is 0 °C. The relative humidity profile is fixed at 99%. The updraft speed increases quadratically with height as

$$w(h) = \frac{(w_0 - w_{max})}{h_{max}} (h_{max} - h)^2 + w_{max} \quad , \quad (8.2)$$

where all symbols are explained in Table 8.1. Integration occurs every 10 m, though data are only stored (and thus polarimetric radar variables are computed) every 100 m. Any distribution of raindrops can be placed at the bottom of the domain and is advected upwards by the updraft. The “default” drop size distribution (DSD) is in the form of the three-parameter gamma model (e.g., Ulbrich 1983):

$$N(D) = N_0 D^\mu \exp(-\Lambda D) \quad , \quad (8.3)$$

with  $N_0 = 0.1 \text{ m}^{-3} \text{ mm}^{-2}$ ,  $\mu = 1$ , and  $\Lambda = 0.62 \text{ mm}^{-1}$ . These values were selected to match a DSD predicted at the bottom of a simulated updraft in the spectral bin microphysics Hebrew University Cloud Model (HUCM; e.g., see descriptions in Khain et al. 2004; 2011; the storm is from the simulation by Ryzhkov et al. 2011). The drop sizes are

partitioned into 80 bins (0.05 mm to 7.95 mm in 0.1-mm increments). Liquid raindrop velocities are given by the Brandes et al. (2002) polynomial function of diameter  $D$  (in mm) with a density correction factor (Foote and duToit 1969; Beard 1985)

$$v_{rain} = \left( \frac{\rho_0}{\rho_{air}} \right)^\beta (-0.1021 + 4.932D - 0.9551D^2 + 0.07934D^3 - 0.002362D^4), \quad (8.4a)$$

whereas the velocity of ice pellets is determined by an expression fitting the velocity of ice pellets in the HUCM:

$$v_{ice} = \left( \frac{\rho_0}{\rho_{air}} \right)^\beta (0.2259 + 1.5954D - 0.0405D^2), \quad (8.4b)$$

The fallspeeds of partially frozen drops change linearly from those of pure liquid to those of pure ice particles, based on mass water fraction. Because the model is steady state, the flux of particles is conserved at each level.

The initial nucleation is assumed to be in the immersion mode. Various foreign particles can be selected for the immersed nuclei by choosing  $B$  values in eqn. (8.1) from the literature (e.g., Barklie and Gokhale 1959; Diehl and Wurzler 2004). For the calculations shown herein, the value for nuclei typical for rainwater ( $B = 2.0 \times 10^{-4} \text{ cm}^{-3} \text{ s}^{-1}$ ) from Barklie and Gokhale (1959) is used. One can express eqn. (8.1) in terms of the fractional change (per unit time) in the number of unfrozen drops yet to be nucleated  $N_u$  following Bigg (1953b):

$$-\frac{1}{N_u} \frac{dN_u}{dt} = V_d B [\exp(\alpha T_s) - 1] \quad . \quad (8.5)$$

Note that Barklie and Gokhale (1959) found the mean value of  $\alpha = 0.65 \text{ }^\circ\text{C}^{-1}$ , independent of the water sample. Equation (8.5) shows that the rate of change of the number of un-nucleated drops increases with drop volume  $V_d$  and supercooling

temperature  $T_s$ . In other words, larger drops nucleate faster than smaller drops, and colder temperatures produce more rapid nucleation of drops of any given size. Suppose one now introduces a cooling rate,

$$\gamma_c = -\frac{dT}{dt} = \frac{dT_s}{dt} . \quad (8.6)$$

Under such conditions, eqn. (8.5) can be written as (PK97)

$$-\frac{1}{N_u} \frac{dN_u}{dt} \frac{dT}{dT_s} = \frac{V_d B}{\gamma_c} [\exp(\alpha T_s) - 1] \quad (8.7)$$

Thus, at a given supercooled temperature  $T_s$ , more rapid cooling (larger  $\gamma_c$ ) leads to *fewer* nucleations per unit time. Consider the implications for an updraft: in the Lagrangian framework of the raindrop, the cooling rate is equivalent to the rate of ascent within the updraft, which lofts drops to successively cooler temperatures. In this case, the cooling rate (8.6) can be written as

$$\gamma_c = -\frac{dT}{dt} = w' \Gamma_w , \quad (8.8)$$

where  $w' = (dh/dt)_{drop}$  is the updraft-modified vertical velocity of the raindrop, and  $\Gamma_w = -(dT/dh)$  is the lapse rate within the updraft, which is taken as moist adiabatic in this study. This leads to the important conclusion that a stronger updraft (implying more rapid ascent of the raindrops) yields less drop nucleations per unit time. In other words, *stronger updrafts provide more rapid cooling, delaying the onset of drop nucleation.*

In the framework of our model, at a given height level (or model grid point), the updraft velocity  $w$  is constant. Thus, we can integrate the differential equation (8.7) at each level:

$$\int_0^{T_s} -\frac{1}{N_u} \frac{dN_u}{dT'_s} dT'_s = \int_0^{T_s} \frac{V_d B}{w' \Gamma_w} [\exp(\alpha T'_s) - 1] dT'_s \quad ,$$

which, after performing a change of variables on the left-hand side of the equation

$$\int_{N_T}^{N_u} -d \ln(N'_u) = \frac{V_d B}{w' \Gamma_w} \int_0^{T_s} [\exp(\alpha T'_s) - 1] dT'_s \quad ,$$

results in

$$-\ln\left(\frac{N_u}{N_T}\right) = \frac{V_d B}{w' \Gamma_w} \left[ \frac{\exp(\alpha T_s)}{\alpha} - T_s \right] \quad , \quad (8.9)$$

where  $N_T$  is the total number of drops. Exponentiating both sides, we obtain an expression for the number of drops (at a given height) not yet nucleated as a function of supercooled temperature  $T_s$ :

$$N_u(T_s) = N_T \exp\left\{ -\frac{V_d B}{w' \Gamma_w} \left[ \frac{\exp(\alpha T_s)}{\alpha} - T_s \right] \right\} \quad . \quad (8.10)$$

So, the fraction of drops that are nucleated at a given height is given by:

$$\frac{N_f(T_s)}{N_T} = 1 - \exp\left\{ -\frac{V_d B}{w' \Gamma_w} \left[ \frac{\exp(\alpha T_s)}{\alpha} - T_s \right] \right\} \quad . \quad (8.11)$$

which is shown schematically in Figure 8.4. Thus, for a given drop size ( $V_d$ ), the fraction of drops that nucleate at a given height is governed by the supercooled temperature at that height  $T_s$  and the upward velocity of the drops  $w'$ . All else being equal, a fractional increase in the updraft strength  $\zeta$  will increase the fraction of un-nucleated drops<sup>9</sup> by a power of  $1/(1 + \zeta)$ .

---

<sup>9</sup> For example, suppose the conditions are such that about 50% of drops of a given size are nucleated at a supercooled temperature  $T_s$ . If the updraft strength at that level is increased by 20%, only about 43.9% of those drops are then nucleated at  $T_s$ .

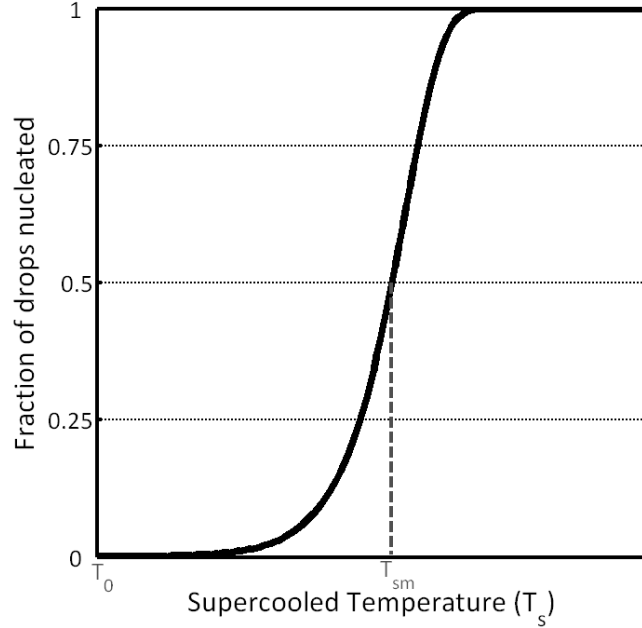


Fig. 8.4: Schematic illustrating the fraction of drops nucleated as a function of supercooled temperature  $T_s$ . The median supercooled temperature  $T_{sm}$  indicates the temperature at which 50% of the drops of a given size are nucleated. Note that  $T_s$  and  $T_{sm}$  are positive; also labeled on the abscissa is  $T_0$  ( $= 0\text{ }^\circ\text{C}$ ).

Following PK97, we can use an approximate form of eqn. (8.9), assuming  $\exp(\alpha T_s) - 1 \approx \exp(\alpha T_s)$ , to find the median supercooled temperature  $T_{sm}$ , or the temperature at which 50% of the drops have been nucleated. Substituting  $N_T/2$  for  $N_u$  and  $T_{sm}$  for  $T_s$  in this form of eqn. (8.9) and solving for  $T_{sm}$ , we obtain:

$$T_{sm} = T_0 - T_m = \frac{1}{\alpha} \ln \left[ \frac{\alpha \Gamma_w w' \ln 2}{V_d B} \right] \quad . \quad (8.12)$$

Note that the median supercooled temperature  $T_{sm}$  is dependent on the updraft velocity; for a fractional increase in updraft strength of  $\zeta$ ,  $T_{sm}$  increases by  $\ln \zeta / \alpha\text{ }^\circ\text{C}$ .

Only a portion of drops within a given size bin will nucleate at a particular temperature (cf. eqn. 8.11), capturing the stochastic nature of drop nucleation. These packets of drops will follow their own unique “growth trajectories” for the remainder of their ascent. Thus, at any given height level, partially-frozen drops in the same size bin



may have progressed to different stages of freezing, depending on their unique growth trajectories. It is expected that this diversity of particle liquid water fractions at a given level in the mixed-phase region of the updraft will contribute to decreased  $\rho_{hv}$ , as is commonly observed, without invoking significant contributions from non-Rayleigh scatterers.

These partially-frozen drops are assumed to have an ice germ in their core, with the remaining unfrozen fractional liquid volume  $f_v$  given by

$$f_v = 1 - \frac{T_s c_w}{L_m} \quad (8.13)$$

following PK97. From this level, the drops continue their ascent in the updraft and begin to freeze according to PK97, who assume ventilated drops undergoing isotropic heat loss via conduction and evaporation to the environment, neglecting riming. The governing heat balance equations are as follows

$$4\pi r^2 \rho_w L_m \frac{dr}{dt} \left(1 - \frac{T_s c_w}{L_m}\right) = \frac{4\pi k_i a r [T_0 - T_a(r)]}{a - r} \quad , \quad (8.14)$$

$$\frac{4\pi k_i a r [T_0 - T_a(r)]}{a - r} = 4\pi a k_a [T_a(r) - T_\infty] \bar{f}_h + 4\pi a L_s D_v (\rho_{va} - \rho_{v\infty}) \bar{f}_v \quad . \quad (8.15)$$

See Table 8.1 for a description of all symbols in the above equations. Because the surface temperature of the drop  $T_a$  is generally unknown, we solve for it in equation (8.15) and use the following relation (from PK97) to eliminate it:

$$\rho_{va} - \rho_{v\infty} = (1 - \phi_v) \rho_{v,sat}(T_\infty) + [T_a(r) - T_\infty] \left(\frac{d\bar{\rho}_v}{dT}\right)_{sat,i} \quad . \quad (8.16)$$

Solving the remaining equations for  $dr/dt$ , one obtains an expression for the growth rate of the ice shell:

$$\frac{dr}{dt} = \frac{k_i[(T_0 + T_\infty)\aleph - L_s D_v \bar{f}_v (1 - \phi_v) \rho_{v,sat}(T_\infty)]}{\rho_w L_m \left(1 - \frac{\Delta T c_w}{L_m}\right) [r^2(k_i - \aleph) + ar\aleph]} , \quad (8.17)$$

where we have defined

$$\aleph = k_a \bar{f}_h + L_s D_v \bar{f}_v (d\bar{\rho}_v/dT)_{sat,i} . \quad (8.18)$$

By dividing both sides of the expression by the particle vertical velocity  $w'$ , one obtains an expression that is used to compute the ice shell thickness at each height level. Once  $r \rightarrow 0$ , the particle is entirely frozen and is considered an “ice pellet.” After this transition, the ice pellet does not grow or interact with any other particles for the remainder of its ascent.

#### *b. Electromagnetic Model*

The next portion of the model involves computing the complex scattering amplitudes of the particles as they ascend and freeze. In order to preserve the physics of freezing, the hydrometeors are treated as two-layer spheroids, with an outer ice shell (the thickness of which is determined explicitly) surrounding an inner core consisting of liquid water. Appendix A discusses the various ways to distribute liquid water on or in a particle using T-Matrix calculations. The complex dielectrics of water and ice  $\epsilon_w$  and  $\epsilon_i$  are functions of temperature and radar wavelength, and are computed following the formulas in Ray (1972), which are also presented in Appendix A. The radar wavelength is assumed to be  $\lambda = 10.97$  cm (S band). The Rayleigh approximation to the scattering amplitudes of a two-layer spheroid is used, following Bohren and Huffman (1983):

$$f_{a,b} = \frac{\pi^2 D^3}{6\lambda^2} \frac{(\epsilon_i - 1)[\epsilon_i + L_{a,b}(1 - \xi)(\epsilon_w - \epsilon_i)] + \xi\epsilon_i(\epsilon_w - \epsilon_i)}{[\epsilon_i + L_{a,b}(1 - \xi)(\epsilon_w - \epsilon_i)][1 + L_{a,b}(\epsilon_i - 1)] + \xi L_{a,b}\epsilon_i(\epsilon_i - \epsilon_w)} . \quad (8.19)$$

In eqn. (8.19),  $\xi$  is the volume fraction of the inner spheroid (i.e., the liquid core) and  $L_{a,b}$  are shape factors for the oblate spheroids with major axis  $D_b$  and minor axis  $D_a$ :

$$L_a = \frac{1 + f^2}{f^2} \left( 1 - \frac{\tan^{-1} f}{f} \right), \quad L_b = \frac{1 - L_a}{2} \quad (8.20)$$

where

$$f = \sqrt{D_b^2/D_a^2 - 1} . \quad (8.21)$$

The axis ratios of all particles are defined for the individual diameter  $D$  size bin by the Brandes et al. (2002, 2005) relation for raindrops:

$$\frac{D_a}{D_b} = 0.9951 + 0.02510D - 0.03644D^2 + 0.005303D^3 - 0.0002492D^4 , \quad (8.22)$$

where  $D$  is in mm. The S-band polarimetric radar variables are calculated from the scattering amplitudes for each hydrometeor species (rain, partially frozen drop, and ice pellet), following Ryzhkov (2001) and Ryzhkov et al. (2011). The particles are assumed to have a mean canting angle of  $0^\circ$ , with a canting angle distribution width dependent on the mass water fraction of the particle:  $10^\circ$  for pure rain, increasing to  $40^\circ$  for pure ice pellets linearly as a function of mass water fraction (e.g., Ryzhkov et al. 2002b, 2009). Because eqn. (8.19) is valid only for the Rayleigh condition, one must determine the appropriate range of diameters for which the Rayleigh approximation is valid at C and X bands using the resonance parameter

$$\mathfrak{R} = D|\epsilon|^{1/2}/\lambda . \quad (8.23)$$

When the Rayleigh approximation is no longer valid, one must use more sophisticated scattering calculations, such as the T-Matrix method (e.g., Mischenko 2000). In addition to the Rayleigh approximation, we have computed the polarimetric radar variables for selected model runs using a T-Matrix method similar to the one used by Aydin and Zhao (1990). Only selected model runs were converted to radar variables using the T-Matrix method because it is computationally expensive as there are numerous ( $>100\ 000$ ) possible particles owing to the various growth trajectories. The computational parameters are treated as before, with raindrops and ice pellets treated as oblate spheroids (composed of pure water and pure ice, respectively) and partially-frozen drops treated as two-layer spheroids, with an outer shell made of ice and the inner core of water. The Rayleigh approximation results (at S band) agree well with the T-Matrix calculations. The Rayleigh-computed profiles of  $Z_H$ ,  $Z_{DR}$ ,  $\rho_{hv}$ , and  $L_{DR}$  are within about 1 dBZ, 0.1 dB, 0.0005, and 0.5 dB, respectively, of the T-Matrix profiles.

#### **4. Model Results**

##### *a. Sensitivity Tests*

Figure 8.5 is a 4-panel display of vertical profiles of the polarimetric radar variables based on model calculations with varying updraft intensities. It is evident that the shape of the  $Z_H$  profile (Fig. 8.5a) is most strongly affected by the updraft intensity, as this variable is dependent on the number concentration of particles. This is because the model is steady state, so the number flux of particles is conserved at each level. The shape of the  $Z_H$  profile reflects this inverse proportionality to the updraft intensity: larger  $w$  corresponds to smaller  $Z_H$ . Superposed on this shape is a  $\sim 7$  dBZ decrease

owing to the difference in refractive index between liquid water and solid ice as drops nucleate and freeze.

The impact of updraft intensity on  $Z_{DR}$ ,  $\rho_{hv}$ , and  $L_{DR}$  is much less apparent, owing to their independence from total number concentration. A striking feature in the  $Z_{DR}$  profiles (Fig. 8.5b) is a zone marked by a sharp decrease in values from over 3 dB at heights below about 1000 m above the melting layer (AML) to 0.4 dB at heights above 2000 m AML. This zone with a sharp decrease in  $Z_{DR}$  is coincident with the  $\sim 7$  dBZ decrease in  $Z_H$  and is what we will be referring to as the “freezing zone.” Note that the location of this freezing zone is shifted upwards slightly with stronger updrafts. The shape of the updraft profile is not as important for the resulting  $Z_{DR}$  profile as the updraft *intensity*. Sensitivity tests were performed using a constant updraft speed  $w$  throughout the domain and are discussed below.

The vertical profile of  $\rho_{hv}$  (Fig. 8.5c) reveals a minimum located at the bottom of the freezing zone, followed by an increase within the freezing zone. Like  $Z_{DR}$ , the height of these features increases with increasing updraft strength. The reason for the minimum  $\rho_{hv}$  is the coexistence of a mixture of particle species in the larger size bins: pure liquid raindrops, solid ice pellets, and partially-frozen drops that have progressed through various stages in the freezing process are all collocated at the same level (Fig. 8.6). Because all particles have diameters  $< 1$  cm, reductions in  $\rho_{hv}$  at S band are small. At C and X bands, reductions may be larger in magnitude. Additionally, larger particles and/or wet growth of ice particles probably are necessary for substantial  $\rho_{hv}$  reductions at all radar wavelengths. Similar to the profile of  $\rho_{hv}$ , the profile of  $L_{DR}$  (Fig. 8.5d) reaches its maximum at the freezing zone, after which it decreases sharply as the

particles become entirely ice. Note that the large maximum in  $L_{DR}$  ( $L_{DR}$  “cap”) often observed in deep convective storms is not reproduced, which suggests that larger particles and/or wet growth is required to reproduce this type of feature (e.g., Jameson et al. 1996; Smith et al. 1999).

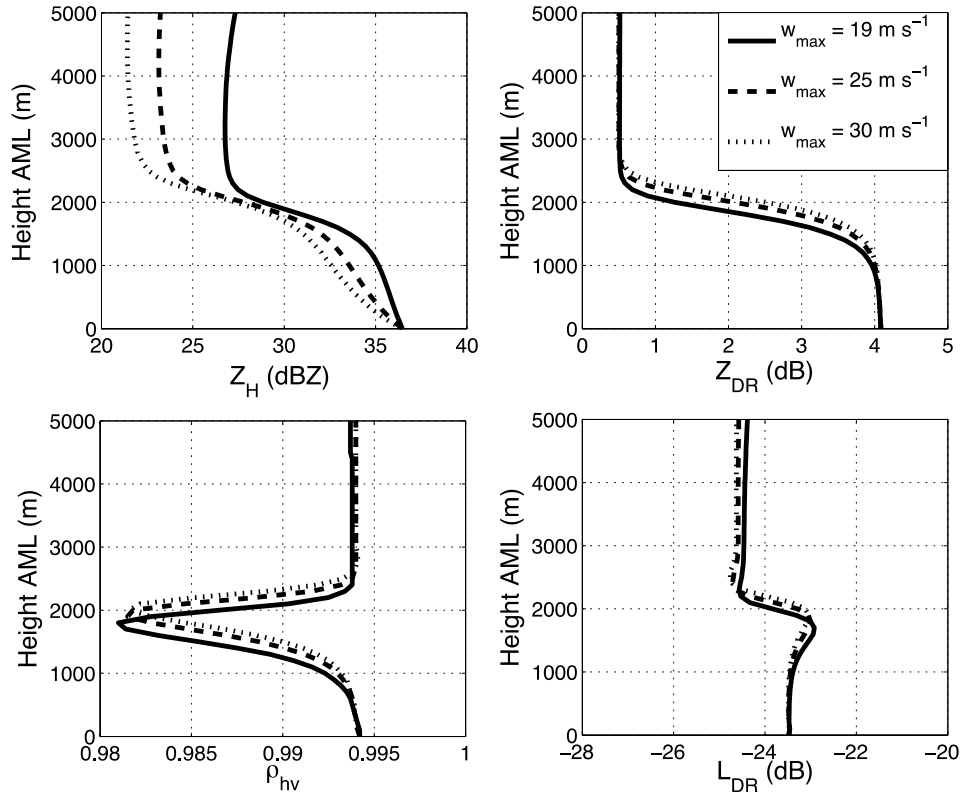


Fig. 8.5: Vertical profiles of (a)  $Z_H$ , (b)  $Z_{DR}$ , (c)  $\rho_{hv}$ , and (d)  $L_{DR}$  computed from output of the freezing model, shown in meters above the melting level (AML). The model parameters used for the calculations include the default DSD (see eqn. 8.3 and associated text) with varying updraft maximum intensity:  $19 \text{ m s}^{-1}$  (solid curves),  $25 \text{ m s}^{-1}$  (dashed curves), and  $30 \text{ m s}^{-1}$  (dotted curves). These calculations are for S band, employing the Rayleigh approximation. In each case,  $w_0 = 15 \text{ m s}^{-1}$ , and  $h_{max} = 5 \text{ km}$ .

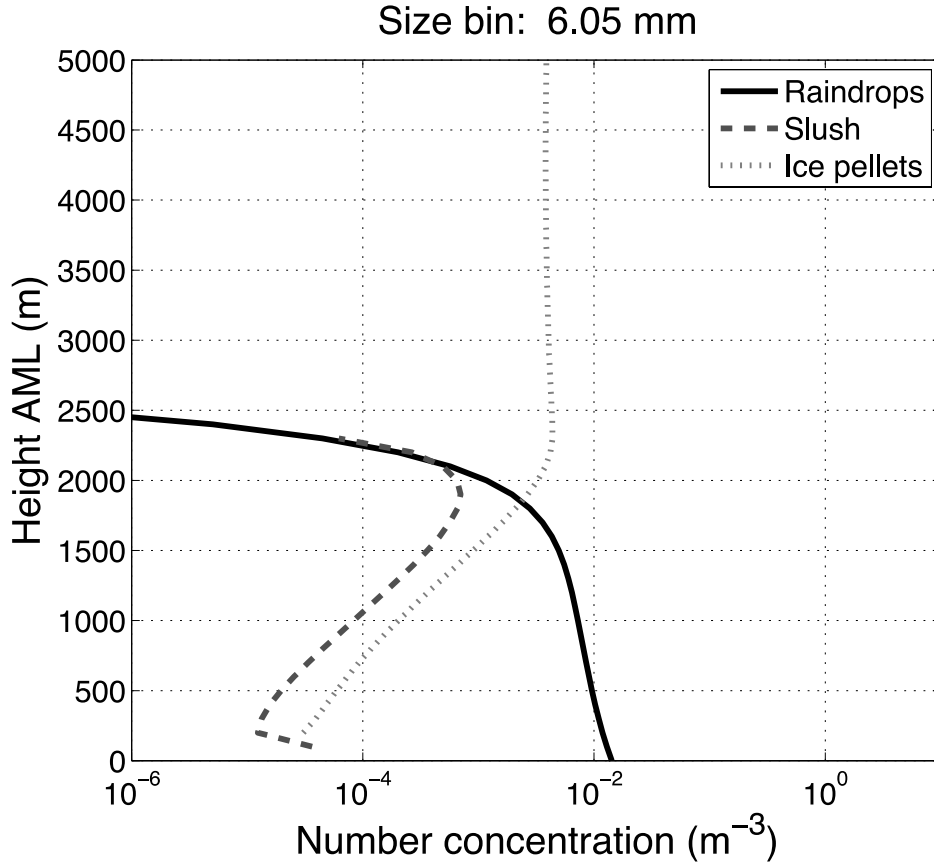


Fig. 8.6: Vertical profiles of the number concentration (in  $\text{m}^{-3}$ ) of the 61<sup>st</sup> size bin corresponding to a liquid drop of size 6.05 mm. The concentration of raindrops is shown in the black solid line, partially-frozen drops (or “slush”) in the dashed dark gray line, and completely frozen ice pellets in the dotted gray line. The default DSD and updraft with  $w_{max} = 25 \text{ m s}^{-1}$  are used, with  $w_0 = 15 \text{ m s}^{-1}$  and  $h_{max} = 5 \text{ km}$ .

An important assumption of previous studies relating changes in the  $Z_{DR}$  column to changes in storm intensity (e.g., Picca et al. 2010; Picca and Ryzhkov 2010) is that the changes in the  $Z_{DR}$  column height are because of changes in updraft intensity. Though intuitive, this relation has not been quantified. In the next set of idealized calculations, the updraft intensity is varied, but the updraft speed is held constant in height to remove the effects of the shape of the updraft profile. The vertical extent of the  $Z_{DR}$  column is quantified using the height of the freezing zone above the melting level. The height of the freezing zone is determined by the height of the maximum

absolute value of the vertical gradient of  $Z_{DR}$ . Results of these tests (Figure 8.7) demonstrate an increasing freezing zone height (meaning a “taller”  $Z_{DR}$  column) with increasing updraft speed. However, the sensitivity is much higher for smaller updraft speeds (10 – 20  $\text{m s}^{-1}$ ). This is because these weaker updrafts yield very slow ascent speeds for the largest raindrops, allowing ample time for them to nucleate and freeze at lower heights.

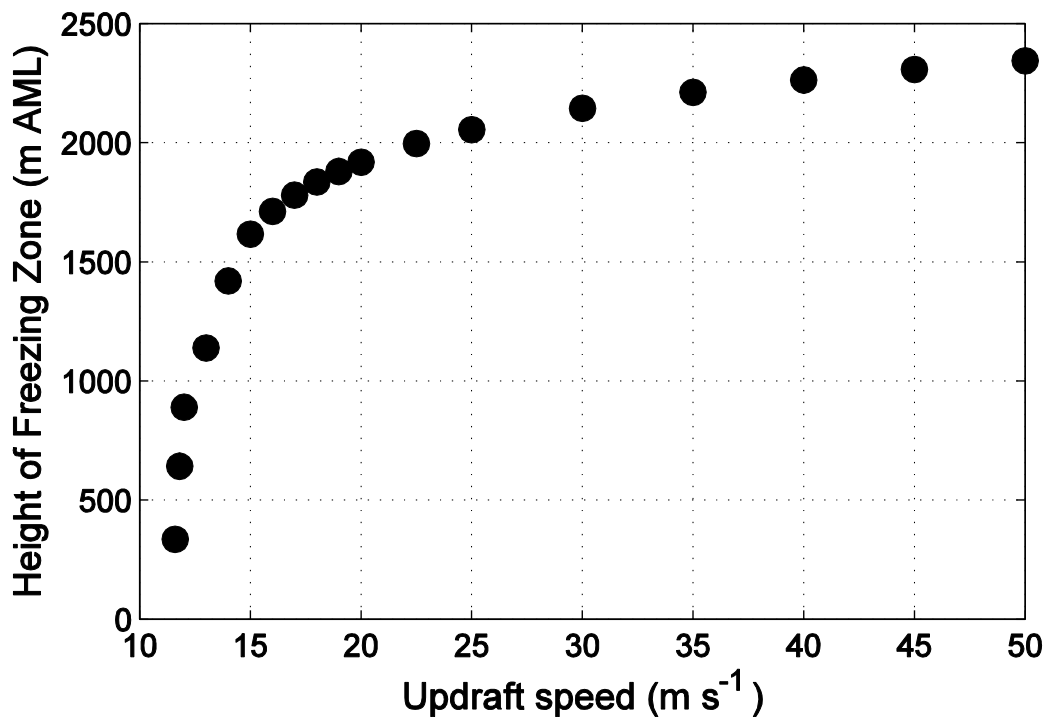


Fig. 8.7: Height of the freezing zone above the melting level as a function of the updraft speed. The default DSD is assumed. For these idealized calculations, the updraft profile is constant throughout the domain, varying from 11  $\text{m s}^{-1}$  to 50  $\text{m s}^{-1}$ .

The model sensitivity to the nucleation scheme is explored next (Fig. 8.8). Here, the “default” settings correspond to those outlined in the model description above, containing the size-dependent median nucleating temperature  $T_m$  as well as a probability distribution function (PDF) of nucleating temperatures to capture the



stochastic nature of drop nucleation (cf. eqn. 8.11). First, the drop-size dependency of  $T_m$  is removed, and all drops are assigned  $T_m = -9.6$  °C. This corresponds to the  $T_m$  of the largest drop size bin in the default settings. Using this scheme (which still includes the PDF and thus stochastic effects) results in a sharper  $Z_{DR}$  gradient in the freezing zone, leading to complete freezing of the drops about 500 m lower than the default settings. The difference between this scheme and the default nucleation setting is most evident at the top of the freezing zone, which is mostly affected by the freezing of smaller drop sizes; in this case, the smaller drops are nucleated (and thus begin the freezing process) at lower heights. The difference is smallest at the bottom of the freezing zone, where the largest drops are the most significant contributors to  $Z_{DR}$ .

Next, the stochastic nucleation process is turned off so that all drops in each size bin nucleate at the same  $T_m$ . As expected, this causes an even sharper  $Z_{DR}$  gradient. Note that in this case, the  $Z_{DR}$  does not begin decreasing until a higher level (1500 m AML). This is because the larger drops do not nucleate at temperatures warmer than  $T_m$ , in contrast to the stochastic nucleation simulations. Thus, the entire freezing process occurs within a 200-m deep layer. If all drops were to *freeze* instantaneously at a given  $T_m$ , the resulting  $Z_{DR}$  profile would be a step function (i.e., no freezing zone). Therefore, it is clear that the treatment of the stochastic nucleation process strongly affects the depth of the freezing zone – that is, the gradient of  $Z_{DR}$  atop  $Z_{DR}$  columns.

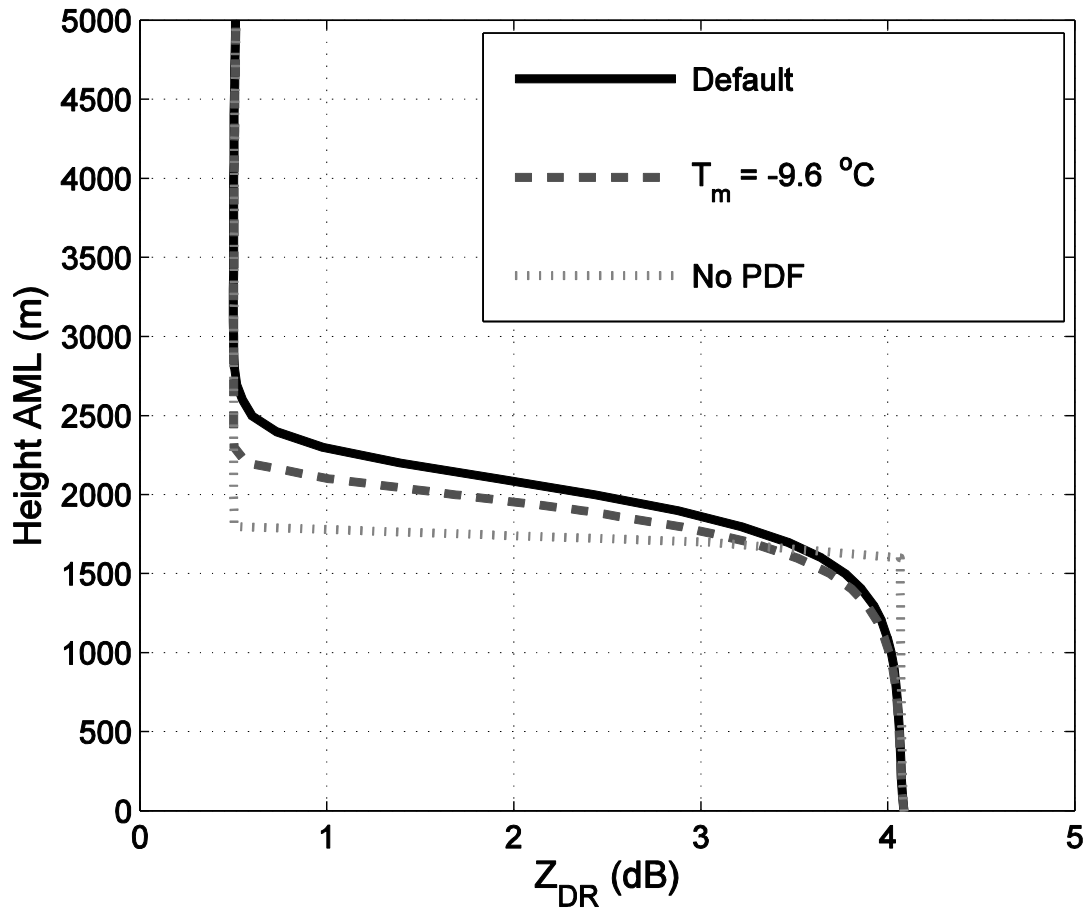


Fig. 8.8: Vertical profiles of  $Z_{DR}$  resulting from model runs with different nucleation schemes. The default scheme described in the text is shown with the black curve and includes the size-dependent mean nucleating temperature and stochastic nucleation process. The dashed dark gray curve represents the runs when all drops are assigned a mean nucleating temperature of  $T_m = -9.6$  °C (the  $T_m$  of the largest drop size in the default run). The gray dotted curve represents a simulation when all drops are assigned a  $T_m = -9.6$  °C and no probability distribution function (PDF); in other words, the stochastic component of nucleation has been removed, and all drops in each size bin simply nucleate at  $T_m$ .

In addition to the factors affecting the characteristics of the freezing zone discussed above, we see from eqn. (8.11) that the PDF governing drop nucleation is dependent on the parameter  $B$ . The parameter  $B$ , which represents the chemical properties of the immersed nucleus in the drops, can vary several orders of magnitude depending on the type of immersed material (e.g., Diehl and Wurzler 2004). Numerical

experiments were performed assuming the values for rainwater, leaf material, pollen, and various mineral dusts (not shown). Though the shape of the  $Z_{DR}$  profile was not significantly altered by varying  $B$ , the height of the freezing zone was affected. Smaller values of  $B$  lead to fewer drop nucleations at a given height level (or, equivalently, to colder  $T_m$ , cf. eqn 8.12) which causes the freezing zone to appear at higher altitudes. The freezing zone height increases by about 550 m for every order of magnitude decrease of  $B$ , demonstrating how immersed materials characterized by smaller  $B$  are less efficient at inducing drop nucleation at relatively warmer temperatures. Note that stronger updrafts also can be thought of in terms of increasing  $T_{sm}$ , leading to higher freezing zones.

#### *b. Comparison with Observations*

The updraft-freezing model predicts the vertical profiles of the polarimetric radar variables within and above  $Z_{DR}$  columns, but how well do these model predictions match the observations? The cross-section in Figure 8.1 of the prominent  $Z_{DR}$  column was reconstructed from several elevation angle sweeps and thus involves some degree of interpolation. Instead, genuine vertical cross-section scans (or range-height indicators, RHIs) are desirable for direct comparisons with the model. Such data were collected on the afternoon of 24 April 2011 by the C-band University of Oklahoma Polarimetric Radar for Innovations in Meteorology and Engineering (OU-PRIME; see Palmer et al. 2011). Data were collected using  $0.1^\circ$  elevation angle spacing. The melting layer is evident in the data at about 2.7 km AGL (Fig. 8.9). At a range of about 29 km, a storm cell displays a pronounced  $Z_{DR}$  column that extends above the

environmental 0 °C level. Vertical profiles extracted from this storm cell are compared to model output (Fig. 8.10). The initial DSD was selected to approximately match the  $Z_H$  and  $Z_{DR}$  at the environmental freezing level, with values  $N_0 = 1000 \text{ m}^{-3} \text{ mm}^{-0.463}$ ,  $\Lambda = 1.35 \text{ mm}^{-1}$ , and  $\mu = -0.537$ , with  $w_{max} = 13.6 \text{ m s}^{-1}$  at  $h_{max} = 5.0 \text{ km}$ , and  $w_0 = 11.9 \text{ m s}^{-1}$ . The modeled profile of  $Z_{DR}$  is consistent with the observed profiles, though the magnitude of the modeled  $Z_{DR}$  gradient in the freezing zone is smaller than the observed profiles (Fig. 8.10a). In other words, the observed  $Z_{DR}$  values drop off more rapidly in height than the modeled values. This may be attributed to contact nucleation, which is expected to enhance the rate of nucleation and freezing in real storms, but was neglected in this model. Also note that at shorter radar wavelengths (C and X bands), resonance scattering effects in the presence of large raindrops can contribute to discrepancies with the S-band calculations. The observed profiles of  $Z_H$  (Fig. 8.10b) display more variability than those of  $Z_{DR}$ . However, the modeled profile of  $Z_H$  lies within the bounds of observations for most of the profile. The small disagreements in the shape of the  $Z_H$  profile are mainly attributed to the assumed updraft profile.

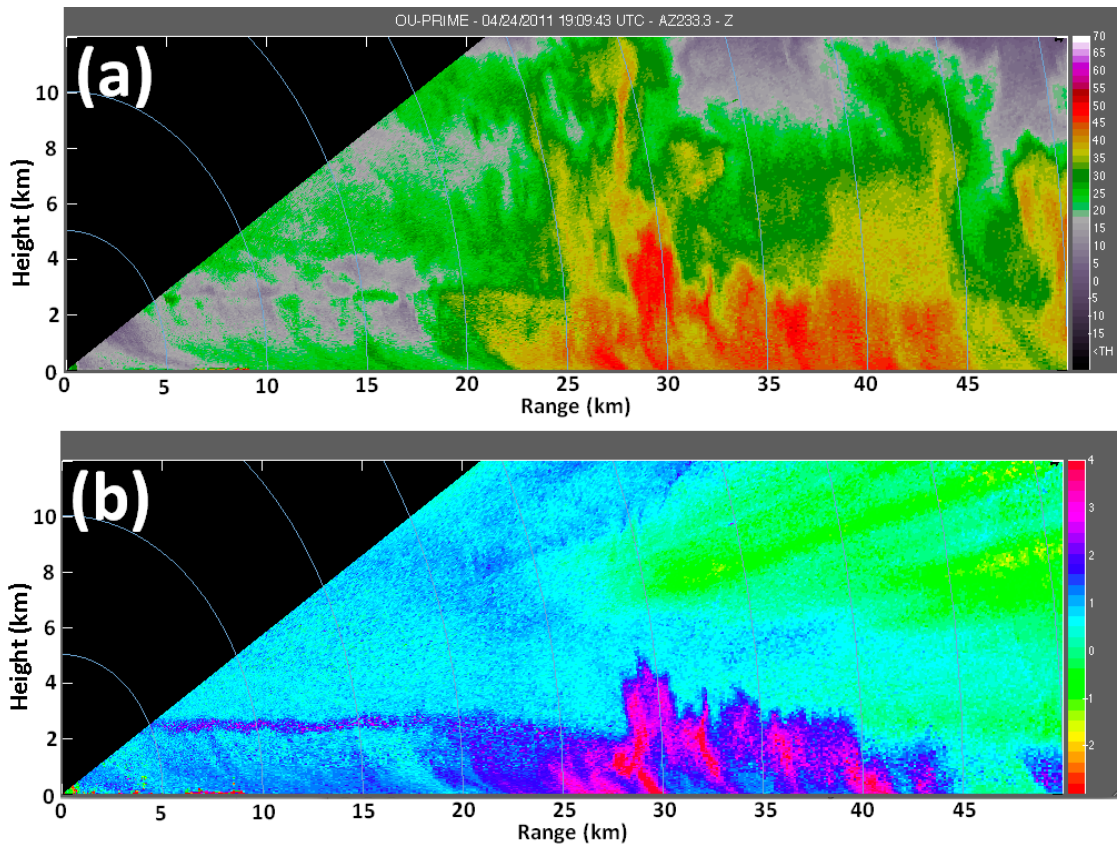


Fig. 8.9: Observations from the C-band OU-PRIME on 24 April 2011, at 1909 UTC, along the azimuth  $233.3^\circ$ . Panels shown are (a)  $Z_H$ , and (b)  $Z_{DR}$ . Range rings are shown every 5 km. The  $Z_{DR}$  column of interest is centered at a range of about 29 km.

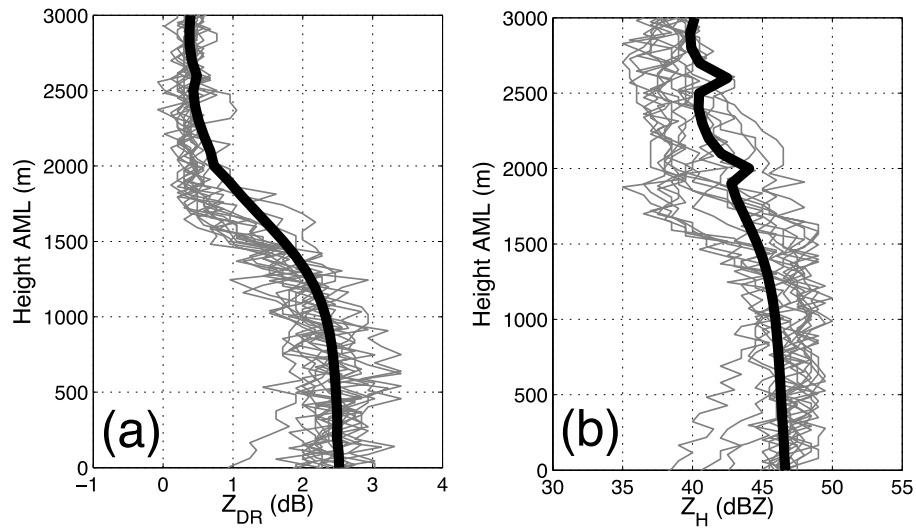


Fig. 8.10: (a) Fifteen observed vertical profiles of  $Z_{DR}$  extracted from the RHI in Figure 8.9, from the  $Z_{DR}$  column centered at a range of about 29 km (gray lines), compared to the model  $Z_{DR}$  profile (thick black curve). (b) As in (a), but  $Z_H$  profiles are shown.

Similar RHI scans were collected in a different climate region: near Bonn, Germany, with the Bonn X-band Polarimetric radar (BOXPOL) operated by the Meteorological Institute of the University of Bonn (Fig. 8.11). Data were collected on 24 June 2011, with  $0.1^\circ$  spacing in elevation, when isolated convective storms were affecting the area. The nearest rawinsonde observations from Essen (approximately 90 km to the northwest) at 1200 UTC show the environmental freezing level at about 1.8 km AGL (not shown). Vertical profiles extracted from these RHI scans compare favorably with the modeled  $Z_{DR}$  profile, using  $\Lambda = 1.4 \text{ mm}^{-1}$ ,  $\mu = -0.495$ ,  $w_{max} = w_0 = 10.4 \text{ m s}^{-1}$  (Fig. 8.12). Again, the gradient of  $Z_{DR}$  (especially at the top of the observed freezing zone) is sharper than the modeled profile, likely owing to contact nucleation being neglected in the model.

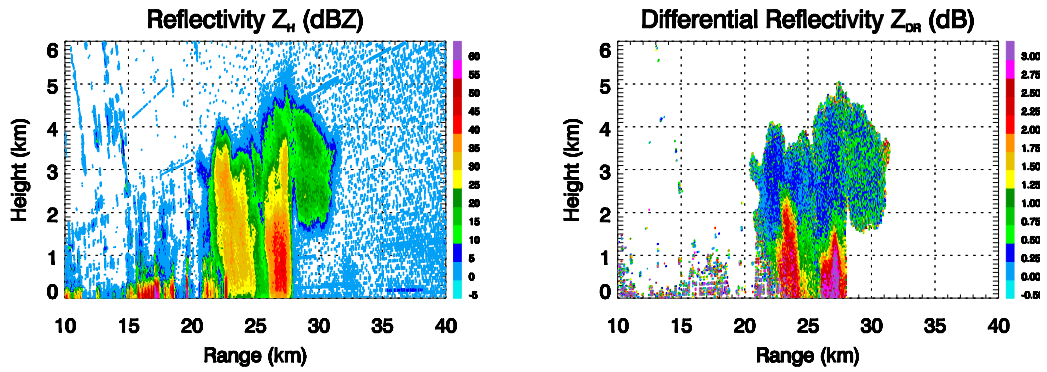


Fig. 8.11: Vertical cross-sections of  $Z_H$  (left) and  $Z_{DR}$  (right) taken along the  $309.5^\circ$  azimuth on 24 June 2011, at 1034 UTC by the X-band BOXPOL radar. Data are courtesy of the Meteorological Institute of the University of Bonn. The  $Z_{DR}$  column of interest is centered at about 23 km range.

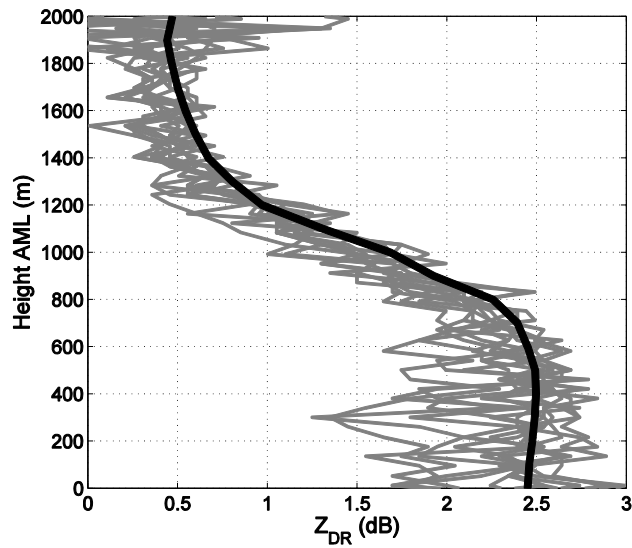


Fig. 8.12: As in Figure 8.10, but for 11 vertical profiles extracted from the RHI in Figure 8.11.

Despite the simplicity of the model employed in this study, it is able to reproduce key features in the upper portions of  $Z_{DR}$  columns: namely, an accurate height above the melting level, similar gradient of  $Z_{DR}$  in the freezing zone, and correct  $Z_{DR}$  values within and above the column. Additionally, the simulated  $Z_H$  profile is in general agreement with the observed profiles, notwithstanding the uncertainty in the actual updraft profile. This implies that, despite neglecting certain processes, the key physics governing the appearance of the top of  $Z_{DR}$  columns are captured in our implementation of the stochastic nucleation process and subsequent explicit treatment of the deterministic freezing of drops.

## 5. Discussion and Summary

The major characteristics of  $Z_{DR}$  columns include the values of  $Z_{DR}$  within and above the columns, the vertical extent of the column above the melting level, and the properties of the freezing zone (i.e., the gradient of  $Z_{DR}$ ,  $\rho_{hv}$  minimum,  $L_{DR}$  maximum, etc.). The theoretical model presented in this study is capable of reproducing many of these observed features.  $Z_{DR}$  values within and above the column can be matched with an initial DSD. The impact of updraft intensity on the vertical extent of the  $Z_{DR}$  column is quantified, demonstrating that stronger updrafts lead to taller  $Z_{DR}$  columns. The  $Z_{DR}$  gradient within the freezing zone is in reasonable agreement with observed  $Z_{DR}$  columns, indicating that the important physical processes (stochastic nucleation followed by deterministic freezing) are captured in the modeled framework. Discrepancies between the modeled and observed profiles (observations show a sharper  $Z_{DR}$  gradient) are instructive, as they may indicate the role of contact nucleation on



expediting the freezing process, especially for the smaller drops. Such a process expedites the freezing process by promoting nucleations at relatively warmer temperatures, particularly for smaller and medium drop sizes for which fallspeed differences are largest. A  $\rho_{hv}$  minimum is produced in the freezing zone, even using the Rayleigh approximation for calculations. This  $\rho_{hv}$  reduction is due to a mixture of different particle types (liquid drops, partially frozen drops, and ice pellets) collocated at the same level (cf. Fig. 8.6), as well as the gradual increase in the width of the distribution of hydrometeor canting angles as freezing progresses. The latter also leads to a slight increase in  $L_{DR}$ . In convective storms containing larger particles, growth by accretion serves to further decrease  $\rho_{hv}$  and increase  $L_{DR}$  (Jameson et al. 1996; Bringi et al. 1997; Hubbert et al. 1998; Smith et al. 1999; Picca and Ryzhkov 2012). More general models with larger particles and/or those that account for wet growth should produce enhanced  $L_{DR}$  and  $\rho_{hv}$  extrema.

The vertical extent of  $Z_{DR}$  columns above the melting level is directly related to updraft strength in two ways: first, stronger updrafts lead to reduced median nucleating temperatures ( $T_m$ ), causing drops to nucleate at relatively colder temperatures. Second, the faster ascent velocity of lofted drops allows the drops to ascend farther before total freezing occurs, in effect reducing the freezing rate. Thus, strong updrafts may loft particles to heights of about  $\sim 2$  km above the updraft-perturbed  $0^\circ\text{C}$  level before complete freezing, in agreement with numerous observed cases. In addition, strong updrafts produce positive temperature perturbations owing to the release of latent enthalpy during condensation; for example, simple parcel theory considerations reveal parcels reaching  $0^\circ\text{C}$  at heights 1 km or more above the *environmental*  $0^\circ\text{C}$  level in

cases of large ( $> 3000 \text{ J kg}^{-1}$ ) CAPE. Therefore, in extreme cases, one may expect  $Z_{DR}$  columns to extend as much as 3 km or more above the *environmental*  $0 \text{ }^\circ\text{C}$  level (cf. Fig. 8.1).

The height of the freezing zone also increases with decreasing parameter  $B$ , which describes the impact of the chemical properties of the immersed material on the median nucleating temperature. According to values found in Barklie and Gokhale (1959) and Diehl and Wurzler (2004), the parameter  $B$  can vary over several orders of magnitude, depending on the immersed foreign particle. For every order of magnitude decrease of  $B$ , the height of the freezing zone increases by about 550 m. Within a convective storm updraft, such an increase corresponds to a decrease in temperature on the order of  $\sim 3 \text{ }^\circ\text{C}$ , in agreement with Wisner et al. (1972). Because the formation and growth of hailstones is sensitive to environmental temperature and the amount of supercooled liquid water and ice present (e.g., PK97; Nelson 1983; Ziegler 1983, among others), such changes in height (and temperature) of the freezing zone may have an impact on these hail growth processes. There have been recent indications that the concentration of aerosols may affect hail growth (e.g., Khain et al. 2011); here, we speculate that in addition, the *type* of aerosols that become immersed in liquid raindrops that are lofted above the environmental freezing level may also play a role in the hail growth process. For example, immersed particles leading to freezing of drops at relatively warmer temperatures would allow more efficient growth into graupel particles by riming, whereas delayed freezing until colder temperatures may result in a larger relative proportion of frozen drops being lofted into the prime hail-growth region of  $-10$  to  $-20 \text{ }^\circ\text{C}$ . Incorporating a probabilistic nucleation and deterministic freezing scheme

into a more general three-dimensional storm-scale numerical model will help verify or refute this speculation.

The ability of the simplified modeling approach to reproduce key observed features in  $Z_{DR}$  columns improves confidence in our understanding of the dominant processes involved in raindrop freezing, and provides a simple yet powerful tool for exploring these processes. Appropriate treatment of raindrop nucleation and freezing is a necessary precursor to employing more general three-dimensional numerical weather prediction models in investigations of  $Z_{DR}$  columns, especially those aiming to elucidate the link between storm behavior and the evolution of  $Z_{DR}$  columns.

Symbol	Meaning
$A$	Constant determined by water sample impurities
$a$	Outer radius of the entire particle
$B$	Constant determined by water sample impurities
$c_w$	Specific heat capacity of water
$D$	Particle diameter
$D_a$	Minor axis of the spheroid
$D_b$	Major axis of the spheroid
$D_v$	Diffusivity of water vapor in air
$f = \sqrt{D_b^2/D_a^2 - 1}$	Function of aspect ratio that determines shape factor
$f_{a,b}$	Scattering amplitude along major/minor axis
$f_h$	Ventilation coefficient of heat
$f_v$	Ventilation coefficient of water vapor
$f_v$	Fractional liquid volume following nucleation
$h$	Height above the melting layer
$h_{max}$	Height of the maximum updraft speed, $w_{max}$
$k_a$	Heat conductivity of air
$k_i$	Heat conductivity of ice
$L_{a,b}$	Shape factors for oblate spheroids
$L_{DR}$	Linear depolarization ratio (in dB)
$L_m$	Latent enthalpy of freezing/melting
$L_s$	Latent enthalpy of sublimation
$N(D)$	Number concentration of particles of diameter $D$ to $D + dD$
$N_0$	DSD intercept parameter
$N_f$	Number concentration of drops of diameter $D$ that are nucleated
$N_T$	Total number concentration of drops of diameter $D$
$N_u$	Number concentration of drops of diameter $D$ yet to be nucleated
$r$	Inner radius of the growing ice shell
$T$	Air temperature
$T_0$	273.15 K
$T_a$	Temperature at the surface of the drop
$T_m$	Median nucleating temperature
$T_s$	Supercooled temperature
$T_{sm}$	Median supercooled temperature
$T_\infty$	Ambient environmental temperature far from the particle
$t$	Time
$V_d$	Volume of raindrops

$v_{rain}$	Velocity of raindrops
$v_{ice}$	Velocity of ice pellets
$w$	Updraft speed
$w'$	Updraft-modified vertical velocity of drop
$w_0$	Updraft speed at the 0 °C level
$w_{max}$	Maximum updraft speed
$Z_{DR}$	Differential reflectivity factor (dB)
$Z_H$	Radar reflectivity factor at horizontal polarization (dBZ)
$\alpha$	Constant = 0.65 °C <sup>-1</sup>
$\beta$	Density correction factor for velocity (0.4)
$\Gamma_w$	Lapse rate within updraft (moist adiabatic)
$\gamma_c$	Cooling rate
$\epsilon_i$	Complex dielectric of ice
$\epsilon_w$	Complex dielectric of liquid water
$\epsilon$	Complex dielectric of the freezing particle
$\Lambda$	DSD slope parameter
$\lambda$	Radar wavelength
$\xi$	Volume fraction of the inner spheroid (core)
$\rho_0$	Reference density = 1.2 kg m <sup>-3</sup>
$\rho_{air}$	Air density at a given height level
$\rho_{hv}$	Co-polar cross-correlation coefficient
$\rho_{va}$	Water vapor density at the particle surface
$\rho_{v,sat}(T_\infty)$	Saturated vapor density at the ambient environmental temperature
$\rho_{v,\infty}$	Ambient water vapor density
$\rho_w$	Density of liquid water
$\phi_v$	Relative humidity
$(d\bar{\rho}_v/dT)_{sat,i}$	Average slope of the saturated vapor density (over ice) as a function of temperature in the neighborhood of $T_\infty$
$\Re$	Resonance parameter
$\zeta$	Fractional increase in updraft speed
$\aleph$	Thermodynamic factor in eqn. (8.17)

Table 8.1: Explanation of symbols used throughout the equations and the text.

## Chapter 9: Summary, Conclusions, and Future Work

The complete suite of backscattering and forward scattering polarimetric radar variables is derived for the linearly orthogonal (H and V polarization) basis. The physical interpretation of these variables is then provided, along with electromagnetic scattering calculations, as well as examples from newly upgraded WSR-88D radars. Artifacts in polarimetric radar data that are routinely observed are also discussed. After describing the theoretical and physical basis for the polarimetric radar variables, we turn to use of these variables for microphysical research.

Understanding the impact of different microphysical processes on the observed polarimetric radar variables is important for a range of applications. Recognizing these characteristic “fingerprints” in the observed data allows for better physical interpretation of polarimetric radar observations and for identification of the dominant microphysical processes ongoing in a given storm at a given time. Such knowledge can then be used to validate microphysics parameterization schemes. If numerical simulations of storms cannot reproduce the observed radar features in real storms, it is clear that certain physical processes are not adequately (or accurately) handled in the parameterizations. Identifying and improving these problematic parameterizations can lead to better storm-scale numerical forecasts. Additionally, appropriate treatment of precipitation physics in models is crucial for efficient polarimetric radar data assimilation. If models cannot reproduce observed polarimetric radar signatures in storms, how can assimilation of the radar data improve model analyses and forecasts?

This dissertation offers a preliminary step towards quantitatively describing the impact of certain processes on the dual-polarization radar variables. Namely, the fingerprints of raindrop size sorting, evaporation, coalescence, and freezing are investigated. Additionally, a model was developed to predict the temperature of raindrops as they descend through an atmosphere with nonzero lapse rate, which can be used for scattering calculations. A combination of explicit bin microphysical models, scattering calculations, and simple thought experiments were used to determine the impacts of these processes on the radar variables.

A pictorial catalog of the impact of the precipitation processes on the polarimetric radar variables  $Z_H$ ,  $Z_{DR}$ ,  $K_{DP}$ , and  $\rho_{hv}$  is provided in Figure 9.1. Note that each of the processes shown has a unique “fingerprint” in the polarimetric radar variables. Some are similar (e.g., evaporation and size sorting). However, as shown in this study, the *magnitudes* of the changes are different for evaporation and size sorting. Though evaporation and size sorting can cause similar decreases in  $Z_H$  and  $K_{DP}$ , the increase in  $Z_{DR}$  for evaporation (on the order of 0.2 to 0.3 dB) is much smaller than that for size sorting (up to 1 dB or more). This underscores the need to understand how these processes affect the radar measurands in *quantitative* terms. Future work is required to quantitatively describe the processes not fully considered in this dissertation: raindrop breakup, aggregation of snowflakes, melting of ice particles, etc.

With the ongoing upgrade of the WSR-88D radar network to dual-polarization capabilities, polarimetric radar data are expected to play an increasingly important role in both operational meteorology and atmospheric science research. Operational meteorologists will benefit from use of the data in warning decision-making, diagnoses

of storm behavior and intensity, hydrometeor identification, and quantitative precipitation estimation, among many other applications. Research scientists will be able to use data for pure microphysics research, as well as validation studies for precipitation physics parameterizations in numerical models, and eventually, polarimetric radar data assimilation. As more data become available, new signatures and polarimetric fingerprints may be discovered, potentially offering a wealth of new topics for research.



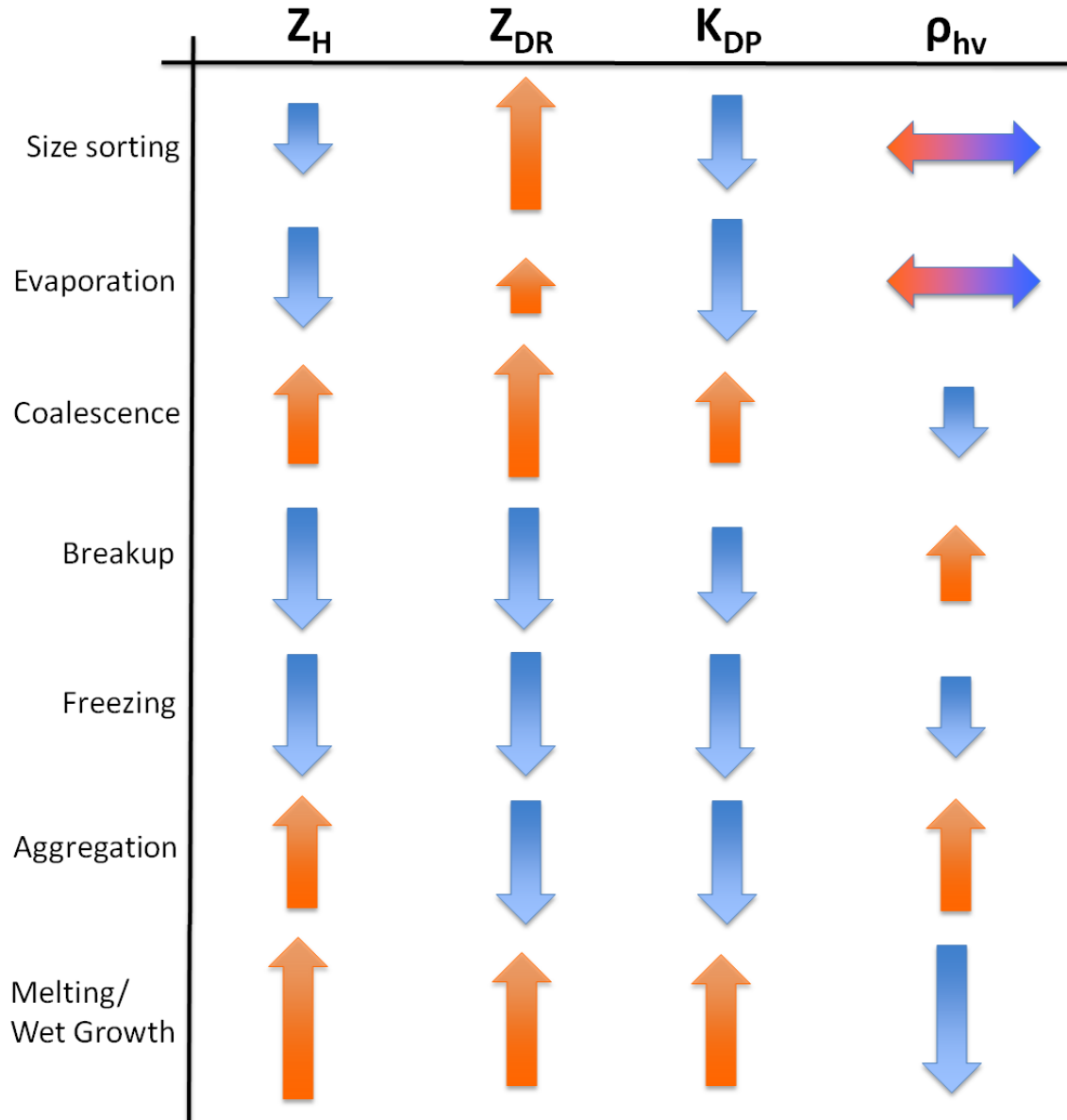


Fig. 9.1: Pictorial catalog of the qualitative polarimetric fingerprints of different microphysical processes. The direction of the arrows indicates the direction of the change in the radar variable owing to the given process. Sideways arrows indicate changes can be in either direction. For a given process, the size of the arrow indicates the magnitude of the change relative to the other variables in a qualitative sense.

## Appendix A: Computing the Complex Dielectric Factor.

### 1. Complex Dielectric Factors for Pure Water and Ice

The electromagnetic scattering properties of hydrometeors and other targets depend on the complex dielectric factor of the substance being illuminated by the incident radiation. Recall that the complex dielectric factor (or relative permittivity)  $\varepsilon$  of a substance characterizes its response to an applied electromagnetic field, including its ability to scatter the radiation, as well as its ability to absorb and dissipate it as thermal energy.

Precipitation particles comprise some combination of liquid water, ice, and air. For simplicity, it is often assumed that the relative permittivity of air  $\varepsilon_{air} \approx 1$ . Formulas for computing the values of  $\varepsilon_{water}$  and  $\varepsilon_{ice}$  are given by Ray (1972):

$$\text{Re}\{\varepsilon\} = \varepsilon_{\infty} + \frac{(\varepsilon_0 - \varepsilon_{\infty}) \left[ 1 + \left(\frac{\lambda_0}{\lambda}\right)^{1-\beta} \sin\left(\frac{\beta\pi}{2}\right) \right]}{1 + 2 \left(\frac{\lambda_0}{\lambda}\right)^{1-\beta} \sin\left(\frac{\beta\pi}{2}\right) + \left(\frac{\lambda_0}{\lambda}\right)^{2(1-\beta)}} , \quad (A1)$$

$$\text{Im}\{\varepsilon\} = \varepsilon_{\infty} + \frac{(\varepsilon_0 - \varepsilon_{\infty}) \left(\frac{\lambda_0}{\lambda}\right)^{1-\beta} \cos\left(\frac{\beta\pi}{2}\right)}{1 + 2 \left(\frac{\lambda_0}{\lambda}\right)^{1-\beta} \sin\left(\frac{\beta\pi}{2}\right) + \left(\frac{\lambda_0}{\lambda}\right)^{2(1-\beta)}} + \frac{\sigma\lambda}{18.8496 \cdot 10^{10}} . \quad (A2)$$

In the case of fresh liquid water,

$$\varepsilon = \varepsilon_{water}$$

$$\varepsilon_0 = 78.54[1 - 4.579 \cdot 10^{-3}(T_C - 25) + 1.19 \cdot 10^{-5}(T_C - 25)^2 - 2.8 \cdot 10^{-8}(T_C - 25)^3]$$

$$\varepsilon_{\infty} = 5.27137 + 0.021647T_C - 0.000131198T_C^2$$

$$\beta = \frac{-16.8129}{(T_C + 273.15)} + 0.0609265$$

$$\lambda_0 = 0.00033836 \exp\left(\frac{2513.98}{T_C + 273.15}\right)$$

$$\sigma = 12.5664 \cdot 10^8$$

and in the case of solid ice (density = 917 kg m<sup>-3</sup>),

$$\varepsilon = \varepsilon_{ice}$$

$$\varepsilon_0 = 203.168 + 2.5T_C + 0.15T_C^2$$

$$\varepsilon_\infty = 3.168$$

$$\beta = 0.288 + 0.0052T_C + 0.00023T_C^2$$

$$\lambda_0 = 0.0009990288 \exp\left[\frac{1.32 \cdot 10^4}{1.9869(T_C + 273.15)}\right]$$

$$\sigma = 1.26 \exp\left[\frac{-1.25 \cdot 10^4}{1.9869(T_C + 273.15)}\right]$$

In the above expressions, the radar wavelength  $\lambda$  is expressed in cm, and the temperature  $T_C$  is in °C. The computed values for  $\varepsilon_{water}$  and  $\varepsilon_{ice}$  over a range of temperatures for the three common weather radar wavelengths (S, C, and X bands) are shown in Figures A1 and A2. Note that  $\varepsilon_{water}$  varies widely over the range of temperatures compared to  $\varepsilon_{ice}$ .

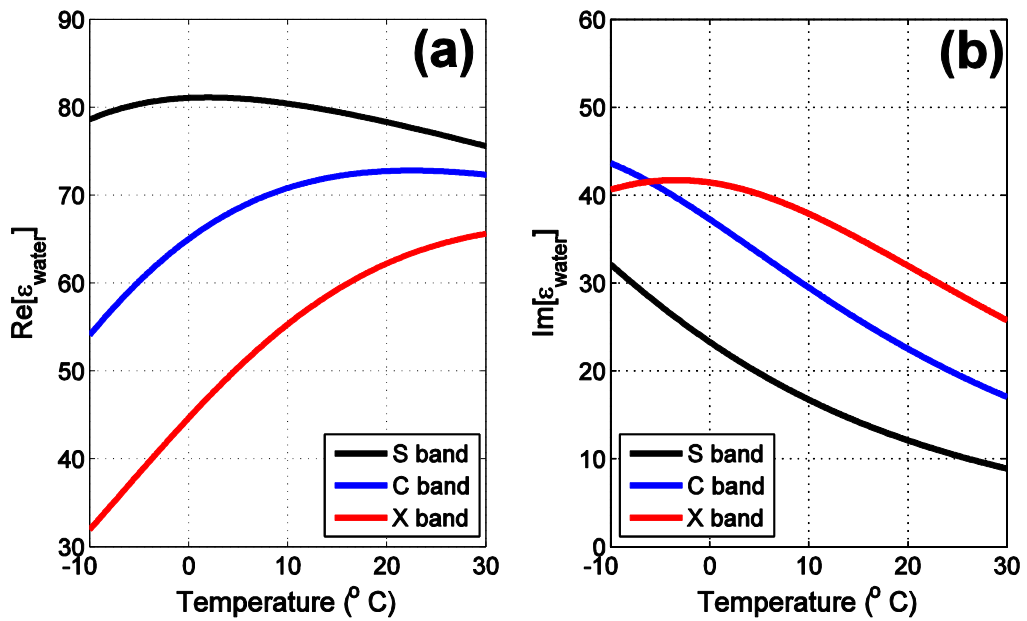


Fig. A1: Values of the (a) real part, and (b) imaginary part of the complex dielectric for water, computed based on the expressions of Ray (1972) for three radar wavelengths: S band (black curves), C band (blue curves), and X band (red curves).

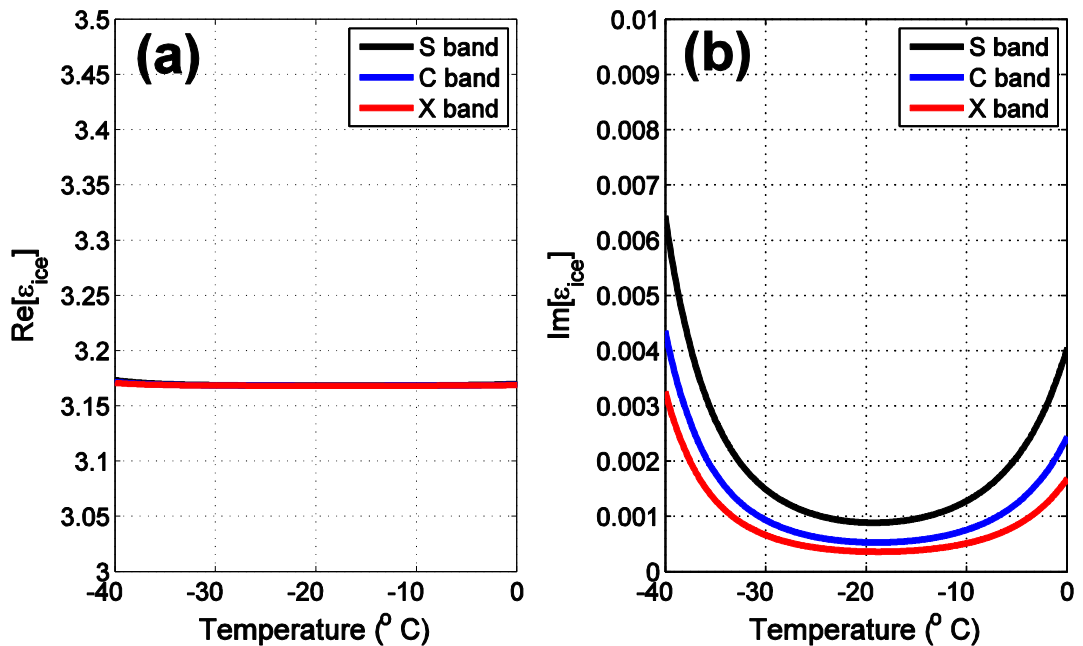


Fig. A2: As in Figure A1, except for ice.

## 2. Complex Dielectric Factors for Mixtures

When hydrometeors are not solid ice or pure liquid water, it is necessary to employ so-called mixing formulas to determine the appropriate complex dielectric. Dry snow, graupel, and low-density hailstones can be considered a mixture of solid ice and air, characterized by a density  $\rho_{particle}$  such that  $\rho_{air} < \rho_{particle} < \rho_{ice}$ . The relative permittivity of such particles is dependent on the volume fraction of ice  $f_{vi}$ , defined as

$$\rho_{particle} = f_{vi}\rho_{ice} + (1 - f_{vi})\rho_{air} \quad . \quad (A3)$$

It follows that

$$f_{vi} = \frac{\rho_{particle} - \rho_{air}}{\rho_{ice} - \rho_{air}} \approx \frac{\rho_{particle}}{\rho_{ice}}. \quad (A4)$$

The mixing formula of Maxwell Garnett (1904)

$$\varepsilon_{particle} = \varepsilon_{air} \left( \frac{1 + 2f_{vi} \frac{\varepsilon_{ice} - \varepsilon_{air}}{\varepsilon_{ice} + 2\varepsilon_{air}}}{1 - f_{vi} \frac{\varepsilon_{ice} - \varepsilon_{air}}{\varepsilon_{ice} + 2\varepsilon_{air}}} \right) \quad (A5)$$

determines the complex dielectric of the particle, which can be rewritten using (A4) and considering  $\varepsilon_{air} \approx 1$  as

$$\varepsilon_{particle} = \frac{1 + 2 \frac{\rho_{particle}}{\rho_{ice}} \frac{\varepsilon_{ice} - 1}{\varepsilon_{ice} + 2}}{1 - \frac{\rho_{particle}}{\rho_{ice}} \frac{\varepsilon_{ice} - 1}{\varepsilon_{ice} + 2}}. \quad (A6)$$

For many radar applications, it is more convenient to express (A6) in the Debye form:

$$\frac{\varepsilon_{particle} - 1}{\varepsilon_{particle} + 2} = \frac{\rho_{particle}}{\rho_{ice}} \frac{\varepsilon_{ice} - 1}{\varepsilon_{ice} + 2}. \quad (A7)$$

Mixed-phase particles include any hydrometeor that comprises some combination of air, ice, and liquid water. This includes melting ice particles and freezing liquid particles. The volume fraction of water  $f_{vw}$  increases (decreases) as

particles progressively melt (freeze) and has a substantial impact on the electromagnetic properties of the particle. However, in addition to the amount of liquid water present in a particle, its distribution is very important. For example, at the onset of melting, snowflakes tend to accumulate most of their liquid water on the outer portions of their branches (e.g., Knight 1979; Matsuo and Sasyo 1981; Fujiyoshi 1986; Mitra et al. 1990). On the other hand, spongy graupel or hailstones tend to accumulate liquid water first in their interior, filling air pockets before accumulating on the exterior (e.g., Rasmussen et al. 1984). High-density hailstones accumulate liquid water in an outer film surrounding the inner core of solid ice (e.g., Rasmussen and Heymsfield 1987). In contrast, a freezing raindrop develops an outer ice shell and freezes inward (e.g., Pruppacher and Klett 1997).

The simplest model of a mixed-phase particle again uses the Maxwell Garnett (1904) formula. However, a choice should be made on how to treat the three constituents (see Fabry and Szyrmer 1999 for a review of numerous ways of treating melting snowflakes). One of the most common approaches for melting snow include treating the snowflake as a “matrix” in which there exist embedded spheroidal water “inclusions” (Fig. A3a). In this case, eqn. (A6) is first used to compute the complex dielectric of the snow matrix ( $\epsilon_{particle}$ ), then

$$\epsilon_{melting}^{(1)} = \epsilon_{particle} \left( \frac{1 + 2f_{vw} \frac{\epsilon_w - \epsilon_{particle}}{\epsilon_{water} + 2\epsilon_{particle}}}{1 - f_{vw} \frac{\epsilon_w - \epsilon_{particle}}{\epsilon_{water} + 2\epsilon_{particle}}} \right). \quad (A8)$$

The other approach is to treat water as the “matrix” containing spheroidal ice-air “inclusions,” (Fig. A3b) in which case

$$\varepsilon_{melting}^{(2)} = \varepsilon_w \left( \frac{1 + 2(1 - f_{vw}) \frac{\varepsilon_{particle} - \varepsilon_w}{\varepsilon_{particle} + 2\varepsilon_w}}{1 - (1 - f_{vw}) \frac{\varepsilon_{particle} - \varepsilon_w}{\varepsilon_{particle} + 2\varepsilon_w}} \right). \quad (A9)$$

These two approaches lead to different results for  $f_{vw} \neq 0$  or  $1$ , which is a source of uncertainty in scattering calculations. Apparently, (A8) works better for lower water fractions and (A9) works better for high water fraction (e.g., Meneghini and Liao 1996; Matrosov 2008; Ryzhkov et al. 2011). Some combinations of (A8) – (A9) have been proposed by these authors, including the expression of Ryzhkov et al. (2011):

$$\varepsilon_{melting} = \frac{1}{2} \left[ (1 + \tau) \varepsilon_{melting}^{(1)} + (1 - \tau) \varepsilon_{melting}^{(2)} \right], \quad (A10)$$

where the parameter

$$\tau = \text{Erf} \left( 2 \frac{1 - f_{vw}}{f_{vw}} - 1 \right) \quad \text{if } f_{vw} > 0.01, \quad (A11)$$

and Erf is the error function.

For melting high-density hailstones, melting graupel in the “soaking” stage, and freezing raindrops, the two-layer approach should be used (Figs. A3c and A3d), where  $\varepsilon_{water}$  and  $\varepsilon_{ice}$  are computed following (A1) – (A2) above.

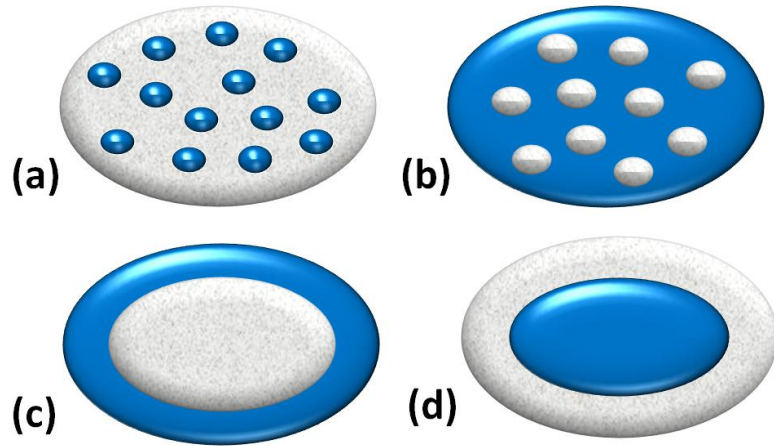


Fig. A3: Schematic cartoon illustrating several different models for treating mixed-phase hydrometeors. (a) Ice matrix with water inclusions; (b) water matrix with ice inclusions; (c) water-coated with an ice core; (d) ice-coated with a water core.

### 3. Impact of the distribution of liquid water on the polarimetric radar variables.

The choice of how water is distributed on or in the particle significantly impacts the polarimetric variables. Figure A4 is a comparison of  $Z_H$  calculated for four different water distribution models of an oblate spheroid composed of water and ice (both spongy models, and both two-layer models). For a given liquid volume fraction  $f_{vw}$ , the normalized  $Z_H$  values can vary by as much as 7 – 10 dBZ, depending on the radar wavelength. In general, the water-coated spheroids produce larger  $Z_H$  for a given  $f_{vw}$ , except for very wet particles at shorter wavelengths.

Figure A5 shows the  $Z_{DR}$  values for the different water distribution models. Note that differences of 2 – 3 dB are possible for the same particle size, shape, and water volume fraction  $f_{vw}$  depending on how the liquid water is distributed. It is not possible to make general statements, such as “Water-coated particles tend to produce larger  $Z_{DR}$ .” This may be true for small values of  $f_{vw}$ , though clearly the behavior is more complex for large  $f_{vw}$  and/or shorter radar wavelengths. For example, at X band, the



largest  $Z_{DR}$  is produced by a spongy particle treated as an ice matrix with water inclusions, whereas for smaller  $f_{vw}$  the  $Z_{DR}$  of water-coated particles is nearly 3 dB larger than the other models. Similar complicated behavior is evident in the normalized  $K_{DP}$  (Fig. A6).

The backscatter differential phase shift ( $\delta$ ) depends strongly on the distribution of liquid water as well (Fig. A7). Whereas  $\delta$  is insignificant at S band (Fig. A7a), it becomes appreciable at C band for water-coated particles (Fig. A7b) and at X band for all models (Fig. A7c). Recall that the distribution of  $\delta$  within the radar sampling volume significantly affects the measured  $\rho_{hv}$ .

$L_{DR}$  values vary significantly for a given  $f_{vw}$  at all wavelengths (Fig. A8). For example, at S band, the  $L_{DR}$  of a water-coated particle can be as much as 6 to 7 dB larger than that of an equally-wet ice-coated particle. This suggests the importance of accretion of liquid water by particles undergoing freezing within convective updrafts in producing the large  $L_{DR}$  values (“ $L_{DR}$  cap”) that are frequently observed (Jameson et al. 1996; Hubbert et al. 1998).

Though attenuation is insignificant at S band for the particle size shown (Figs. A9a,A10a), it becomes important for C and X bands (Figs. A9b-c, A10b-c). Note that the distribution model producing the largest values of  $A_H$  and  $A_{DP}$  depends strongly on the value of  $f_{vw}$ . For example, at X band, water-coated particles composed of 10% liquid water by volume produce the largest  $A_{DP}$ . In contrast, particles with  $f_{vw}$  near 80% that are treated as spongy with an ice matrix and water inclusions produce more than twice the differential attenuation as water-coated particles with the same  $f_{vw}$ .

In summary, the choice of how liquid water is distributed on or within a particle can substantially affect the calculated polarimetric radar variables, especially for shorter radar wavelengths. The choice of liquid water distribution model is thus of great importance, and should be appropriate for the relevant microphysics.

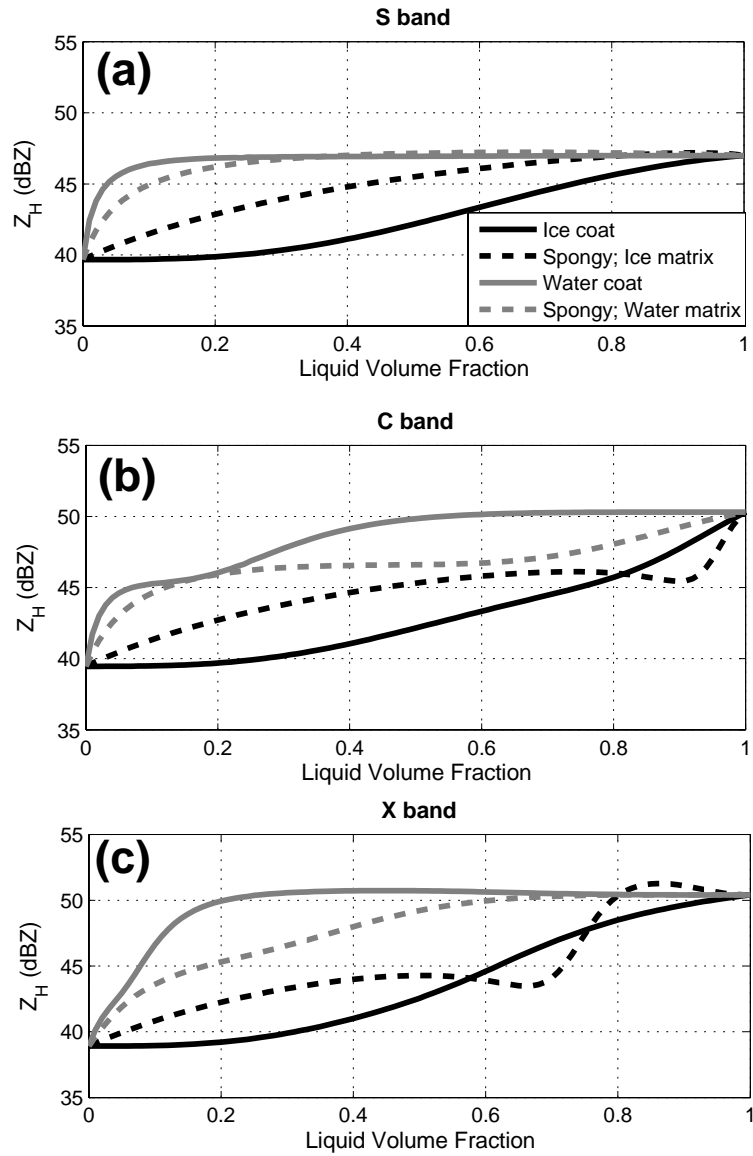


Fig. A4: Normalized values of the radar reflectivity factor at horizontal polarization ( $Z_H$ ) as a function of liquid water volume fraction computed for a 6-mm particle, using four models of water distribution: ice coat with water core (black solid curves), spongy with an ice matrix and water inclusions (black dashed curves), water coat with an ice core (gray solid curves), and spongy with a water matrix and ice inclusions (gray dashed curves). Calculations performed using a T-Matrix code, for three radar wavelengths: (a) S band (10.97 cm), (b) C band (5.4 cm), and (c) X band (3.2 cm). Particle axis ratio is that of an equivalent-sized raindrop.

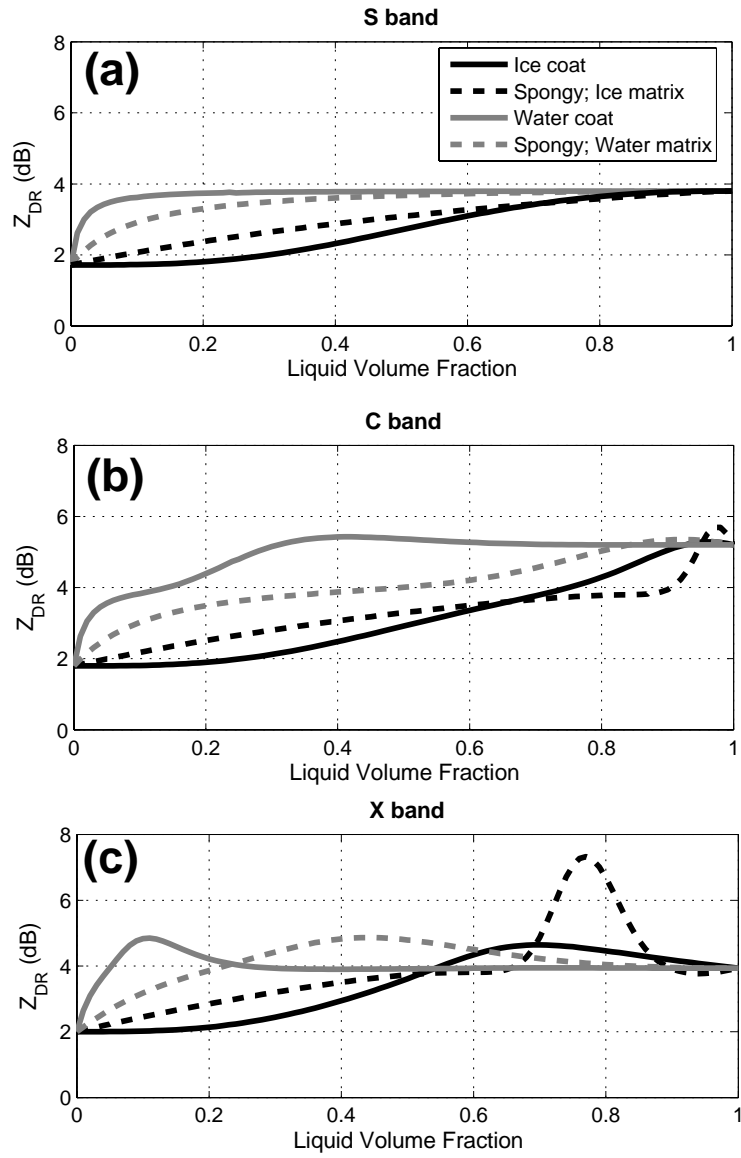


Fig. A5: As in Fig. A4, but differential reflectivity factor ( $Z_{DR}$ ) is shown.

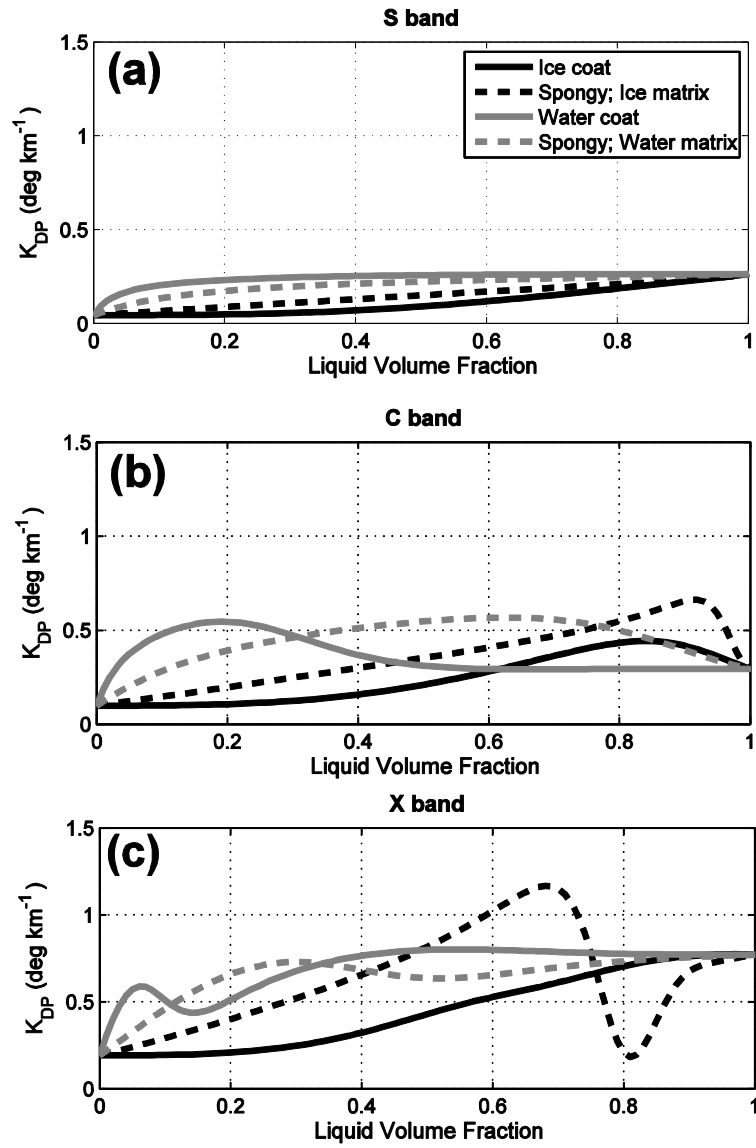


Fig. A6: As in Figs. A4-A5, but normalized values of specific differential phase ( $K_{DP}$ ) are shown.

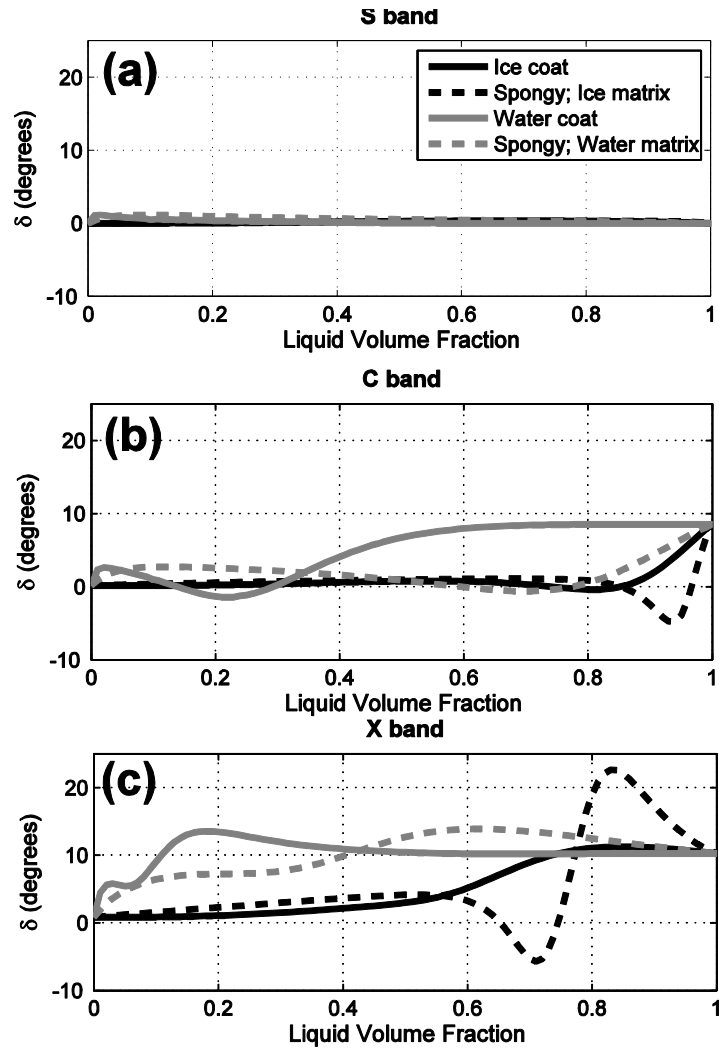


Fig. A7: As in Figs. A4-A6, but the backscatter differential phase shift ( $\delta$ ) is shown.

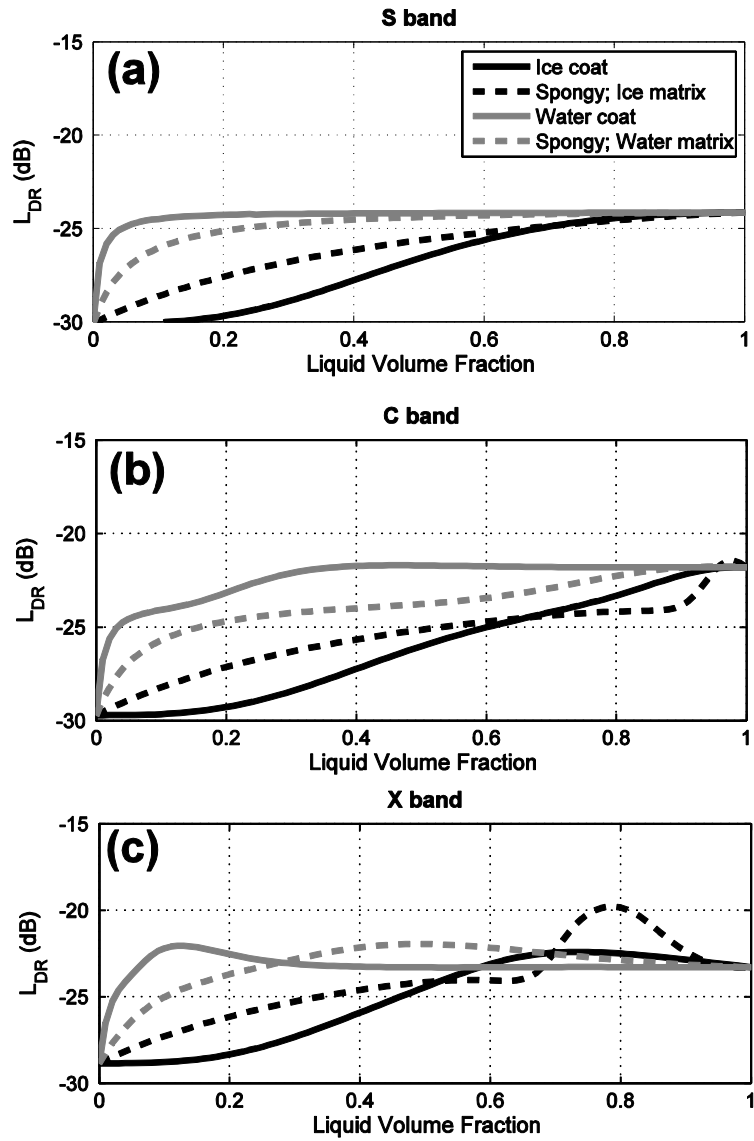


Fig. A8: As in Figs. A4-A7, but the linear depolarization ratio ( $L_{DR}$ ) is shown.

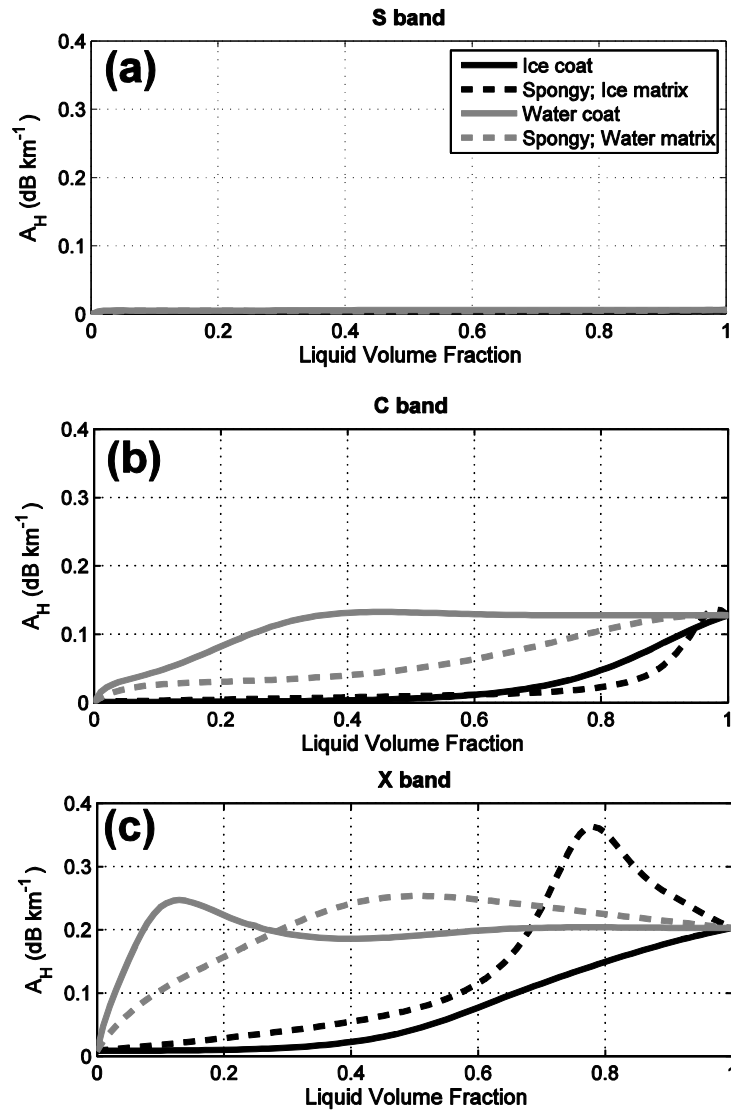


Fig. A9: As in Figs. A4-A8, but normalized values of the specific attenuation at horizontal polarization ( $A_H$ ) are shown.



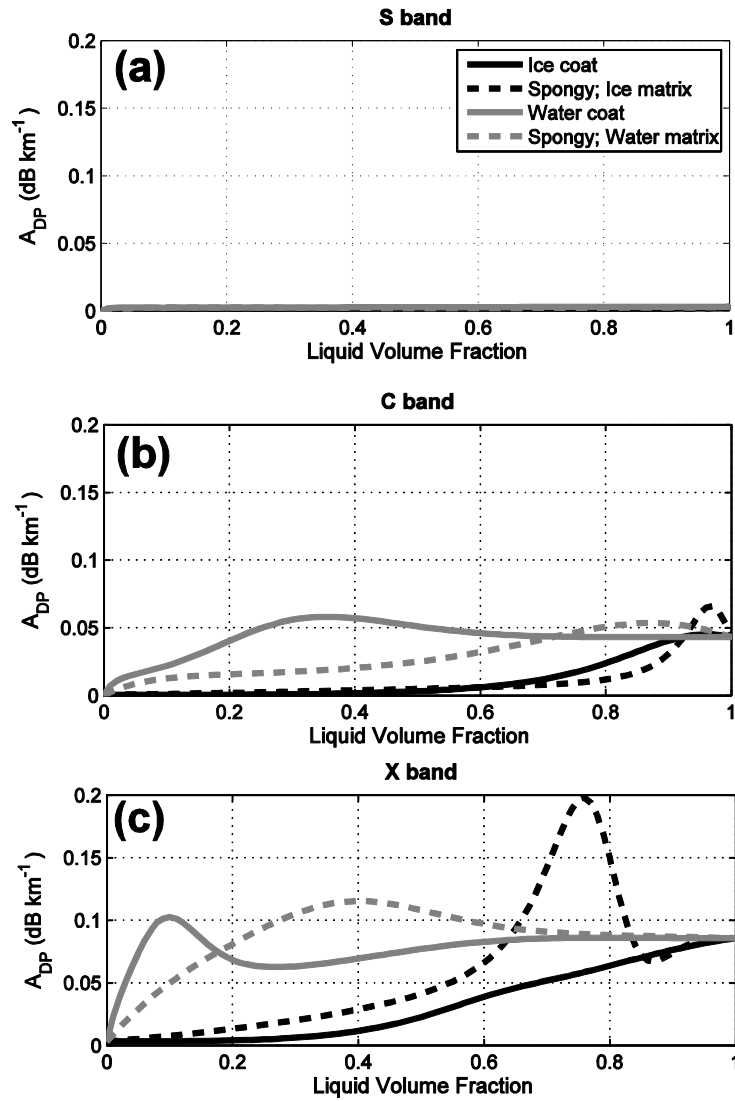


Fig. A10: As in Figs. A4-A9, but specific differential attenuation ( $A_{DP}$ ) is shown.

## Appendix B

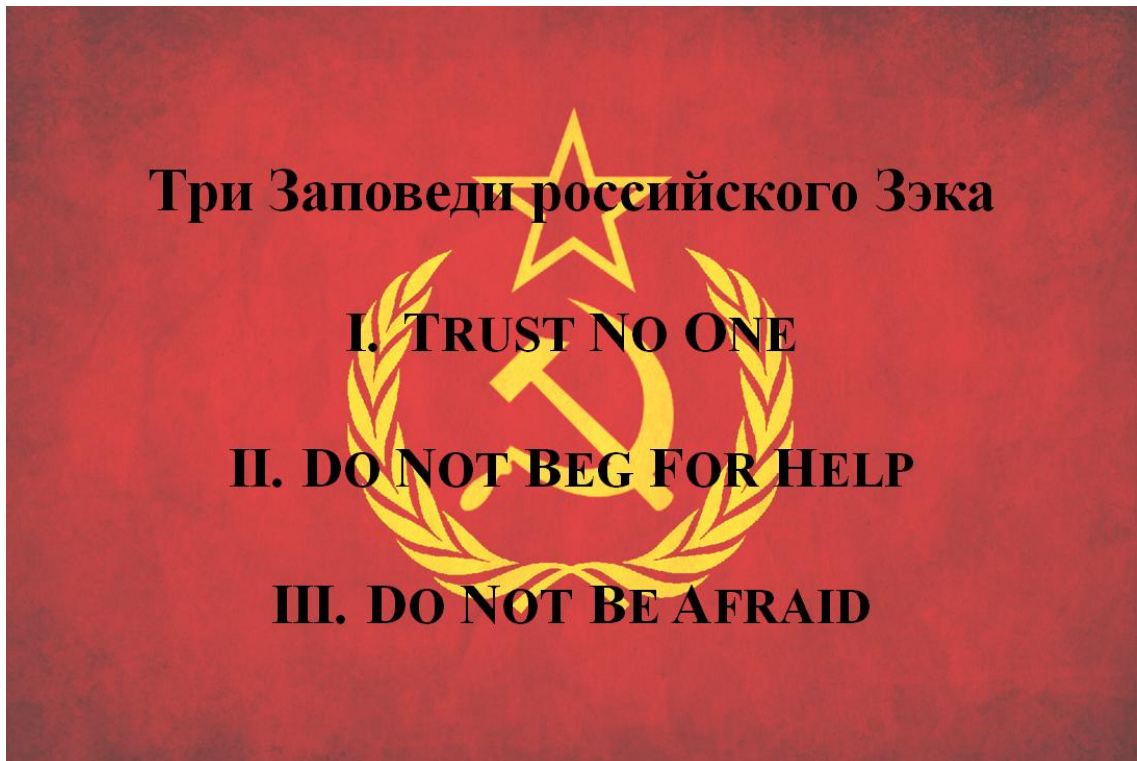


Fig. B1: Три Заповеди российского Зэка (Three Commandments of the Russian Convict).

## References

- Aksoy, A., D. C. Dowell, and C. Snyder, 2009: A multicas e comparative assessment of the Ensemble Kalman Filter for assimilation of radar observations. Part I: Storm-scale analyses. *Mon. Wea. Rev.*, **137**, 1805–1824.
- Anderson, M.E., L.D. Carey, W.A. Petersen, and K.R. Knupp, 2011: C-band dual-polarimetric [*sic*] radar signatures of hail. *Electronic J. Operational Meteor.*, **12**(2), 1-30.
- Andrić, J., M.R. Kumjian, D.S. Zrnić, J.M. Straka, and V.M. Melnikov, 2012: Polarimetric signatures above the melting layer in winter storms: An observational and modeling study. *J. Appl. Meteor. Climatol.*, **in review**.
- Atlas, D., and A.C. Chmela, 1957: Physical-synoptic variations of drop-size parameters. *Proc. 6<sup>th</sup> Weather Radar Conf.*, Amer. Meteor. Soc., Boston, **4**, 21-29.
- Atlas, D., and V.G. Plank, 1953: Drop-size history during a shower. *J. Meteor.*, **10**, 291-295.
- Atlas, D., and C.W. Ulbrich, 1977: Path- and area-integrated rainfall measurement by microwave attenuation in the 1-3-cm band. *J. Appl Meteor.*, **16**, 1322-1331.
- Atlas, D., R.C. Srivastava, and R.S. Sekhon, 1973: Doppler radar characteristics of precipitation at vertical incidence. *Rev. Geophys.*, **11**, 1-35.
- Aydin, K., and Y. Zhao, 1990: A computational study of polarimetric radar observables in hail. *IEEE Trans. Geosci. Remote Sens.*, **28**, 412-422.
- Aydin, K., S.H. Park, and T.M. Walsh, 1998: Bistatic dual-polarization scattering from rain and hail at S- and C-band frequencies. *J. Atmos. Oceanic Technol.*, **15**, 1110-1121.
- Bader, M.J., S.A. Clough, and G.P. Cox, 1987: Aircraft and dual-polarization radar observations of hydrometeors in light stratiform precipitation. *Quart. J. Roy. Meteor. Soc.*, **113**, 491-515.
- Balakrishnan, N., and D.S. Zrnić, 1990a: Estimation of rain and hail in mixed-phase precipitation. *J. Atmos. Sci.*, **47**, 565-583.
- Balakrishnan, N. and D.S. Zrnić, 1990b: Use of polarization to characterize precipitation and discriminate large hail. *J. Atmos. Sci.*, **47**, 1525-1540.
- Barklie, R.H.D., and N.R. Gokhale, 1959: The freezing of supercooled water drops. McGill University, Stormy Weather Group, Sci. Report, MW-30, 43-64.

- Battan, L.J., 1977: Rain resulting from melting ice particles. *J. Appl. Meteor.*, **16**, 595-604.
- Beard, K.V., 1985: Simple altitude adjustments to raindrop velocities for Doppler radar analysis. *J. Atmos. Oceanic Technol.*, **2**, 468-471.
- Beard, K.V., and C. Chuang, 1987: A new model for the equilibrium shape of raindrops. *J. Atmos. Sci.*, **44**, 1509-1524.
- Beard, K.V. and H.T. Ochs, 1995: Collisions between small precipitation drops. Part II: Formulas for coalescence, temporary coalescence, and satellites. *J. Atmos. Sci.*, **52**, 3977-3996.
- Benjamin, S.G., K.A. Brewster, R.L. Brummer, B.F. Jewett, T.W. Schlatter, T.L. Smith, and P.A. Stamus, 1991: An isentropic three-hourly data assimilation system using ACARS aircraft observations. *Mon. Wea. Rev.*, **119**, 888-906.
- Benjamin, S.G., K.J. Brundage, P.A. Miller, T.L. Smith, G.A. Grell, D. Kim, J.M. Brown, and T.W. Schlatter, 1994: The Rapid Update Cycle at NMC. Preprints, *10<sup>th</sup> Conf. on Numerical Weather Prediction*, Portland, OR, Amer. Meteor. Soc., 566-568.
- Benjamin, S.G., D. Dévényi, S.S. Weygandt, K.J. Brundage, J.M. Brown, G.A. Grell, D. Kim, B.E. Schwartz, T.G. Smirnova, and T.L. Smith, 2004: An hourly assimilation-forecast cycle: The RUC. *Mon. Wea. Rev.*, **132**, 495-518.
- Bigg, E.K., 1953a: The supercooling of water. *Proc. Phys. Soc. B*, **66**, 688-694.
- Bigg, E.K., 1953b: The formation of atmospheric ice crystals by the freezing of droplets. *Quart. J. of the Roy. Meteor. Soc.*, **79**, 510-519.
- Blair, S.F., D.R. Deroche, J.M. Boustead, J.W. Leighton, B.L. Barjenbruch, and W.P. Gargan, 2011: A radar-based assessment of the detectability of giant hail. *Electronic J. Severe Storms Meteor.*, **6**(7), 1-30.
- Bohren, C.F., and D.R. Huffman, 1983: *Absorption and Scattering of Light by Small Particles*. Wiley-VCH, Weinheim, Germany, 530 pp.
- Borowska, L., A.V. Ryzhkov, D.S. Zrnić, C. Simmer, and R.D. Palmer, 2011a: Attenuation and differential attenuation of 5-cm-wavelength radiation in melting hail. *J. Appl. Meteor. and Climatol.*, **50**, 59-76.
- Borowska, L., D.S. Zrnić, A.V. Ryzhkov, P. Zhang, and C. Simmer, 2011b: Polarimetric estimates of a 1-month accumulation of light rain with a 3-cm wavelength radar. *J. Hydrometeorol.*, **12**, 1024-1039.

- Brandes, E.A., J. Vivekanandan, J.D. Tuttle, and C.J. Kessinger, 1995: A study of thunderstorm microphysics with multiparameter radar and aircraft observations. *Mon. Wea. Rev.*, **123**, 3129-3143.
- Brandes, E.A., A.V. Ryzhkov, and D.S. Zrnić, 2001: An evaluation of radar rainfall estimates from specific differential phase. *J. Atmos. Oceanic Technol.*, **18**, 363-375.
- Brandes, E.A., G. Zhang, and J. Vivekanandan, 2002: Experiments in rainfall estimation with a polarimetric radar in a subtropical environment. *J. Appl. Meteor.*, **41**, 674-685.
- Brandes, E.A., G. Zhang, and J. Vivekanandan, 2004a: Comparison of polarimetric radar drop size distribution retrieval algorithms. *J. Atmos. and Oceanic Technol.*, **21**, 584-598.
- Brandes, E.A., G. Zhang, and J. Vivekanandan, 2004b: Drop size distribution retrieval with polarimetric radar: Model and application. *J. Appl. Meteor.*, **43**, 461-475.
- Brandes, E.A., G. Zhang, and J. Vivekanandan, 2005: Corrigendum. *J. Appl. Meteor.*, **44**, 186-186.
- Brandes, E.A., K. Ikeda, G. Zhang, M. Schönhuber, and R. Rasmussen, 2007: A statistical and physical description of hydrometeor distributions in Colorado snowstorms using a video disdrometer. *J. Appl. Meteor. and Climatol.*, **46**, 634-650.
- Bringi, V.N., and V. Chandrasekar, 2001: *Polarimetric Doppler Weather Radar*. Cambridge University Press, 336 pp.
- Bringi, V.N., V. Chandrasekar, N. Balakrishnan, and D.S. Zrnić, 1990: An examination of propagation effects on radar measurements at microwave frequencies. *J. Atmos. Oceanic Technol.*, **7**, 829-840.
- Bringi, V.N., K. Knupp, A. Detwiler, L. Liu, I.J. Caylor, and R.A. Black, 1997: Evolution of Florida thunderstorms during the Convection and Precipitation Electrification Experiment: The case of 9 August 1991. *Mon. Wea. Rev.*, **125**, 2131-2160.
- Brown, P.S., 1986: Analysis of the Low and List drop-breakup formulation. *J. Climate Appl. Meteor.*, **25**, 313-321.
- Brown, P.S., 1987: Parameterization of drop-spectrum evolution due to coalescence and breakup. *J. Atmos. Sci.*, **44**, 242-249.
- Brown, P.S., 1993: Analysis and parameterization of the combined coalescence, breakup, and evaporation processes. *J. Atmos. Sci.*, **50**, 2940-2951.

- Brown, P.S., 1994: Vertical variation of the steady-state drop spectrum in a one-dimensional rain shaft. *J. Atmos. Sci.*, **51**, 2075-2085.
- Brown, P.S., 1995: Structural stability of the coalescence/breakup equation. *J. Atmos. Sci.*, **52**, 3857-3865.
- Brussard, G., 1976: A meteorological model for rain-induced cross polarization. *IEEE Trans. Antennas and Propagation*, **24**, 5-11.
- Cao, Q., G. Zhang, E. Brandes, T. Schuur, A.V. Ryzhkov, and K. Ikeda, 2008: Analysis of video disdrometer and polarimetric radar data to characterize rain microphysics in Oklahoma. *J. Appl. Meteor. Climatol.*, **47**, 2238-2255.
- Carey, L.D., W.A. Petersen, M. Thurai, M.E. Anderson, E.V. Schultz, C.J. Schultz, and K. Knupp, 2010: Precipitation properties of a cool-season tornadic storm inferred from C-band dual-polarimetric radar and 2D-video disdrometer observations. *Extended Abstracts*, 25<sup>th</sup> Conf. on Severe Local Storms, Amer. Meteor. Soc., Denver, CO, 15.5. [Available online at <http://ams.confex.com/ams/pdfpapers/175764.pdf>]
- Caylor, I.J., and A.J. Illingworth, 1987: Radar observations and modelling of warm rain initiation. *Quart. J. of the Roy. Meteor. Soc.*, **113**, 1171-1191.
- Caylor, I.J., and V. Chandrasekar, 1996: Time-varying crystal orientation in thunderstorms observed with multiparameter radar. *IEEE Trans. Geosci. Remote Sens.*, **34**, 847-858.
- Clabo, D.R., A.G. Detwiler, and P.L. Smith, 2009: Polarimetric radar signatures of hydrometeors observed within mature convective storms. *Extended Abstracts*, 34<sup>th</sup> Conf. on Radar Meteorology, Amer. Meteor. Soc., Williamsburg, VA, P13.5 [Available online at <http://ams.confex.com/ams/pdfpapers/155110.pdf>].
- Conway, J.W., and D.S. Zrnić, 1993: A study of embryo production and hail growth using dual-Doppler and multiparameter radars. *Mon. Wea. Rev.*, **121**, 2511-2528.
- Dawson, D.T., M. Xue, J.A. Milbrandt, and M.K. Yau, 2010: Comparison of evaporation and cold pool development between single-moment and multi-moment bulk microphysics schemes in idealized simulations of tornadic thunderstorms. *Mon. Wea. Rev.*, **138**, 1152-1171.
- Diehl, K., and S. Wurzler, 2004: Heterogeneous drop freezing in the immersion mode: Model calculations considering soluble and insoluble particles in the drops. *J. Atmos. Sci.*, **61**, 2063-2072.
- Doviak, R.J. and D.S. Zrnić, 1993: *Doppler Radar and Weather Observations*. Academic Press, 562 pp.

- Doviak, R.J., V. Bringi, A.V. Ryzhkov, A. Zahrai, and D.S. Zrnić, 2000: Considerations for polarimetric upgrades to operational WSR-88D radars. *J. Atmos. Oceanic Technol.*, **17**, 257-278.
- Dowell, D.C., L.J. Wicker, and C. Snyder, 2011: Ensemble Kalman Filter assimilation of radar observations of the 8 May 2003 Oklahoma City supercell: Influences of reflectivity observations on storm-scale analyses. *Mon. Wea. Rev.*, **139**, 272-294.
- Draine, B.T., 1988: The discrete-dipole approximation and its application to interstellar graphite grains. *Astrophys. J.*, **333**, 848-872.
- Draine, B.T., and P.J. Flatau, 1994: Discrete-dipole approximation for scattering calculations. *J. Opt. Soc. Am. A*, **11**, 1491-1499.
- Dye, J.E., C.A. Knight, V. Toutenhoofd, and T.W. Cannon, 1974: The mechanism of precipitation formation in northeastern Colorado cumulus. III. Coordinated microphysical and radar observations and summary. *J. Atmos. Sci.*, **31**, 2152-2159.
- Fabry, F., and W. Szyrmer, 1999: Modeling of the melting layer. Part II: Electromagnetic. *J. Atmos. Sci.*, **56**, 3593-3600.
- Federer, B., and A. Waldvogel, 1978: Time-resolved hailstone analyses and radar structure of Swiss storms. *Quart. J. Roy. Meteor. Soc.*, **104**, 69-90.
- Ferrier, B.S., 1994: A double-moment multiple-phase four-class bulk ice scheme. Part I: Description. *J. Atmos. Sci.*, **51**, 249-280.
- Foote, G.B., and P.S. duToit, 1969: Terminal velocity of raindrops aloft. *J. Appl. Meteorology*, **8**, 249-253.
- Fujiyoshi, Y., 1986: Melting snowflakes. *J. Atmos. Sci.*, **43**, 307-311.
- Gershenson, Yu. M., and A.B. Shupyatsky, 1961: Scattering of elliptically polarized radio waves by nonspherical atmospheric particles. *Tr. Cent. Aerolog. Obs.*, **36**, 102-108.
- Giangrande, S.E., 2007: Investigation of polarimetric measurements of rainfall at close and distant ranges. Ph.D. dissertation, University of Oklahoma, 236 pp.
- Giangrande, S.E. and A.V. Ryzhkov, 2008: Estimation of rainfall based on the results of polarimetric echo classification. *J. Appl. Meteor. and Climatol.*, **47**, 2445-2462.
- Giangrande, S. E., A. V. Ryzhkov, and J. Krause, 2005: Automatic detection of the melting layer with a polarimetric prototype of the WSR-88D radar. Extended Abstracts, *32nd Int. Conf. on Radar Meteorology*, Albuquerque, NM, USA, Amer. Meteor. Soc., CD-ROM, 11R.2.

- Giangrande, S.E., J.M. Krause, and A.V. Ryzhkov, 2008: Automatic designation of the melting layer with a polarimetric prototype of the WSR-88D radar. *J. Appl. Meteor. and Climatology*, **47**, 1354-1364.
- Gillespie, J.R. and R. List, 1976: Evolution of raindrop size distributions in steady-state rainshafts. Preprints, *Int. Conf. Cloud Physics*, Boulder, Amer. Meteor. Soc., 472-477.
- Gillespie, J.R., and R. List, 1978: Effects of collision-induced breakup on drop size distributions in steady-state rain-shafts. *Pure Appl. Geophys.*, **117**, 599-626.
- Gosset, M., 2004: Effect of nonuniform beam filling on the propagation of radar signals at X-band frequencies. Part II: Examination of differential phase shift. *J. Atmos. Oceanic Technol.*, **21**, 358-367.
- Grzych, M.L., B.D. Lee, and C.A. Finley, 2007: Thermodynamic analysis of supercell rear-flank downdrafts from project ANSWERS. *Mon. Wea. Rev.*, **135**, 240-246.
- Gu, J.-Y., A.V. Ryzhkov, P. Zhang, P. Neilley, M. Knight, B. Wolf, and D.-I. Lee, 2011: Polarimetric attenuation correction in heavy rain at C band. *J. Appl. Meteor. and Climatology*, **50**, 39-58.
- Gunn, R., and G.D. Kinzer, 1949: The terminal velocity of fall for water droplets in stagnant air. *J. Meteor.*, **6**, 243-248.
- Gunn, R., and J.S. Marshall, 1955: The effect of wind shear on falling precipitation. *J. Meteor.*, **12**, 339-349.
- Hall, M.P.M., J.W.F. Goddard, and S.M. Cherry, 1984: Identification of hydrometeors and other targets by dual-polarization radar. *Rad. Sci.*, **19**, 132-140.
- Heinselman, P.L., and A.V. Ryzhkov, 2006: Validation of polarimetric hail detection. *Wea. Forecasting*, **21**, 839-850.
- Hendry, A., and G.C. McCormick, 1974: Polarization properties of precipitation particles related to storm structure. *J. Rech. Atmos.*, **8**, 189-200.
- Hendry, A., and G.C. McCormick, 1976: Radar observations of alignment of precipitation particles by electrostatic fields in thunderstorms. *J. Geophys. Res.*, **81**, 5353-5357.
- Herzogh, P.H. and A.R. Jameson, 1992: Observing precipitation through dual-polarization radar measurements. *Bull. Amer. Meteor. Soc.*, **73**, 1365-1374.
- Heverly, J.R., 1949: Supercooling and crystallization. *Trans. Amer. Geophys. Union*, **30**, 205-210.



- Hitschfeld, W., 1960: The motion and erosion of convective storms in severe vertical wind shear. *J. Atmos. Sci.*, **17**, 270-282.
- Hobbs, P.V., and A. L. Rangno, 2004: Super-large raindrops. *Geophys. Res. Lett.*, **31**, L13102.
- Hogan, R., P. Field, A. Illingworth, R. Cotton, and T. Choullarton, 2002: Properties of embedded convection in warm-frontal mixed-phase cloud from aircraft and polarimetric radar. *Quart. J. Roy. Meteorol. Soc.*, **128**, 451 – 476
- Höller, H., M. Hagen, P.F. Meischner, V.N. Bringi, and J. Hubbert, 1994: Life cycle and precipitation formation in a hybrid-type hailstorm revealed by polarimetric and Doppler radar measurements. *J. Atmos. Sci.*, **51**, 2500-2522.
- Holroyd, E.W., III, 1971: The meso- and microscale structure of Great Lakes snowstorm bands: A synthesis of ground measurements, radar data, and satellite observations. Ph.D. dissertation, University at Albany, State University of New York, 148 pp.
- Holt, A.R., 1984: Some factors affecting the remote sensing of rain by polarization diversity radar in the 3- to 35-GHz frequency range. *Radio Sci.*, **19**, 1399-1412.
- Holt, A.R., and J.W. Shepherd, 1979: Electromagnetic scattering by dielectric spheroids in the forward and backward directions. *J. Phys. A Math. Gen.*, **12**, 159-166.
- Hu, M., M. Xue, and K. Brewster, 2006a: 3DVAR and cloud analysis with WSR-88D level-II data for the prediction of Fort Worth tornadic thunderstorms. Part I: Cloud analysis and its impact. *Mon. Wea. Rev.*, **134**, 675-698.
- Hu, M., M. Xue, J. Gao, and K. Brewster, 2006b: 3DVAR and cloud analysis with WSR-88D level-II data for the prediction of Fort Worth tornadic thunderstorms. Part II: Impact of radial velocity analysis via 3DVAR. *Mon. Wea. Rev.*, **134**, 699-721.
- Hu, Z., and R. Srivastava, 1995: Evolution of raindrop size distribution by coalescence, breakup, and evaporation: Theory and observations. *J. Atmos. Sci.*, **52**, 1761–1783.
- Hubbert, J., and V.N. Bringi, 2000: The effects of three-body scattering on differential reflectivity signatures. *J. Atmos. Oceanic Technol.*, **17**, 51-61.
- Hubbert, J.C., V.N. Bringi, L.D. Carey, and S. Bolen, 1998: CSU-CHILL polarimetric radar measurements from a severe hail storm in eastern Colorado. *J. Appl. Meteor.*, **37**, 49-775.
- Hubbert, J.C., S.M. Ellis, M. Dixon, and G. Meymaris, 2010a: Modeling, error analysis, and evaluation of dual-polarization variables obtained from simultaneous horizontal and

vertical polarization transmit radar. Part I: Modeling and antenna errors. *J. Atmos. Oceanic Technol.*, **27**, 1583-1598.

Hubbert, J.C., S.M. Ellis, M. Dixon, and G. Meymaris, 2010b: Modeling, error analysis, and evaluation of dual-polarization variables obtained from simultaneous horizontal and vertical polarization transmit radar. Part II: Experimental Data. *J. Atmos. Oceanic Technol.*, **27**, 1599-1607.

Illingworth, A.J., Goddard, J.W.F., Cherry, S.M., 1987: Polarization radar studies of precipitation development in convective storms. *Quart. J. Roy. Meteor. Soc.*, **113**, 469-489.

Jameson, A.R., 1983a: Microphysical interpretation of multi-parameter radar measurements in rain. Part I: Interpretation of polarization measurements and estimation of raindrop sizes. *J. Atmos. Sci.*, **40**, 1792-1802.

Jameson, A.R., 1983b: Microphysical interpretation of multi-parameter radar measurements in rain. Part II: Estimation of raindrop distribution parameters by combined dual-wavelength and polarization measurements. *J. Atmos. Sci.*, **40**, 1803-1814.

Jameson, A.R., 1985a: Microphysical interpretation of multi-parameter radar measurements in rain. Part III: Interpretation and measurement of propagation differential phase shift between orthogonal linear polarizations. *J. Atmos. Sci.*, **42**, 607-614.

Jameson, A.R., 1985b: Deducing the microphysical character of precipitation from multiple-parameter radar polarization measurements. *J. Climate and Appl. Meteor.*, **24**, 1037-1047.

Jameson, A.R., and E.A. Mueller, 1985: Estimation of propagation-differential phase shift from sequential orthogonal linear polarization radar measurements. *J. Atmos. Oceanic Technol.*, **2**, 133-137.

Jameson, A.R., M.J. Murphy, and E.P. Krider, 1996: Multiple parameter radar observations of isolated Florida thunderstorms during the onset of electrification. *J. Appl. Meteor.*, **35**, 343-354.

Johnson, D.A., and J. Hallett, 1968: Freezing and shattering of supercooled water drops. *Quart. J. Roy. Meteor. Soc.*, **94**, 468-482.

Johnson, D.B., 1982: Raindrop multiplication by drop breakup. *J. Appl. Meteor.*, **21**, 1048-1050.

- Jung, Y., M. Xue, G. Zhang, and J.M. Straka, 2008: Assimilation of simulated polarimetric radar data for a convective storm using the Ensemble Kalman Filter. Part II: Impact of polarimetric data on storm analysis. *Mon. Wea. Rev.*, **136**, 2246-2260.
- Jung, Y., M. Xue, and G. Zhang, 2010: Simulations of polarimetric radar signatures of a supercell storm using a two-moment bulk microphysics scheme. *J. Appl. Meteor. and Climatol.*, **49**, 146-163.
- Kennedy, P.C. and S.A. Rutledge, 2011: S-band dual-polarization radar observations of winter storms. *J. Appl. Meteor. and Climatol.*, **50**, 844-858.
- Kennedy, P.C., S.A. Rutledge, W.A. Petersen, and V.N. Bringi, 2001: Polarimetric radar observations of hail formation. *J. Appl. Meteor.*, **40**, 1347-1366.
- Kessler, E., 1969: *On the Distribution and Continuity of Water Substance in Atmospheric Circulations*. *Meteor. Monogr.*, **32**, Amer. Meteor. Soc., 84 pp.
- Khain, A.P., A. Pokrovsky, M. Pinsky, A. Seifert, and V. Phillips, 2004: Simulation of effects of atmospheric aerosols on deep turbulent convective clouds using a spectral microphysics mixed-phase cumulus cloud model. Part I: Model description and possible applications. *J. Atmos. Sci.*, **61**, 2963-2982.
- Khain, A.P., D. Rosenfeld, A. Pokrovsky, U. Blahak, and A. Ryzhkov, 2011: The role of CCN in precipitation and hail in a mid-latitude storm as seen in simulations using a spectral (bin) microphysics model in a 2D frame. *Atmos. Res.*, **99**, 129-146.
- Knight, C.A., and N.C. Knight, 1970: Hailstone embryos. *J. Atmos. Sci.*, **27**, 659-666.
- Knight, C.A., and N.C. Knight, 1974: Drop freezing in clouds. *J. Atmos. Sci.*, **31**, 1174-1176.
- Knight, C.A., 1979: Observations of the morphology of melting snow. *J. Atmos. Sci.*, **36**, 1123-1130.
- Knight, C.A., and N.C. Knight, 2001: Hailstorms. *Severe Convective Storms, Meteor. Monogr.*, **28**, 223-254, C. Doswell, ed.
- Knight, N.C., 1981: The climatology of hailstone embryos. *J. Appl. Meteor.*, **20**, 750-755.
- Kollias, P., B.A. Albrecht, and F.D. Marks, Jr., 2001: Raindrop sorting induced by vertical drafts in convective clouds. *Geophys. Res. Lett.*, **28** (14), 2878-2790.
- Krehbiel, P.R., T. Chen, S. McCrary, W. Rison, G. Gray, and M. Brook, 1996: The use of dual-channel circular-polarization radar observations for remotely sensing storm electrification. *Meteor. Atmos. Phys.*, **59**, 65-82.

- Kumjian, M.R., and A.V. Ryzhkov, 2008a: Polarimetric signatures in supercell thunderstorms. *J. Appl. Meteor. and Climatol.*, **47**, 1940-1961.
- Kumjian, M.R. and A.V. Ryzhkov, 2008b: Microphysical size sorting revealed by dual-polarization Doppler radar. Extended Abstracts, *88<sup>th</sup> Annual AMS Meeting*, New Orleans, Amer., Meteor. Soc., P2.13.
- Kumjian, M.R., and A.V. Ryzhkov, 2009: Storm-relative helicity revealed from polarimetric radar measurements. *J. Atmos. Sci.*, **66**, 667-685.
- Kumjian, M.R., and A.V. Ryzhkov, 2010: The impact of evaporation on polarimetric characteristics of rain: Theoretical model and practical implications. *J. Appl. Meteor. and Climatol.*, **49**, 1247 – 1267.
- Kumjian, M.R., and A.V. Ryzhkov, 2012: The impact of size sorting on the polarimetric radar variables. *J. Atmos. Sci.*, **in press**.
- Kumjian, M.R., J.C. Picca, S. Ganson, A.V. Ryzhkov, J. Krause, and A.P. Khain, 2010a: Polarimetric radar characteristics of large hail. *Extended Abstracts*, 25<sup>th</sup> Conf. on Severe Local Storms, Amer. Meteor. Soc., Denver, CO, 11.2.
- Kumjian, M.R., J.C. Picca, S.M. Ganson, A.V. Ryzhkov, and D.S. Zrnić, 2010b: Three-body scattering signatures in polarimetric radar data. NOAA/NSSL report, 12 pp. Available [http://publications.nssl.noaa.gov/wsr88d\\_reports/FINAL\\_TBSS.doc](http://publications.nssl.noaa.gov/wsr88d_reports/FINAL_TBSS.doc) online at
- Kumjian, M.R., A.V. Ryzhkov, V.M. Melnikov, and T.J. Schuur, 2010c: Rapid-scan super-resolution observations of a cyclic supercell with a dual-polarization WSR-88D. *Mon. Wea Rev.*, **138**, 3762-3786.
- Kumjian, M.R., S.M. Ganson, and A.V. Ryzhkov, 2012a: Freezing of drops within convective updrafts: Microphysical and polarimetric model. *J. Atmos. Sci.*, **in review**.
- Kumjian, M.R., A.V. Ryzhkov, S. Trömel, M. Diederich, K. Mühlbauer, and C. Simmer, 2012b: Retrievals of warm-rain microphysics using X-band polarimetric radar data. *Extended Abstracts*, 92<sup>nd</sup> Annual Meeting of the Amer. Meteor. Soc., and 26<sup>th</sup> Conf. on Hydrology, New Orleans, LA, P406 and 7.6A.
- Langham, E.J., and B.J. Mason, 1958: The heterogeneous and homogeneous nucleation of supercooled water. *Proc. Royal Society*, **A247**, 493-505.
- Lemon, L.R., 1998: The radar “three-body scatter spike”: An operational large-hail signature. *Wea. Forecasting*, **13**, 327-340.
- Li, X., and R.C. Srivastava, 2001: An analytical solution for raindrop evaporation and its application to radar rainfall measurements. *J. Appl. Meteor.*, **40**, 1607–1616.

- Lim, E., and J. Sun, 2010: A velocity dealiasing technique using rapidly updated analysis from a four-dimensional variational Doppler radar data assimilation system. *J. Atmos. Oceanic Technol.*, **27**, 1140-1152.
- List, R., and J.R. Gillepsie, 1976: Evolution of raindrop spectra with collision-induced breakup. *J. Atmos. Sci.*, **33**, 2007-2013.
- List, R. and G.M. McFarquhar, 1990: The evolution of three-peak raindrop size distributions in one-dimensional shaft models. Part I: Single-pulse rain. *J. Atmos. Sci.*, **47**, 2996-3006.
- List, R., N.R. Donaldson, and R.E. Stewart, 1987: Temporal evolution of drop spectra to collisional equilibrium in steady and pulsating rain. *J. Atmos. Sci.*, **44**, 362-372.
- Lo, K.K., and R.E. Passarelli, Jr., 1982: A three-parameter snow growth model. Preprints, *Conf. on Cloud Physics*, Chicago, Amer. Meteor. Soc., 197-200.
- Loney, M.L., D.S. Zrníć, J.M. Straka, and A.V. Ryzhkov, 2002: Enhanced polarimetric radar signatures above the melting level in a supercell storm. *J. Appl. Meteor.*, **41**, 1179-1194.
- Low, T.B. and R. List, 1982a: Collision, coalescence, and breakup of raindrops. Part I: Experimentally established coalescence efficiencies and fragment size distributions in breakup. *J. Atmos. Sci.*, **39**, 1591-1606.
- Low, T.B. and R. List, 1982b: Collision, coalescence, and breakup of raindrops. Part II: Parameterization of fragment size distributions. *J. Atmos. Sci.*, **39**, 1607-1618.
- MacGorman, D.R., and W.D. Rust, 1998: *The Electrical Nature of Storms*. Oxford University Press, 442 pp.
- Maddox, R.A., J. Zhang, J.J. Gourley, and K. Howard, 2002: Weather radar coverage over the contiguous United States. *Weather and Forecasting*, **17**, 927-934.
- Mansell, E.R., 2010: On sedimentation and advection in multimoment bulk microphysics. *J. Atmos. Sci.*, **67**, 3084 – 3094.
- Markowski, P.M., J.M. Straka, and E.N. Rasmussen, 2002: Direct surface thermodynamic observations within the rear-flank downdrafts of nontornadic and tornadic supercells. *Mon. Wea. Rev.*, **130**, 1692-1721.
- Markowski, P.M., J.M. Straka, and E.N. Rasmussen, 2003: Tornadogenesis resulting from the transport of circulation by a downdraft: Idealized numerical simulations. *J. Atmos. Sci.*, **60**, 795-823.

- Marshall, J.S., 1953: Precipitation trajectories and patterns. *J. Meteor.*, **10**, 25-29.
- Marshall, J.S., and W. Mc K. Palmer, 1948: The distribution of raindrops with size. *J. Meteor.*, **5**, 165-166.
- Matrosov, S.Y., 2008: Assessment of radar signal attenuation caused by the melting hydrometeor layer. *IEEE Trans. Geosci. Remote Sens.*, **46**, 1039-1047.
- Matsuo, T. and Y. Sasyo, 1981: Empirical formula for the melting rate of snowflakes. *J. Meteor. Soc. Japan*, **59**, 1-9.
- Maxwell Garnett, J.C., 1904: Color in metal glasses and in metallic films. *Philos. Trans. Roy. Soc. London*, **A203**, 385-420.
- McCormick, G.C., and A. Hendry, 1970: The study of precipitation backscatter at 1.8 cm with a polarization diversity radar. *Preprints 15<sup>th</sup> Radar Meteorology Conf.*, Champaign-Urbana, Amer. Meteor. Soc., 35-38.
- McCormick, G.C., and A. Hendry, 1975: Principles for the radar determination of the polarization properties of precipitation. *Rad. Sci.*, **10**, 421-434.
- McFarquhar, G.M., 2004: A new representation of collision-induced breakup of raindrops and its implications for the shapes of raindrop size distributions. *J. Atmos. Sci.*, **61**, 777-794.
- Meischner, P.F., V.N. Bringi, D. Heimann, and H. Höller, 1991: A squall line in southern Germany: Kinematics and precipitation formation as deduced by advanced polarimetric and Doppler radar measurements. *Mon. Wea. Rev.*, **119**, 678-701.
- Melnikov, V.M., 2006: One-lag estimators for cross-polarization measurements. *J. Atmos. Oceanic Technol.*, **23**, 915-926.
- Melnikov, V.M., and D.S. Zrnić, 2007: Autocorrelation and cross-correlation estimators of polarimetric variables. *J. Atmos. Oceanic Technol.*, **24**, 1337-1350.
- Melnikov, V.M., D.S. Zrnić, R.M. Rabin, and P. Zhang, 2008: Radar polarimetric signatures of fire plumes in Oklahoma. *Geophys. Res. Lett.*, **35**, L14815.
- Melnikov, V.M., D.S. Zrnić, and R.M. Rabin, 2009: Polarimetric radar properties of smoke plumes: A model. *J. Geophys. Res.*, **114**, D21204.
- Meneghini, R., and L. Liao, 1996: Comparisons of cross sections of melting hydrometeors as derived from dielectric mixing formulas and a numerical method. *J. Appl. Meteor.*, **35**, 1658-1670.

- Metcalf, J.I., 1997: Temporal and spatial variations of hydrometeor orientation of hydrometeors in thunderstorms. *J. Appl. Meteor.*, **36**, 315-321.
- Mie, G., 1908: Beiträge zur Optik trüber Medien speziell kolloidaler Metallösungen. *Ann. Phys.*, **25**, 377-445.
- Milbrandt, J.A., and M.K. Yau, 2005a: A multimoment bulk microphysics parameterization. Part I: Analysis of the role of the spectral shape parameter. *J. Atmos. Sci.*, **62**, 3051-3064.
- Milbrandt, J.A., and M.K. Yau, 2005b: A multimoment bulk microphysics parameterization. Part II: A proposed three-moment closure scheme and description. *J. Atmos. Sci.*, **62**, 3065-3081.
- Milbrandt, J.A., and R. McTaggart-Cowan, 2010: Sedimentation-induced errors in bulk microphysics schemes. *J. Atmos. Sci.*, **67**, 3931-3948.
- Minervin, V.E., and A.B. Shupyatsky, 1963: Radar method of determining the phase state of clouds and precipitation. *Tr. Cent. Aerolog. Obs.*, **47**, 63-84.
- Mishchenko, M. I., 2000: Calculation of the amplitude matrix for a nonspherical particle in a fixed orientation. *Appl. Opt.*, **39**, 1026-1031.
- Mitra, S.K., O. Vohl, M. Ahr, and H.R. Pruppacher, 1990: A wind tunnel and theoretical study of the melting behavior of atmospheric ice particles. IV: Experiment and theory for snow flakes. *J. Atmos. Sci.*, **47**, 584 – 591.
- Moisseev, D., and V. Chandrasekar, 2007: Examination of the  $\mu$ - $\Lambda$  relation suggested for drop size distribution parameters. *J. Atmos. Oceanic Technol.*, **24**, 847-855.
- Morgunov, S.P., and A.B. Shupyatsky, 1964: Evaluation of artificial modification efficiency from the polarization characteristics of the echo signal. *Tr. Cent. Aerolog. Obs.*, **57**, 49-54.
- Morris, M., P. Chilson, T.J. Schuur, and A.V. Ryzhkov, 2009: Microphysical retrievals from simultaneous polarimetric and profiling radar observations. *Ann. Geophys.*, **27**, 4435-4448.
- Nelson, S.P., 1983: The influence of storm flow structure on hail growth. *J. Atmos. Sci.*, **40**, 1965-1983.
- NEXRAD Joint System Program Office, 1984: Validation phase, part 2 update. NEXRAD Technical Requirements (NTR) Doc. R400A-SP203, 225 pp.
- Palmer, R.D., D. Bodine, M.R. Kumjian, B. Cheong, G. Zhang, Q. Cao, H.B. Bluestein, A. Ryzhkov, T.-Y. Yu, and Y. Wang, 2011: Observations of the 10 May 2010 tornado

outbreak using OU-PRIME: Potential for new science with high-resolution polarimetric radar. *Bull. Amer. Meteor. Soc.*, **92**, 871-891.

Park, H.-S., A. Ryzhkov, D. Zrnić, and K.E Kim, 2009: The hydrometeor classification algorithm for polarimetric WSR-88D. Description and application to an MCS. *Wea. Forecasting*, **24**, 730-748.

Picca, J.C., and A.V. Ryzhkov, 2010: Polarimetric signatures of melting hail at S and C bands: Detection and short-term forecast. Extended Abstracts, *26<sup>th</sup> Conf. on Interactive Information and Processing Systems (IIPS)*, Atlanta, GA, Amer. Meteor. Soc., 10B.4.

Picca, J.C., and A.V. Ryzhkov, 2012: A dual-wavelength polarimetric analysis of the 16 May 2010 Oklahoma City extreme hailstorm. *Mon. Wea. Rev.*, **140**, 1385-1403.

Picca, J.C., M.R. Kumjian, and A.V. Ryzhkov, 2010:  $Z_{DR}$  columns as a predictive tool for hail growth and storm evolution. Extended Abstracts, *25th Conference on Severe Local Storms*, American Meteorological Society, Denver, Colorado, 11.3.

Pitter, R.L., and H.R. Pruppacher, 1973: A wind tunnel investigation of freezing of small water drops falling at terminal velocity in air. *Quart. J. Roy. Meteor. Soc.*, **99**, 540-550.

Pruppacher, H.R., and K.V. Beard, 1970: A wind tunnel investigation of the internal circulation and shape of water drops falling at terminal velocity in air. *Quart. J. Roy. Meteor. Soc.*, **96**, 247-256.

Pruppacher, H.R. and J.D. Klett, 1978: *Microphysics of Clouds and Precipitation*, 2nd ed. Oxford University Press, 953 pp.

Pruppacher, H.R. and R.L. Pitter, 1971: A semi-empirical determination of the shape of cloud and raindrops. *J. Atmos. Sci.*, **28**, 86-94.

Rasmussen, E.N., and A.J. Heymsfield, 1987: Melting and shedding of graupel and hail. Part I: Model physics. *J. Atmos. Sci.*, **44**, 2754-2763.

Rasmussen, R.M., V. Levizzani, and H.R. Pruppacher, 1984: A wind tunnel study on the melting behavior of atmospheric ice particles. III: Experiment and theory for spherical ice particles of radius  $> 500 \mu\text{m}$ . *J. Atmos. Sci.*, **41**, 381-388.

Rauber, R.M., K. V. Beard, and B. M. Andrews, 1991: A mechanism for giant raindrop formation in warm, shallow convective clouds. *J. Atmos. Sci.*, **48**, 1791-1797.

Ray, P., 1972: Broadband complex refractive indices of ice and water. *Appl. Optics*, **11**, 1836-1844.



Rayleigh, Lord, 1871: On the light from the sky, its polarization and colour, *Philos. Mag.*, **41**, 107-120, 274-279.

Rogers, R.R. and M.K. Yau, 1989: *A Short Course in Cloud Physics*, 3rd ed. Elsevier Press, 290 pp.

Rosenfeld, D. and Y. Mintz, 1988: Evaporation of rain falling from convective clouds as derived from radar measurements. *J. Appl. Meteor.*, **27**, 209-215.

Rosenfeld, D. and C.W. Ulbrich, 2003: Cloud microphysical properties, processes, and rainfall estimation opportunities. *Radar and Atmospheric Science: A Collection of Essays in Honor of David Atlas. Meteorological Monographs*, **30**, 237-258.

Ryzhkov, A.V., 1991: Polarimetric information measurements in radar meteorology. Theoretical model (in Russian). *Radioelectron. Commun. Syst.*, **2**, 17-23.

Ryzhkov, A.V., 2001: Interpretation of polarimetric radar covariance matrix for meteorological scatterers: Theoretical analysis. *J. Atmos. and Oceanic Technol.*, **18**, 315-328.

Ryzhkov, A.V., 2007: The impact of beam broadening on the quality of radar polarimetric data. *J. Atmos. Oceanic Technol.*, **24**, 729-744.

Ryzhkov, A.V., and D. S. Zrnić, 1996: Assessment of rainfall measurement that uses specific differential phase. *J. Appl. Meteor.*, **35**, 2080-1090.

Ryzhkov, A. V., D. S. Zrnić, 1998a: Discrimination between rain and snow with a polarimetric radar. *J. Appl. Meteor.*, **37**, 1228–1240.

Ryzhkov, A. V., D. S. Zrnić, 1998b: Beamwidth effects on the differential phase measurements of rain. *J. Atmos. Oceanic Technol.*, **15**, 624-634.

Ryzhkov, A.V., and D.S. Zrnić, 2005: Radar polarimetry at S, C, and X bands. Comparative analysis and operational implications. Extended Abstracts, *32<sup>nd</sup> Conf. on Radar Meteorology*, Albuquerque, NM, Amer. Meteor. Soc., 9R.3.

Ryzhkov, A.V., and D.S. Zrnić, 2007: Depolarization in ice crystals and its effect on radar polarimetric measurements. *J. Atmos. Oceanic Technol.*, **24**, 1256-1267.

Ryzhkov, A.V., D.S. Zrnić, and B.A. Gordon, 1998: Polarimetric method for ice water content determination. *J. Appl. Meteor.*, **37**, 125-134.

Ryzhkov, A.V., P. Zhang, R.J. Doviak, and C. Kessinger, 2002a: Discrimination between weather and sea clutter using Doppler and dual-polarization weather radars. *XXVII General Assembly of the International Union of Radio Science*, Maastricht, Netherlands, International Union of Radio Science, CD-ROM, 1383.

- Ryzhkov, A.V., D.S. Zrnić, J.C. Hubbert, V.N. Bringi, J. Vivekanandan, and E.A. Brandes, 2002b: Polarimetric radar observations and interpretation of co-cross-polar correlation coefficients. *J. Atmos. Oceanic Technol.*, **19**, 340-354.
- Ryzhkov, A.V., T.J. Schuur, D.W. Burgess, P.L. Heinselman, S.E. Giangrande, and D.S. Zrnić, 2005a: The joint polarization experiment. *Bull. Amer. Meteor. Soc.*, **86**, 809-824.
- Ryzhkov, A.V., S.E. Giangrande, V.M. Melnikov, and T.J. Schuur, 2005b: Calibration issues of dual-polarization radar measurements. *J. Atmos. Oceanic Technol.*, **22**, 1138-1155.
- Ryzhkov, A.V., T.J. Schuur, D.W. Burgess, and D.S. Zrnić, 2005c: Polarimetric tornado detection. *J. Appl. Meteor.*, **44**, 557-570.
- Ryzhkov, A.V., S.E. Giangrande, and T.J. Schuur, 2005d: Rainfall estimation with a polarimetric prototype of WSR-88D. *J. Appl. Meteor.*, **44**, 502-515.
- Ryzhkov, A.V., S.E. Giangrande, A. Khain, M. Pinsky, and A. Pokrovsky, 2008: Exploring model-based polarimetric retrieval of vertical profiles of precipitation. *Extended Abstracts*, 5<sup>th</sup> European Conf. on Radar in Meteorology and Hydrology, Helsinki, Finland, Finnish Meteorological Institute, P6.1.
- Ryzhkov, A., S. Ganson, A. Khain, M. Pinsky, and A. Pokrovsky, 2009: Polarimetric characteristics of melting hail at S and C bands. *34<sup>th</sup> Conference on Radar Meteorology*, Williamsburg, VA, Amer. Meteor. Soc., 4A.6. Available online at [<http://ams.confex.com/ams/pdfpapers/155571.pdf>]
- Ryzhkov, A.V., M. Pinsky, A. Pokrovsky, and A. Khain, 2011: Polarimetric radar observations operator for a cloud model with spectral microphysics. *J. Applied. Meteor. and Climatol.*, **50**, 873-894.
- Sachidananda, M., and D.S. Zrnić, 1985:  $Z_{DR}$  measurement considerations for a fast scan capability radar. *Rad. Sci.*, **20**, 907-922.
- Sachidananda, M. and D.S. Zrnić, 1986: Differential propagation phase shift and rainfall rate estimation. *Radio Sci.*, **21**, 235-247.
- Sachidananda, M., and D.S. Zrnić, 1987: Rain rate estimates from differential polarization measurements. *J. Atmos. Oceanic Technol.*, **4**, 588-598.
- Sauvageot, H., and M. Koffi, 2000: Multimodal raindrop size distributions. *J. Atmos. Sci.*, **57**, 2480-2492.

- Schenkman, A.D., M. Xue, A. Shapiro, K. Brewster, and J. Gao, 2011a: The analysis and prediction of the 8–9 May 2007 Oklahoma tornadic mesoscale convective system by assimilating WSR-88D and CASA radar data using 3DVAR. *Mon. Wea. Rev.*, **139**, 224-246.
- Schenkman, A.D., M. Xue, A. Shapiro, K. Brewster, and J. Gao, 2011b: Impact of CASA radar and Oklahoma Mesonet data assimilation on the analysis and prediction of tornadic mesovortices in a MCS. *Mon. Wea. Rev.*, **139**, 3422-3445.
- Schlatter, P.T., 2003: Polarimetric radar and in-situ measurements of a nontornadic supercell. M.S. Thesis, School of Meteorology, University of Oklahoma, 97 pp.
- Schuur, T.J., A.V. Ryzhkov, D.S. Znić, and M. Schönhuber, 2001: Drop size distributions measured by a 2D video disdrometer: Comparison with dual-polarization radar data. *J. Appl. Meteor.*, **40**, 1019-1034.
- Seifert, A., 2008: On the parameterization of evaporation of raindrops as simulated by a one-dimensional rainshaft model. *J. Atmos. Sci.*, **65**, 3608-3619.
- Seifert, A., A. Khain, U. Blahak, and K.D. Beheng, 2005: Possible effects of collisional breakup on mixed-phase deep convection simulated by a spectral (bin) cloud model. *J. Atmos. Sci.*, **62**, 1917-1931.
- Seliga, T.A., and V.N. Bringi, 1976: Potential use of radar differential reflectivity measurements at orthogonal polarizations for measuring precipitation. *J. Appl. Meteor.*, **15**, 69-76.
- Seliga, T.A., and V.N. Bringi, 1978: Differential reflectivity and differential phase shift: Applications in radar meteorology. *Radio Sci.*, **13**(2), 271-275.
- Seliga, T.A., R.G. Humphries, and J.I. Metcalf, 1990: Polarization diversity in radar meteorology: Early developments. *Radar in Meteorology: Battan Memorial and 40<sup>th</sup> Anniversary Radar Meteorology Conference*, D. Atlas, Ed., Amer. Meteor. Soc., 109-114.
- Shapiro, A., 2005: Drag-induced transfer of horizontal momentum between air and raindrops. *J. Atmos. Sci.*, **62**, 2205-2219.
- Shupyatsky, A.B., 1959: Radar scattering by nonspherical particles. *Trans. Cent. Aerolog. Obs.*, **30**, 39-52.
- Shupyatsky, A.B., and S.P. Morgunov, 1963: The application of polarization methods to radar studies of clouds and precipitation. *Tr. Vsesoiuznoe Nauchi Meteor. Soveshchaniia Leningrad*, 295-305.
- Skolnick, M.I., 1980: *Introduction to Radar Systems*. McGraw-Hill, New York, 772 pp.

- Smith, P.L., 1984: Equivalent radar reflectivity factors for snow and ice particles. *J. Climate and Applied Meteorology*, **23**, 1258-1260.
- Smith, P.L., D.J. Musil, A.G. Detwiler, and R. Ramachandran, 1999: Observations of mixed-phase precipitation within a CaPE thunderstorm. *J. Appl. Meteor.*, **38**, 145-155.
- Snook, N., M. Xue, and Y. Jung, 2011: Analysis of a tornadic mesoscale convective vortex based on Ensemble Kalman Filter assimilation of CASA X-band and WSR-88D radar data. *Mon. Wea. Rev.*, **139**, 3446-3468.
- Snyder, C., and F. Zhang, 2003: Assimilation of simulated Doppler radar observations with an Ensemble Kalman Filter. *Mon. Wea. Rev.*, **131**, 1663–1677.
- Snyder, J.C., H.B. Bluestein, G. Zhang, and S.J. Frasier, 2010: Attenuation correction and hydrometeor classification of high-resolution, X-band, dual-polarized mobile radar measurements in severe convective storms. *J. Atmos. Oceanic Technol.*, **27**, 1979-2001.
- Srivastava, R.C., 1978: Parameterization of raindrop size distributions. *J. Atmos. Sci.*, **35**, 108-117.
- Srivastava, R., 1985: A simple model of evaporatively driven downdraft: Application to microburst downdraft. *J. Atmos. Sci.*, **42**, 1004–1023.
- Srivastava, R., 1987: A model of intense downdrafts driven by the melting and evaporation of precipitation. *J. Atmos. Sci.*, **44**, 1752–1774.
- Straka, J.M., and M.S. Gilmore, 2006: Does the influence of oblate-like distortions in larger raindrops make a difference in collection and evaporation parameterizations? *J. Appl. Meteor. and Climatol.*, **45**, 1582-1591.
- Straka, J.M., D.S. Zrnić, and A.V. Ryzhkov, 2000: Bulk hydrometeor classification and quantification using polarimetric radar data: Synthesis of relations. *J. Appl. Meteor.*, **39**, 1341-1372.
- Szumowski, M.J., R.M. Rauber, H.T. Ochs III, and L.J. Miller, 1997: The microphysical structure and evolution of Hawaiian rainband clouds. Part I: Radar observations of rainbands containing high reflectivity cores. *J. Atmos. Sci.*, **54**, 369-385.
- Tardif, R. and R.M. Rasmussen, 2010: Evaporation of non-equilibrium raindrops as a fog formation mechanism. *J. Atmos. Sci.*, **67**, 345 – 364.
- Teshiba, M.S., P.B. Chilson, A.V. Ryzhkov, T.J. Schuur, R.D. Palmer, 2009: A combined wind profiler and polarimetric weather radar method for the investigation of precipitation and vertical velocities. *J. Atmos. Oceanic Technol.*, **26**, 1940–1955.

- Testud, J., E. Le Bouar, E. Obligis, and M. Ali-Mehenni, 2000: The rain profiling algorithm applied to polarimetric weather radar. *J. Atmos. Oceanic Technol.*, **17**, 332-356.
- Thériault, J.M., and R.E. Stewart, 2010: A parameterization of the microphysical processes forming many types of winter precipitation. *J. Atmos. Sci.*, **67**, 1492-1508.
- Thurai, M., and V.N. Bringi, 2005: Drop axis ratios from a 2D video disdrometer. *J. Atmos. Oceanic Technol.*, **22**, 966-978.
- Thurai, M., V.N. Bringi, M. Szakáll, S.K. Mitra, K.V. Beard, and S. Borrmann, 2009: Drop shapes and axis ratio distributions: comparison between 2D video disdrometer and wind-tunnel measurements. *J. Atmos. Oceanic Technol.*, **26**, 1427-1432.
- Tokay, A., O.W. Thiele, A. Kruger, and W.F. Krajewski, 1999: New measurements of drop size distribution and its impact on radar rainfall retrievals. Preprints, *29<sup>th</sup> Int. Conf. on Radar Meteorology*, Montreal, PQ, Canada, Amer. Meteor. Soc., 659-662.
- Tong, M., and M. Xue, 2005: Ensemble Kalman Filter assimilation of Doppler radar data with a compressible nonhydrostatic model: OSS experiments. *Mon. Wea. Rev.*, **133**, 1789-1807.
- Tuttle, J.D., V.N. Bringi, H.D. Orville, F.J. Kopp, 1989: Multiparameter radar study of a microburst: Comparison with model results. *J. Atmos. Sci.*, **46**, 601-620.
- Tzivion, S., G. Feingold, and Z. Levin, 1989: The evolution of raindrop spectra. Part II: Collisional collection/breakup and evaporation in a rainshaft. *J. Atmos. Sci.*, **46**, 3312-3327.
- Ulaby, F., R. Moore, and A. Fung, 1982: *Microwave remote sensing*. Vol. II, Addison – Wesley Publishing Company, 1064 pp.
- Ulbrich, C.W., 1983: Natural variations in the analytical form of the raindrop size distribution. *J. Climate Appl. Meteor.*, **22**, 1764-1775.
- Ulbrich, C.W., and D. Atlas, 2007: Microphysics of raindrop size spectra: tropical continental and maritime storms. *J. Appl. Meteor. and Climatol.*, **46**, 1777-1791.
- Umlinger, W.G., 1981: A new formula for raindrop terminal velocity. *Proc. 20<sup>th</sup> Conf. on Radar Meteorology*, Boston, Amer. Meteor. Soc., 389-391.
- Vali, G., 1971: Quantitative evaluation of experimental results on the heterogeneous freezing nucleation of supercooled liquids. *J. Atmos. Sci.*, **28**, 402-409.
- Vali, G., 1994: Freezing rate due to heterogeneous nucleation. *J. Atmos. Sci.*, **51**, 1843-

1856.

Vivekanandan, J., W.M. Adams, and V.N. Bringi, 1991: Rigorous approach to polarimetric radar modeling of hydrometeor orientation distributions. *J. Appl. Meteor.*, **30**, 1053-1063.

Wacker, U., and C. Lüpkes, 2009: On the selection of prognostic moments in parametrization schemes for drop sedimentation. *Tellus*, **61A**, 498–511.

Wacker, U. and A. Seifert, 2001: Evolution of rain water profiles resulting from pure sedimentation: Spectral vs. parameterized description. *Atmos. Res.*, **58**, 19-39.

Waterman, P.C., 1969: Scattering by dielectric obstacles. *Alta Frequenza*, (Speciale), 348-352.

Williams, C.R., P.E. Johnston, W.L. Ecklund, K.S. Gage, and D.A. Carter, 2000: Rain drop size distribution deduced from UHF and S-band profilers used in support of ground validation of the TRMM satellite. *Proc. URSI National Radio Science Meeting*, Boulder, CO, International Union of Radio Science, 296.

Wilson, J.W., and D. Reum, 1988: The flare echo: Reflectivity and velocity signature. *J. Atmos. Oceanic Technol.*, **5**, 197-205.

Wisner, C., H.D. Orville, and C. Myers, 1972: A numerical model of a hail-bearing cloud. *J. Atmos. Sci.*, **29**, 1160-1181.

Young, K.C., 1975: The evolution of drop spectra due to condensation, coalescence, and breakup. *J. Atmos. Sci.*, **32**, 965-973.

Yu, T.-Y., R.R. Rondinel, and R.D. Palmer, 2009: Investigation of non-Gaussian Doppler spectra observed by weather radar in a tornadic supercell. *J. Atmos. Oceanic Technol.*, **26**, 444-461.

Yussouf, N., and D.J. Stensrud, 2012: Comparison of single-parameter and multi-parameter Ensembles for assimilation of radar observations using the Ensemble Kalman Filter. *Mon. Wea. Rev.*, **140**, 562-586.

Zawadzki, I., and M. De Agostinho Antonio, 1988: Equilibrium raindrop size distributions in tropical rain. *J. Atmos. Sci.*, **45**, 3452-3459.

Zhang, G., J. Vivekanandan, and E.A. Brandes, 2001: A method for estimating rain rate and drop size distribution from polarimetric radar measurements. *IEEE Trans. Geosci. Remote Sens.*, **39** (4), 830-840.

- Zhang, G., J. Vivekanandan, and E.A. Brandes, R. Meneghini, and T. Kozu, 2003: The shape-slope relation in gamma raindrop size distributions: Statistical error or useful information? *J. Atmos. Oceanic Technol.*, **20**, 1106-1119.
- Zhang, G., J. Sun, and E.A. Brandes, 2006: Improving parameterization of rain microphysics with disdrometer and radar observations. *J. Atmos. Sci.*, **63**, 1273–1290.
- Ziegler, C., 1985: Retrieval of thermal and microphysical variables in observed convective storms. Part I: Model development and preliminary testing. *J. Atmos. Sci.*, **42**, 1487-1509.
- Ziegler, C.L., P.S. Ray, and N.C. Knight, 1983: Hail growth in an Oklahoma multicell storm. *J. Atmos. Sci.*, **40**, 1768-1792.
- Zrnić, D.S., 1987: Three-body scattering produces precipitation signature of special diagnostic value. *Radio Sci.*, **22**, 76-86.
- Zrnić, D.S., 1991: Complete polarimetric and Doppler measurements with a signal receiver radar. *J. Atmos. Oceanic Technol.*, **8**, 159-165.
- Zrnić, D.S., and A.V. Ryzhkov, 1996: Advantages of rain measurements using specific differential phase. *J. Atmos. Oceanic Technol.*, **13**, 454-464.
- Zrnić, D.S. and A.V. Ryzhkov, 1999: Polarimetry for weather surveillance radars. *Bull. Amer. Meteor. Soc.*, **80**, 389-406.
- Zrnić, D.S. and A.V. Ryzhkov, 2004: Polarimetric properties of chaff. *J. Atmos. Oceanic Technol.*, **21**, 1017-1024.
- Zrnić, D.S., N. Balakrishnan, C.L. Ziegler, V.N. Bringi, K. Aydin, and T. Matejka, 1993: Polarimetric signatures in the stratiform region of a mesoscale convective system. *J. Appl. Meteor.*, **32**, 678-693.
- Zrnić, D.S., R.J. Doviak, G. Zhang, and A.V. Ryzhkov, 2010a: Bias in differential reflectivity due to cross coupling through the radiation patterns of polarimetric weather radars. *J. Atmos. Oceanic Technol.*, **27**, 1624-1637.
- Zrnić, D.S., G. Zhang, V. Melnikov, and J. Andrić, 2010b: Three-body scattering and hail size. *J. Appl. Meteor. Climatol.*, **49**, 687-700.